ISSN 2188-1456

JAEA R&D Review 2013

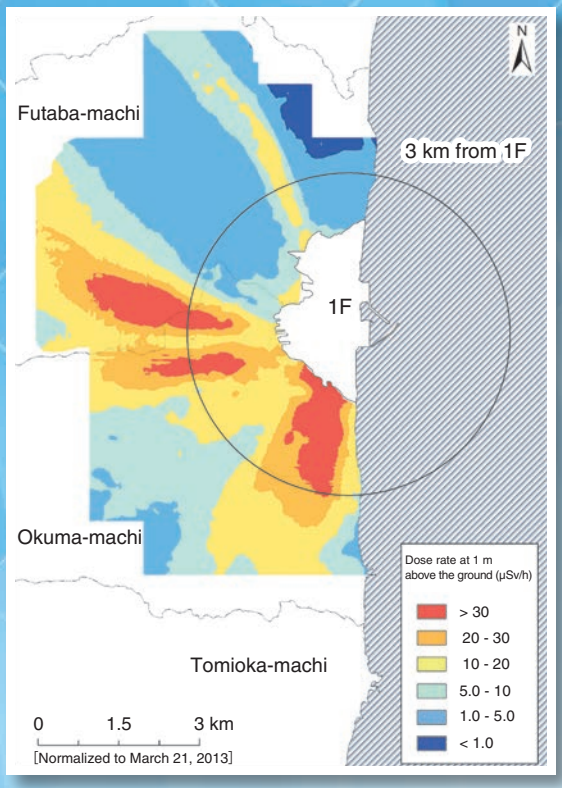

Dose rate distribution map around the TEPCO's Fukushima Daiichi NPS (1F), which was traced out using an unmanned helicopter

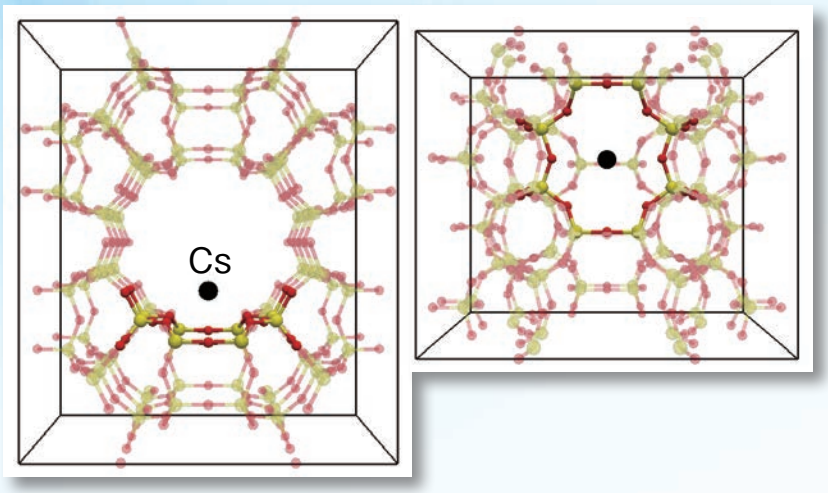

Atomic-scale cesium absorption on a type of zeolite called mordenite

Message from the President

松浦祥次郎

President Shojiro MATSUURA

We sincerely thank you for your understanding and continued support of our research and development activities. Since the foundation of the Japan Atomic Energy Agency (JAEA), this publication has been brought out every year with the intention of informing you of the day-to-day accomplishments of the JAEA.

As the only research institute in Japan dedicated to comprehensive nuclear research and development, the JAEA plays a primary role in steadily promoting research and development in nuclear technology and, in the wake of the accident at the Fukushima Daiichi Nuclear Power Station of Tokyo Electric Power Company, Incorporated (TEPCO), has focused on investing efforts toward the recovery of the damaged reactor site and the reconstruction of the affected area. Furthermore, with serious consideration of the fact that we have not been successful in the maintenance of the prototype fast breeder reactor Monju and in preventing the radioactive material leak at the Hadron Experimental Facility of Japan Proton Accelerator Research Complex (J-PARC), we are in the process of promoting activities for establishing a safety culture in accordance with the fundamental policies of Japanese government. Moreover, the employees are working as a unit towards a structural reform for restoring the trust of society in the institute, in accordance with the plan that the JAEA prescribed.

More than two and a half years have passed since the accident at the TEPCO's Fukushima Daiichi Nuclear Power Station; in this time, the JAEA has been engaged in post-accident environmental remediation and decommissioning of the damaged reactors by fully utilizing the integrated capability of the scientific and technical experts and its research facilities. To deal with the environmental pollution by radioactive materials, Fukushima Environmental Safety Center, of the Headquarters of Fukushima Partnership Operations, has been set up as the base of our operations. Here, we have performed research and development activities such as analyses of soil and water, tests accompanying decontamination such as the control of amount and volume reduction of the contaminated waste from the soil after the accident, demonstration tests on a decontamination model in high-dose regions, and studies on decontamination efficacy evaluation methods. In addition, for research and development related to the decommissioning of units 1 to 4 of the TEPCO's Fukushima Daiichi Nuclear Power Station, we have promoted tests on the long-term integrity of the fuel assembly in the spent fuel storage pool, the characterization of the fuel debris for the preparation of its removal, and the treatment and disposal of radioactive waste caused by the accident.

For future research and development of the fast breeder reactor cycle technology, including Monju, we will proceed in accordance with the review of the nuclear energy policy of Japanese government. We will prioritize the safety of Monju and will also perform operations management and work toward international standardization of the safety design requirements of fast breeder reactors. Moreover, for the activities on the backend of nuclear energy utilization, which are necessary irrespective of the future nuclear energy policy, we have performed research and development on decommissioning, and the treatment and disposal of radioactive waste.

In the research and development aimed at the practical utilization of nuclear fusion energy, we, as a domestic agency/implementing agency of Japan under roles based on the international framework (ITER Project/BA activity), have been promoting our operations using the world's most advanced technologies along the plan that the JAEA prescribed. As part of the research and development on quantum beam science, we have been producing a variety of results in areas ranging from the fundamentals of science and technology to industrial applications, through various quantum beam facility groups owned by the JAEA. Moreover, we have recognized that ensuring nuclear safety is an important step in the use of nuclear power, and we have diligently conducted nuclear safety research for the improvement of safety in the utilization of nuclear energy. In addition, we have promoted a wide variety of engineering research activities, which will serve as the basis in the development of nuclear energy utilization in Japan; these activities have led to many accomplishments.

Hereafter, we are steadily proceeding with structural reforms in accordance with the plan that the JAEA has set forth. With the increased expectations toward the JAEA's role in nuclear technology development after the TEPCO's Fukushima Daiichi Nuclear Power Station accident, we are now actively involved in medium-to-long-term human resource development for nuclear technology, industry–academia–government collaborations, promotion of international cooperation with overseas research institutes, and the dissemination of the achievements made in research and development, without failing to prioritize operations.

We are pleased that you will gain further understanding of the accomplishments of the JAEA through this publication, and we thank you for your continued encouragement and guidance in our research and development activities.

2 Research and Development of Advanced Nuclear System

3 Research and Development on Geological Disposal of High-Level Radioactive Waste

4 Nuclear Fusion Research and Development

About This Publication and the Outline of Organization of JAEA

This publication introduces the latest accomplishments of research and development (R&D) in the JAEA, which are chaptered by area of study. Each chapter corresponds to the activities of one R&D Directorate. As shown in the organization chart and the map below, the R&D Directorates perform their activities through R&D Institutes and Centers, which are located widely in Japan as the sites for R&D. Some R&D directorates are located at one site, others are at two or more. The following outlines the activities undertaken by R&D Directorates and R&D Institutes and Centers.

1. The **Headquarters of Fukushima Partnership Operations** is engaged in R&D to recover from the accident at the Tokyo Electric Power Company, Incorporated Fukushima Daiichi Nuclear Power Station. Partnership operations for plant restoration have set up "Special Teams for Technologies Development" at three centers of JAEA: the Nuclear Science Research Institute, the Nuclear Fuel Cycle Engineering Laboratories, and the Oarai Research and Development Center. These centers conduct R&D to restore the interior of the nuclear power plant. Fukushima Environmental Safety Center in the Fukushima prefecture is conducting R&D concerning decontamination technologies to restore the environment, develop outreach activities concerning radiation, and study measurement of radioactive materials in the human body by whole-body counters. In addition, Nuclear Plant Decommissioning Safety Research Establishment has been established, and we are working on the analysis and research of radioactive materials and development of remote controlled robot and its demonstration plant.
2. The **Advanced Nuclear System Research and Development Directorate** is carrying out R&D aimed at commercializing the fast breeder reactor (FBR) and its nuclear fuel cycle. The R&D of plant technology using the prototype fast breeder reactor "MONJU" is being undertaken at the Tsuruga Head Office (Fast Breeder Reactor Research and Development Center), R&D for innovative FBR technology is being conducted at the Oarai Research and Development Center, and R&D on manufacturing plutonium fuel and reprocessing spent FBR fuel is being conducted at the Tokai Research and Development Center (Nuclear Fuel Cycle Engineering Laboratories).
3. The **Geological Isolation Research and Development Directorate** is carrying out multidisciplinary R&D aimed at improving the reliability of geological isolation of high-level radioactive waste in Japan. A particular focus involves establishing techniques for investigating the deep geological environment through research on crystalline rocks at the Tono Geoscience Center and research on sedimentary rocks at the Horonobe Underground Research Center. At the Tokai Research and Development Center, the focus is on improving technologies for designing disposal facilities and safety assessment. In addition, work has been ongoing to develop a next generation knowledge management system based on the above R&D activities.
4. The **Fusion Research and Development Directorate** is performing fusion R&D as a domestic agency of the International Thermonuclear Experimental Reactor (ITER) project and an implementing agency of the Broader Approach (BA) activities. The procurement activity of the ITER project, the upgrade of JT-60 to a superconducting machine as the BA activity, fusion plasma research, and R&D on various element technologies are carried out in the Naka Fusion Institute. Moreover, the International Fusion Energy Research Center project and the Engineering Validation and Engineering Design Activities of the International Fusion Material Irradiation Facility as the BA activity are performed mainly in the Aomori Research and Development Center.

Japan Atomic Energy Agency -Outline of Organization-

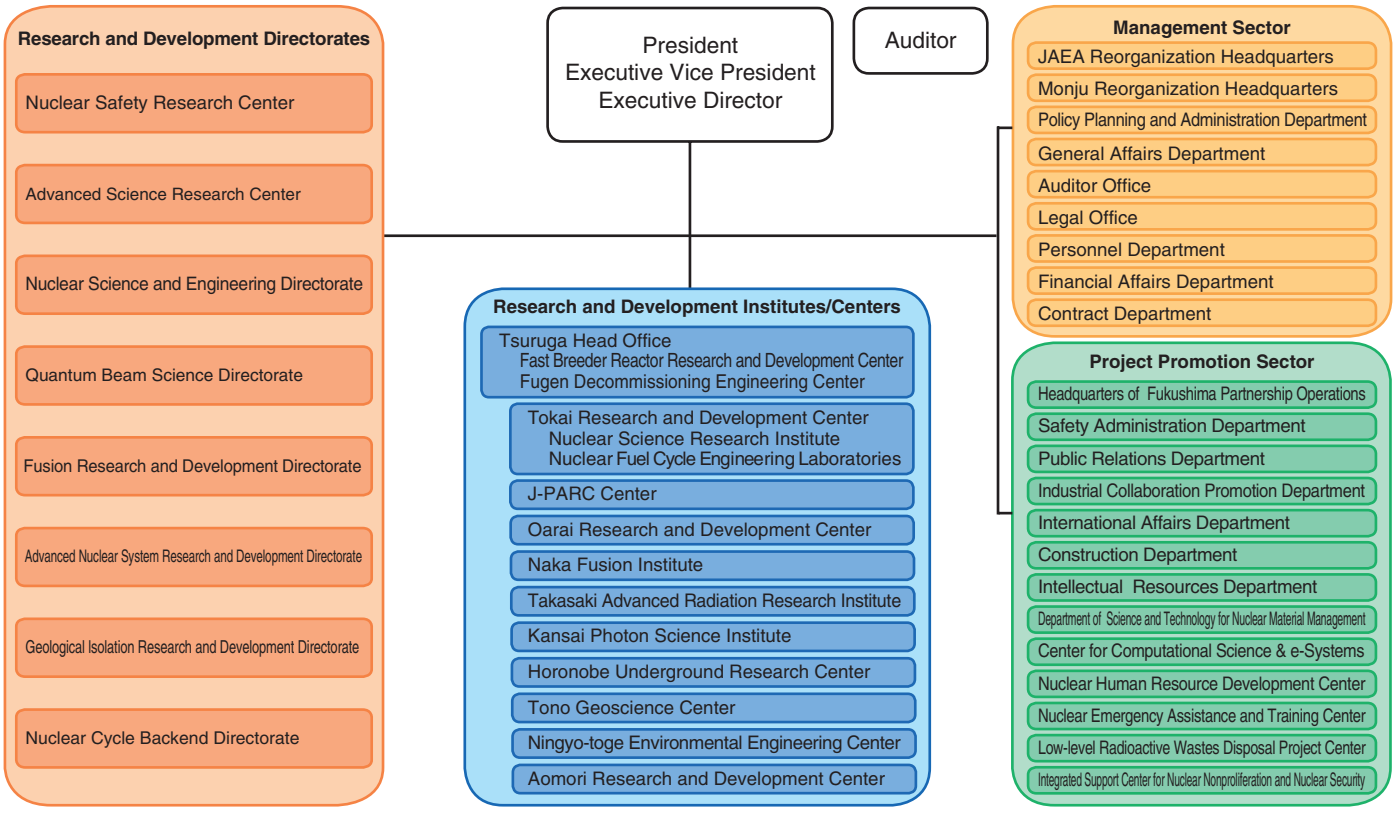

as of October, 2013

5. The **Quantum Beam Science Directorate** is engaged in research using neutron facilities in the Tokai Research and Development Center (Nuclear Science Research Institute) and the J-PARC Center. Work using electron beams, gamma ray, and ion beam facilities is done in the Takasaki Advanced Radiation Research Institute. Research using lasers and synchrotron radiation is performed at the Kansai Photon Science Institute.
6. The **Nuclear Safety Research Center** is in charge of safety research for supporting national nuclear safety regulatory bodies that regulate nuclear power plants, nuclear fuel cycle facilities, and radioactive waste disposal facilities. This work is done at the Tokai Research and Development Center (Nuclear Science Research Institute) and at the Tsuruga Head Office.
7. The **Advanced Science Research Center** conducts pioneering research in basic fields of nuclear power science, mainly through the Tokai Research and Development Center (Nuclear Science Research Institute) and the Takasaki Advanced Radiation Research Institute.
8. The **Nuclear Science and Engineering Directorate** is engaged in key and basic research on various elemental technologies that support the use of nuclear power. These efforts are carried out in the Tokai Research and Development Center (Nuclear Science Research Institute) and the Oarai Research and Development Center.
9. The **Nuclear Hydrogen and Heat Application Research Center** conducts R&D on technology for the use of high-temperature heat supplied from naturally safe, high-temperature, gas-cooled reactors and technology for using this heat to produce hydrogen. These studies are done in the Oarai Research and Development Center.
10. The **Nuclear Cycle Backend Directorate** develops technologies for safe and rational decommissioning of nuclear power facilities as well as measures for processing and disposing radioactive waste. This work is performed in the Tokai Research and Development Center.
11. The **Center for Computational Science & e-Systems** develops pioneering simulation technology and basic technology in computational science as well as operates and maintains computer equipment. This occurs mainly in the Tokai Research and Development Center (Nuclear Science Research Institute).
12. The **Department of Science and Technology for Nuclear Material Management** and the **Integrated Support Center for Nuclear Nonproliferation and Nuclear Security** develop technologies for nuclear nonproliferation and safeguards to ensure the peaceful use of nuclear energy. These developments are done in the Tokai Research and Development Center (Nuclear Science Research Institute) and the Techno Community Square Ricotti.
13. The **R&D Institutes and Centers**, located at 11 sites in Japan, manage and improve the performance of facilities and equipment to support the abovementioned R&D Directorates in safe and efficient R&D activities.

R&D Institutes/Centers of JAEA

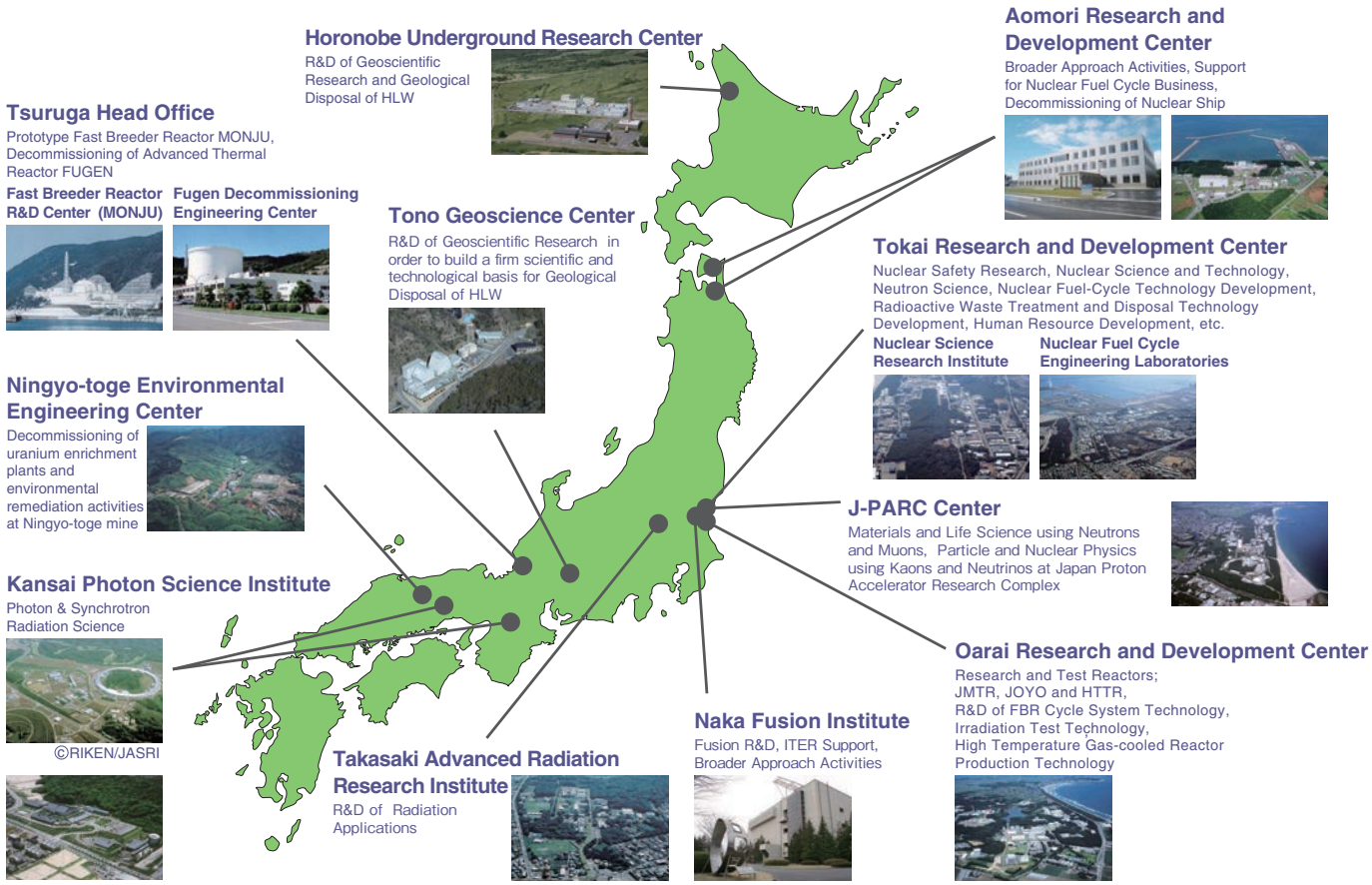

Environmental Remediation and Plant Decommissioning

Fig.1-1 JAEA's post-accident efforts at environmental remediation for recovery of Fukushima
These activities are discussed on the web page of the Headquarters of Fukushima Partnership Operations of the JAEA. (https://fukushima.jaea.go.jp/en/)

Environmental Remediation

As a designated public institution established under the Basic Law on Natural Disasters, we started taking actions immediately following the Great East Japan Earthquake on March 11, 2011. We have undertaken diversified actions such as dispatching technical experts. As countermeasures to the problems that are still continuing now, we are taking the following actions (Fig.1-1) for the recovery of Fukushima.

Radiation Monitoring of Environment

It is necessary to grasp the precise contamination status and radiation dose rate of the radioactive material in order to assess the health effects and develop a decontamination plan. Therefore, a continuous investigation of the radioactive cesium (Cs) density in the seabed sediment (Topic 1-1) is being performed. In addition, under a contract with MEXT, air dose rate maps were obtained by a car-borne survey in East Japan (Topic 1-2) and by airborne monitoring around the Tokyo Electric Power Company, Incorporated (TEPCO) Fukushima Daiichi Nuclear Power Station (NPS) (Topic 1-3). In addition, measurement of the soil radioactivity distribution, aerial monitoring throughout Japan, and measurement of purified water in the Japan Atomic Energy Agency (JAEA) branch areas are being performed.

Environmental Restoration Activities

Quick decontamination is necessary for the recovery of the environment. Under a trust from the Cabinet Office, guideline formulation, decontamination catalog development, and decontamination technology verification projects are being performed. Waste reduction by decontamination of gravel (Topic 1-4) is being studied. By evaluating the changes in the topographical characteristics and vegetation distribution, a long-term environment change research project in Fukushima has begun. Clarification of the soil contamination mechanism (Topics 1-5, 1-6, 1-7) and a study of the mobile Cs maintenance mechanism in forests (Topic 1-8) are being performed. In addition, the development of a drinking water purifier (Topic 1-9) and the study of Cs behavior inside and outside of the incinerator are under way. On the basis of the above studies, investigations toward the optimization and increased efficiency of decontamination for environmental recovery will be continued in the future.

Human Resources Development

Upon request from Fukushima prefecture, we responded by dispatching lecturers for a decontamination work lecture class led by the Nuclear Human Resource Development Center. We held the class 15 times, and 7819 persons completed it by March, 2013. In addition, under the support system developed upon request from the Cabinet Office, Ministry of the Environment, we acted to spread knowledge about decontamination by dispatching experts to municipalities and cooperating in decontamination plan development, performing decontamination technology consultation and instruction, and providing inhabitant briefing session support.

Communications and Public Relations

We dispatched experts who explained radiation data and a scientific interpretation method and conducted meetings to answer typical questions about radiation for about 1700 groups, for example, all the nursery schools, kindergartens, elementary schools, and junior high schools in Fukushima prefecture. We held these meetings in 210 places for 17286 persons by March, 2013.

Measurement and Estimation of Exposed Dose

We measured the internal radiation exposure using the whole body counter (WBC) at the Tokai Research and Development Center and a mobile WBC car for inhabitants upon request from Fukushima prefecture. By the end of March, 2013, we had measured 41043 people. In addition, the radiation exposure doses for inhabitants under different conditions (Topic 1-10) and for people who treated sludge including radioactive Cs (Topic 1-11) were evaluated.

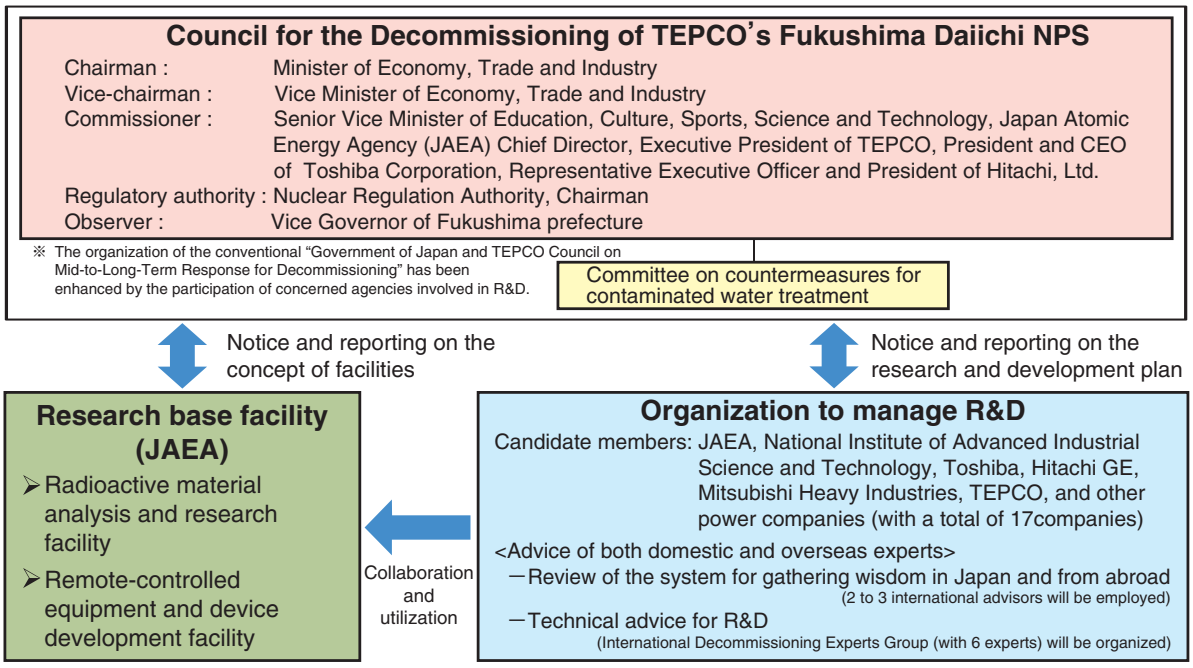

Fig.1-2 Organizational chart of research and development promotion
We are studying the establishment of research base facilities and conducting research and development based on the national R&D plan. [Council for the Decommissioning of TEPCO's Fukushima Daiichi Nuclear Power Station (June 27,2013)]

Plant Decommissioning

Immediately after the accident, we began providing technical advice to the government and TEPCO, and conducting research for decommissioning and radioactive waste management into the mid- and long-term.

Removal of Spent Fuel and Fuel Debris

In the accident, as sea water was injected into the spent fuel pool for emergency cooling, the possibility of corrosion problems with various materials was considered. Therefore, hydrazine was added to salt-containing water in order to reduce the dissolved oxygen. We evaluated the effect of irradiation on deoxidation by hydrazine (Topic 1-12).

It is important to grasp the characteristics of the molten core materials (the fuel debris) before defueling for safe handling, storage, processing, and disposal of the fuel debris. We are conducting R&D to investigate the characteristics using simulated debris (Topic 1-13), examine the reactions between the sea water used for emergency cooling and the fuel debris (Topic 1-14), study criticality control in order to prevent re-criticality even if the form of the fuel debris or the water volume changes during defueling (Topic 1-15), and determine material accountancy and control measures for the fuel debris when it is removed from the core (Topic 1-16).

Estimation of Status inside Vessel and Investigation of Cause of Accident

The fuel in the reactors reached a high temperature and became molten when the core cooling system ceased operation in the station blackout due to the tsunami. To elucidate the progress of the melting phenomena in the reactor core, we evaluated the nuclide inventory at the time of the nuclear accident (Topic 1-17).

Several committees were established by the Government, the Diet of Japan, and the Rebuild Japan Initiative Foundation, as well as TEPCO, to investigate the accident and published their respective reports. We reviewed these reports to gain insights useful for near-term regulatory activities, including accident investigation (Topic 1-18).

Radioactive Waste Management

A massive volume of contaminated water has been generated as a result of the tsunami and the inflow of ground water into the reactor buildings; this contaminated water is temporarily stored at the plant site.

Some water treatment systems are being applied to remove radioactive nuclides, e.g., cesium and strontium, from the contaminated water. We are addressing the long-term storage, processing, and disposal of secondary waste produced by treatment of the contaminated water, which presents important challenges; making computational analyses of the cesium absorption mechanism in zeolites (Topic 1-19); and examining ways to simplify the water treatment process (Topic 1-20).

Remote Decontamination Technology

Decontamination technology that uses remote access devices has to be developed to reduce the radiation dose of workers in the reactor buildings. It is necessary for effective decontamination to comprehend the component nuclides, their penetration into the floors or walls, and the distribution of the radioactive contaminants. We conducted a radioanalysis of the concrete core boring samples taken from the reactor buildings (Topic 1-21).

Future Plan

We will study the establishment of research base facilities and conduct research and development based on the national R&D plan (Fig.1-2).

1–1 Time Series Observations in the Coastal Regions off Northern Ibaraki
— Factors Controlling Concentrations of Radiocesium in Seabed Sediment —

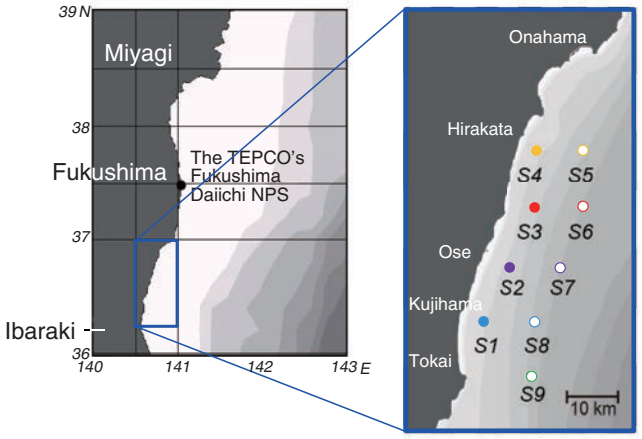

Fig.1-3 Sampling area and stations
Seabed sediments were collected in the region 70–110 km south of 1F. Bottom depths of the stations were 30–100 m. A series of sampling campaigns was started in June 2011, and all sampling was conducted by R/V Seikai (monitoring ship of the Japan Atomic Energy Agency).

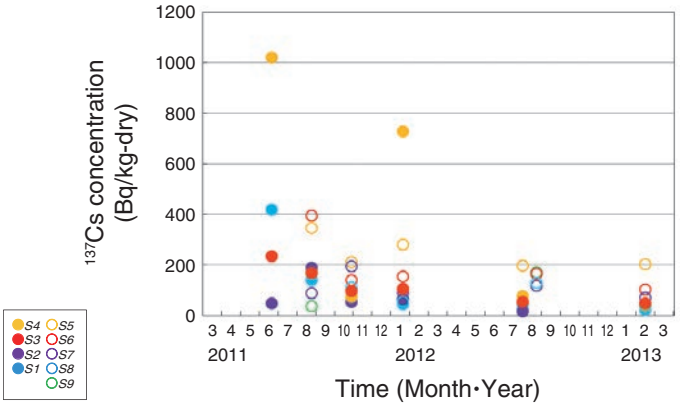

Fig.1-4 Time series of concentration of cesium-137 (^{137}Cs) in upper (0~3 cm) layer of seabed sediment
^{137}Cs concentrations in seabed sediment decreased with time overall, but an episodic variation was observed at several stations. It can be considered that radiocesium-bound fine sediment is transported continuously near the seabed.

For several months after the accident at the TEPCO's Fukushima Daiichi NPS (1F), seawater containing accident-derived radiocesium flowed into the coastal regions off northern Ibaraki (Fig.1-3). We therefore set nine stations in the region and have been investigating the temporal variation in the radiocesium concentration in seabed sediment and the factors controlling the concentration by time-series observations.

The observed concentrations of cesium-137 (^{137}Cs) in the upper (0~3 cm) layer of seabed sediment ranged between 16 and 1020 Bq/kg (Fig.1-4). Although the concentrations decreased with time overall, a temporarily high concentration was observed at several stations.

In the shallow regions (less than 50 m of bottom depth), most of the sedimentary radiocesium was adsorbed onto coarse (>75 μm) components, but the concentrations were low. On the other hand, a portion of the radiocesium was adsorbed onto fine-grained sediment, which is easily remobilized by bottom currents, with higher concentrations. From these characteristics, it can be considered that the episodic variation of radiocesium concentration indicates temporal accumulation of fine-grained particles near the seabed associated with the bottom currents.

Depth profiles of ^{137}Cs in the sediment showed that, in the shallow region, a large proportion of the ^{137}Cs was accumulated in the deep (>3 cm) layers of the sediment. The higher concentrations of sedimentary radiocesium in the deep layers are attributable to a higher contact probability of dissolved radiocesium with sediment, as well as efficient vertical transport of radiocesium to the deeper layer of sediment via bioturbation.

We also found that most of the radiocesium in the coastal sediment was incorporated into lithogenic (i.e., clay) components, and this incorporation was almost irreversible. These characteristics would be a primary reason for such a slow decrease in the concentrations of sedimentary radiocesium.

The findings of this study will be applied to a simulation model that predicts the distribution of radiocesium on the seafloor.

Reference

Otosaka, S. et al., Sedimentation and Remobilization of Radiocesium in the Coastal Area of Ibaraki, 70 km South of the Fukushima Dai-Ichi Nuclear Power Plant, Environmental Monitoring and Assessment, vol.185, issue 7, 2013, p.5419–5433.

1–2 Creating Dose Rate Maps over Wide Areas in Collaboration with Municipalities
— Detailed Measurements of Air Dose Rates Using Car-Borne Survey —

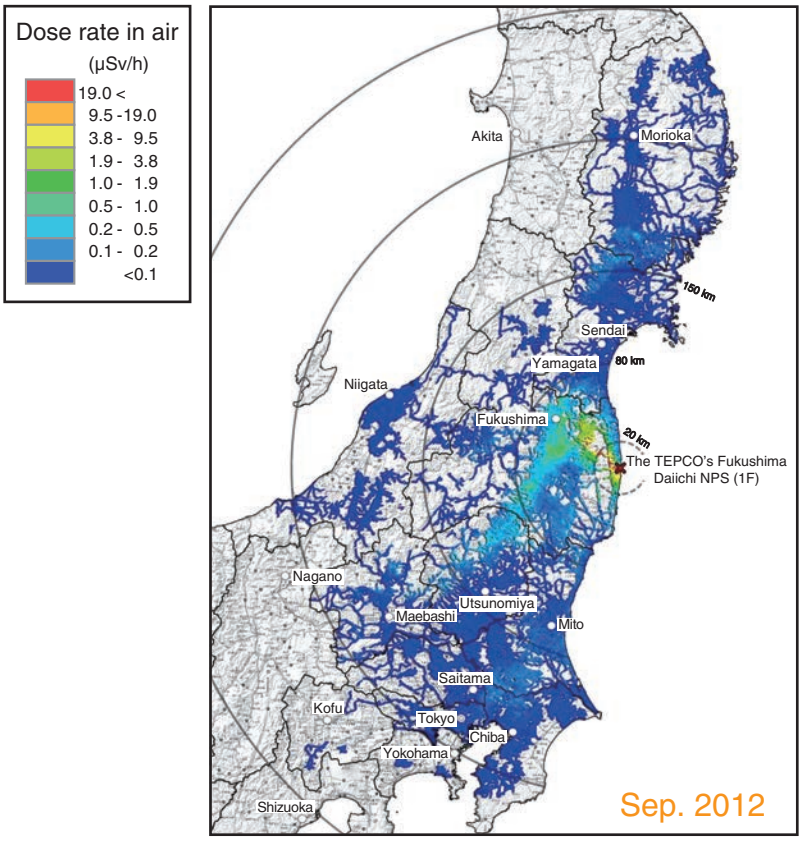

Fig.1-5 Example of large-scale car-borne survey data using KURAMA
Air dose rates measured every 3 seconds on roads are averaged in 100 m squares, and dose rate ranges are shown by different colors.

In order to properly estimate the effects of radionuclides released by the accident at the TEPCO's Fukushima Daiichi NPS (1F) on the environment and human health for a long period and take appropriate countermeasures, it has been necessary to obtain detailed information on the air dose rates over wide areas. We established a system that can obtain a large amount of air dose rate data in a short period using a car-borne survey, and have periodically constructed detailed air dose rate maps.

In the car-borne survey, the mobile survey system KURAMA-II developed at Kyoto University was employed. The system is compact and easy to operate; moreover, it has the advantage that the obtained air dose rates and positional data are transferred through a cellular phone network, and stored on a data storage server in real time. To ensure the quality of the measurements made using the KURAMA-II system, we developed a spectrum-dose conversion operator (G (E) function) necessary for accurate dose rates measurements, and have performed calibration tests with standard radiation sources.

Measurements are intended to be performed over wide areas where a certain amount of radiocesium could have been deposited in the accident at 1F. Consequently, extended areas in east Japan from Iwate Prefecture to Yamanashi Prefecture have been covered in the car-born survey. In addition to measurements on main roads performed by ourselves, about 200 municipalities have been asked to perform detailed measurements including those on small roads, resulting in creation of detailed air dose rate maps over wide areas as shown in Fig.1-5.

The present study was implemented under a commission from the Ministry of Education, Culture, Sports, Science and Technology of Japan (MEXT).

Reference

Japan Atomic Energy Agency, Report on Establishment of Evaluation Methods for Long-Term Consequences due to Radioactive Substances Released by the TEPCO's Fukushima Daiichi NPT Accident. Commissioned by MEXT in FY2012, Ministry of Education, Culture, Sports, Science and Technology of Japan (MEXT), 2013, p.36-45 (in Japanese), http://fukushima.jaea.go.jp/initiatives/cat03/entry05.html

1–3 Measurement Method without Exposure to Radiation Dose

— Radiation Measurement of Area Surrounding 1F using Unmanned Helicopter —

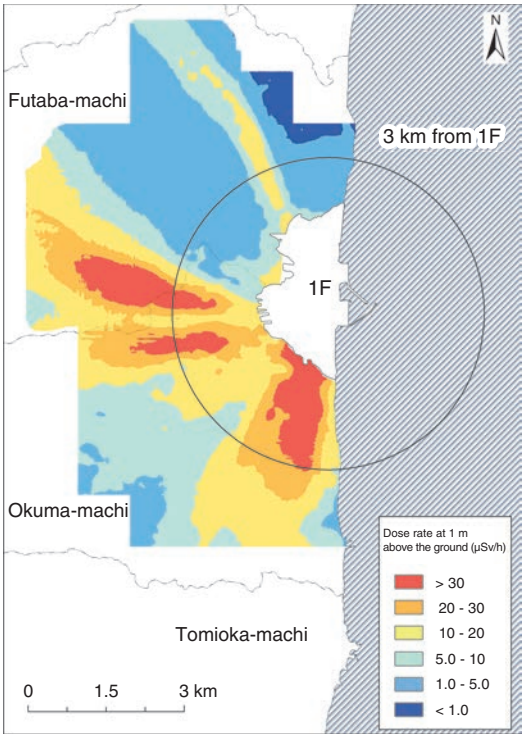

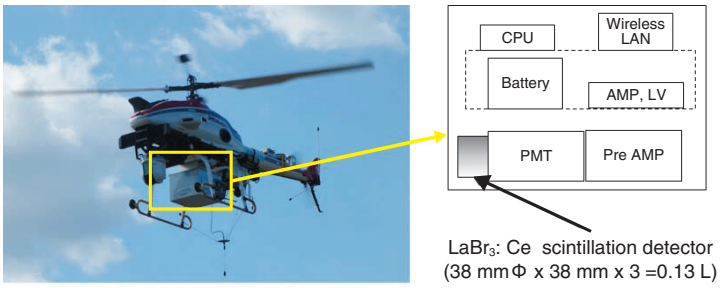

Fig.1-6 Radiation monitoring system using an unmanned helicopter
The radiation monitoring system using an unmanned helicopter can save the position information from DGPS and the count rates of the $LaBr_3$: Ce detector every 1 s. The position of the helicopter can be displayed in real time. LAN: Local area network. PMT: Photomultiplier tube.

Fig.1-7 Map of dose rate in area surrounding the 1F
This map was made by converting the acquired data into the dose rate at a height of 1 m above the ground. The dose rate was normalized to that of March 21, 2013. The map includes the dose rate of natural radiation.

After the accident at the TEPCO's Fukushima Daiichi NPS (1F), a method by which the radiation in a large area can be promptly measured was needed. We clarified the radiation distribution in Japan by aerial radiation monitoring using aircraft (a manned helicopter). However, because Japanese regulations prohibited travel within a 3 km range of the 1F, aerial radiation monitoring using the aircraft was not performed. Thus, we attempted to make a radiation distribution map using a radiation detector installed in an autonomous unmanned helicopter (AUH).

The AUH employed an R-MAX G1 made by Yamaha Motor Co., Ltd. The AUH consists of an unmanned helicopter used for pesticide dispersion with an added capacity for autonomous functioning (Fig.1-6). We developed a radiation monitoring system that was installed in the AUH. We adopted the $LaBr_3$: Ce scintillation detector to obtain the energy spectrum of γ-rays. This system could save not only the positional information obtained by differential GPS (DGPS), but also the radiation data, every 1 s. The data from the scintillator (gross count rates) were converted into the air dose rate at 1 m above the ground using a pre-set parameter. A contour map based on the analyzed dose rate at a 1 m height was made using Geographic Information System (GIS) software. The unmanned helicopter flew about 80 m in altitude above the ground at a speed of 8 m/s. The line spacing of the flight was 80 m for agreement with the flight altitude. The measurement results obtained by the AUH system exhibited a good correlation with those of measurements by a survey meter on the ground.

The contour map of the dose rate around the 1F is shown in Fig.1-7. The high dose rate area extends not only in the southern direction but also in the western direction from the 1F. Moreover, the high dose-rate area in the western direction was divided into two areas. It can also be seen that the high dose-rate area extended in the northwestern direction. The shape of the distribution is attributed to the weather conditions at the time of the accident and the topography.

This map is available to the public on the homepage of the Nuclear Regulation Authority (http://fukushima.jaea.go.jp/initiatives/cat03/pdf04/5-1-2.pdf).

The present study was conducted under a contract with the Ministry of Education, Culture, Sports, Science and Technology of Japan (MEXT) in fiscal year 2013.

Reference

Japan Atomic Energy Agency, Report of Investigation of "Study on Distribution and Migration of Radioactive Substances around Fukushima Daiichi Nuclear Power Plant", Ministry of Education, Culture, Sports, Science and Technology of Japan (MEXT), 2013, p.46-52 (in Japanese), http://fukushima.jaea.go.jp/initiatives/cat03/pdf05/02-2.pdf

1–4 Surface Grinding of Gravel for Waste Reduction and Reuse
— Decontamination Test of Gravel by General-Purpose Machine —

Fig.1-8 Decontamination test by milling method
We tested gravel decontamination using a general-purpose barrel finishing machine with 20 kg of gravel, 20 ℓ of water, 150 rounds per min, and 20–60 min of grinding time per batch.

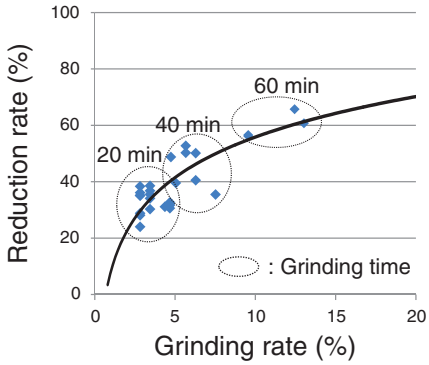

Fig.1-9 Relationship between grinding rate and reduction rate
In this test, we confirmed a reduction rate of up to 66% relative to the surface dose rate. We will research the correlation between the ground amount and reduction rate to determine the reduction effect if the ground amount increases.

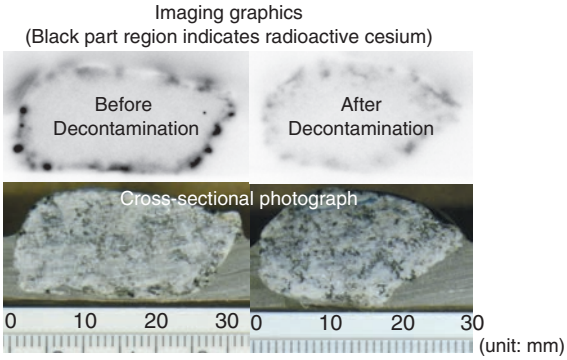

Fig.1-10 Distribution state of radioactive cesium before and after testing
Using an IP, we confirmed that Cs gathers mainly in the black mica parts and decreases in the ground parts of the gravel after decontamination (grinding time is 20 min).

In houses and public facilities, gravel (pebbles, etc.) with radioactive cesium (Cs) is laid on. To reduce the air dose rate, the gravel is stripped and led to waste. Gravel with low-level contamination is reused after high-pressure water washing to remove fine-grained soil attached to its surface. Considering the high price of gravel compared to that of crushed stone and the need for waste reduction, an effective method of decontaminating gravel with high-level contamination is expected to be selected.

Surface grinding of gravel has the potential for producing a strong decontamination effect. Therefore, we tried to find an effective procedure for decontaminating gravel by rubbing it against itself using a milling method in which the grinding time and amount of water added are varied.

We observed the condition of gravel during and after the test and confirmed that the surface of the gravel was ground properly (Fig.1-8). However, in this test, there were no ground parts on the concave regions of the gravel because the milling was done with only gravel and water, without grinding material.

The test results were as follows. When the grinding time was 20 min, the mean grinding rate was about 4%, and the mean reduction rate of the surface dose rate was about 37%. Furthermore, when the grinding time was 60 min, the mean grinding rate was about 10%, and the mean reduction rate of the surface dose rate of the gravel was about 60% (up to 66%). Both of these rates were low for these grinding times (Fig.1-9).

To confirm the cause of the low reduction rate, we observed the distribution of Cs in the gravel before and after decontamination using an imaging plate (IP). By comparing the observation of a cross-section of gravel (granite) that was sliced in half and imaging graphics obtained with the IP (Fig.1-10), we confirmed that the Cs was mostly attached to the black mica around the surface of the gravel and penetrated slightly below the surface.

In this test, we used gravel that had been laid on heavily in the garden and rooftop of Rifure-Tomioka. It took considerable time to grind the gravel because it was slightly harder than the gravel that was bought for a mock test. Furthermore, the reduction rate became lower than expected because the gravel contained mica, which tended to absorb Cs. Various types of gravel are laid on in houses. The color, shape, size, and hardness of the gravel vary, so we must select reasonable conditions for decontamination work. On the basis of the result of this test, we will research decontamination methods and conditions for reusing gravel and reducing waste.

Reference

Japan Atomic Energy Agency, Decontamination Works in the Evacuation Zones concerning the Fukushima Daiichi Nuclear Power Plant Disaster【Part of the Decontamination Pilot Projects】 Report, 2012, p.107 (in Japanese).

1–5 Supercomputer Solves Mystery of Strong Affinity of Soil to Radioactive Cesium

— First-Principles Calculation Reveals Mechanism of Cesium Adsorption to Soil —

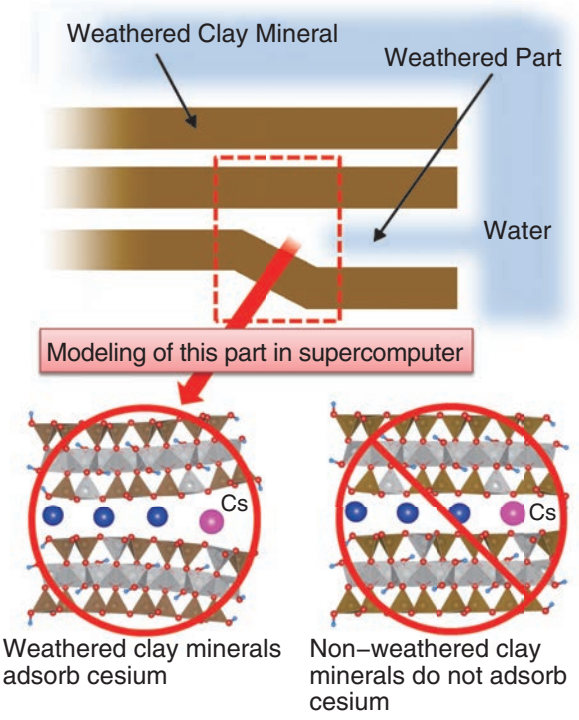

Fig.1-11 Schematic of clay mineral and model of its weathered part
We modeled the weathered part of mica shown in the figure and evaluated the energy difference between the mineral before and after adsorption of cesium. As a result, we showed that the weathered clay adsorbs cesium, although the non-weathered clay does not.

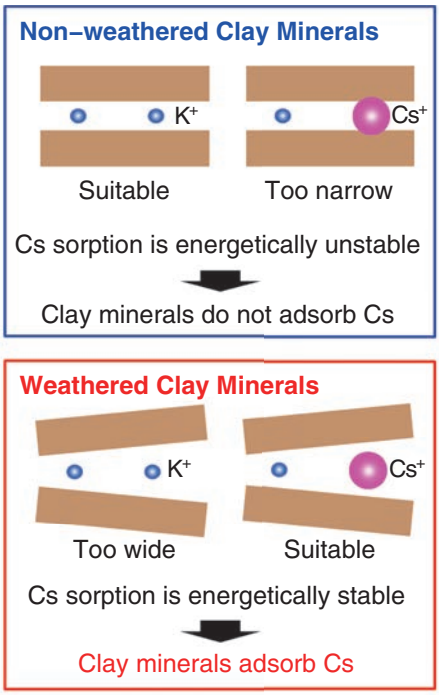

Fig.1-12 Schematic of adsorption mechanism of cesium to weathered clay minerals
Non-weathered clay minerals have pockets whose sizes are not suitable for cesium ions. Thus, the energy increases when cesium ions are adsorbed by non-weathered clay minerals. However, weathered clay minerals have pockets with sizes suitable for cesium ions, so the energy decreases when they adsorb cesium ions.

A large amount of radioisotopes was released into the environment by the accident at the TEPCO's Fukushima Daiichi NPS after the large earthquake and tsunami on March 11, 2011. The government conducted large-scale decontamination in the Fukushima area, which produced a large amount of waste. The handling of such a large amount of waste became a new serious problem because it is not easy to prepare storage places for it. To solve this problem, it is necessary to reduce the volume of the waste. However, standard technology for such reduction has not been developed. One reason is the lack of knowledge about the microscopic mechanism of adsorption. Weathered clay minerals are known to adsorb cesium, but no one knows the mechanism. To identify the mechanism, we performed first-principles calculations on the adsorption reaction of cesium to clay minerals.

First, we made a model of the weathered clay mineral in the supercomputers at the Japan Atomic Energy Agency and calculated the energy difference between the mineral before and after adsorption (Fig.1-11). As a result, we found that *only* weathered clay minerals adsorb cesium. In contrast, non-weathered ones do not exhibit adsorption. Further calculations revealed the adsorption mechanism (Fig.1-12). Non-weathered clay minerals have pockets with sizes suitable for the potassium ion's radius. On the other hand, when clay minerals are weathered, they have wider pockets that are suitable for cesium ions, whose radius is larger than that of potassium ions.

We revealed the adsorption mechanism of cesium to clay minerals by first-principles calculations. We hope to develop a simulation technique for desorption of radioactive cesium from clay minerals on the basis of this knowledge of the adsorption mechanics and contribute to volume reduction of the waste.

Reference

Okumura, M. et al., Mechanism of Strong Affinity of Clay Minerals to Radioactive Cesium: First-Principles Calculation Study for Adsorption of Cesium at Frayed Edge Sites in Muscovite, Journal of the Physical Society of Japan, vol.82, no.3, 2013, p.033802-1-033802-5.

1–6 Specific Sorption of Radiocesium by Minerals

— Toward Remediation of Soils Contaminated by Radiocesium —

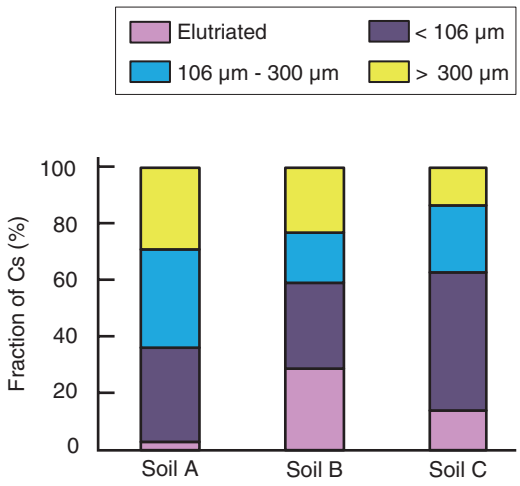

Fig.1-13 Size fractions of radiocesium in soils sampled in Fukushima Prefecture
Radiocesium was distributed in size fractions larger than the clay fraction, which was elutriated.

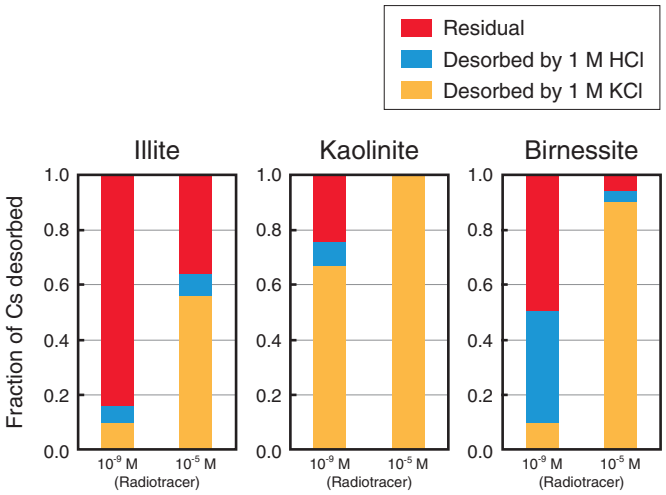

Fig.1-14 Desorbed fraction of radiocesium from minerals at different cesium concentrations
When the Cs concentration was very low (10^{-9} M), more Cs remained after treatment with desorption reagent solution.

Cesium (Cs) is known to be tightly associated with clay minerals. In particular, radiocesium is tightly associated with the interlayer of layered illite minerals contained in the small particulate fraction; consequently, the associated radiocesium cannot be desorbed by treatment with either acid or a cation solution. This tight association resulted in immobility of radiocesium after it was deposited to the soil in the accident at the TEPCO's Fukushima Daiichi NPS. For remediation of the contaminated soil, the clay fraction was eliminated by sieving. However, most of the radiocesium remained in some soils after the sieving treatment (Fig.1-13).

To clarify the tight association of radiocesium with minerals other than illite-like minerals, we conducted sorption and desorption experiments with radiocesium on 17 minerals using 1 M KCl and 1 M HCl solutions as desorption reagent solutions. Because the chemical concentration of radiocesium was extremely low, two different concentrations of radiocesium were considered: a contamination level of 8000 Bq/kg and a minor elemental level in the soil. At the contamination level of radiocesium, 0.3 and 0.5 fractions of radiocesium remained in kaolinite and birnessite, respectively, after the treatment (Fig.1-14).

In the natural environment, minerals are altered by weathering to generate tight association sites in the altered minerals. Unfortunately, the number of tightly associated sites is very limited in kaolinite and birnessite compared to that in illite. When the concentration of radiocesium is extremely low, most of the radiocesium is easily bound in the tightly associated sites.

This finding of a tight association of radiocesium with non-illite minerals reveals a more effective remediation method for contaminated soils. For instance, the soil fraction of less than 300 μm suggests a threshold for the appropriate remediation method of the contaminated soil fraction.

Reference

Ohnuki, T. et al., Adsorption Behavior of Radioactive Cesium by Non–Mica Minerals, Journal of Nuclear Science and Technology, vol.50, no.4, 2013, p.369–375.

1–7 Transport of Radionuclides in Depth Direction

— Investigation on Depth Distribution of Radionuclides in the Soil of Fukushima —

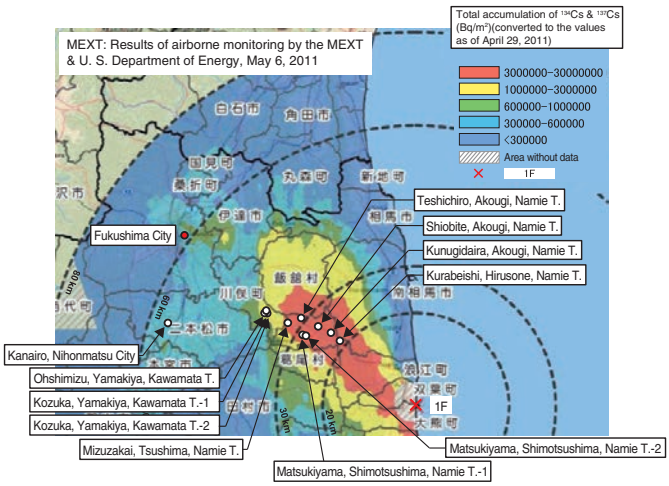

Fig.1-15 Locations investigated (although the distribution map was published on May 6, 2011, the values are those ones converted to as of April 29, 2011)

The investigation was conducted at 11 locations in Nihonmatsu City, where ^{131}I was detected from soil at that time, and Kawamata and Namie Towns, where R114 runs along the valley of Abukuma Highland. The sites are located northwest of 1F in an area through which a plume of RNs is considered to have passed.

Table 1-1 K_d values of ^{137}Cs and ^{131}I onto each soil sample

Sorption experiments by a batch method were conducted for soil samples taken at 11 locations (two different depths for each location).

Location	Soil	Depth (cm)	Distribution coefficient(K_d)					
			^{137}Cs(Cs^+ : cation)			^{131}I(I^- : anion)		
			pH	K_d(ml/g)	Error(±)	pH	K_d(ml/g)	Error(±)
Kanairo, Nihonmatsu City	Sandy	4–12	6.2	3.30E+03	2.38E+02	6.1	1.36E+00	1.34E−01
	Clayish	21–38	6.5	6.10E+04	9.75E+04	6.5	9.24E−00	1.31E−01
Kozuka, Yamakiya, Kawamata T.-1	Sandy	10–20	6.5	1.30E+04	5.15E+03	7.6	1.76E+01	1.85E−02
		32–43	6.2	4.24E+04	8.75E+04	6.1	2.37E+01	2.25E−01
Kozuka, Yamakiya, Kawamata T.-2	Sandy	15–20*1	5.8	1.87E+04	6.68E+03	5.8	4.44E+00	1.66E−01
		35–40*1	6.4	8.67E+03	1.63E+03	6.2	2.84E+01	2.92E−01
		5–15*2	6.1	2.88E+03	1.73E+02	6.2	1.84E+01	2.08E−01
		21–30*2	7.5	3.37E+03	2.40E+02	6.4	2.76E+01	2.58E−01
Ohshimizu, Yamakiya, Kawamata T.	Sandy	5–15	6.8	1.51E+04	6.52E+03	6.6	1.25E+00	8.78E−02
		33–41	7.3	4.31E+04	4.14E+04	7.1	5.52E−01	1.25E−01
Mizuzakai, Tsushima, Namie T.	Organic	8–18	5.8	2.24E+03	1.19E+02	5.8	3.08E+01	5.18E−01
		40–50	5.5	2.37E+03	1.26E+02	5.5	2.33E+01	4.12E−01
Matsukiyama, Shimotsushima, Namie T.-1	Sandy	8–19	6.7	4.01E+03	3.56E+02	6.6	1.20E+01	1.90E−01
		55–65	6.2	2.17E+04	1.60E+04	6.2	1.31E+01	1.54E−01
Matsukiyama, Shimotsushima, Namie T.-2	Organic	5–15	5.6	2.84E+03	1.86E+02	5.6	8.78E+00	1.35E−01
		20–30	5.6	2.97E+03	2.03E+02	5.6	1.30E+01	1.65E−01
Teshichiro, Akougi,Namie T.	Sandy	7–15	6.5	2.98E+03	1.92E+02	6.4	9.31E+01	6.58E−01
		29–36	6.1	7.43E+03	1.25E+03	6.2	5.99E+01	5.18E−01
Shiobite, Akougi, Namie T.	Sandy	10–23	5.8	2.16E+03	1.10E+02	5.7	1.42E+02	1.47E+00
		31–44	5.7	2.18E+03	1.07E+02	5.6	1.67E+01	3.08E−01
Kunugidaira, Akougi, Namie T.	Organic	10–15	6.0	2.08E+03	9.85E+01	6.1	1.19E+01	1.00E−01
		30–35	6.0	2.86E+03	1.85E+02	6.1	1.03E+01	1.36E−01
Kurabeishi, Hirusone, Namie T.	Sandy	10–25	6.5	2.16E+03	1.08E+02	6.6	2.08E+01	3.16E−01
	Clayish	33–46	6.5	3.53E+04	4.79E+04	6.5	2.58E+00	1.47E+01

Error: counting error, *1: soil core 1, *2: soil core 2

The accident at the TEPCO's Fukushima Daiichi NPS (1F), which was caused by the Great East Japan Earthquake in March 2011, led to the release of volatile radionuclides (RNs) that were deposited on the surrounding environment (e.g., soils, forests, residential land) around Fukushima Prefecture. The Ministry of Education, Culture, Sports and Technology (MEXT) initiated a project for making the distribution maps of dose rate, etc. in cooperation with Ministry of Agriculture, Forestry and Fisheries, JAEA, universities, etc. This work was conducted as part of the project described above.

The Geoslicer investigation examined the depth distribution of RNs in the soil as of about three months after the 1F accident. A total of 11 locations were selected in Nihonmatsu City, Kawamata Town, and Namie Town (Fig.1-15). Plate-shaped soil samples from a maximum depth of about 1 m (10 cm wide and 2 cm thick) were obtained, and soil samples for RN analysis were taken after the soil was observed and described. The γ decay nuclides were analyzed using a Ge semiconductor detector.

Both cesium-134 (^{134}Cs) and cesium-137 (^{137}Cs) were detected in all the locations investigated, and tellurium-129m (^{129m}Te) and silver-110m (^{110m}Ag) were detected only in locations where the dose rates were high. For the depth distribution of radiocesium (RC), at many of the locations investigated, RC more than 99% of the inventory distributed within depths of 10 cm and 14 cm in soil in the surface layer (mainly sandy soil) and in soil at locations that are supposed to have been used as farmland (mainly organic and clayish soils), respectively. The apparent diffusivities (D_a) derived from penetration profiles near the surface layer showed similar levels (10^{-11} m^2/s) for all the RNs detected, although the D_a values tended to be higher in the soil at locations that are supposed to have been used as farmland (D_a = 0.1~1.5 × 10^{-10} m^2/s) than in soil in the surface layer (D_a = 0.65~4.4 × 10^{-11} m^2/s). Because the distribution coefficients (K_d) of cations (Cs^+) and anions (I^-) differed significantly (Table 1-1), the respective D_a values were estimated to differ significantly. However, they were at similar levels for all the RNs; therefore, the D_a values were believed to be controlled by dispersion caused by rain water flow.

Thus, we can say that transport of RC in the soil is always quite slow because the K_d values onto soil are quite large. The transport of RNs in soil is strictly related to K_d, which depends on the minerals constituting the soil, their contents, the content of organic matter, and other factors. In particular, the clay mineral component affects the reversibility and irreversibility of sorption. For the long-term prediction of RC transport, it is essential to understand those details, and this remains as future work.

The present study was sponsored by the Ministry of Education, Culture, Sports, Science and Technology of Japan (MEXT).

Reference

Sato, H. et al., Investigation and Research on Depth Distribution in Soil of Radionuclides Released by the TEPCO Fukushima Dai-Ichi Nuclear Power Plant Accident, MRS Online Proceedings Library, vol.1518, 2013, 6p.

1–8 Retention of Mobile Radiocesium in Forest Surface Soils
— Quantifying Microbial Uptake and Abiotic Adsorption —

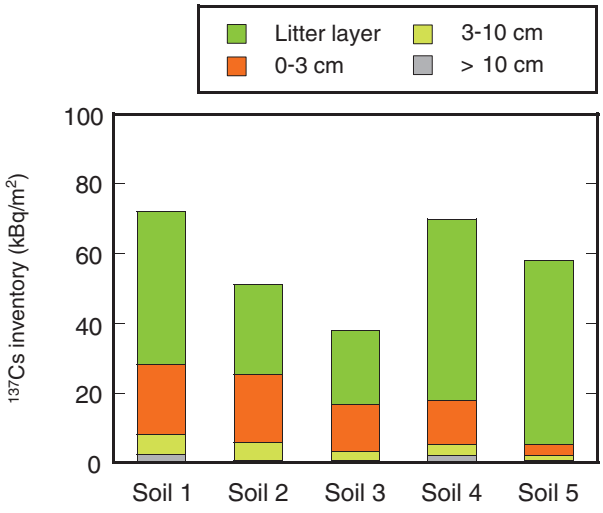

Fig.1-16 Vertical distribution of ^{137}Cs in forest soils three months after the accident
At five forest sites in Fukushima prefecture, 50%–91% and 6%–39% of the total ^{137}Cs deposition were observed in the aboveground litter layer (■) and the topmost (0–3 cm) soil layer (■), respectively.

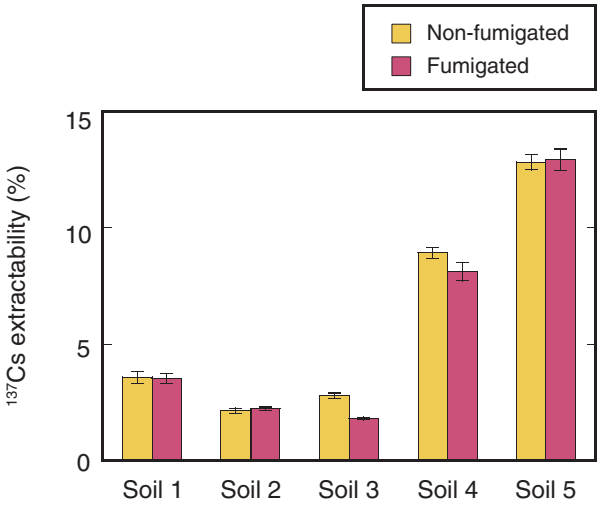

Fig.1-17 Extractability of ^{137}Cs in five forest surface (0–3 cm) soils
Cesium-137 was extracted with K_2SO_4 from soils before (non-fumigated) and after (fumigated) chloroform fumigation. No increase in the ^{137}Cs extractability was observed after the destruction of microbial biomass by chloroform fumigation.

The accident at the TEPCO's Fukushima Daiichi NPS released a huge amount of radiocesium into the environment and caused serious radioactive contamination of forest ecosystems. Our investigation, which was conducted in Fukushima Prefecture three months after the accident, revealed that >89% of the cesium-137 (^{137}Cs) deposited onto forest floors remained in the aboveground litter and topmost (0–3 cm) soil layers (Fig.1-16). In forest ecosystems affected by the accident at the Chernobyl NPS in 1986, ^{137}Cs has reportedly still been observed in surface soils and has become a major potential source for soil-to-plant transfer. Therefore, a better understanding of the mechanisms of retention and migration of ^{137}Cs in forest surface soils is urgently needed.

We focused on microbial involvement in the retention process of mobile ^{137}Cs in forest surface soils because some types of microorganisms in soils are believed to accumulate ^{137}Cs and thus influence the cycling of ^{137}Cs in forest ecosystems. Surface (0–3 cm) soil samples were collected from five forest sites in Fukushima Prefecture one year after the accident, and the following experiments were conducted.

First, soils were extracted with potassium sulfate (K_2SO_4) solution, and the extracts were analyzed for ^{137}Cs. The extraction process liberated 2.1%–12.8% of the total ^{137}Cs as easily exchangeable ions from the soils. Two soils with a higher content of clay-sized particles and organic carbon showed higher ^{137}Cs extractability (Fig.1-17, Soils 4 and 5). Next, the soils were fumigated with chloroform to destroy microbial biomass and then extracted with K_2SO_4. Microbial biomass was extracted from all of the soils; however, no increase in the ^{137}Cs extractability was observed (Fig.1-17).

The results indicate that the uptake of ^{137}Cs by soil microorganisms is less important for retention of mobile ^{137}Cs in the forest surface soils than ion-exchange adsorption by abiotic components. We are now conducting a similar experiment on litter and soil samples collected under different meteorological conditions to fully understand the role of soil microorganisms in controlling the mobility of ^{137}Cs in natural biotic systems.

The present study was sponsored in part by the Ministry of Education, Culture, Sports, Science and Technology of Japan (MEXT).

Reference

Koarashi, J. et al., Retention of Potentially Mobile Radiocesium in Forest Surface Soils Affected by the Fukushima Nuclear Accident, Scientific Reports, vol.2, no.1005, 2012, p.01005–1–01005–5.

1–9 Water Purifier for Securing Water

— Development of Grafted Adsorbent for Cs Removal —

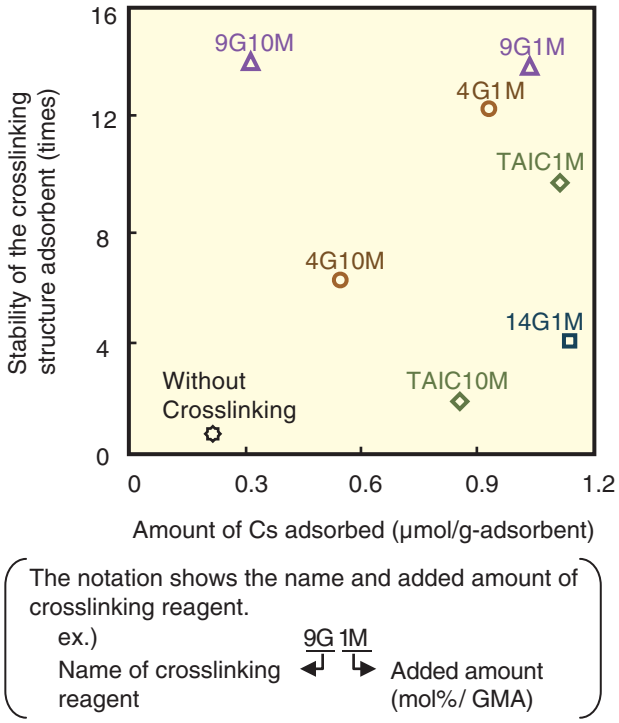

Fig.1-18 Efficiency of crosslinking structure for adsorbent stability
Amount of Cs adsorbed and adsorbent stability (defined as the amount of Mo eluted from the adsorbent without crosslinking structure divided by that with crosslinking structure). High-efficiency adsorbents are plotted in upper right corner.

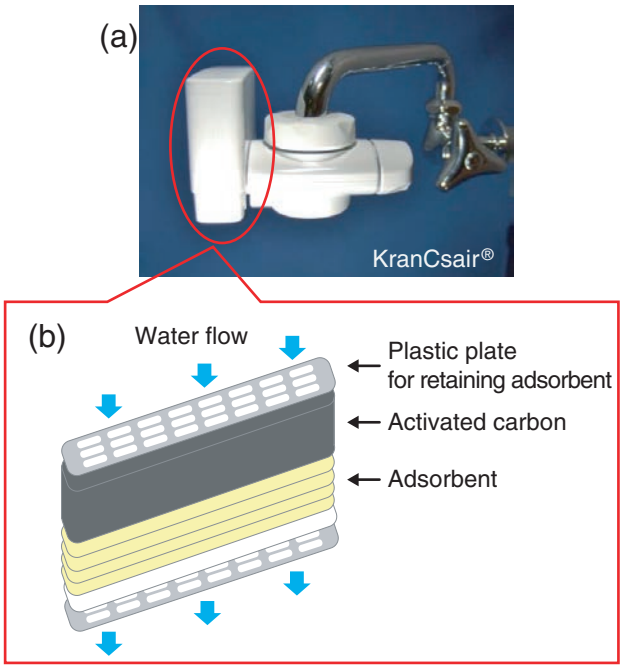

Fig.1-19 (a) Water purifier for Cs removal and (b) internal structure of cartridge
We have commercialized a cartridge-type water purifier. This original cartridge, which incorporates the developed adsorbent, is replaced easily.

More than two years have elapsed since the accident at the TEPCO's Fukushima Daiichi NPS, and the radioactive cesium (Cs) concentration in environmental water has been reduced. However, the results of a 2012 monitoring investigation of the drinking water in Fukushima reported by the Ministry of the Environment showed that radioactive Cs was detected in 6 of 436 samples. Therefore, securing 'water' is demand.

We developed a grafted adsorbent for removing soluble Cs immediately after this accident. The developed adsorbent consisted of ammonium 12-molybdophosphate (AMP) as the adsorbent functional group supported on a nonwoven polyethylene fabric acting as the substrate by radiation-induced graft polymerization. In a previous result, this adsorbent exhibited instability: The supported AMP released easily from the adsorbent. In this study, the unstable adsorbent was improved by introducing a crosslinking structure to realize very little AMP elution. Introducing a crosslinking structure to the grafted glycidyl methacrylate (GMA) chain of the adsorbent was attempted by adding three types of polyethylene glycol dimethacrylate (4G, 9G, or 14G) or triallyl isocyanurate (TAIC) as the crosslinking reagent to a monomer.

The efficiency of the improved adsorbent was investigated by batch-wise adsorption tests. The adsorbent was cut into pieces 1 cm^2 (0.02 g) in size and immersed in 50 mℓ of 50 μg/ℓ Cs solution under stirring for 24 h.

It was clarified that the amount of AMP eluted (calculated as the eluted Mo) from the adsorbents with the introduced crosslinking structure was less than that without the structure (Fig.1-18). Further, the amount of Cs adsorbed on most adsorbents with the crosslinking structure was greater than that adsorbed without the structure.

An evaluation by an external organization verified that this improved adsorbent satisfies the Food Sanitation Act and Water Supply Act, and we developed a cartridge-type water purifier called KranCsair® (Fig.1-19(a)). This original cartridge, which incorporates the developed adsorbent, is replaced easily (Fig.1-19(b)). A monitoring test of the developed purifier was conducted in Fukushima. On the basis of the result, we will determine the final product specifications.

Reference

Mikami, T., Shibata, T. et al., Development of a Water Purifier by EB-Grafted Fiber, Setsubi to Kanri, vol.47, no.4, 2013, p.95-99 (in Japanese).

1–10 Assessment of Doses to Inhabitants Living in Fukushima Prefecture
— Approach to Assessing the Doses Considering Areal Differences in Contamination and Interpopulational Differences in Lifestyle Habits —

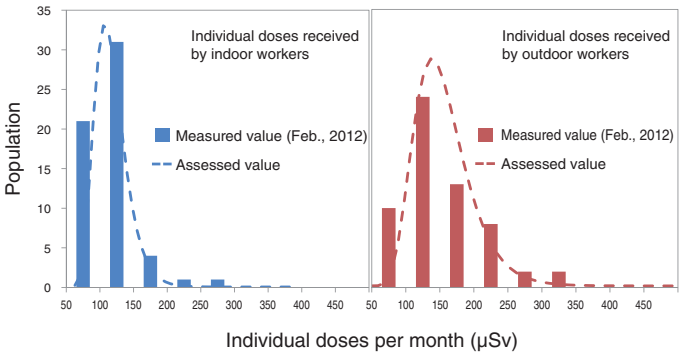

Fig.1-20 Comparisons of measured and assessed values of individual doses
Doses to outdoor and indoor workers in Fukushima City were assessed, taking into account areal differences in contamination and interpopulational differences in lifestyle habits. A comparison of the measured and assessed individual doses revealed good agreement, which indicated the validity of our assessment method.

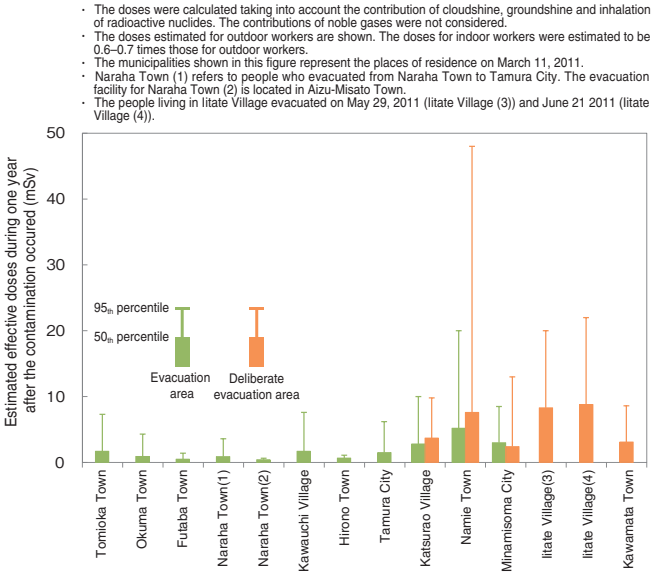

Fig.1-21 Estimated effective doses during one year after contamination occurred
Estimated doses during one year after contamination occurred were around 1–10 mSv in many municipalities, including the evacuated area and deliberate evacuation area. Doses received by the residents of Namie Town and Iitate Village were 4.9–48 mSv and 5.2–22 mSv, respectively.

The accident at the TEPCO's Fukushima Daiichi NPS resulted in widespread land contamination. Many residents are exposed to radiation in their daily lives while they continue to live in the affected areas. To manage the exposure of the population appropriately, the development of a dose assessment method is urgently required.

The doses received by the population in daily life are generally assessed using (1) data on the radionuclide concentrations or exposure rates and (2) data on lifestyle habits related to exposure pathways. If the average values of these data were used, it would be difficult to determine individual doses. Thus, we developed a method of assessing the dose distributions of a population living in the same area.

To develop the model, we measured the ambient dose equivalent rates and prepared data on lifestyle habits, which were obtained from surveys on the periods of time spent inside and outside, with the cooperation of participants in various types of occupations. After we determined the distributions of the ambient dose equivalent rates and the lifestyle data, we assessed the distributions of doses received by the population. We also measured data on individual doses due to external exposure with personal dosimeters. The validity of the assessment was confirmed by comparing the results of the assessment and the measured data (Fig.1-20).

In addition, we assessed the range of doses received by the evacuees during one year after the accident using the method developed above. This assessment takes into account the doses received during evacuations to multiple facilities and the evacuees' lives after that. Fig.1-21 shows the result of the dose assessment for outdoor workers. In most of the municipalities included in the evacuated areas, the range of effective doses is 1–10 mSv for outdoor workers during one year after the accident. In Namie Town and Iitate Village, where evacuation was delayed after contamination occurred, the effective doses were higher than in other municipalities: 4.9–48 mSv and 5.2–22 mSv, respectively. Our study provides ranges of doses that are more detailed than the results published by the World Health Organization and are based on scientific grounds by taking into account areal differences in contamination and individual differences in lifestyle habits.

Reference

Takahara, S. et al., Assessment of Radiation Doses to the Public in Areas Contaminated by the Fukushima Daiichi Nuclear Power Station Accident, Proceedings of International Symposium on Environmental Monitoring and Dose Estimation of Residents after Accident of TEPCO's Fukushima Daiichi Nuclear Power Station, Kyoto, Japan, 2012, p.212–220.

1–11 For the Safe Handling of Dehydrated Sludge Contaminated by Radioactive Cesium

— Dose Estimate for Workers and Public with Incineration and Disposal of Dehydrated Sludge —

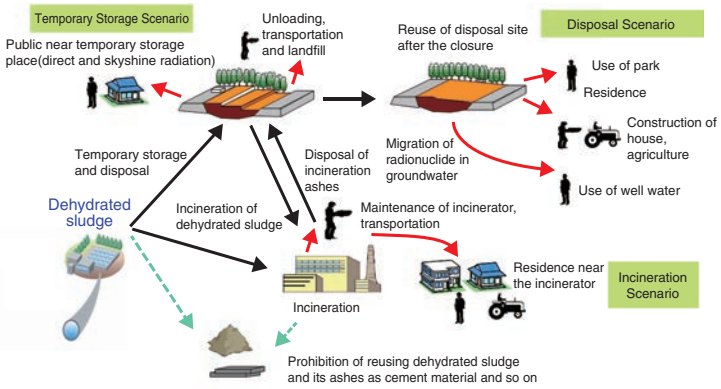

Fig.1-22 Scenarios for incineration and disposal of dehydrated sludge contaminated by radioactive cesium
External and internal exposure pathways in the transportation, incineration, and temporary storage of the sludge are specified on the basis of information on actual work conditions and treatment record for the sludge. Specified scenarios and pathways are guaranteed to be exhaustive through a comparison with the pathways used in previous clearance level estimate.

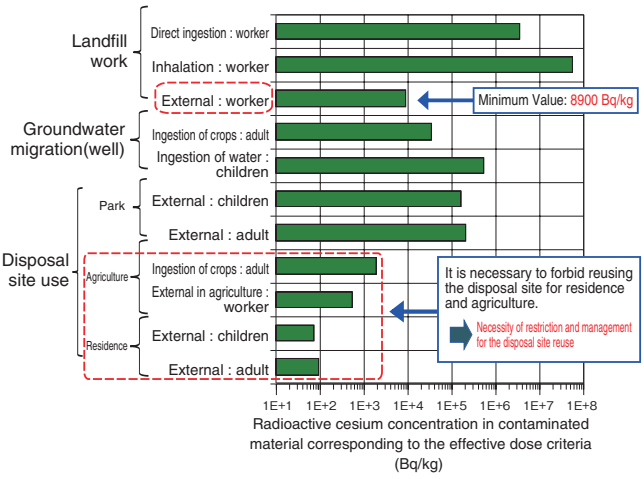

Fig.1-23 Estimated results of limiting radioactive cesium concentration to ensure safe incineration and disposal
Minimum radioactive cesium concentration in dehydrated sludge and incineration ashes, corresponding to the effective dose criterion (1 mSv/y for engaging in treatment of materials contaminated by the severe accident, and 10 μSv/y for post-closure in disposal), is estimated to be 8900 Bq/kg under the condition of limited reuse of the site.

The ground surface environment in Fukushima Prefecture and the surrounding area has been contaminated by radionuclides released from the TEPCO's Fukushima Daiichi NPS. Soil particles that adsorbed radioactive cesium flow into sewage and water resources for tap water. Dehydrated sludge containing high concentrations of radioactive cesium was generated by sewage and water supply processing. The contaminated sludge should be incinerated and disposed of while ensuring the radiation safety of the workers and the public. However, there was no criterion for treatment of the sludge.

The dose to the workers and the public during incineration and disposal was estimated to provide the technical information for determining the criterion. We calculated the minimum radioactive cesium concentration from the dose results, corresponding to the effective dose criterion indicated by Nuclear Safety Commission of Japan (Near-term policy to ensure the safety for treating and disposing contaminated waste around the site of Fukushima Dai-ichi Nuclear Power Plants, NSC, June 3, 2011).

We focused on the similarity between the actual situation of general incineration and disposal and a series of scenarios in previous clearance level estimation. By incorporating additional exposure pathways peculiar to the sludge into the scenarios based on the clearance level estimation, we could set up comprehensive and reliable scenarios and pathways over a short period of time, as shown in Fig.1-22. According to the information on the actual work conditions and treatment record of the sludge, suitable parameters in each scenario were set for a realistic estimation.

The estimated doses for the main exposure pathways are shown in Fig.1-23. Under the condition of a radioactive cesium concentration of less than 8000 Bq/kg, general incineration and disposal of the sludge is justifiable under the restriction that disposal site reuse be limited to residential and agricultural use.

This result was used as technical information for determining the criterion for sludge treatment by the Ministry of Land, Infrastructure, Transport and Tourism.

Reference

Takeda, S. et al., Dose Estimate for Incineration and Disposal of Dehydrated Sludge Contaminated by Radioactive Cesium of High Activity Concentration, Hoken Butsuri, vol.47, no.4, 2012, p.247-259 (in Japanese).

1–12 Inhibiting Corrosion of Metallic Materials in Spent Fuel Pools
— Verification of Removal Effect of Dissolved Oxygen Using Hydrazine —

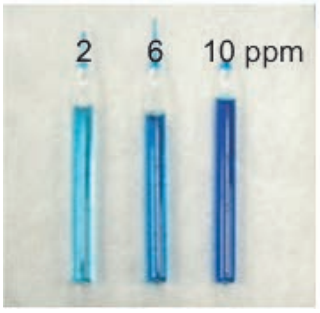

Fig.1-24 Analyses of the dissolved oxygen (DO) concentration in water
The color becomes darker depending on the DO concentration.

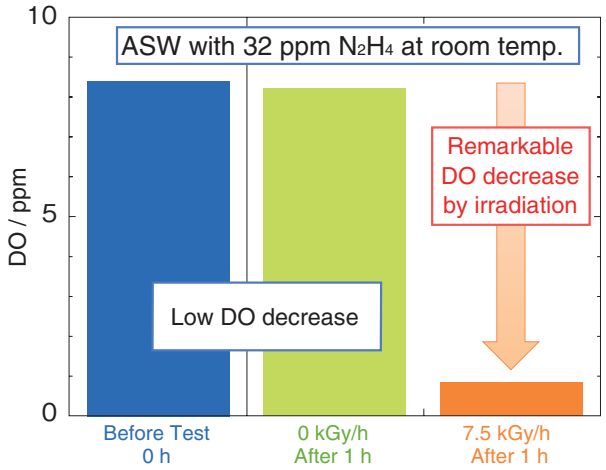

Fig.1-25 Changes in dissolved oxygen concentration with γ-ray irradiation
DO in artificial seawater (ASW) containing hydrazine (N_2H_4) was effectively removed by γ-ray irradiation.

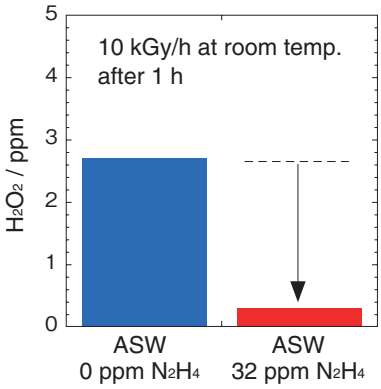

Fig.1-26 Inhibition of hydrogen peroxide (H_2O_2) production
The concentration of H_2O_2 generated by water radiolysis was reduced by adding N_2H_4.

At the TEPCO's Fukushima Daiichi NPS (1F), the cooling functions of the spent fuel pools (SFPs) failed with the loss of the electric power supply, so sea water was injected into the SFPs of 1F2–1F4 by fire trucks as an emergency measure for avoiding fuel exposure to the air.

Although the corrosion of metallic materials in SFPs is normally prevented by the circulation of purified water, accelerated corrosion is a matter of concern in the case of water mixed with seawater. For example, the SFPs' water might leak owing to localized corrosion (e.g., pitting corrosion, crevice corrosion) of the stainless steel used as a liner material.

As a measure for inhibiting corrosion, hydrazine is generally used as an inhibitor for boiler systems. Therefore, it was also injected into the SFPs of 1F to remove dissolved oxygen (DO), which accelerates corrosion. It is well known that hydrazine can easily remove DO in hot water (over 200 ºC), although it was unknown whether hydrazine can remove DO in water mixed with seawater at room temperature and under a radiation environment.

Therefore, we evaluated the removal of DO by adding hydrazine to artificial seawater (ASW) using a Co-60 γ-ray source to simulate the conditions in the SFPs.

The DO concentration in ASW containing 32 ppm of hydrazine was measured before and after 1 h of irradiation at a dose rate of 7.5 kGy/h. In this measurement, a coloring reagent was used, which darkened in color with increasing DO concentration, as shown in Fig.1-24.

As a result, as shown in Fig.1-25, for the sample that was not irradiated, the decrease in DO concentration was minimal. In contrast, the DO concentration in the sample exposed to γ-ray radiation decreased significantly.

This result showed that hydrazine injected into SFP water mixed with seawater could effectively remove DO even under a low temperature condition with γ-rays radiated from spent fuels. Moreover, we found that the addition of hydrazine could reduce hydrogen peroxide, which was generated by water radiolysis and is, like DO, a corrosive species (Fig.1-26).

The above results demonstrate that DO and hydrogen peroxide could be removed by hydrazine addition and irradiation, and it is expected that corrosion of metallic materials in the SFPs could be inhibited.

On the basis of this research, hydrazine has been periodically injected into the SFPs of 1F to inhibit corrosion.

Reference

Motooka, T. et.al., Effect of Gamma Ray Irradiation on Deoxygenation by Hydrazine in Artificial Seawater, Nippon Genshiryoku Gakkai Wabun Ronbunshi, vol.11, no.4, 2012, p.249-254 (in Japanese).

1–13 Characterization of Fuel Debris in Severe Accident

— Properties of Fuel Debris for Developing Defueling Operations —

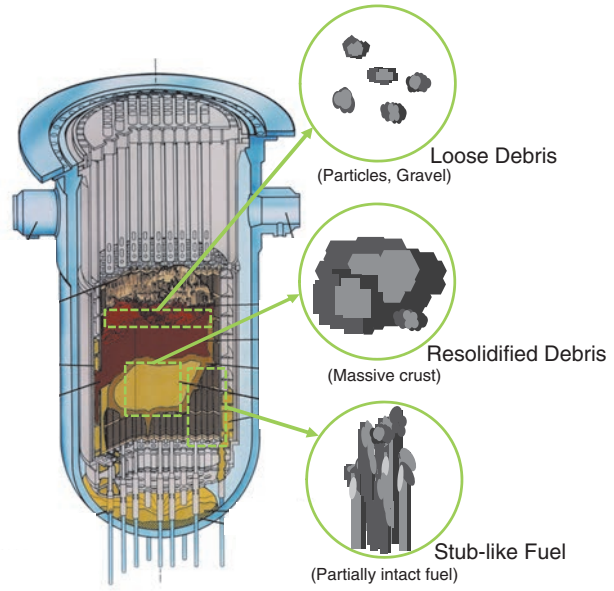

Fig.1-27 Image of fuel debris from TMI-2 accident
Fuel debris from the TMI-2 accident had various features depending on the location.

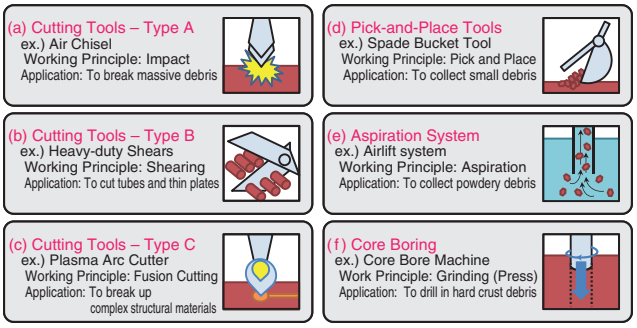

Fig.1-28 Categories of defueling tools
Defueling tools in TMI-2 categorized into six groups according to working principle. These tools were selected according to the features of the debris.

Table 1-2 Properties of fuel debris for defueling
The properties of fuel debris were selected considering their effect on the tools' performance.

Tools*	Shape	Size	Density	Thermal Properties: Melting Point	Thermal Properties: Heat Capacity	Thermal Properties: Thermal Conductivity	Mechanical Properties: Hardness	Mechanical Properties: Elastic Modulus	Mechanical Properties: Fracture Toughness
(a)									✓
(b)							✓	✓	✓
(c)			✓	✓	✓	✓			
(d)	✓	✓	✓						
(e)	✓	✓	✓						
(f)					✓	✓	✓	✓	✓

*Refer to Fig.1-28

For decommissioning of the TEPCO's Fukushima Daiichi NPS (1F), removal of the fuel debris, which is a mixture of molten fuel and structural materials, is planned to start around 2020. It is necessary to clarify the characteristics of the fuel debris in order to design and develop the defueling process and tools.

First, we surveyed the defueling process in the Three Mile Island Unit 2 accident (hereafter, TMI-2). Several types of debris existed in the reactor, such as loose debris (particles, gravel), resolidified molten debris (massive crust), and stub-like fuel (partially melted fuel) (Fig.1-27). Various defueling tools were selected according to the features of the fuel debris.

In the 1F accident, the relocation and components of the debris were estimated to differ from those in TMI-2, e.g., molten core and concrete interaction on the pedestal floor. However, some types of defueling tools used in TMI-2 can be applied to 1F defueling because the debris in 1F and TMI-2 is assumed to have similar characteristics.

The useful tools in TMI-2 defueling were categorized into six groups according to their operating principles, such as impact and shearing (Fig.1-28). The important properties of the fuel debris for defueling were selected considering their effect on the tools' performance (Table 1-2). Of these properties, the mechanical properties (hardness, elastic modulus, fracture toughness) must be identified as preferential items, because few data on these characteristics of fuel debris are available in past severe accident studies.

We have to use some techniques without large samples to measure these mechanical properties because we can obtain only very small actual debris samples early in the sampling operation. The hardness is measured by the indentation method as the Vickers hardness. The elastic modulus can be measured by the ultrasonic wave pulse echo method, and the fracture toughness is also measured by the indentation fracture method.

We will suggest some types of non-radioactive surrogate debris materials for the development of defueling tools on the basis of these properties.

Reference

Yano, K. et al., Direction on Characterization of Fuel Debris for Defueling Process in Fukushima Daiichi Nuclear Power Station, Proceedings of International Nuclear Fuel Cycle Conference (GLOBAL2013), Salt Lake City, Utah, USA, 2013, paper 8167, p.1554–1559., in CD-ROM.

1–14 What Has Formed on the Fuel Debris Surface by Sea Water Injection?

— High-Temperature Reaction Products between Simulated Fuel Debris and Salt Deposits —

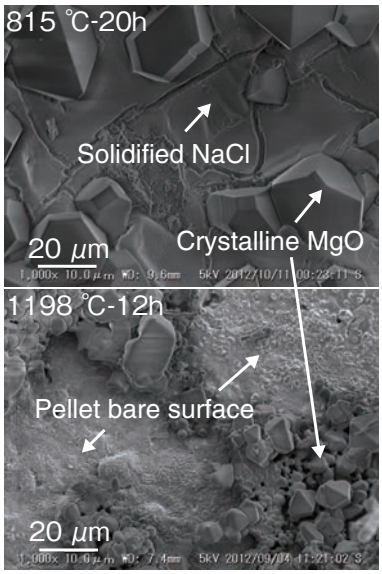

Fig.1-29 SEM images of $(U,Zr)O_2$ pellet surface heat-treated with sea salt
After heat treatment at 815 °C, solidified NaCl covers the pellet surface, and crystalline MgO is deposited. After heat treatment at 1198 °C, crystalline MgO is the main residue.

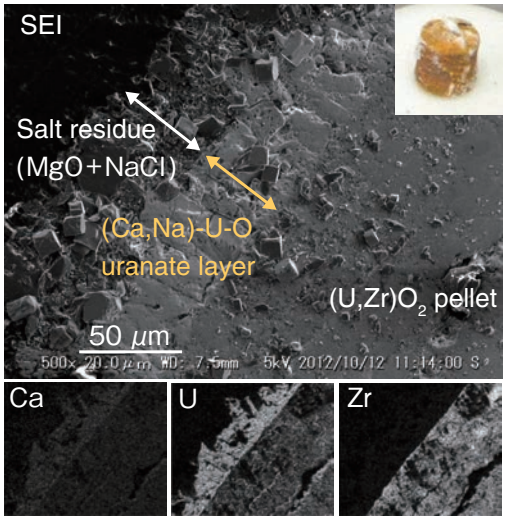

Fig.1-30 SEM and X-ray images of cross section of $(U,Zr)O_2$ pellet heat-treated with sea salt at 1002 °C under airflow
Formation of a (Ca,Na)–U–O uranate layer 50 μm in thickness is confirmed between the pellet surface and salt residue layer.

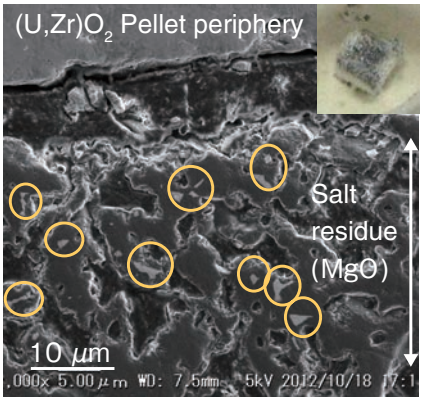

Fig.1-31 SEM image of cross section of $(U,Zr)O_2$ pellet heat-treated with sea salt at 1002 °C under argon gas flow
Within the salt residue layer on the pellet surface, fine pieces of $(Ca,U)O_{2+x}$ are scattered (in circles). Uranate forms temporarily, and it is reduced to the dioxide during isothermal heat treatment.

In the accident at the TEPCO's Fukushima Daiichi NPS, sea water was injected into the reactor cores for emergency cooling. Sea salt may have been deposited on the high-temperature surface of the core melt at the bottom of the reactor vessels. To investigate the possible impacts of sea water injection on the chemical and physical state of the corium debris, we performed experiments on the high-temperature reactions between sea salt and $(U,Zr)O_2$ simulated corium debris (sim-debris).

First, the decomposition behavior of sea salt at high temperatures was observed. Fig.1-29 shows scanning electron microscopy (SEM) images of the surface of a $(U,Zr)O_2$ pellet heat-treated with sea salt under an argon gas flow. The melting point of NaCl, the main constituent of sea salt, is about 800 °C. After heat treatment at 815 °C, the pellet surface was covered with a solidified NaCl layer, together with crystalline MgO decomposed from magnesium salts. Because NaCl is gradually vaporized at higher temperatures, MgO remains as the main salt residue after heat treatment at 1198 °C.

The reaction products from sea salt and sim-debris were then identified. Fig.1-30 shows the cross section of a $(U,Zr)O_2$ pellet heat-treated with sea salt under an airflow. We have found that a dense layer of calcium and sodium uranate formed on the pellet surface at 1002 °C under an airflow, with a thickness of more than 50 μm. On the other hand, under an argon gas flow, the calcium in sea salt is likely to dissolve into the cubic sim-debris phase to form a solid solution, $(Ca,U,Zr)O_{2+x}$. The diffusion depth is only 5–6 μm from the surface after treatment at 1198 °C for 12 h. Another interesting finding is a scattering of fine pieces of $(Ca,U)O_{2+x}$ in the MgO residue layer on the pellet surface, as shown in Fig.1-31. In the heating process, calcium uranate forms temporarily because of an oxidizing gas (SO_x) evolved from the thermal decomposition of magnesium and calcium sulfates. During isothermal treatment under an argon gas flow, the uranate is reduced to the dioxide solid solution.

From the results of these experiments, we predict that (1) MgO is the main salt residue that may be concomitant with the corium debris to be retrieved, (2) uranate of calcium and sodium may have formed on the debris surface under high oxygen partial pressures, (3) fine pieces of $(Ca,U)O_{2+x}$ may be included in the MgO layer under low oxygen partial pressures.

Reference
Takano, M. et al., High Temperature Reaction between Sea Salt Deposit and $(U,Zr)O_2$ Simulated Corium Debris, Journal of Nuclear Materials, vol.443, issues 1–3, 2013, p.32–39.

1–15 Prevention of Re-Criticality in Fuel Debris in the Damaged Cores
— Criticality Characteristics of Fuel Debris Containing Concrete —

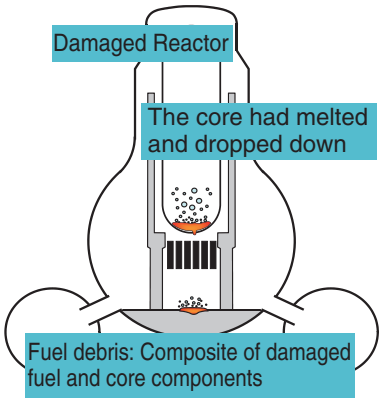

Fig.1-32 Fuel debris in damaged core
Tens of thousands of kilograms of fuel debris, namely, a composite of fuel and core components, has been generated as a result of severe core meltdown at the 1F.

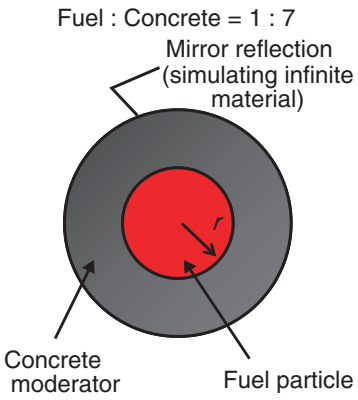

Fig.1-33 Example of calculation model of fuel debris
This model represents an example of supposed fuel debris consisting of small fuel particles dispersed in concrete.

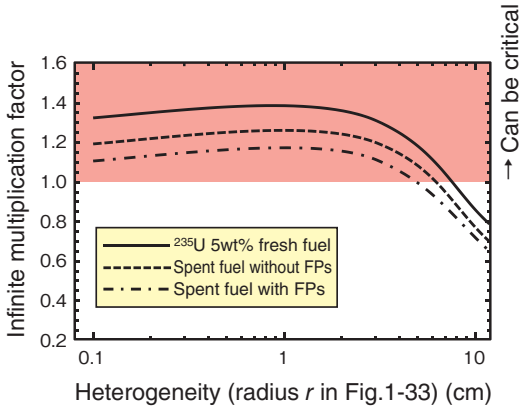

Fig.1-34 Infinite multiplication factor of supposed fuel debris
It is indicated that the fuel debris modeled in Fig.1-33 can be critical under various conditions. Such fuel debris must be controlled carefully to prevent re-criticality.

The Great East Japan Earthquake on March 11, 2011 caused a severe accident at the TEPCO's Fukushima Daiichi NPS (1F). As shown in Fig.1-32, the cores of the reactors in 1F1–1F3 were seriously damaged owing to a failure of the core cooling system. The amount of fuel debris, which is a composite of damaged fuel and other core components, is estimated to be tens of thousands of kilograms in each unit.

There has been no indication of re-criticality of the fuel debris since the accident. The risk of re-criticality during removal of the fuel debris from each core should still be considered carefully because the minimum critical mass of the fresh fuel is only tens of kilograms. Although criticality control of normal fuel handling is designed on the basis of some determined fuel conditions, there are many unknowns regarding the fuel debris, such as its composition or shape. Therefore, an exhaustive criticality database including any conjectured conditions of the fuel debris, called a "criticality map," needs to be prepared to judge the criticality risk quickly on the disclosure of its actual conditions.

We are analyzing the criticality of fuel debris considering many parameters, such as water content or fuel burn-up, by referring to previous studies in the literature.

An example of the calculation model is shown in Fig.1-33. The model represents fuel dispersed in concrete, which is a major material of the pedestal floor of the containment vessel.

The infinite multiplication factors of the fuel debris are shown in Fig.1-34. The lines in the red area indicate the conditions under which the fuel debris may be critical. Moreover, another calculation shows that the minimum critical mass of the fuel debris can be less than several thousand kilograms, which is significantly smaller than the amount of fuel in each core. The fuel debris containing concrete, therefore, must be handled cautiously to prevent re-criticality.

We continue the effort to complete the criticality map by computation and critical experiments considering fuel debris under diverse conditions, such as a submerged fuel–concrete mixture and a composite of fuel and the steel of the pressure vessel. The results are expected to provide useful information for judging the criticality risk for any actual fuel debris, and to contribute to the development of reliable re-criticality prevention and detection measures.

Reference

Izawa, K. et al., Infinite Multiplication Factor of Low-Enriched UO_2-Concrete System, Journal of Nuclear Science and Technology, vol.49, no.11, 2012, p.1043–1047.

1–16 Nuclear Material Accountancy for Molten Core Material by γ-ray Measurement

— Development of Nuclear Material Measurement Technology using Passive γ Spectrometry of Molten Core Material —

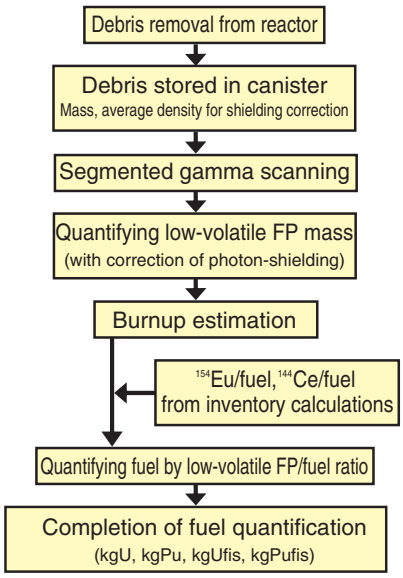

Fig.1-35 Data flow of γ spectrometry for U, Pu quantification
U and Pu are quantified by coupling passive γ spectrometry for radioactivity quantification of FP with FP/U, Pu correlation by inventory calculation, and photon transport calculation.

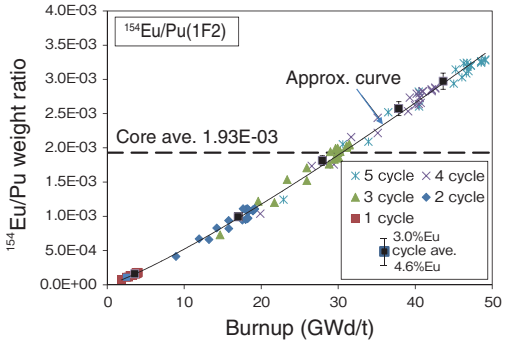

Fig.1-36 Correlation between ^{154}Eu and Pu quantity (1F2)
^{154}Eu: Pu ratio increases monotonically with respect to burnup.

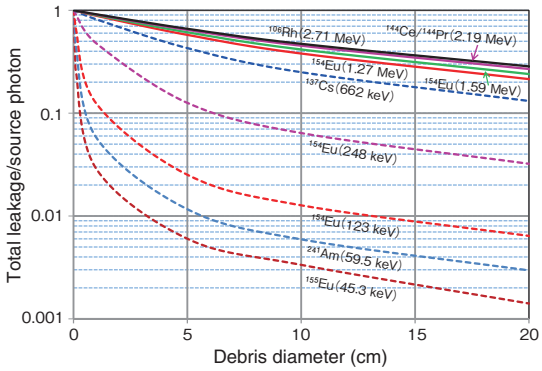

Fig.1-37 Sensitivity of leakage photon spectrum to debris size
High-energy γ-rays leak more easily than low-energy γ-rays. Self-shielding correction is essential to obtain the source photon intensity because of strong attenuation in large pieces of fuel debris.

Even after the accident at the TEPCO's Fukushima Daiichi NPS (1F), it is required to provide assurance to the national and international communities that uranium (U) and plutonium (Pu) in the molten fuels have not been diverted to military use. We have been conducting a feasibility study of U and Pu quantification measurement by passive γ spectrometry of molten core material (fuel debris) from outside of a canister after the removal of fuel debris.

Although U and Pu themselves emit γ-rays, it is very difficult to measure them directly because their energies are much lower than the energies of fission products (FPs). We focused on the high-energy γ-emitting and low-volatile FPs that coexist with U and Pu in the fuel melting process during a severe accident. Cerium (Ce) and europium (Eu) are well known as low-volatile FPs, and ^{144}Ce and ^{154}Eu emit high-energy (>1 MeV) γ-rays. Experience in quantifying U and Pu by measuring γ-rays from ^{144}Ce in fuel debris was gained in the TMI-2 accident.

Fig.1-35 shows the assumed data flow of passive γ spectrometry of FPs for U and Pu quantification. Because this is an indirect methodology for quantifying U and Pu using FP/U and the Pu ratio by an inventory calculation at the time of the 1F accident, the sensitivity to various parameters that affect the quantities of FPs, U, and Pu was analyzed. Fig.1-36, as an example, shows a good correlation between the ratio of ^{154}Eu to Pu and burnup, regardless of the neutron flux and water void fraction, because the variance is offset.

In γ-ray measurement of fuel debris, it is necessary to analyze the sensitivities to parameters such as the self-attenuation in the fuel debris and the geometry of the fuel debris and canister. A fundamental analysis was performed using a simple spherical model with a variety of parameters, such as the debris size, composition, porosity, density, homogeneity, or heterogeneity. It is assumed that low-energy γ-rays (<500 keV) are sensitive to the size and composition of the debris, and high-energy γ-rays (>1 MeV) are less sensitive. Fig.1-37 shows the sensitivity of the energy-dependent leakage photon ratio to the debris size. For ^{154}Eu, strong attenuation was observed, up to about 20% and 50% with fuel debris 2.5 cm and 10 cm in diameter, respectively. Correction of self-shielding is essential. The use of the correlation between the difference in the photopeak flux and the energy of ^{154}Eu has been analyzed as an option.

We will continue the feasibility study of this methodology by numerical analysis with the canister model and conceptual system design, and improve the precision of nuclear material quantification.

Reference
Sagara, H., Tomikawa, H. et al., Feasibility Study of Passive Gamma Spectrometry of Molten Core Material from Fukushima Dai-Ichi Nuclear Power Station Unit 1, 2 and 3 Cores for Special Nuclear Material Accountancy —Low-Volatile FP & Special Nuclear Material Inventory Analysis and Fundamental Characteristics of Gamma-ray from Fuel Debris —, Journal of Nuclear Science and Technology, vol.51, issue 1, doi: 10.1080/00223131.2014.852994.

1–17 Calculation of Decay Heat Causing Core Meltdown

— Three-Dimensional Decay Heat Analysis for the TEPCO's Fukushima Daiichi NPS —

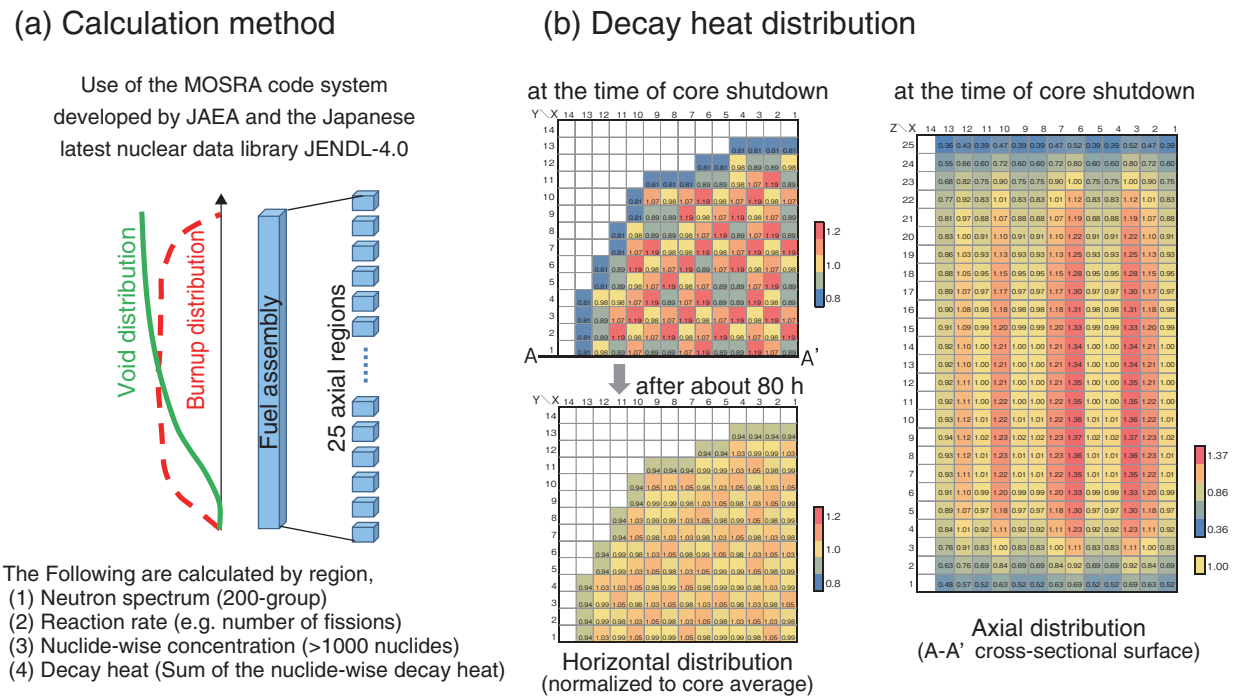

Fig.1-38 Calculation method and sample result of decay heat distribution in 1F2
The 3D decay heat distribution was calculated considering the distributions of the neutron spectra, burnup, and void fraction. The fuel loading pattern was based on that of a typical boiling water reactor.

Even after a nuclear reactor is shut down, nuclides such as fission products (FPs) decay, and decay heat is generated. The accident at the TEPCO's Fukushima Daiichi NPS (1F) was caused by a failure of the ultimate decay heat removal because of the loss of electric power due to the tsunami.

Understanding the core melt progression in accidents enables the location of melted fuel to be estimated and supports further improvements in the safety of nuclear reactors. The detailed analysis of the core melt progression begins with a prediction of the decay heat distribution in the core at the time of shutdown. Although there are some simple formulae for estimating the decay heat, they do not yield an accurate time-dependent decay heat distribution in the core. Thus, we newly developed data and a code to predict the time-dependent three-dimensional decay heat distribution. They were applied to the decay heat analysis of each core of 1F1, 1F2, and 1F3. In this method, each core is divided into four or five horizontal regions corresponding to different fuel assembly types or refueling batches, and each region is furthermore divided into 25 axial regions that have different burnup values and void fractions, as shown in Fig.1-38 (a). For each region, the nuclide-wise concentration is calculated for more than 1000 nuclides considering the operating conditions of each plant until core shutdown. Then, we can obtain the nuclide-wise decay heat in each region using the decay and heat generation constants. The region-wise decay heat is calculated by summing the nuclide-wise decay heat.

Fig.1-38 (b) shows the obtained decay heat distribution of 1F2, the core melting time of which is estimated to be about 80 h after core shutdown. The decay heat at the time of core shutdown is approximately proportional to the power density under normal operating conditions because the decay heat just after shutdown is dominated by the concentrations of short-lived FPs, which are in equilibrium according to the power density of each region. After that, the decay heat distribution gradually becomes flatter owing to the disappearance of the short-lived FPs. The obtained three-dimensional decay heat information is useful for future detailed analyses of the core melting progression because the decay heat is an important parameter for the movement of melted materials.

Reference

Okumura, K. et al., Nuclear Data for Severe Accident Analysis and Decommissioning of Nuclear Power Plant, Proceeding of the 2012 Symposium on Nuclear Data, November 15–16, 2012, Research Reactor Institute, Kyoto University, Kumatori, Japan, JAEA–Conf 2013–002, 2013, p.15–20.

1–18 What's the Point of Analyzing the Fukushima Accident?

— Review of Five Investigation Reports on Fukushima Accident —

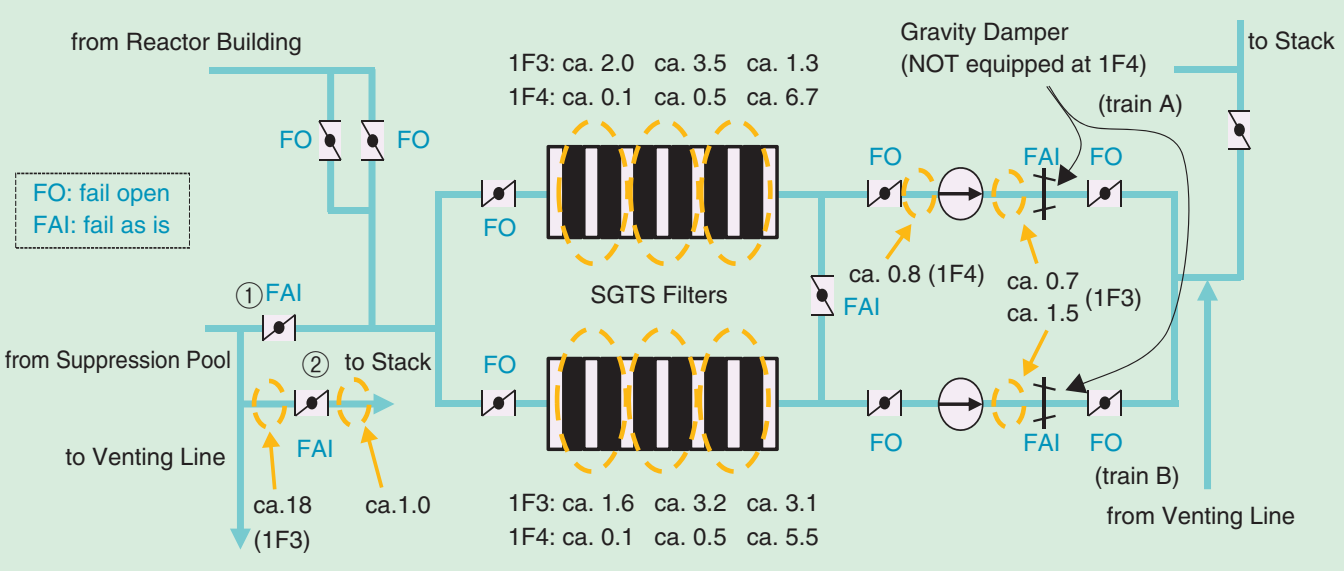

Fig.1-39 Dosimetries at standby gas treatment system (SGTS) filters for 1F3 and 1F4 (unit: mSv/h)
Based on the dosimetries on the SGTS filters at 1F4, it is presumed that venting gases flowed from the 1F3 reactor building through the SGTS line(s) into the 1F4 reactor building. On the other hand, venting gas flow through the SGTS lines is assumed to be unlikely because different trends were observed in the dosimetries on the SGTS filters at 1F3, and the dosimetry downstream of the valve connected with the stack (② in the figure) was significantly low. However, the possibility of venting gas flow should be further examined because the dosimetry of the filter in the center was the highest, and the containment pressure did not exceed the design pressure for a long time.

On March 11, 2011, an earthquake and subsequent tsunami resulted in a severe accident at the TEPCO's Fukushima Daiichi NPS (1F). Four independent committees were established by the Japanese government, the Diet of Japan, the Rebuild Japan Initiative Foundation, and the TEPCO to investigate the accident and published their respective reports. In addition, the Nuclear and Industrial Safety Agency analyzed the causes of the accident to obtain the lessons learned from it.

This study reviews the five reports, clarifies the differences in their positions, from a technological point of view, and identifies undiscussed issues to obtain insights useful for near-term regulatory activities, including the accident investigation by the Nuclear Regulation Authority. As a result, the different positions identified are related to the reason of emergency diesel generator trips, the reason of manual trip of the isolation condensers at 1F1, reactor depressurization at 1F1, containment integrity and venting operation, and the hydrogen leak path. For example, the hydrogen explosions at 1F1 and 1F3 are assumed to be the result of hydrogen leaking directly from the containments, and the explosion at 1F4 is assumed to be caused by reverse hydrogen flow from 1F3 during venting. This study pointed out that the contribution of venting gases should be further examined based on the fact that containment venting was executed shortly before the explosions at 1F1 and 1F3 and on the measured dosimetries on the standby gas treatment system (SGTS) filters (Fig.1-39).

In addition, the following undiscussed issues are identified.

(1) Adequacy of Operating Procedures Applied at 1F1: In-depth analysis of the basic concepts for preparing the operating procedures by comparison with those at Tsuruga 1F1 is required.

(2) Design Concepts of SGTS Valves on Loss of Drive Forces: The design concepts of "fail open" and "fail as is" when the drive force for the valves is lost should be clarified by examining the actual designs at other plants.

(3) Design Concepts of Valves Configured in Containment Venting Lines: The design concepts for the venting lines, which consist of one rupture disk and two normally closed valves placed in series, should be studied.

(4) Operating Basis of Startup of Containment Cooling Systems: Although suppression pool cooling was initiated after the earthquake at 1F1 and 1F2, it was not started up at 1F3 considering the effects of tsunami-induced kataseism. It is necessary to identify the causes of this difference.

Reference

Watanabe, N., Tamaki, H. et al., Review of Five Investigation Committees' Reports on the Fukushima Dai-Ichi Nuclear Power Plant Severe Accident, Nippon Genshiryoku Gakkai Wabun Ronbunshi, vol.12, no.2, 2013, p.113-127 (in Japanese).

1–19 Mechanism of Cesium Absorption on Zeolite

— First-Principles Study of Structural Effects on Absorption in Zeolites —

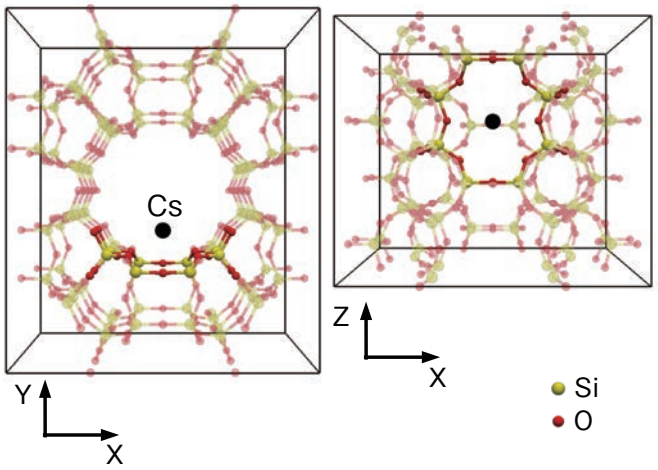

Fig.1-40 Crystal structure of zeolite called mordenite
Mordenite has a framework made of silicon (Si) and oxygen (O) atoms. If some of the Si atoms are replaced with aluminum (Al) atoms, mordenite can absorb cations such as cesium ions (Cs^+). The dense part of the framework represents the Cs absorption site, which appears in Fig.1-41.

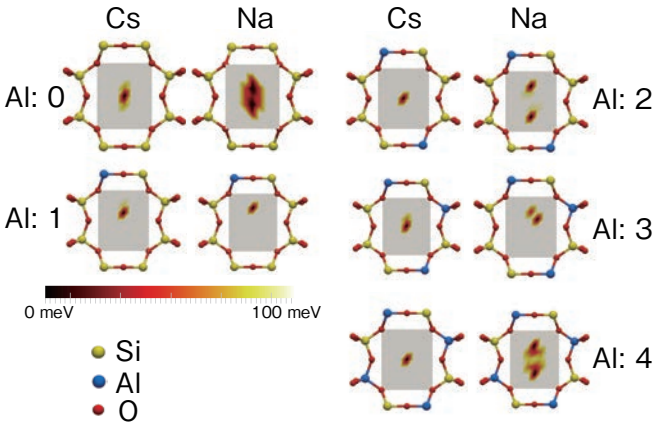

Fig.1-41 Absorption energy distribution at Cs^+ absorption site
At the Cs absorption site described in Fig.1-40, the absorption energies of Cs and sodium (Na) ions are plotted for various numbers of Al atoms (indicated after "Al:" in the figure). Dark area corresponds to lower-energy region.

After the accident at the TEPCO's Fukushima Daiichi NPS, the treatment of nuclear waste water, which includes radionuclides such as radioactive cesium, became an important problem. Cesium is presently removed from waste water by absorbent materials, for example, zeolite. Although more than 100 types of zeolite have been discovered so far, some of them absorb cesium well, and some absorb very little. If we develop a new zeolite that absorbs more cesium and has better controllability of absorption and removal, treatment of waste water will advance.

To develop desirable zeolites, we have to know how zeolites absorb cesium. However, it is difficult to directly observe the absorption behavior of cesium because it occurs at the microscopic scale. In this case, numerical simulations at the atomic scale are effective for revealing the absorption mechanism.

The characteristics of zeolites that absorb Cs selectively are known empirically. However, the principles of the selectivity mechanism have been unclear. To clarify these principles, we calculate in detail the absorption energy at the Cs absorption site in mordenite (Fig.1-40), which is a zeolite with a high Cs-selective absorbability. We adopted the first-principles calculation method to evaluate the absorption energy because it is the most accurate and reliable. The results are shown in Fig.1-41. This figure shows density plots of the absorption energy of Cs and sodium (Na). For Na, the minimum points are distributed, and therefore a Na ion is weakly bound at the site. On the other hand, a Cs ion is strongly bound at only one minimum-energy point in the center of the site. Thus, we determined why Cs is bound more strongly than Na at this site. By numerical simulations, we also identified various characteristics of Cs-selective absorption, some of which were previously unknown.

With this deeper understanding of the absorption mechanism, we can appropriately plan the development of high-performing absorbent materials. This development can contribute to not only treatment of waste water but also decontamination of environmental radionuclides.

Reference

Nakamura, H. et al., First-Principles Calculation Study of Mechanism of Cation Adsorption Selectivity of Zeolites: A Guideline for Effective Removal of Radioactive Cesium, Journal of the Physical Society of Japan, vol.82, no.2, 2013, p.023801–1–023801–4.

1–20 Decontamination of Radioactive Cobalt and Manganese with Radioactive Cesium

— Simplified Treatment Process of Radioactive Liquid Waste by Adding Hexacyanoferrate(II) Ions —

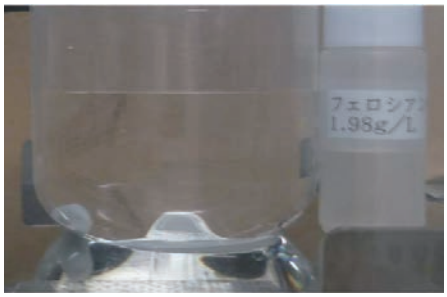

Contaminated water (left) and potassium hexacyanoferrate(II) solution (right)

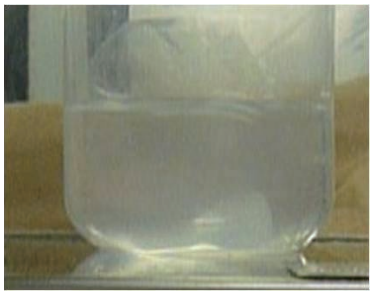
Cloudy solution after adding hexacyanoferrate(II) solution to the contaminated water

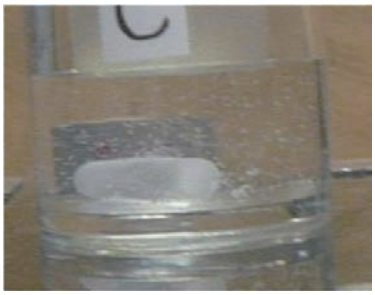
Solution after reaction

Fig.1-42 Simplified treatment process experiment
Hexacyanoferrate(II) ions react with transition metal ions, and this reaction produces precipitation of the transition metal hexacyanoferrate(II). This precipitation product may selectively adsorb Cs. Therefore, decontamination of both radioactive transition metals and Cs is expected to be achieved by adding potassium hexacyanoferrate(II) solution to the contaminated water from 1F.

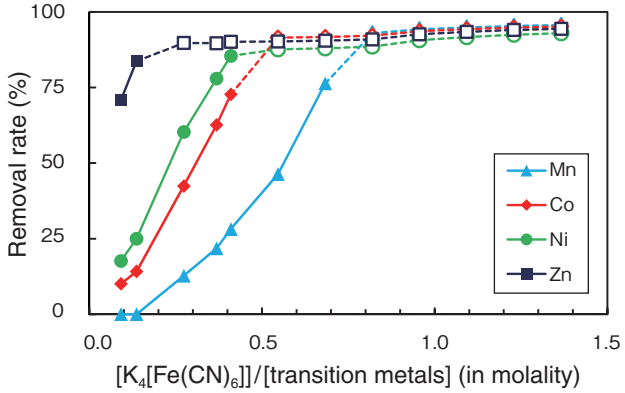

Fig.1-43 Effect of ratio of hexacyanoferrate/transition metals on removal rate of transition metals
The removal rates of the transition metals exhibited some differences. It is possible to remove every radioactive transition metal by adding a sufficient amount of hexacyanoferrate(II) ions.

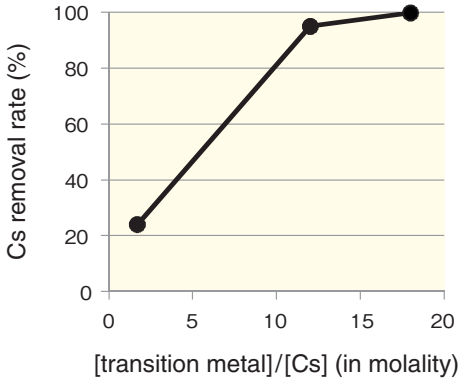

Fig.1-44 Increase of Cs removal rate
The Cs removal rate increased with [transition metal]/[Cs].

At the TEPCO's Fukushima Daiichi NPS (1F), an enormous volume of contaminated water has been generated by reactor cooling and groundwater inflow, and is temporarily stored at the site. The contaminated water bears not only fission products from the spent fuels, such as cesium (Cs), but also activated corrosion products from the reactor materials, such as manganese (Mn) and cobalt (Co).

Adsorption with insoluble hexacyanoferrate(II) is a well-known method of removing radioactive Cs from liquid waste. For radioactive Mn and Co decontamination, co-precipitation with iron hydroxide is generally used. In fact, part of the contaminated water was actually treated by applying these methods at 1F.

It is known that the insoluble transition metal hexacyanoferrate(II) selectively adsorbs Cs among alkaline elements. Hexacyanoferrate(II) of Ni, Co, and Fe are typical compounds used to adsorb Cs, and they are products of the reaction of hexacyanoferrate(II) ions and transition metals. In iron co-precipitation, transition metals are co-precipitated with iron hydroxide, which is a product of the reaction with iron ions and hydroxide ions, because of their chemical similarity.

We developed a simplified treatment process for both radioactive transition metals and Cs decontamination. Fundamental experiments using both non-radioactive and radioactive solutions were conducted. As shown Fig.1-42, the treatment process consists of two reactions. The first reaction is in-situ generation of the transition metal hexacyanoferrate(II) by adding potassium hexacyanoferrate(II) solution to the contaminated water. The second reaction is Cs adsorption on the first reaction product.

The properties of the in-situ generation of insoluble hexacyanoferrate(II) adsorbent were examined using non-radioactive transition metal elements. As shown in Fig.1-43, the removal rate rose as the ratio $[K_4[Fe(CN)_6]]$/[transition metal] increased. For $[K_4[Fe(CN)_6]]$/[transition metal] > 1, the removal rates of transition metals were greater than 90%.

The Cs adsorption was also examined to investigate the removal rate of Cs. As shown in Fig.1-44, the removal rate of Cs was 95% when [transition metal]/[Cs] was 12. The removal rate of Cs reached 99% when [transition metal]/[Cs] was 18.

These results show that this new treatment process has the potential to remove both radioactive transition metals and Cs effectively when the ratio of Cs and transition metals is appropriate for the reactions.

At 1F, contaminated water has been treated by other treatment processes. We hope that our proposed process will be applied for the removal of Cs and transition metals from radioactive liquid waste in various decontamination processes in and around 1F.

Reference

Takahatake, Y., Shibata, A. et al., Decontamination of Radioactive Liquid Waste with Hexacyanoferrate(II), Procedia Chemistry, vol.7, 2012, p.610–615.

1–21 Comprehension of Radioactive Contamination inside the Reactor Buildings
— Radioanalysis of Concrete Core Boring Samples —

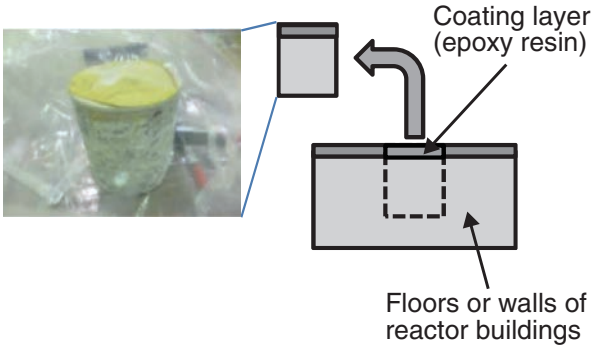

Fig.1-45 Photograph of concrete core boring sample
Radioanalysis of concrete core boring samples 10 cm in diameter was conducted. The samples were taken from the floors and walls of the 1F reactor buildings.

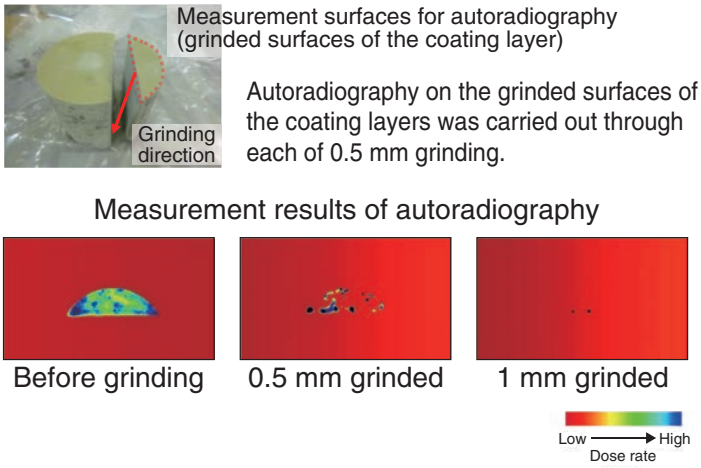

Fig.1-46 Evaluation of penetration depth of radioactive contaminant
The penetration depth of the radioactive contaminant was evaluated by autoradiograph measurements of ground surfaces of the coating layer. Heterogeneous penetration of the radioactive contaminant to a 1 mm depth below the surface was observed for the sample taken from 1F2.

Decontamination technology that uses remote access devices has to be developed to reduce the radiation dose of workers in the reactor buildings toward the decommissioning of the TEPCO's Fukushima Daiichi NPS (1F). For effective decontamination, it is necessary to comprehend the status of radioactive contamination inside the reactor buildings, specifically, the component nuclides, penetration into the floors or walls, and distribution of the radioactive contaminant. In particular, detailed radioanalysis is needed to evaluate the penetration of the radioactive contaminant into the floors or walls. We conducted a series of radioanalysis tests of concrete core boring samples taken from the floors and walls of the 1F reactor buildings (Fig.1-45) at the post-irradiation examination facilities in the Oarai Research and Development Center. Various radioanalytical techniques such as α- and γ-spectrometry and autoradiography, which have been developed in the facilities so far, were used for the radioanalysis of core boring samples; the penetration of the radioactive contaminant was thus evaluated.

The results of the radioanalysis tests showed ^{134}Cs and ^{137}Cs as the dominant contaminant nuclides, with a ratio of radioactivity of ^{134}Cs:^{137}Cs = 2:3 in August 2012. It was revealed that the radioactive contaminant has penetrated heterogeneously to a 1 mm depth from the surface of the coating layer of the floor (2.5 mm thick) at the maximum (Fig.1-46). Of note is the difference in the penetration depth in the coating layer between 1F1/1F3 and 1F2: 0.5 and 1 mm, respectively. Removal tests of the radioactive contaminant near the surfaces of the coating layer were then conducted by several cleaning methods using pure water or citric acid and an ablation gel for further investigation of the difference in the penetration depth of the radioactive contaminant. The removal tests yielded almost complete removal of the residual radioactive contaminant that penetrated to a 1 mm depth from the surface of the coating layer. This result indicates that the radioactive contaminant can be characterized not by penetration into the coating layer itself by, for example, a chemical reaction with the coating layer material, but by adherence of the contaminant in microcracks or breaches on the surface of the coating layer, considering the heterogeneous penetration of the radioactive contaminant into the coating layer. This result suggests the potential applicability of the above-mentioned removal method without actual removal of the coating layer.

These radioanalysis results are reflected in the remote decontamination plan for the 1F reactor buildings in terms of the selection of suitable removal methods for the radioactive contaminant and optimization of the demonstration test conditions for the decontamination apparatus.

Reference

Maeda, K., Osaka, M. et al., Results of Detailed Analyses Performed on Boring Cores Extracted from the Concrete Floors of the Fukushima Daiichi Nuclear Power Plant Reactor Buildings, Proceedings of International Nuclear Fuel Cycle Conference (GLOBAL2013), Salt Lake City, Utah, USA, 2013, paper 7403, p.272–277., in CD-ROM.

R&D of Fast Reactor Cycle Technology

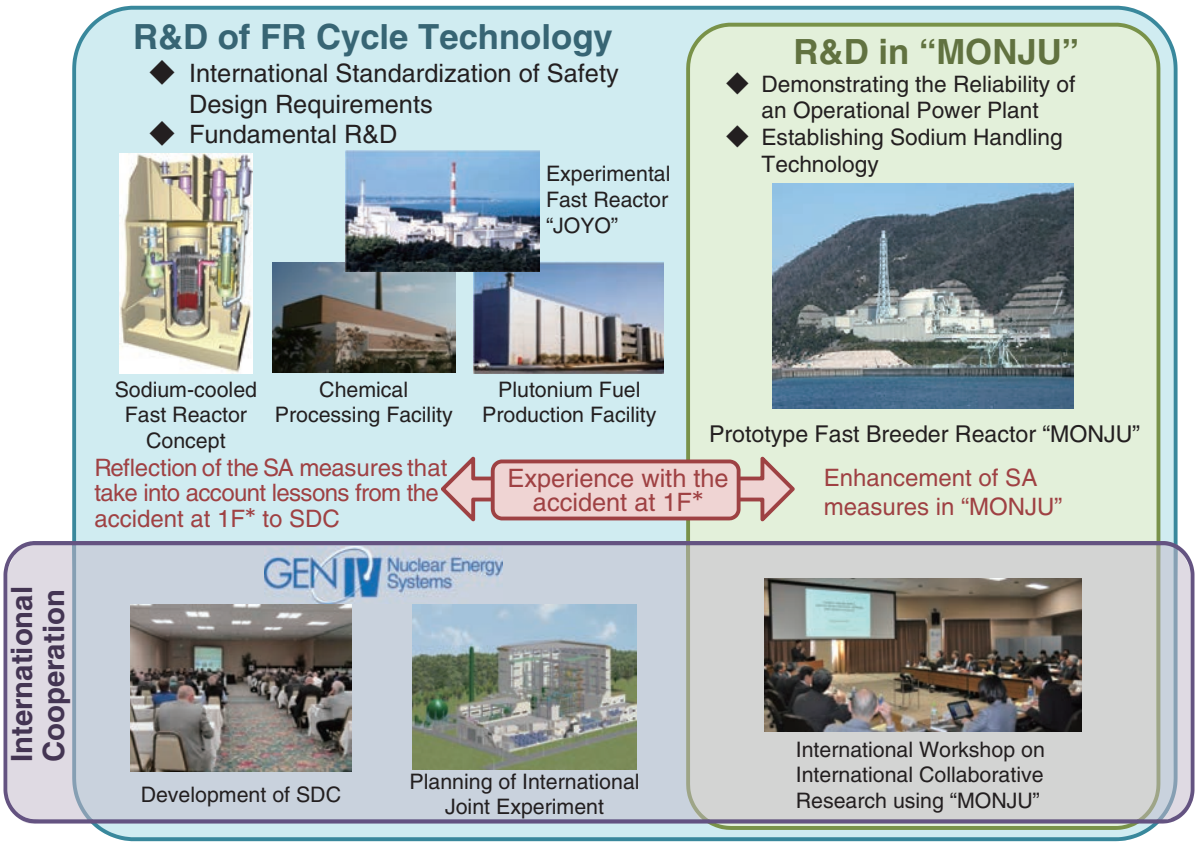

*1F: The Tokyo Electric Power Company, Incorporated Fukushima Daiichi Nuclear Power Station

Fig.2-1 Overview of research and development of fast reactor cycle technology
We are implementing activities related to international standardization of safety design requirements and conservation of the technical basis as efforts for the near term until national policies are reconsidered. As part of these efforts, we are promoting research and development utilizing international cooperation, such as development of the SDC and planning of an international joint experiment on safety issues.

Until FY 2011, research and development activities were conducted toward the commercialization of fast reactor cycle technology with the cooperation of the electric utilities; the main target was the concept of a combination of a sodium-cooled fast reactor, advanced aqueous reprocessing, and simplified pelletizing fuel fabrication. Currently, national policies are being reconsidered because of the impact of the accident at the Tokyo Electric Power Company, Incorporated Fukushima Daiichi Nuclear Power Station (1F). In accordance with the situation, we have implemented activities focused on the efforts required for conservation of the technical basis and international standardization of safety design requirements for the near term utilizing international cooperation, while reflecting the experience gained in the accident at 1F (Fig.2-1). In May 2013, the Safety Design Criteria (SDC) that we proposed were approved at the Generation-IV International Forum (GIF). This chapter describes the resulting enhancement of the safety and reliability considering the features of a sodium-cooled fast reactor and basic research on fuel cycle technology.

The Japan Sodium-cooled Fast Reactor (JSFR) is designed to have high resistance against earthquakes and tsunamis by adopting a seismic isolation system for the reactor building and a natural convection capability for cooling after an abnormal shutdown (Topic 2-1).

Regarding an ultrasonic flowmeter for the cooling system, a measure that enables precise measuring results to be obtained even for flows exhibiting great spatial and temporal variation was identified. The result shows that the ultrasonic flowmeter has the potential for adoption in the plant system (Topic 2-2).

To develop an under-sodium viewer aimed at visual and volumetric inspection of the internal structures in a reactor vessel, data were obtained to justify the present improvement measure with regard to wetting of the ultrasonic sensor surface by liquid sodium, which affects the sensor performance (Topic 2-3).

The strength properties of 316FR and Modified 9Cr-1Mo steel, which are adopted as structural materials for JSFR, were formulated on the basis of an evaluation of the material test data. This makes the structural design more reliable (Topic 2-4).

Regarding sodium/water reaction, which is an important issue for ensuring the safety and protection of the steam generator, experiments were conducted as a joint study with the Commissariat à l'Énergie Atomique et aux Énergies Alternatives (CEA), France. A reaction jet that was produced during heat transfer tube failure and the effect on the resistance characteristics of a heat transfer tube were evaluated (Topic 2-5).

With respect to basic research on the fuel cycle, the oxygen-to-metal ratio, which significantly affects various physical properties of uranium–plutonium mixed oxide fuel, such as the thermal conductivity, could be controlled at will. These technologies became applicable to fuel fabrication and irradiation behavior evaluation (Topic 2-6).

2–1 Robustness of JSFR against Earthquakes and Tsunamis
— Effectiveness of Natural Convection in a Decay Heat Removal System —

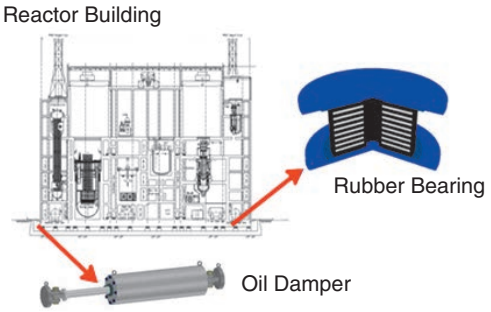

Fig.2-2 Advanced seismic isolation system
Thicker laminated rubber bearings and oil dampers mitigate the seismic force to the reactor building.

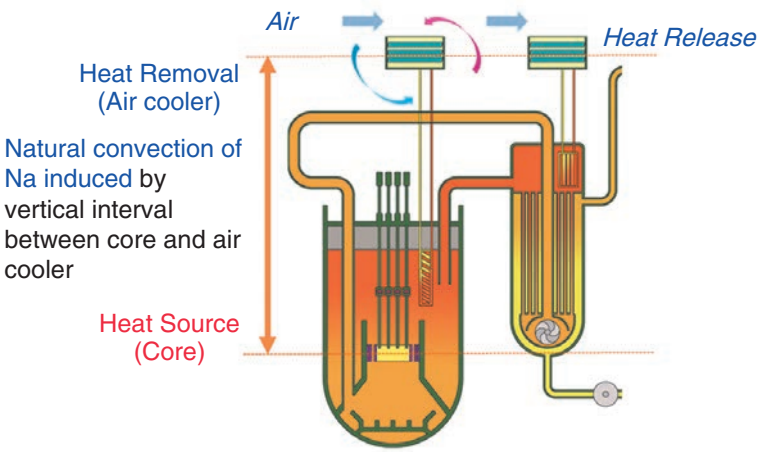

Fig.2-3 Decay heat removal with natural convection in SFR
Natural convection system achieves long-period cooling without power supply.

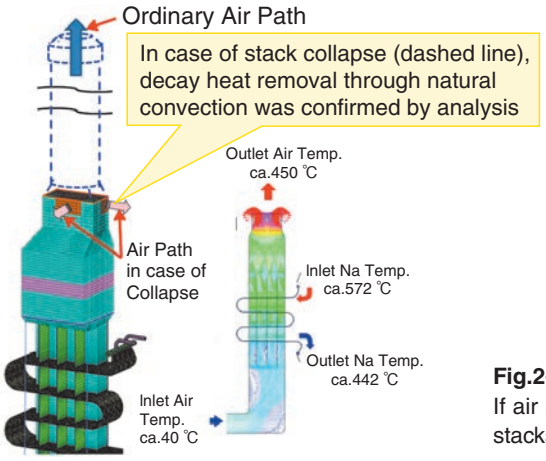

Fig.2-4 Air cooler analysis in case of stack collapse
If air path at their root is alive, air cooler can work even if all stacks collapse.

The integrity of major components of the Japan Sodium-cooled Fast Reactor (JSFR) against the TEPCO's Fukushima Daiichi NPS seismic conditions is confirmed thanks to the adoption of an advanced seismic isolation system that mitigates the horizontal seismic force to a reactor building by using thicker laminated rubber bearings with a longer period and oil dampers (Fig.2-2), which improved the damping performance. Furthermore, against subsequent tsunamis, JSFR is aiming to improve the safety characteristics by adopting a decay heat removal system with natural convection.

Because sodium is liquid under a wide temperature range, it exhibits remarkable heat transfer performance, which leads to a large temperature difference between the sodium inlet and outlet of the reactor. Therefore, decay heat can be removed by natural convection of the coolant sodium due to the density difference that is induced by the vertical interval between a core and an air cooler; in fact, the final heat sink is air (Fig.2-3). Thanks to the natural convection decay heat removal system (DHRS), the JSFR requires no active components such as pumps or blowers, which depend heavily on a power supply. Thus, the inlet/outlet dampers at the air cooler alone can operate the JSFR DHRS using only an emergency DC battery in the reactor building.

Furthermore, the natural convection DHRS has an advantage in terms of the robustness of an emergency AC power supply against tsunamis. In the event of an emergency shutdown in a sodium-cooled fast reactor, structural materials must be protected against thermal shock due to a rapid temperature transition in the sodium. For this reason, some sodium flow must be maintained after reactor shutdown. The conventional forced circulation DHRS has pony motors at the main pumps. The pony motors have to be activated within several seconds using diesel generators (DGs) to control the sodium flow if the off-site power supply is lost. Because the DGs require an auxiliary system consisting of a lubricating oil system and a sea water cooling system, the sea water system, including the water intake components, must be protected against tsunamis. On the other hand, because the JSFR does not require this type of quick DG initiation thanks to the natural convection DHRS, a gas turbine generator (GT) with self-air cooling can be used as the emergency power supply, even though it takes more than 30 s to activate. Hence, the JSFR emergency AC power supply can withstand even a sea water cooling system failure.

In addition, decay heat removal can be maintained even in the event of stack collapse due to an airplane attack as long as the vertical interval between the heat exchanger tubes of the air cooler and an air path at the bottom of the stack above the air cooler can be maintained (Fig.2-4).

In the future, the JSFR design concept will be improved to satisfy the Generation IV SFR safety design criteria based on these studies.

The present study was conducted as part of the "Technical development program on a commercialized FBR plant" commissioned by the Ministry of Economy, Trade and Industry (METI).

Reference

Hayafune, H., Kato, A. et al., Evaluation of Severe External Events on JSFR, Proceedings of International Conference on Fast Reactors and Related Fuel Cycles; Safe Technologies and Sustainable Scenarios (FR13), Paris, France, 2013, paper INV–059, 11p., in USB Flash Drive.

2–2 Measurement of Temporospatially Fluctuating Flow
— Development of Ultrasonic Flowmeter for Fast Reactor —

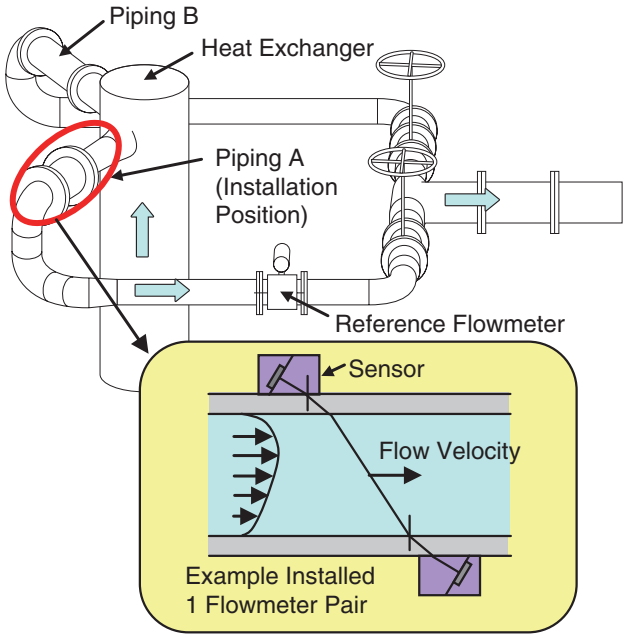

Fig.2-5 Test loop of ultrasonic flowmeter
Several pairs of ultrasonic flowmeters were set in a water test loop to examine their applicability to a temporospatially fluctuating flow. The parameters are the position and number of flowmeters used to measure the instantaneous velocity profile in the fluctuating flow.

Table 2-1 Comparison of main specifications of prototype and commercial fast reactors in Japan
In commercial reactor design, high-chrome steel with low thermal expansion is used for piping, and the pipe drawing is shortened. Further, the flow velocity is increased because the loop number is reduced.

Specification	Prototype	Commercial
Electricity output	280 MWe	1500 MWe
Piping material	SUS	High-chrome steel
Number of loops	3	2
Flow velocity	6 m/s	9 m/s

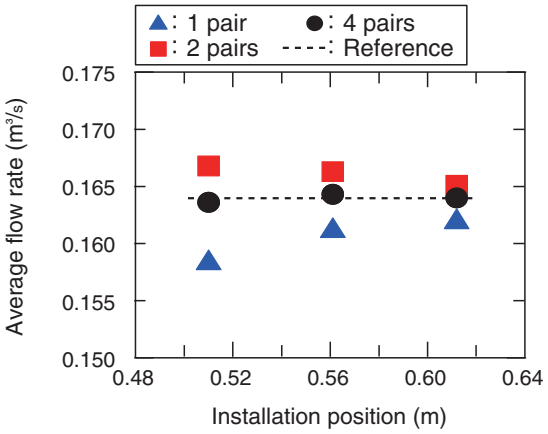

Fig.2-6 Measurement characteristics depending on installation position and number of ultrasonic flowmeters
Increase in number of flowmeter pairs resulted in constant flow rate even near the nozzle (highly fluctuating flow).

As one of the fundamental engineering tasks towards commercialization of a fast reactor cycle technology, a flow rate measurement technique for the sodium coolant is developed. The development requirements and investigation results are presented below.

As shown in Table 2-1, because the piping material is a nonmagnetic stainless steel, an electromagnetic flowmeter has been used as the flowmeter in fast reactors that use a liquid metal, such as the prototype reactor "MONJU". However, because the piping material in a commercial reactor is a high-chrome magnetic steel, which can shorten the required piping length, the electromagnetic flowmeter cannot be applied. In addition, the flow velocity is increased to reduce the loop number and simplify the heat transport systems. Because of the short straight pipes and high velocity, the flowmeter needs to measure a flow that exhibits greater temporospatial fluctuation than before. Because an examination of the flowmeter under fluctuating flow conditions and with high-chrome steel pipes revealed that an ultrasonic flowmeter was most suitable, its applicability was investigated experimentally.

A schematic of the test loop is shown in Fig.2-5. Because the test loop can circulate water at a flow velocity comparable to that in a commercial reactor, the flow condition of a temporospatially fluctuating flow can be simulated. Although the flowmeters are installed in piping A and B at the outlets of a heat exchanger, the measured flow rate should preferably be independent of the installation position to increase the layout design flexibility. Then, the installation position and the number of ultrasonic flowmeters (which corresponds to the measured instantaneous velocity profile in the pipe cross section) were changed, and the flow rate measurement was tested.

A test result is shown in Fig.2-6. For one or two pairs of flowmeters, the measured flow rate varied with the installation positions relative to the heat exchanger outlet. On the other hand, for four pairs of flowmeters installed at intervals of 90° in the circumference angle, the position dependency of the measured flow rate was reduced, and the flow rates were the same as that measured by the reference flowmeter. This result indicates that the ultrasonic flowmeter can be applied to the temporospatially fluctuating flow.

The present study was performed under a contract with Mitsubishi Fast Breeder Reactor (MFBR) Systems, Inc., as part of a study that was entrusted to MFBR Systems, Inc., by the Ministry of Education, Culture, Sports, Science and Technology of Japan (MEXT).

Reference

Hirabayashi, M. et al., Development of Ultrasonic Flowmeter for Sodium-Cooled Fast Breeder Reactor –Applicability Verification of Multi-Path Ultrasonic Flowmeter–, Jikken Rikigaku, vol.12, no.4, 2012, p.391-397 (in Japanese).

2–3 Aiming at Improved Visualization Technology for Reactor Structures
— Experiment on Sodium Wetting on USV Sensor Surface —

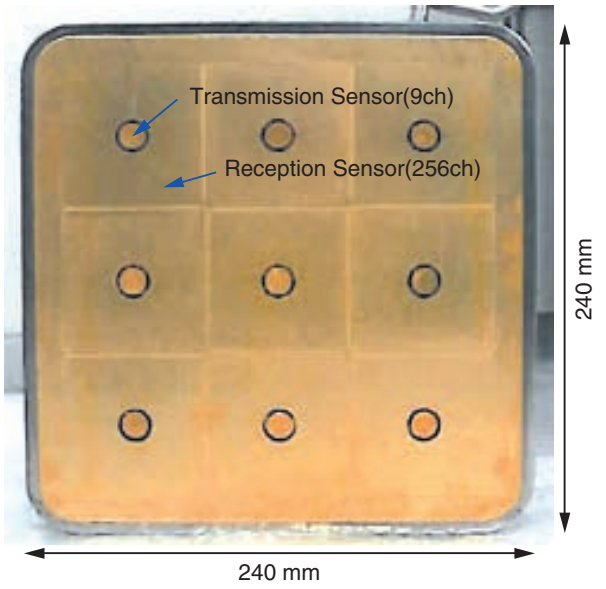

Fig.2-7 Surface of USV sensor
The USV sensor surface was gilded to improve the wetting between the sensor and the sodium and to heighten the sensitivity to transmission and reception of supersonic waves.

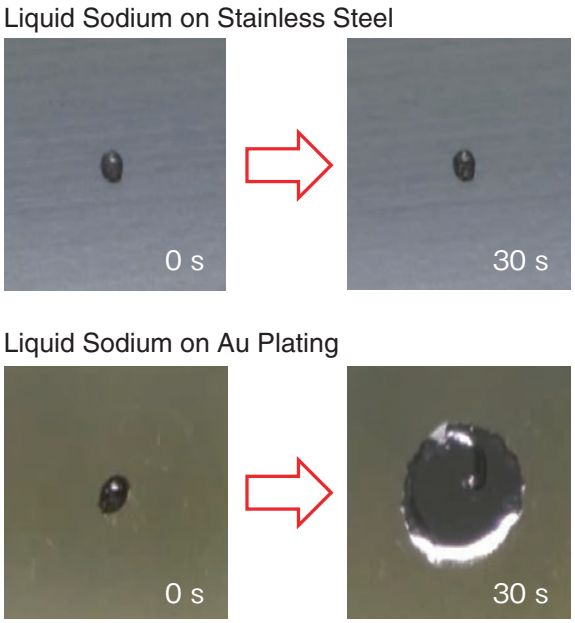

Fig.2-8 Improvement of sodium wetting by gilding processing
The sodium wetting was improved remarkably by gilding the sensor surface.

Liquid sodium, which is used in fast reactors, has many advantages as a coolant; however, it is difficult to optically observe the inside of the reactor vessel because of its opaqueness. Therefore, an under-sodium viewer (USV) was developed to inspect the structural integrity of the reactor vessel, and the improvement of the sodium wetting on the sensor surface is studied for practical use.

The USV transmits supersonic waves into liquid sodium and receives the reflection waves from the structures in the reactor. The structures are visualized by analyzing the period from transmission to reception of the supersonic waves, so it is important to improve the sensitivity to supersonic waves for practical use of the USV. Current knowledge suggests that the sensitivity to supersonic waves depends on the contact properties between sodium and the sensor surface, namely, sodium wetting. Therefore, we tried to improve the sodium wetting by gilding the sensor surface (Fig.2-7) and tested the sodium wetting under various plating conditions.

In the experiment, the test pieces were made under various plating conditions, using materials such as gold (Au), which was used in the present sensor; indium (In), which has a low melting temperature; palladium (Pd), which is a novel metal; and nickel (Ni), which is generally used as substrate plating.

As a result, the sodium wetting (spreading behavior) was found to be determined by the characteristics of the surface plating, particularly its solubility. Fig.2-8 shows the differences in the sodium wetting after gilding processing. The sodium droplet spreads on the Au plating but not on the stainless steel.

The difference is attributed to a more active dissolution reaction when the plating has a higher solubility. In this experiment, the sodium wetting was most substantially improved with Au plating; the reason is that the solubility of Au is 25mol%, which is higher than that of In, Pd, or Ni.

This study showed that gilding processing of the present USV sensor was an appropriate method to improve the sodium wetting. We plan to advance the research on sodium wetting, including theoretical considerations, focusing on the interfacial chemical reaction between sodium and the sensor surface and the effects of impurities in the sodium.

Reference

Kawaguchi, M. et al., Reactive Wetting of Metallic Plated Steels by Liquid Sodium, Journal of Nuclear Science and Technology, vol.48, no.4, 2011, p.499–503.

2–4 Codification of Materials for Demonstration Fast Reactor in JSME Code

— Establishment of Standards for Material Strength and Elevated Temperature Design for 316FR and Modified 9Cr-1Mo Steels —

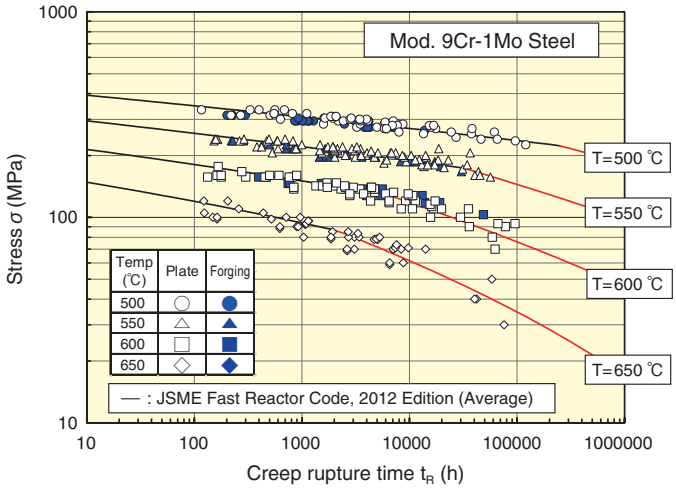

Fig.2-9 Creep rupture time of Mod. 9Cr-1Mo steel
Creep rupture data in which the rupture time exceeded 100000 h (approximately 11 years) were obtained. The slope of a graph of rupture time and stress was found to vary below and above half of the 0.2% yield strength at temperature. It was inferred that the longer the rupture time, the smaller the effects of plastic deformation.

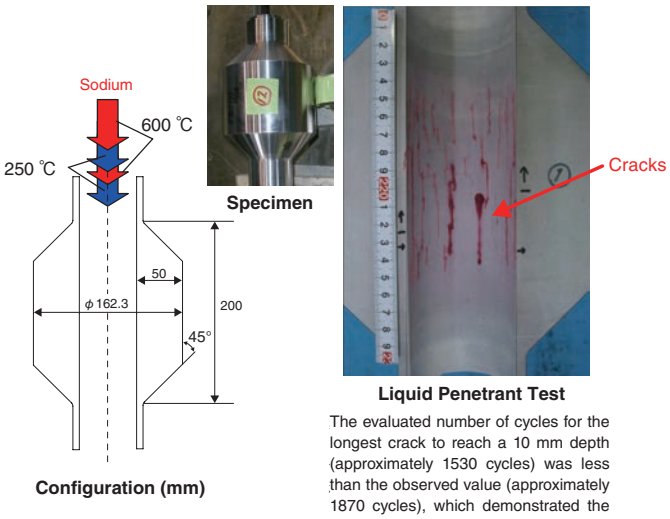

The evaluated number of cycles for the longest crack to reach a 10 mm depth (approximately 1530 cycles) was less than the observed value (approximately 1870 cycles), which demonstrated the appropriateness of the evaluation.

Fig.2-10 Example of structural test of Mod. 9Cr-1Mo steel using sodium
A thick cylindrical specimen was subjected to a sodium flow with a temperature that varied cyclically between 600 °C and 250 °C that generated thermal loads. It was demonstrated that the analysis was appropriate. By performing more tests under different conditions, the adequacy of the margins in the design standard was confirmed.

Future fast reactors need to be more reliable, and their design has to be more flexible. The development of structural materials is one of the keys to achieving this goal, and extensive research and development have been conducted. For the Japanese demonstration fast reactor, which is in the design study phase, structural materials have been selected that are most suitable for meeting the requirements for components, such as higher strength at elevated temperatures or lower thermal expansion rates; 316FR steel was selected for the reactor vessels and internals, and Modified 9Cr-1Mo (Mod.9Cr-1Mo) steel was chosen for most parts of the coolant system, including the primary piping system. The 316FR steel was developed in Japan by the Japan Atomic Energy Agency and partners for fast reactor use. Mod.9Cr-1Mo steel was originally developed by the Oak Ridge National Laboratory in the United States, and extensive R&D programs were conducted in Japan in order to apply it to fast reactors.

The temperature during steady-state operation of the demonstration fast reactor will be approximately 550 °C, and a design life of 60 years is planned. To establish methodologies to achieve these goals, material data were obtained and evaluated under various conditions such as creep, in which tensile stress is continuously applied at elevated temperatures; fatigue, in which thermal stresses are repeatedly imposed; and creep-fatigue, in which creep and fatigue loadings are superimposed. For example, long-term creep tests, in which a heated specimen fails by tensile stress imposed by a dead weight, were conducted; the maximum rupture time so far obtained exceeds 100000 h (11.4 years). A database has been established, and the data were analyzed from mechanical and metallurgical viewpoints to formulate the properties. In the formulation, the focus for 316FR steel was on taking advantage of its superior properties under fast reactor conditions, and for Mod.9Cr-1Mo steel, it was on representing the creep properties, which vary depending on the stress levels (Fig.2-9). The creep strength of 316FR steel at 300000 h and 550 °C, evaluated using the formulated properties, was 1.7 times higher than that of the conventional material SUS304, and the increase was 2.3 times for Mod.9Cr-1Mo steel compared with 2 1/4Cr-1Mo steel. Moreover, structural tests in a sodium environment that is closer to that in fast reactor applications confirmed that the design method developed for conventional materials is applicable to these two materials with sufficient conservatism (Fig.2-10). The above results led to a significant increase in the freedom of structural design for the demonstration fast reactor.

The above achievements are codified in the Japan Society of Mechanical Engineers Code for Nuclear Power Generation Facilities, Rules on Design and Construction for Nuclear Power Plants, Section II Fast Reactor Standards, 2012 (in Japanese).

Reference

Asayama, T. et al., Creep–Fatigue Evaluation Methodologies and Related Issues for Japan Sodium Cooled Fast Reactor (JSFR), Procedia Engineering, vol.55, 2013, p.309–313.

2–5 Investigation of Sodium/Water Reaction in Collaboration with France
— Sodium/Water Reaction Test for Steam Generator Heat Transfer Tube —

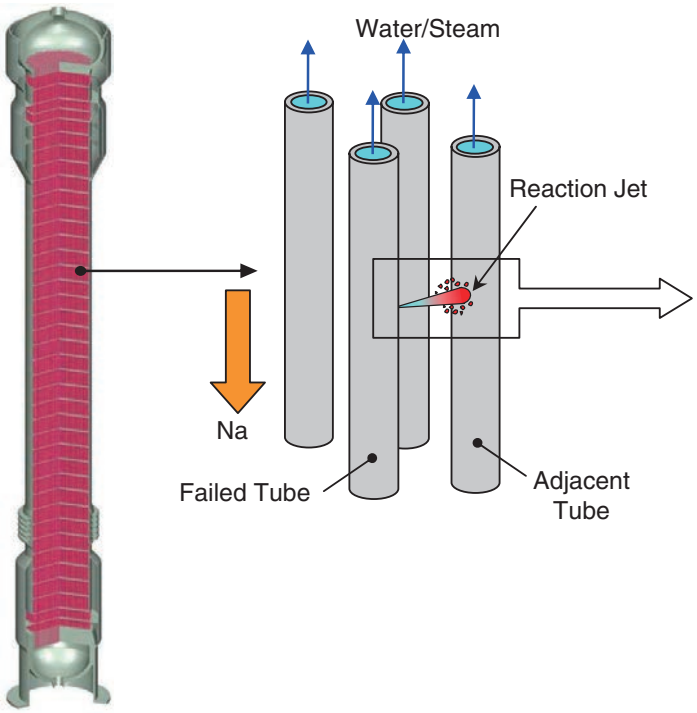

Fig.2-11 Steam generator and Na/water reaction jet
Steam generators exchange heat between sodium and water through heat transfer tubes. If a failed tube is left in place, a sodium/water reaction jet attacks adjacent tubes.

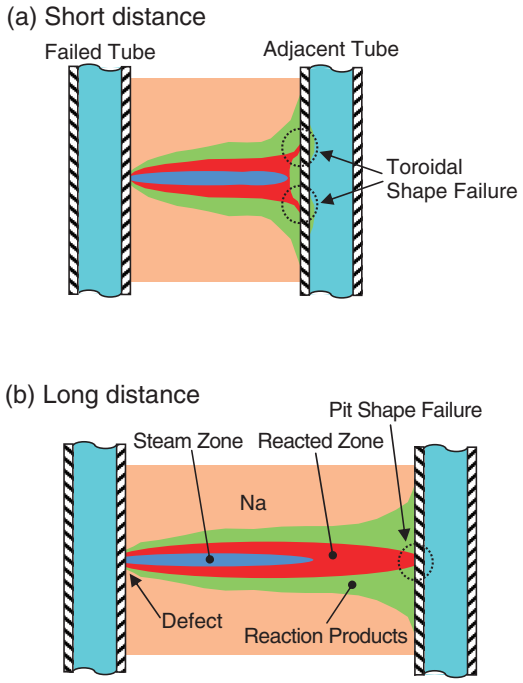

Fig.2-12 Na/water reaction jet and tube failure area
The Na/water reaction jet consists of two zones: an inner unreacted steam zone and an outer reacted zone. (a) The annular reacted zone attacks a tube to cause a toroidal failure at a short distance, and (b) the reacted zone attacks a tube at a point to cause a pit-shaped failure at a long distance.

In steam generators in sodium-cooled fast reactors (SFRs), water is turned into steam by heat from sodium (Na) to supply steam to a turbine/generator system. Heat transfer tubes are incorporated in a steam generator; sodium flows outside the tubes and water or steam flows inside the tubes for heat exchange (Fig.2-11).

In the event of heat transfer tube failure, water or steam leaks into the sodium side and reacts with Na to produce a high-temperature reaction jet and an erosion or corrosion attack. If this reaction jet continues to attack adjacent tubes, tube failure is also assumed to occur on adjacent tubes (Fig.2-11, right). To prevent this tube failure escalation, the plant safety system monitors the coolant pressure changes and the concentration of hydrogen, which is produced by Na/water reactions, in the coolant. As soon as a Na/water reaction is detected, the safety system removes water or steam from the heat transfer tubes in a steam generator to terminate the reaction.

To ensure this safety function in steam generators, the reaction jet resistance of the heat transfer tubes needs to be investigated. Because the reaction jet resistance depends on the water leak rate, inter-tube distance, and Na temperature, the heat transfer tubes have to be examined under various conditions to study the influence of these parameters. Na/water reaction tests to obtain the tube resistance data were conducted in Japan (the Japan Atomic Energy Agency, JAEA) and France (Commissariat à l'Énergie Atomique et aux Énergies Alternatives, CEA), but both institutes collaborated for efficient data acquisition.

CEA fabricated heat transfer tube test specimens for this collaboration, and these specimens were loaded into a sodium vessel of JAEA's Na/water reaction test equipment. This test equipment provided the same environment as in real steam generators (~500 °C, ~18 MPa), and the experiment could be performed under a wide range of conditions appropriate to its purpose. Water or steam was injected toward the tube specimen in the sodium vessel, and a reaction jet was formed here and attacked the tube specimen to penetrate the tube wall. The tube penetration times were measured to define the reaction jet resistance characteristics. The internal structure of the reaction jet was also revealed by the configuration on the failed tube surface after the test and the temperature distribution in the reaction jet. Fig.2-12 illustrates aspects of the reaction jets and tube failure areas at different inter-tube distances.

Japan and France will continue this collaboration to accumulate further data concerning the tube resistance characteristics for a few years. The collaborative study is expected to contribute to enhancing the safety of steam generators in both countries' SFRs.

Reference

Beauchamp, F., Nishimura, M. et al., Cooperation on Impingement Wastage Experiment of Mod. 9Cr–1Mo Steel using SWAT–1R Sodium–Water Reaction Test Facility, Proceedings of International Conference on Fast Reactors and Related Fuel Cycles; Safe Technologies and Sustainable Scenarios (FR13), Paris, France, 2013, paper IAEA–CN–199–119, 10p., in USB Flash Drive.

2–6 Controlling Oxygen Content of U–Pu Mixed Oxide Fuel

— Oxygen Potential Measurement and Application to Fuel Technologies —

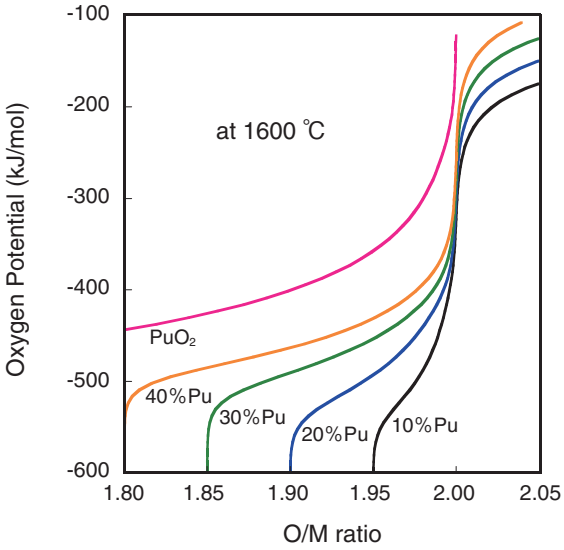

Fig.2-13 Oxygen potential of MOX at 1600 °C as functions of O/M ratio and Pu content
The O/M ratio decreases with decreasing oxygen potential and increasing Pu content. The O/M ratio can be controlled by controlling the oxygen potential and temperature.

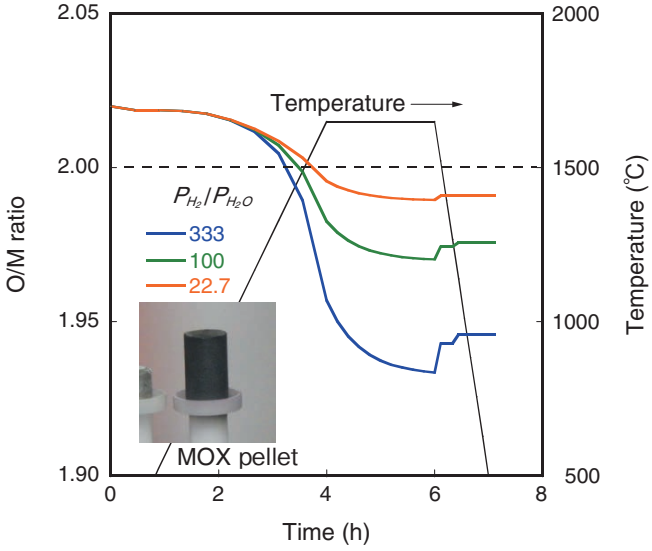

Fig.2-14 O/M change of $(U_{0.7}Pu_{0.3})O_{2-x}$ during heat treatment
The O/M ratio of MOX changes with P_{H_2}/P_{H_2O} ratio. The O/M ratio reaches 1.94 at 1650 °C in atmosphere with P_{H_2}/P_{H_2O} = 333. Photograph shows MOX pellet set in the measurement system.

Uranium–plutonium mixed oxide (MOX) has been used as a fuel for sodium-cooled fast reactors; it has a fluorite structure with an oxygen-to-metal (O/M) ratio of 2.00. UO_2 can take extra oxygen and exist in a hyper-stoichiometric composition with a range of O/M > 2.00. Pu atoms are substituted for U atoms, and a MOX solid solution is formed. On the other hand, MOX can exist in a hypo-stoichiometric region of O/M < 2.00 by forming oxygen vacancies. Changes in the O/M ratio significantly affect various properties of MOX, such as the thermal conductivity. Therefore, it is important to control the O/M ratio to develop fuel technologies.

It is necessary to know the relationship among the O/M ratio, temperature, and oxygen potential to develop O/M control techniques. In this work, the oxygen potential (ΔG_{O_2}) of MOX was measured by the gas equilibrium method. The oxygen potential is a quantity used in thermodynamics to describe the oxygen chemical stability in MOX and can be obtained using eq.(1).

$$\Delta G_{O_2} = RT \ln P_{O_2}, \quad \cdots\cdots (1)$$

where R is the gas constant. A gas mixture of Ar/H_2 to add moisture was used for oxygen potential control. In this gas system, the oxygen potential is determined by the reaction $H_2O \Leftrightarrow H_2 + 1/2O_2$ and controlled by adjusting the P_{H_2}/P_{H_2O} ratio. Many data (more than 1000 points) were obtained and evaluated, and an equation representing the oxygen potential was derived as a function of the O/M ratio, temperature, and Pu content. On the basis of this equation, a technique for evaluating the O/M ratio was developed.

Fig.2-13 shows the relationship between the oxygen potential and the O/M ratio at 1600 °C. The oxygen potential increases with increasing Pu content. This technology for evaluating the oxygen potential has been applied to the fuel pellet fabrication process and irradiation behavior analysis. The O/M change in $(U_{0.7}Pu_{0.3})O_{2-x}$ during heat treatment is plotted as a function of the P_{H_2}/P_{H_2O} ratio in Fig.2-14. The figure shows that the P_{H_2}/P_{H_2O} ratio affects the variation in O/M. Further, the chemical stability of fission products inside irradiated pellets can be evaluated using this technology.

Reference

Kato, M., Oxygen Potentials and Defect Chemistry in Nonstoichiometric $(U,Pu)O_2$, Stoichiometry and Materials Science–When Numbers Matter, 2012, p.203–218.

R&D Supporting the Technology and Reliability of Geological Disposal in Japan

Geological disposal is one of the options for isolating high-level radioactive waste (HLW) produced during nuclear power generation from human environments over a long period of time. This is an issue that remains critical in spite of the revision of the national nuclear energy policy and one that must now be dealt with by the present generation. In Japan, spent fuel from power reactors is reprocessed to extract reusable uranium and plutonium for power generation purposes. The liquids separated from the spent fuel during chemical reprocessing are solidified into a stable glass form. According to the Japanese concept, vitrified wastes are encapsulated in a thick steel overpack, which is surrounded by highly compacted bentonite and placed in a stable geological environment below 300 m (Fig.3-1). Geological disposal of HLW will be a long-term project lasting more than 100 years. The project begins with site selection, continues to repository construction and operation, which will be followed by post-closure monitoring. It is thus very important to proceed with the project efficiently, as a national responsibility, by continuously reinforcing the technical base and, more importantly, building public confidence. To this end, we have made and continue to make steady progress in research and development (R&D) in various fields, such as geoscientific research, engineering technology, and safety assessment, to improve the technology used for and reliability of geological disposal in Japan. Our efforts are also focused on promoting public understanding through the dissemination of relevant information and on opening our R&D facilities to the public.

A particular focus of our current R&D is on projects at two underground research laboratories (URLs)—one at Mizunami for research on crystalline rocks and the other at Horonobe for research on sedimentary formations (Fig.3-2)—with the main aim of developing a sound technical basis for the formulation and implementation of safety regulations. In March 2013, shaft excavation reached a depth of 500 m at Mizunami and 350 m at Horonobe, and some research galleries were made available for use. Multidisciplinary investigations are ongoing, as the reliability of a variety of investigative techniques should be tested and confirmed before site characterization begins in earnest (Topics 3-1, 3-2, 3-3, 3-4). Underground tunnels serve as a place for the public to experience deep geological environments first-hand and appreciate our R&D activities. In addition, studies on tectonics, volcanic and faulting activities, and so on have been underway for evaluating the long-term stability of geological environments in Japan (Topic 3-5).

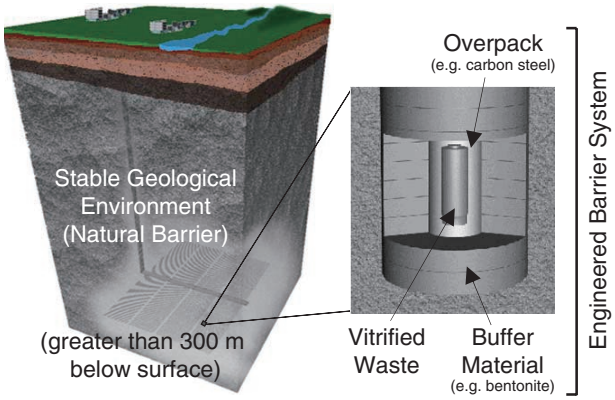

Fig.3-1 Basic concept of geological disposal of high-level radioactive waste in Japan

In parallel with this geoscientific research, we are conducting an extensive study for performance assessment of multibarrier systems, engineered barrier systems, and long-term chemical and migration behavior of radionuclides at Tokai to improve geological disposal technology (Topics 3-6, 3-7, 3-8).

These studies involve the use of geological environment data obtained at both URLs. A prototype knowledge management system that was developed in 2009 has been improved to systematically provide multiple lines of evidence and R&D results. In 2012, the Information Synthesis and Interpretation System (ISIS), which supports the implementer in planning, performing, and evaluating the preliminary investigation, was developed by integrating each expert system, using the experience and know-how that experts have garnered through R&D activities.

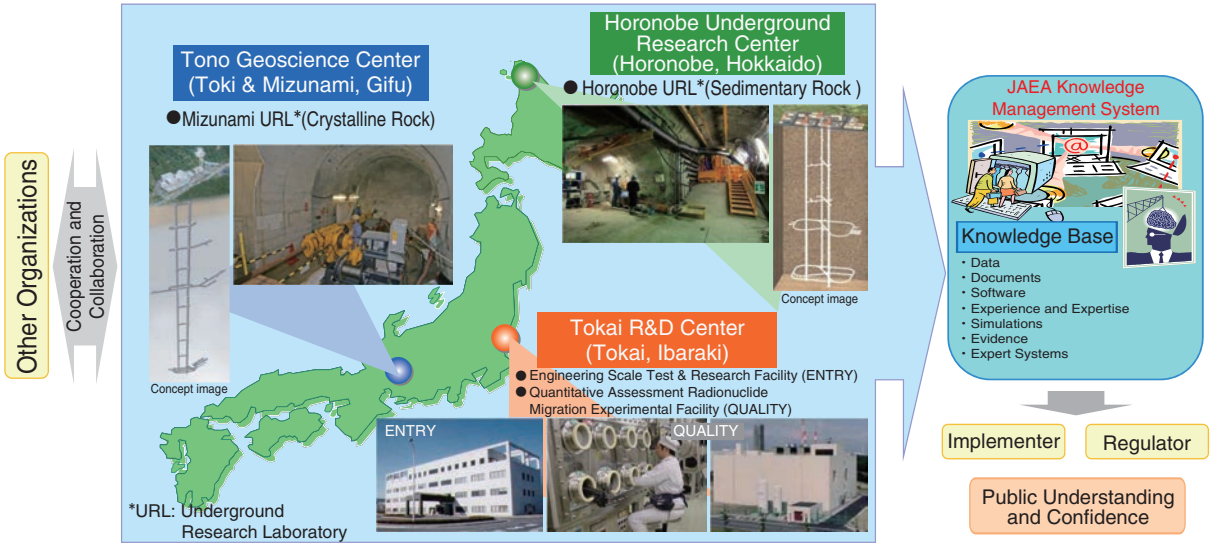

Fig.3-2 Japan Atomic Energy Agency's R&D activities

3–1 Spatial Distribution of Fractures in Granite
— Influence of the Initial Cooling of the Granitic Pluton —

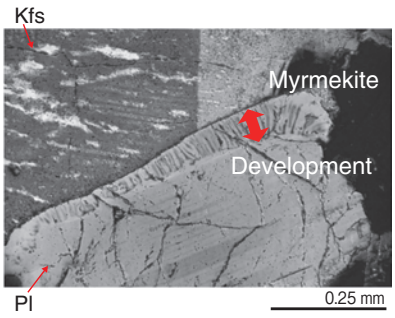

Fig.3-3 Micrometer-scale texture (myrmekite) indicative of cooling process of pluton
Myrmekite occurs at plagioclase (Pl) rim in contact with K-feldspar (Kfs).

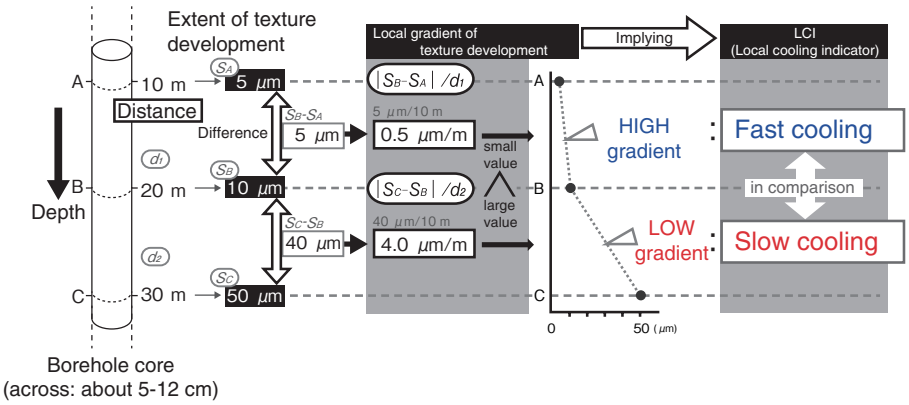

Fig.3-4 Local cooling indicator
Concept of local gradient of texture development between two positions, defining the local cooling indicator (LCI). High local gradient (small value) denotes relatively fast local cooling.

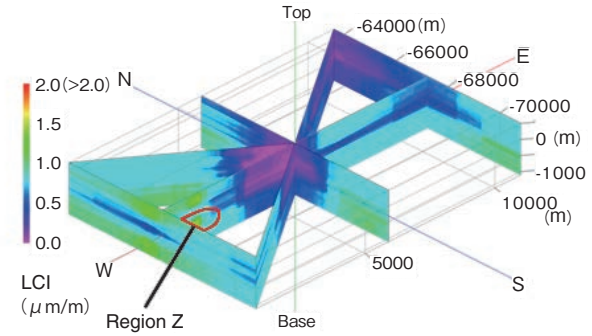

Fig.3-5 Contoured spatial distribution of LCI in the Toki granitic body
Cool colors denote fast local cooling.

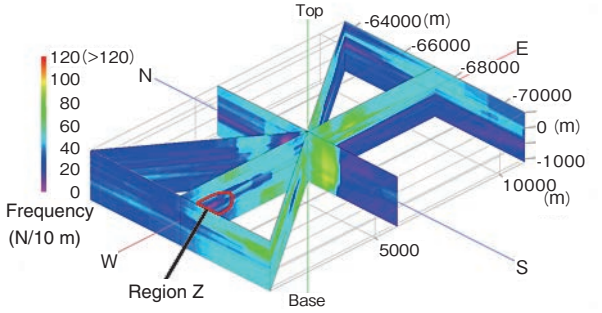

Fig.3-6 Contoured spatial distribution of fracture frequency
Warm colors indicate high fracture frequency.

Fractures in granitic rock (crystalline rock) can act as groundwater pathways. Therefore, understanding the fracture distribution is important for the safety assessment of the disposal of high-level radioactive waste. The present study proposes that the cooling process in a granitic pluton will provide key insight for understanding the fracture distribution on the basis of thermal stress.

Our earlier study revealed that the extent of micrometer-scale textures (e.g., myrmekite; Fig.3-3) is a powerful parameter for quantifying the cooling process in plutonic rocks. The degree of texture development was measured at two neighboring positions, and the difference was divided by the distance between the two positions (Fig.3-4). The resulting quantity is defined here as the local cooling indicator (LCI). This is a revolutionary procedure for evaluating the thermal stress during cooling.

The spatial distribution of the LCI was constructed on the basis of about 670 textures from 19 boreholes in the Toki granitic body, Central Japan (Fig.3-5). There is a relationship between the distribution patterns of the LCI (Fig.3-5) and the fracture frequency (Fig.3-6); i.e., regions of fast local cooling correspond to regions of high fracture frequency and vice versa (e.g., the central region and region Z). This relationship implies that thermal stress contributes to fracture genesis. The spatial distribution of the fracture frequency in a granitic pluton is constrained mainly by the LCI. This case study employs a petrographical method, i.e., the LCI, and provides a constructive study on evaluating the fracture distribution in granite.

A further study will examine the intrusion and emplacement process of a granitic magma. The heterogeneity of rock facies and chemistry in the granite, which was attributed to intrusion and emplacement of the granitic magma, yields a difference in the petrophysical properties. Fracturing is closely associated with this difference. In this way, we aim to elucidate the fracture formation and development processes with higher resolution.

Reference

Yuguchi, T. et al., Three–Dimensional Fracture Distribution in Relation to Local Cooling in a Granitic Body: An Example from the Toki Granitic Pluton, Central Japan, Engineering Geology, vols.149–150, 2012, p.35–46.

3–2 Advancing In Situ Rock Stress Measurement Techniques at the Mizunami Underground Research Laboratory — Case Study: Successful Overcoring Tests Excluding Groundwater —

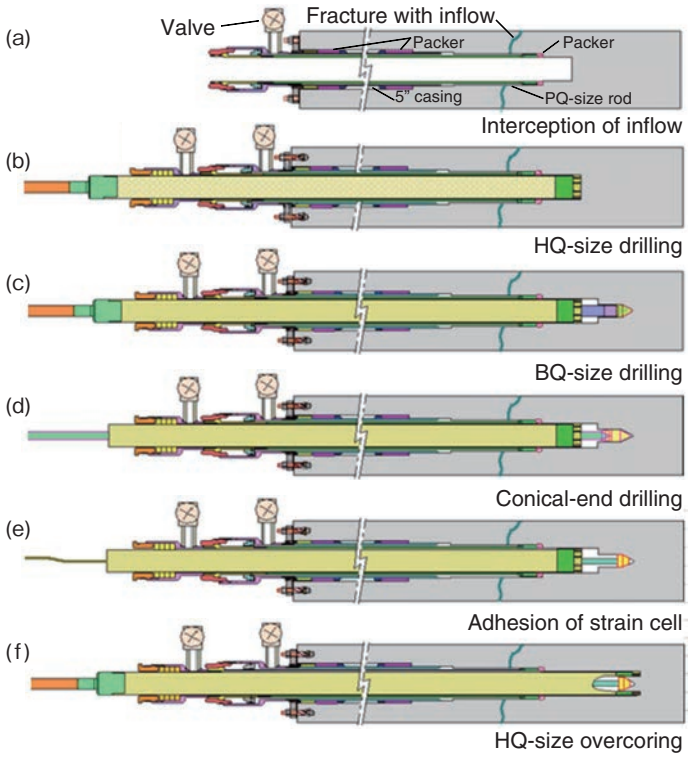

Fig.3-7 Drilling tool to prevent inflow and its measurement procedure
To protect the strain cell from groundwater inflow, an oversized casing was installed at the point of the borehole (HQ-size: ϕ100 mm), where the strain cell is attached.

Fig.3-8 Rock stress measurement
GL.-300 m gallery.

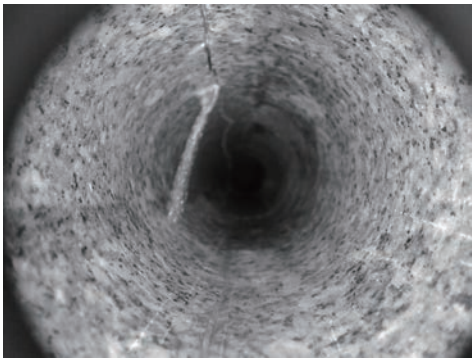

Fig.3-9 Groundwater inflow in borehole
Diameter of borehole: ϕ100 mm.

The evaluation of *in situ* rock stress is important in the design and construction of underground structures such as underground power stations and geological disposal facilities for high-level radioactive waste. In fact, *in situ* stress is recognized as the primary factor in the development of an excavation disturbed zone (EDZ). An EDZ is likely to be less stable than the undisturbed rock mass and to provide higher permeability pathways for groundwater flow near excavations.

Hydraulic fracturing tests in a borehole drilled from the surface and overcoring tests in boreholes drilled from a gallery were used to determine the *in situ* rock stresses. In 2009, the Japanese Geotechnical Society standardized the techniques used in compact conical-ended borehole overcoring (CCBO). However, the CCBO technique does not work if groundwater is present because water reduces the effective adhesion of the strain cell to the rock. Furthermore, the occurrence of disking at the conical-ended overcore does not allow evaluation of the *in situ* stress.

As a countermeasure, we developed a tool to prevent groundwater inflow (Fig.3-7) and adapted the tool for use in CCBO *in situ* stress determination in the GL.-200 m and -300 m galleries at the Mizunami Underground Research Laboratory (Figs.3-8, 3-9). Numerical analysis was used to interpret the stress concentrations around the conical-ended core in this case study. The conclusions are as follows:

(1) The *in situ* rock stresses were successfully determined using the inflow prevention tool.
(2) Numerical analysis indicates that tensile stress occurred at the ridgeline of the conical-ended overcore and microfractures developed at this measurement point.
(3) This work confirms the importance of determining the borehole orientation with respect to the regional stress fields to reduce the risk of core disking.

Reference

Sato, T. et al., Study of Core Disking Phenomenon on Compact Conical-Ended Borehole Overcoring Technique –A Case Study for Measurement in Borehole with Inflow at Toki Granite–, Journal of MMIJ, vol.129, nos.2-3, 2013, p.59-64 (in Japanese).

3–3 Long-Term Investigation of an Excavation Damaged Zone around a Gallery
— Seismic Tomography Survey for Investigation of an EDZ —

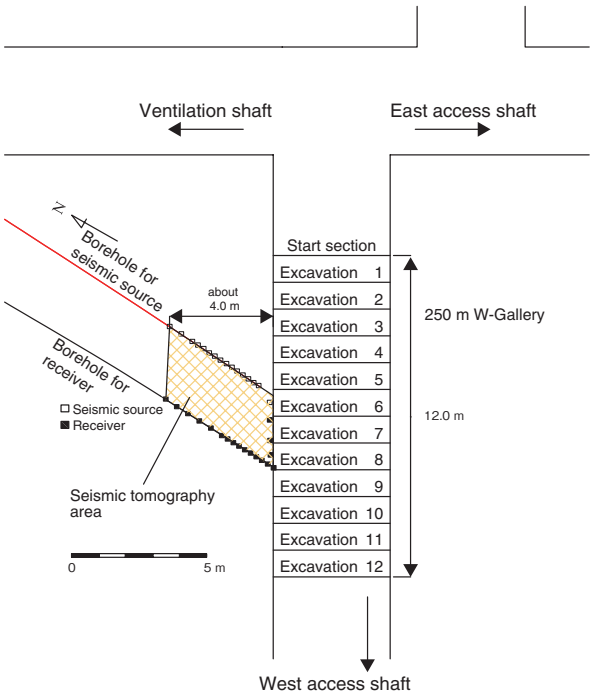

Fig.3-10 Layout of the seismic tomography
This figure shows a plan view of the 250 m gallery off the west shaft (250 m W-Gallery).

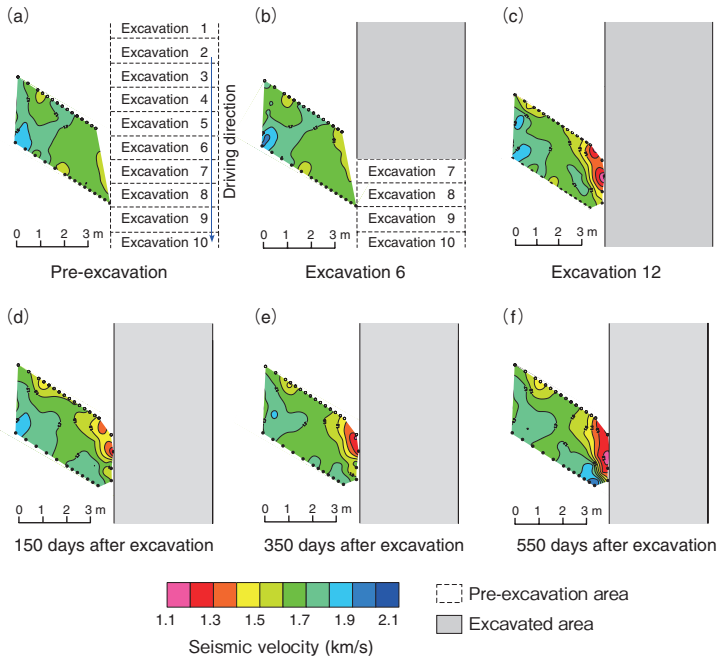

Fig.3-11 Results of seismic tomography survey
These figures show the velocity contour maps at each investigation stage.

In response to the excavation of an underground opening, the host rock properties such as the rock strength and permeability are expected to change. The resulting zone is called the excavation damaged zone (EDZ). In geological disposal of high-level radioactive waste, an EDZ is expected to provide critical pathways for radionuclides. Therefore, it is important to develop a technique for quantitative assessment of the EDZ.

To investigate the EDZ, seismic tomography surveys have been widely conducted in the field. This technique investigates the seismic velocity in rock by measuring the travel time of seismic waves. When a seismic wave passes through fractures in rock, its velocity decreases. In this study, we estimate the extent of the EDZ on the basis of the decrease in seismic wave velocity at the Horonobe Underground Research Laboratory.

Fig.3-10 shows a plan view of the layout of the seismic tomography in a gallery at a depth of 250 m. Seismic tomography was conducted at the 250 m W-Gallery during excavation (Excavations 1 to 12) and after the excavation of the gallery was complete. Fig.3-11 shows the results of the seismic tomography survey. In the pre-excavation and Excavation 6 stages, shown in figures (a) and (b), the seismic velocity did not change remarkably. In Excavation 12, shown in figure (c), a low-velocity area in which the velocity decreased to around 1.3 km/s developed about 1.0 m into the gallery wall. After the gallery was completely excavated, the low-velocity area was smaller at 150 days after excavation, as shown in figure (d), but had expanded again at 350 and 550 days after excavation, as shown in figures (e) and (f), respectively. Consequently, it was found that the EDZ can be expected to develop about 1.0 m into the gallery wall and that the extent of the low-velocity area changes with time.

We aim to examine the long-term change in the low-velocity area in detail. In addition, we will conduct permeability tests and measure the saturation around the tomography area to investigate the change in the hydrogeological properties in the EDZ.

Reference

Aoyagi, K. et al., Geomechanical Assessment of Excavation Damaged Zone in the Horonobe Underground Research Laboratory, Japan, Proceedings of the 13th Japan Symposium on Rock Mechanics & 6th Japan–Korea Joint Symposium on Rock Engineering, Okinawa, Japan, 2013, p.905–910, in CD–ROM.

3–4 Regional Estimate of Fracture Permeability
— Hydrogeological Investigation of Sedimentary Rocks —

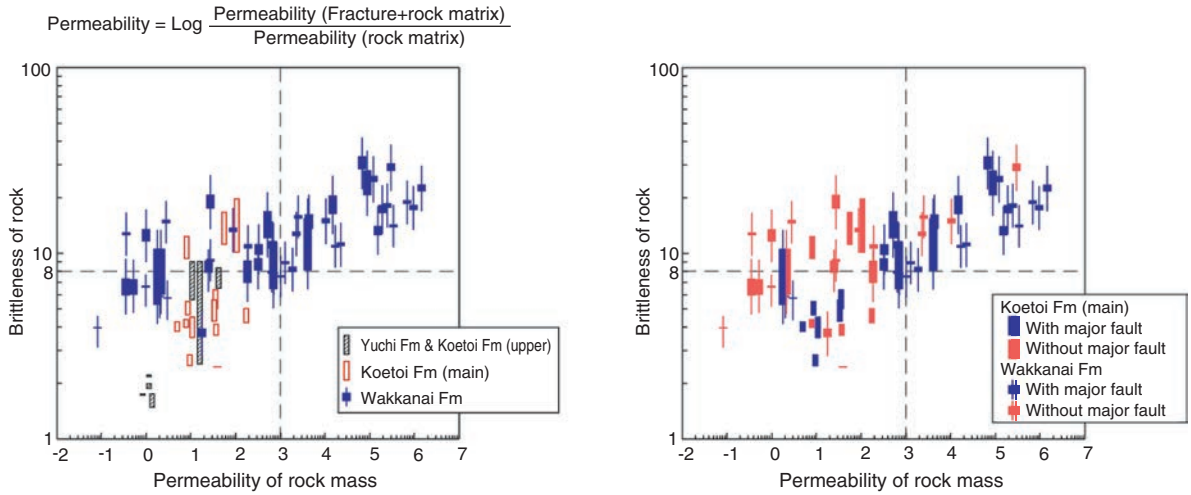

Fig.3-12 Relationship between brittleness of rock and permeability of rock mass
When the brittleness is lesser than 8, the permeability of a rock mass is low even if fractures/faults develop.

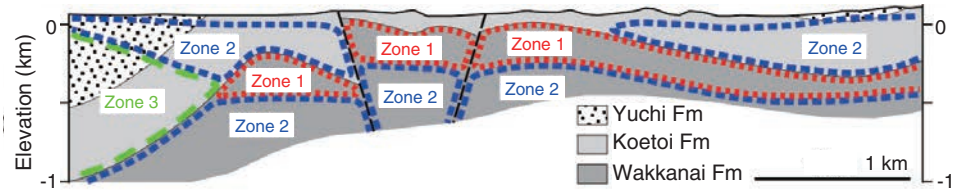

	Brittleness of rock (BRI)	Permeability of rock mass
Zone 3	BRI≦2	Low
Zone 2	2＜BRI＜8	Low
Zone 1	8≦BRI	High

Fig.3-13 Distribution of brittleness of rock and permeability of rock mass based on geological map
Permeability of rock mass (including fractures) can be inferred from brittleness of rock from geological map.

The fracture permeability of a rock mass is an important parameter for retardation assessment of radionuclide migration and, consequently, for the design and construction of an underground facility. Therefore, the regional distribution of the fracture permeability should be understood before determining the location and layout of the facility. However, it is impossible to measure the entire fracture permeability; hence, some estimation of the permeability from the limited available data is required. In sedimentary rocks, the matrix permeability is often estimated by geophysical surveys or stratigraphic analyses, but it is difficult to estimate the fracture permeability.

The relationship between the strength and stress state of rocks and the fracture permeability was studied to develop a technique for estimating the regional fracture permeability in sedimentary rocks. Usually in the formation of fractures, a brittle deformation tends to result in high-permeability fractures, whereas a ductile deformation tends to result in low-permeability fractures. Whether the deformation is brittle or ductile depends on the strength, stress state, strain rate, and temperature at the time of the deformation. Considering the strength and stress state, a softer rock or a higher confined stress relative to the pore pressure is likely related to ductile deformation. For the depth (>300 m) at which high-level radioactive wastes are disposed of, the strengths and stress states of rocks are the most sensitive and important parameters; i.e., it is assumed that the fracture permeability is closely associated with the strengths and stress states of rocks.

Geological, hydrological, and rock mechanical tests of sedimentary rocks distributed in and around the Horonobe Underground Research Laboratory (URL) revealed that, when the brittleness of a rock is less than 8, the permeability of the rock mass is low even if fractures/faults develop (Fig.3-12: the brittleness is defined as unconfined compressive strength ÷ effective vertical stress × 2). This threshold is consistent with deformational theory assuming elastic material. The regional brittleness can be estimated using a geological map. Fig.3-13 shows the distribution of the brittleness and permeability of rock masses in and around the Horonobe URL. The relationship between the brittleness and permeability of the rock masses facilitates estimation of the regional fracture permeability in sedimentary rocks.

Reference

Ishii, E. et al., The Relationships among Brittleness, Deformation Behavior, and Transport Properties in Mudstones: An Example from the Horonobe Underground Research Laboratory, Japan, Journal of Geophysical Research, vol.116, issue B9, 2011, p.B09206–1–B09206–15.

3–5 Dating Fault Activity
— K-Ar Age of Fault Clay —

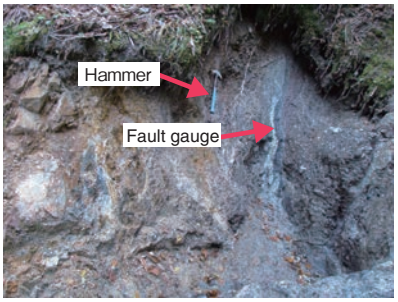

Fig.3-14 Outcrop of fault gauge (Sakai Toge fault, Nagano prefecture)
The black belt indicated by the red arrow is the fault gauge. A hammer (40 cm in length) is included for scale.

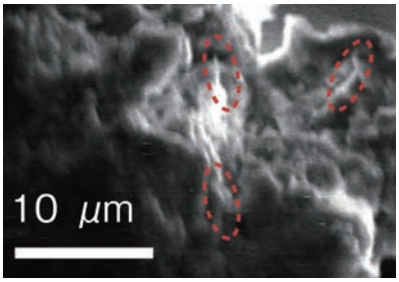

Fig.3-16 SEM image of sample M403.7R from fault gauge in Toki granite
Red dashed circle indicate needle illite crystals.

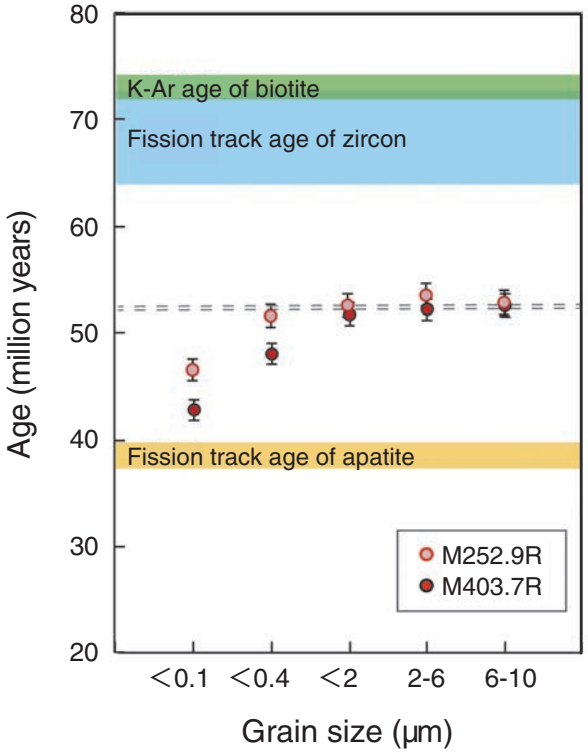

Fig.3-15 Age trend of sample from fault gauge in Toki granite
A younger age is obtained for a smaller grain size sample. The sampling depth was 252.9 m for M252.9R and 403.7 m for M403.7R.

The activity of faults around a target locality is evaluated to assess the safety for geological disposal and it is important to determine the period of fault activity for specific faults. Although the period of fault activity is generally determined by the stratigraphy of dated formations, dating methods for fault derived material are also developed for inapplicable cases, e.g., when no sedimentary rocks are distributed in the locality or when a fault is found in the tunnel.

Fault-derived material is generated by violent friction between rocks in contact as a fault moving. A fault gauge is a type of fault-derived material (Fig.3-14). Authigenic clay minerals formed by alteration are contained in the fault gauge. Methods of separating specific minerals and evaluating the obtained age are developed to date the authigenic clay minerals in the fault gauge, because the age of these minerals defines the end of fault activity. Illite, a clay mineral, can be dated by K–Ar dating, which is scaled to the decay of potassium-40 to argon-40.

Methods evaluating the authigenic illite age in sedimentary rocks are developed. Finer-grained samples reportedly show younger ages. The application of illite dating to illite in the fault gauge is under development. The low-temperature structure illite is assumed to be authigenic in the evaluation method of sedimentary illite age. Another evaluation method proposes scanning electron microscopy (SEM) observation of illite crystals in collected illite samples because illite crystals form needles in rapid growth during brief thermal activity after a fault moves, whereas they form sheets in slow growth during diagenesis of sedimentary rocks.

Two samples were collected from the main pit of Mizunami Underground Research Laboratory, which penetrates the Toki granite. They showed younger ages for finer grain fractions (Fig.3-15). SEM observation of the samples revealed needle illite formed after the fault activity (Fig.3-16). High-temperature structure crystals were also detected in the samples, although the faults were in the granite host rock. This indicates a problem with determining alteration after fault movement; the alteration generates not only low-temperature crystals but also high-temperature crystals. We will study the illite geochronology for presupposition of the dating method and methods of sample preparation and observation.

Reference

Yamasaki, S., Umeda, K. et al., Constraining the Timing of Brittle Deformation and Faulting in the Toki Granite, Central Japan, Chemical Geology, vol.351, 2013, p.168–174.

3–6 Estimating Long-Term Evolution of Environment and Materials around Radwaste in Deep Underground
— Development of Assessment Methodology Considering Geochemical Changes in the Near-Field —

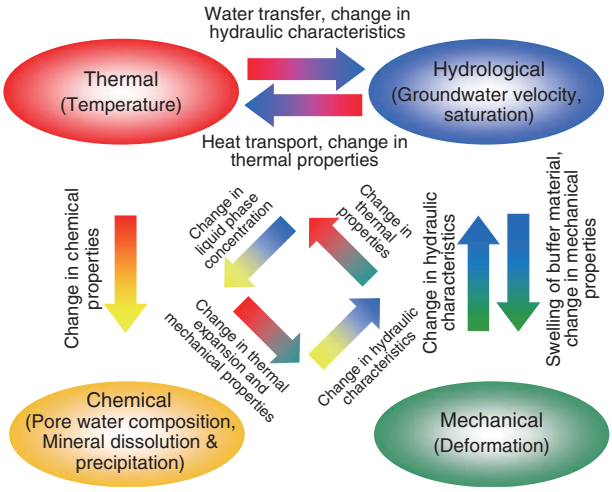

Fig.3-17 Conceptual model of coupled processes in near-field
It is believed that after an engineered barrier is set, a complicated condition involving heat release from vitrified waste, groundwater migration, swelling of buffer material, and geochemical reactions in pore water is induced.

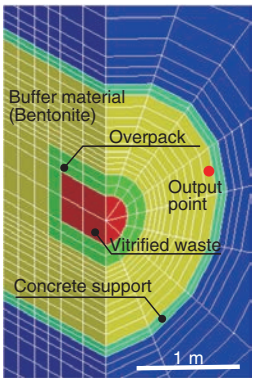

Fig.3-18 Analysis object
The red circle indicates output point in Fig.3-20. The layout assumes horizontal emplacement.

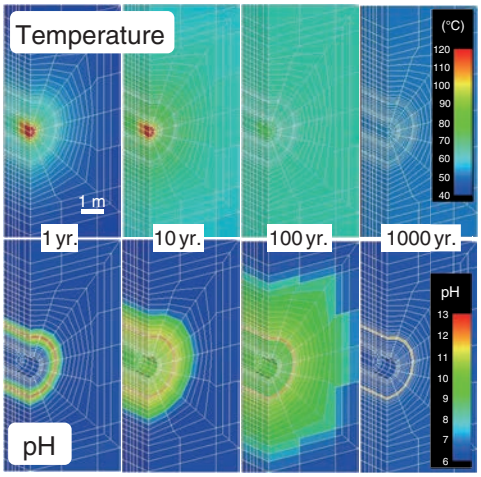

Fig.3-19 Analyzed example: evolution of temperature and pH in the near-field
The disposal system is assumed to be set in sedimentary rock 450 m in depth.

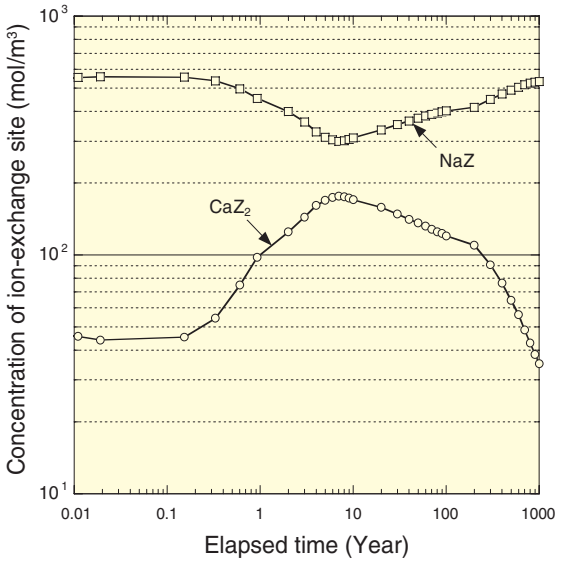

Fig.3-20 Analyzed example: history of concentration of ion-exchange sites in the buffer material
Z is an ion-exchange group. Na and Ca concentrations change to half and four times their initial values, respectively, in 10 years and are both restored to their initial values after 1000 years.

For the safety assessment of the geological disposal of high-level radioactive waste, it is necessary to quantify the coupled thermo-hydro-mechanical-chemical (THMC) processes in the near-field. Because laboratory and *in-situ* experiments cannot realize real phenomena, numerical models are used as a practical approach to bridging the gap between experiments and real phenomena in long-term near-field evolution, meeting the need for post-closure safety assessment.

This study investigated the geochemical changes arising from the infiltration of groundwater into a bentonite buffer under a thermal regime of radiogenic heating arising from vitrified waste using a computer simulation of a developed THMC model (Figs.3-17, 3-18).

From the analysis results, the temperature in the engineered barrier system (EBS) reached a maximum within 20 years. The temperature of the buffer material on the overpack side was approximately 95 °C. The temperature of the EBS is found to drop to 50 °C after 1000 years. Although the groundwater becomes alkaline under the influence of the concrete support, it returns to the initial pH until after 1000 years (Fig.3-19). In the event of infiltration by saline groundwater, sulfate precipitates as gypsum around the overpack in the buffer material, and the Na-type bentonite is changed to Ca-type by exposure to Ca ions released from the concrete supports (Fig.3-20). These results were consistent with the current scenarios assumed for geological disposal. It will be possible to estimate the extent of the overpack corrosion in the EBS using this developed THMC model.

The present study was sponsored by the Ministry of Economy, Trade and Industry (METI).

Reference

Suzuki, H., Nakama, S. et al., A Long-Term THMC Assessment on the Geochemical Behavior of the Bentonite Buffer, Genshiryoku Bakkuendo Kenkyu, vol.19, no.2, 2012, p.39-50 (in Japanese).

3–7 Effect of Natural Organic Matter on Migration of Radionuclides
— Metal Ion Binding Abilities of Deep Groundwater Humic Substances —

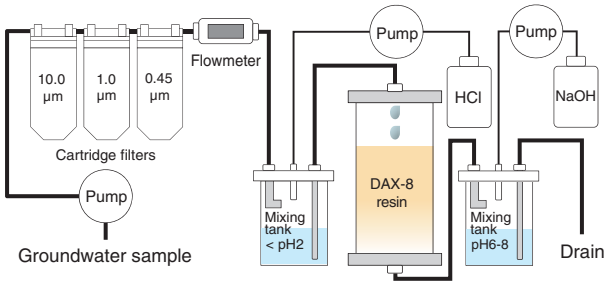

Fig.3-21 Sequential extraction system used for isolation of groundwater humic substances (HSs)
HSs were isolated from groundwater on the basis of their sorption affinity to hydrophobic resin (DAX-8) below pH2.

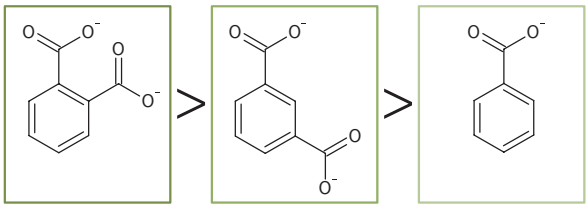

Fig.3-23 Magnitude relation between the stability constants (β) of Eu^{3+} to simple carboxylic acids and their structural features
The complex is more stable as the number of carboxyl group increases and their positions approach each other.

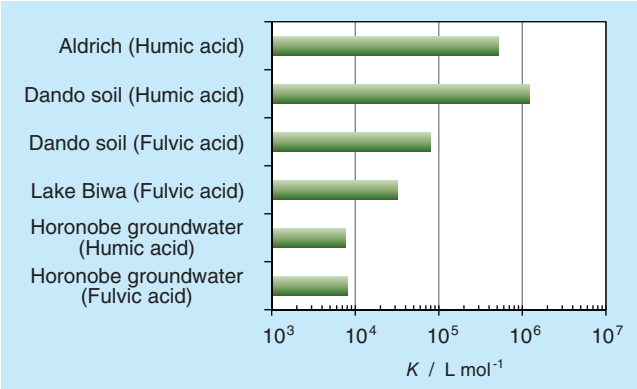

Fig.3-22 Conditional binding constants (K) of Eu^{3+} to groundwater HSs and comparison with those of HSs from surface environments in Japan
The K values were obtained at pH5.0, 0.1 mol L^{-1} $NaNO_3$, and a loading level (C_{Eu}/C_L) of 0.7–76 (C_{Eu} and C_L denote total concentration of Eu^{3+} and carboxyl group contents of HSs, respectively).

Humic substances (HSs) are a type of natural organic matter that is ubiquitous in the environment. They can form soluble and stable complexes with metal ions. Because HSs are known to be dissolved even in deep groundwater, their effect on facilitating the migration of radionuclides in underground environments is a major concern for safety assessment of geological disposal systems for high-level radioactive waste.

Previous works in other countries have shown that deep groundwater HSs have the same degree of affinity for binding radionuclides as HSs from surface environments. However, it is not always true that such findings can be extended to all deep groundwater HSs because the structural feature of HSs can depend strongly on their origin.

In this study, HSs were isolated from deep groundwater at the Horonobe Underground Research Laboratory site (Fig.3-21), and the conditional binding constants (K) of Eu^{3+} for the groundwater HSs were then evaluated by a spectroscopic method. It was found that the groundwater HSs had the smallest K value among the HSs examined, which were two orders of magnitude smaller than those of the humic acid in the Aldrich and Dando soils (Fig.3-22). On the basis of the relationship between the stability constants (β) of Eu^{3+} to the simple carboxylic acids and their structural features (Fig.3-23), the low affinity for Eu^{3+} might be due to the fact that the carboxylate groups in the humic molecule are separated by a considerable distance.

These results demonstrate that some deep groundwater HSs in Japan have binding affinities that differ from those of HSs obtained from surface environments. In addition, our results show that the existing model and database, which were developed for HSs from surface environments, cannot be useful for deep groundwater HSs. Thus, these findings suggest that a model and database for deep groundwater HSs should be developed for realistic modeling.

The present study was partially funded by the Ministry of Economy, Trade and Industry (METI).

Reference

Terashima, M. et al., Europium-Binding Abilities of Dissolved Humic Substances Isolated from Deep Groundwater in Horonobe Area, Hokkaido, Japan, Journal of Nuclear Science and Technology, vol.49, no.8, 2012, p.804-815.

3–8 Evaluation of Bentonite Alteration in a TRU Waste Geological Repository
— Modeling of Smectite Dissolution Rate under a Range of Chemical Conditions —

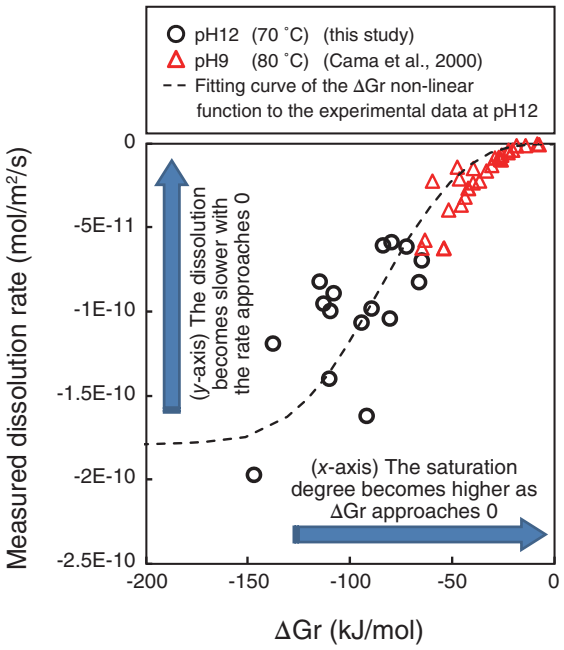

Fig.3-24 Smectite dissolution rate as a function of the degree of saturation
Dissolution rates of smectite measured at pH12 (70 °C) decrease (dissolution becomes slower) with an increase in the degree of saturation (ΔGr on the *x*-axis is a function of the degree of saturation and approaches 0 with an increase in the degree of saturation). Dissolution rates of Cama et al. (2000) obtained at pH9 (80 °C) show the same tendency.

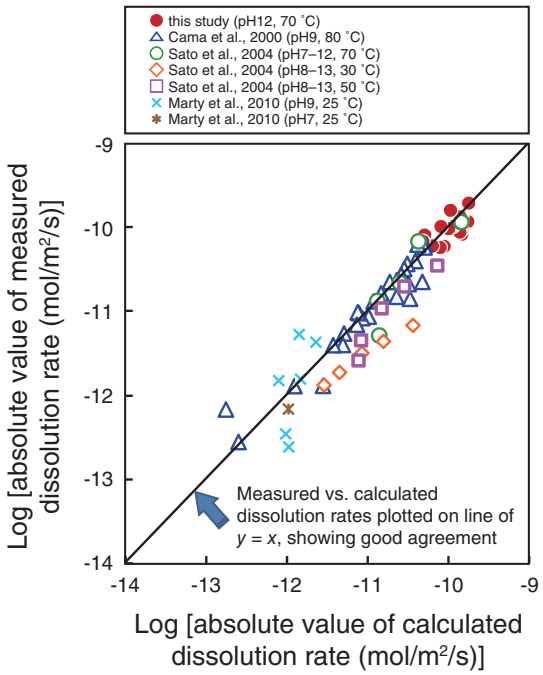

Fig.3-25 Comparison of calculated and experimentally measured smectite dissolution rates
Smectite dissolution rates calculated from the rate equation developed in this study are in good agreement with those measured experimentally at pH7–13 and 25–80 °C under a range of saturation conditions.

Smectite-rich bentonites have a number of attractive physicochemical properties that make them suitable for use as a buffer material in the geological disposal of transuranic (TRU) wastes. Cementitious materials, used for their familiar engineering properties, can, however, generate high alkaline conditions of pH ≥ 12.5. Such a high pH can potentially cause alteration of bentonite, including the dissolution of smectite, and consequently the loss of the attractive physicochemical properties (e.g., the osmotic swelling capacity and consequently the plasticity and impermeability) of the bentonite buffer. The dissolution of smectite is, therefore, a key process in the evaluation of the long-term evolution of the bentonite buffer.

In this study, laboratory experiments were conducted to establish the smectite dissolution behavior under high alkaline conditions, and a dissolution rate equation for smectite was derived. A novel method using atomic force microscopy developed by Hokkaido University and Kanazawa University was used to observe the change in smectite particle size during dissolution. On the basis of the observed changes in particle size, an average dissolution rate for each experiment was determined statistically. The dissolution rates of smectite at pH12 were found to decrease with an increase in the degree of saturation (Fig.3-24). By combining these results with other published rate data obtained at pH9, a rate equation describing the dependence of smectite dissolution on the pH, temperature, and degree of saturation was determined. The smectite dissolution rates predicted by the rate equation are in good agreement with experimentally measured values at pH7–13 and 25–80 °C under a range of saturation conditions (Fig.3-25). The rate equation can therefore be used to describe the smectite dissolution rates in the bentonite buffer in response to changes in the chemical conditions expected over the temporal and spatial scales of geological disposal of TRU wastes.

Part of this study was conducted under a contract with the Hokkaido University.

Reference

Oda, C. et al., Reactive-Transport Model Analyses of Bentonite Alteration Behavior at Alkaline Condition Generated by Cement-Water Interaction in a TRU Wastes Repository, Nendo Kagaku, vol.51, no.2, 2013, p.34-49 (in Japanese).

Toward Practical Use of Fusion Energy

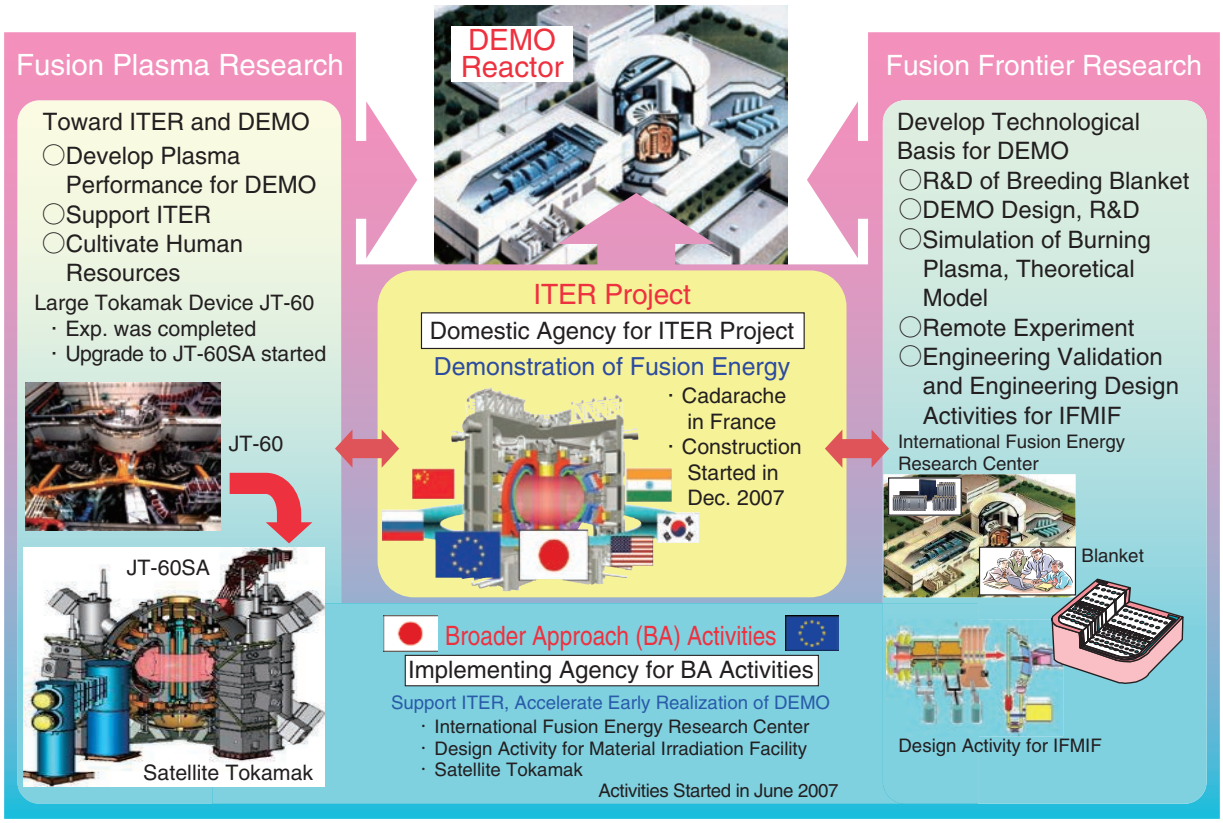

Fig.4-1 Steps involved in the development of fusion DEMO reactor
Fusion plasma research and fusion frontier research are being pursued to develop a DEMO reactor, aiming for early realization of fusion energy.

Crucial Research and Development on Fusion Plasma Research and Fusion Frontier Research toward the practical use of fusion energy is being pursued through intensive international cooperation, for example, the International Thermonuclear Experimental Reactor (ITER) project, Broader Approach (BA) activities, and other collaborations (Fig.4-1), aiming for early realization of a fusion DEMO reactor.

ITER Project

The ITER project is an international cooperative project to demonstrate the scientific and technological feasibility of fusion energy through the construction and operation of an experimental reactor. The ITER agreement came into force in October 2007, and the Japan Atomic Energy Agency (JAEA) was designated as the domestic agency for the ITER project in Japan. The JAEA proceeded with preparing the equipment that Japan has agreed to provide and achieved various results in terms of technological development (Topics 4-1, 4-2). In particular, the JAEA began the production of a superconducting coil for the actual machine ahead of any other country participating in ITER.

BA Activities

The BA activities are joint projects by Japan and the EU for conducting supporting research for ITER and research and development (R&D) for a DEMO reactor, which is the next step of ITER, aiming for early realization of fusion energy. The BA agreement came into force in June 2007, and the JAEA was designated as the implementing agency of the BA activities in Japan.

The BA activities consist of three projects: projects in the International Fusion Energy Research Center (IFERC), the engineering validation and engineering design activities of the International Fusion Materials Irradiation Facility/Engineering Validation and Engineering Design Activities (IFMIF/EVEDA), and the Satellite Tokamak Program (STP). Topics 4-3 and 4-4 describe the results achieved in the R&D activities toward a DEMO reactor in the IFERC. Topics 4-5 and 4-6 describe the results obtained by IFMIF/EVEDA. In the STP, the construction of JT-60SA has progressed well (Topic 4-7). Topics 4-8 and 4-9 are also results contributing to JT-60SA.

Fusion Plasma Research

The analysis of the JT-60 experimental data was promoted, and inter-machine experiments were conducted for the purpose of achieving high economic efficiency of the fusion reactor by attaining a high plasma pressure. Topic 4-10 is a result that clarifies the mechanism of the formation of high plasma pressure.

Fusion Frontier Research

Various R&D activities are executed at the BA site in Rokkasho, aiming at the construction of a technological basis for a DEMO reactor. Topic 4-11 describes theoretical simulation research that uses the high-performance computer at IFERC; the result can provide a basis for controlling the plasma in a DEMO reactor.

4–1 Multi-Parameter Measurement Using Laser Polarimetry for Fusion Reactor

— Simultaneous Measurement of Magnetic Field, Electron Density, and Electron Temperature —

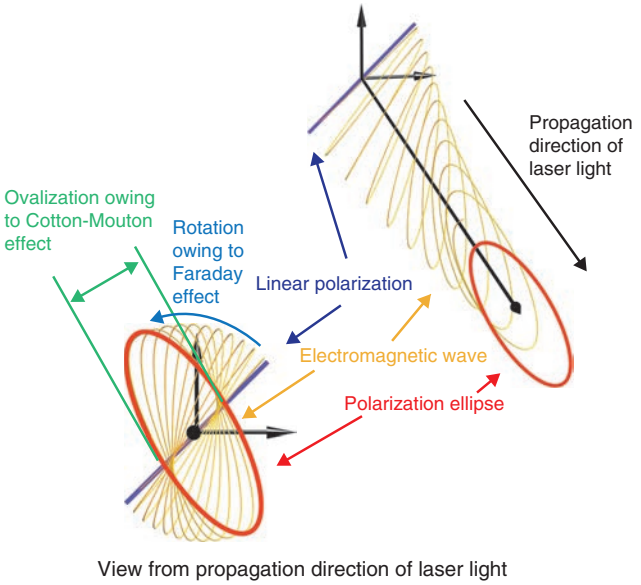

Fig.4-2 Change in polarization state during propagation of laser light in plasma
The ovalization of the polarization state is associated with the Cotton–Mouton effect, and the rotation of the ellipse is associated with the Faraday effect.

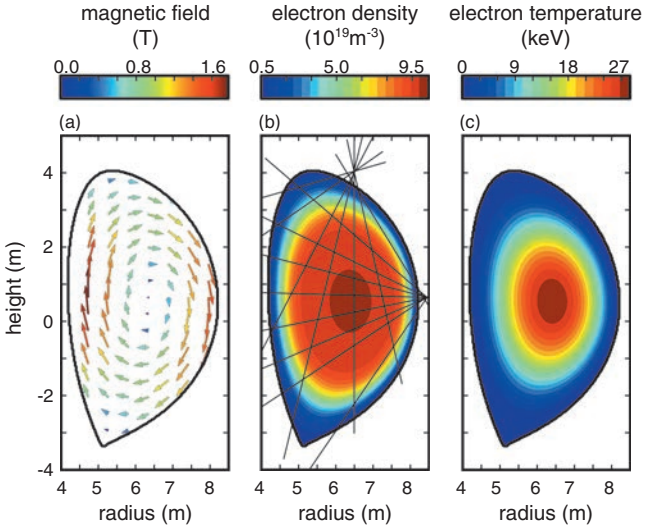

Fig.4-3 Reconstruction of laser polarimetry measurement data
(a) Magnetic field profile, (b) electron density profile, (c) electron temperature profile. Solid lines in (b) illustrate the laser paths.

It is well known that information about the magnetic field structure in a plasma is essential for steady-state and high-performance operation of tokamak devices. Laser polarimetry is a method of measuring the magnetic field in the plasma. The change in the polarization state of laser light propagated in the plasma depends on the magnetic field and electron density. The magnetic field profile can be reconstructed from the laser polarimetry measurement data and the information on the electron density provided by other diagnostics. When the electron density and temperature are high (e.g., in burning plasma), the change in the polarization state becomes complicated. Therefore, it has been a concern that laser polarimetry will not be applicable to magnetic field measurement in a future reactor.

The change in the polarization state approximates the superposition of the two fundamental processes, the Faraday effect and the Cotton–Mouton effect (Fig.4-2). In plasma with a high electron temperature, the Faraday effect is degraded, whereas the Cotton–Mouton effect is enhanced. Laser polarimetry is typically used when the Cotton–Mouton effect is small, and only the Faraday effect is measured. However, this study proposes laser polarimetry using long wavelengths to obtain a large Cotton–Mouton effect and proposes the reconstruction of the electron temperature from the measurement data for the Faraday and Cotton–Mouton effects. It is reasonably expected that such reconstruction is possible by using the different dependences of both effects on the electron temperature.

The above expectation was tested under the conditions of the ITER poloidal polarimeter. Using the measurement data from the polarimeter and information on the location of the plasma boundary, the simultaneous reconstruction of the magnetic field, electron density, and electron temperature was successfully demonstrated. Fig.4-3 shows the reconstruction results. These results not only show that magnetic field measurement is possible in the case of a complicated change in the polarization state, but also pioneer a new application of laser polarimetry to electron density measurement.

Existing fusion experimental devices use many diagnostics. However, a future reactor needs to be operated with fewer diagnostics. This study suggests that multi-parameter measurement using laser polarimetry shows promise for future reactors.

Reference

Imazawa, R. et al., Separation of Finite Electron Temperature Effect on Plasma Polarimetry, Review of Scientific Instruments, vol.83, issue 12, 2012, p.123507–1–123507–5.

4–2 Manufacturing of ITER Divertor Prototype

— First Step toward Manufacturing of Actual ITER Divertor —

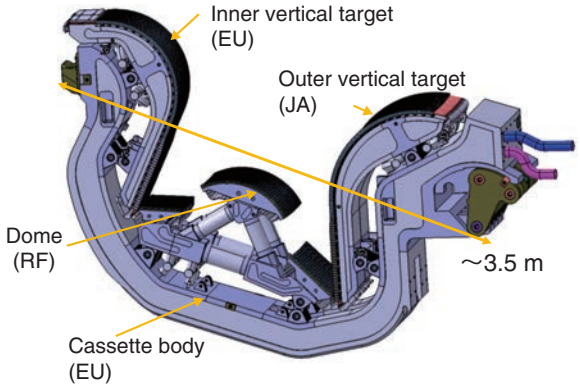

Fig.4-4 ITER divertor (cassette structure)
The ITER divertor has a cassette structure. High heat flux components, such as the inner vertical target, outer vertical target, and dome, are installed in the cassette body. There are 54 cassettes in the tokamak.

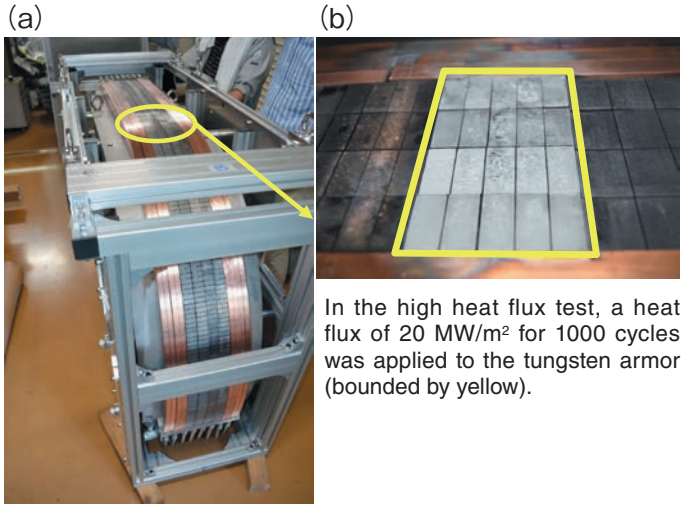

Fig.4-5 Appearance of prototype PFU and tungsten armor
(a) Test frame with four PFUs.
(b) Tungsten armor tiles after high heat flux test. Tungsten has recrystallized. However, no degradation of the heat removal capability was found through 1000 cycles at 20 MW/m^2.

The Japan Atomic Energy Agency (JAEA), designated as the Japanese Domestic Agency (JADA), is currently manufacturing various components for ITER construction. The ITER divertor components are being manufactured by three parties (the European Domestic Agency (EUDA), the Russian Federation Domestic Agency (RFDA), and JADA). The JADA is responsible for manufacturing the outer vertical target shown in Fig.4-4.

The divertor exhausts impurities that come from the plasma. The divertor plate is subjected to a high heat flux from the impact of the impurities. To withstand the high heat flux, the surface of the divertor plate is covered with refractory materials. The inner target and outer target, which are subject to severe heat flux, are covered with carbon fiber composite, and the other components are covered with tungsten. These armor materials are metallurgically bonded to the copper alloy (CuCrZr) cooling tubes to achieve a high heat removal capability. Unique technologies that have been independently developed by the three parties are used to bond the armor materials and the cooling tubes. The JADA currently uses a brazing technology for the bonding. In the ITER project, qualification of the manufacturing process for the divertor must be demonstrated by each party to validate its technical capability. The parties manufacture prototype components that consist of the same materials that will be used for the real components and perform a high heat flux test to demonstrate the durability of the prototype components.

The JADA manufactured the first set of plasma-facing units (PFU#1) as a first step in manufacturing the divertor, as shown in Fig.4-5. PFU#1 has been transported to the RFDA for a high heat flux test in the RFDA's facility. Before the manufacturing of PFU#1, the JADA conducted qualification activities, such as mechanical and nondestructive testing of the braze joints and welding joints. In addition, the brazing process was formally witnessed by the ITER organization during the manufacture of PFU#1. In the high heat flux test in the RFDA, PFU#1 showed excellent durability against a repetitive heat flux of 20 MW/m^2 for 1000 cycles with no degradation of the heat removal capability and no surface crack initiation.

The second high heat flux test campaign in the RFDA is scheduled for autumn 2013. After that, the manufacturing of the real divertor components will begin.

Reference

Suzuki, S. et al., Development of the Plasma Facing Components in Japan for ITER, Fusion Engineering and Design, vol.87, issues 5–6, 2012, p.845–852.

4–3 Success in Beryllide Pebble Fabrication

— Development of Granulation Technology for Neutron Multiplier Needed for Production of Fusion Reactor Fuel —

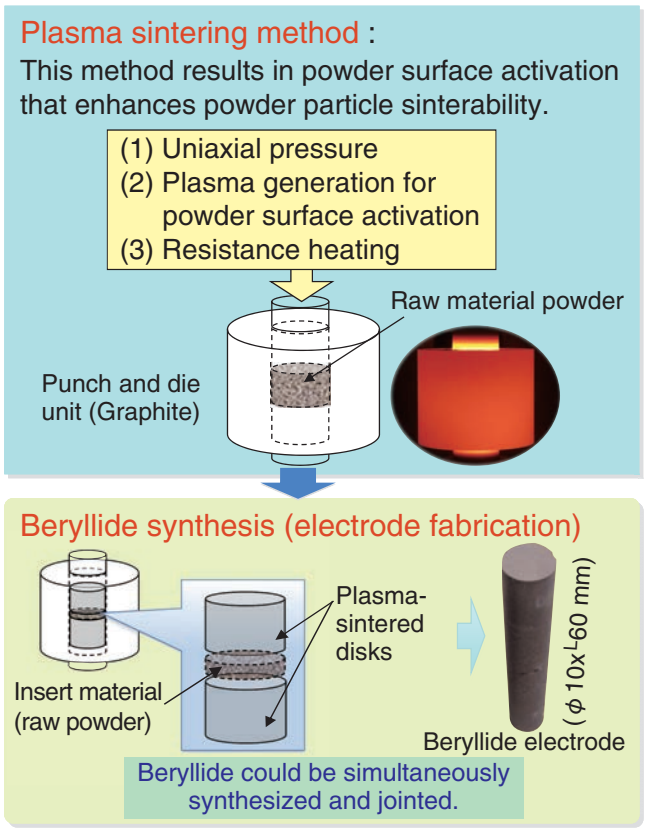

Fig.4-6 New beryllide synthesis by the plasma sintering method
Beryllide could be simultaneously synthesized and jointed. Further, a beryllide electrode was successfully fabricated by the plasma sintering method.

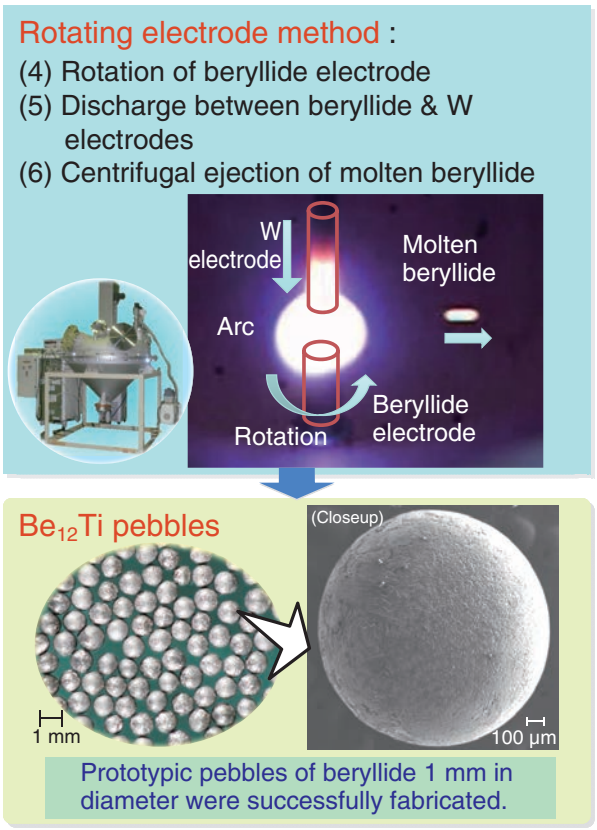

Fig.4-7 Granulation by the rotating electrode method
Prototypic beryllide pebbles 1 mm in diameter were successfully fabricated for the first time worldwide.

The tritium used as a fuel in fusion reactors is produced by irradiation of lithium with neutrons that are generated by nuclear fusion reactions. A neutron multiplier is essential in effectively generating the fuel because this material increases the number of neutrons by reactions with the fusion neutrons. Beryllium metal, which is a conventional material for the neutron multiplier, has a low chemical stability at high temperatures. This has led to the development of fabrication technology for more stable beryllium intermetallic compounds (beryllides). Beryllide can be obtained by conventional powder metallurgy methods; however, it is very brittle.

Therefore, a plasma sintering method was applied in which synthesis is conducted after the surface of the raw material powder is cleaned by electric discharge. Further, this synthesis method was optimized in the DEMO R&D building at the International Fusion Energy Research Center site in Rokkasho-mura, Aomori-ken as a series of Broader Approach activities. As a consequence, an easily processed beryllide rod was successfully fabricated by the plasma sintering method (Fig.4-6).

Furthermore, using the beryllide rod as an electrode in the rotating electrode method, beryllide pebbles 1 mm in diameter were successfully fabricated for the first time worldwide (Fig.4-7); this value of the diameter is a target dimension for use in fusion reactors.

The present result substantiates the fuel tritium production tests in ITER and greatly contributes to the establishment of fuel production technology. Moreover, this result represents great progress in establishing fuel production technology toward the fusion demonstration reactor (DEMO) in the future.

Reference

Nakamichi, M. et al., Novel Granulation Process of Beryllide as Advanced Neutron Multipliers, Fusion Engineering and Design, vol.88, issues 6–8, 2013, p.611–615.

4–4 Accuracy Validation of Nuclear Data for Fusion Reactor Design

— Toward More Accurate Fusion Reactor Design —

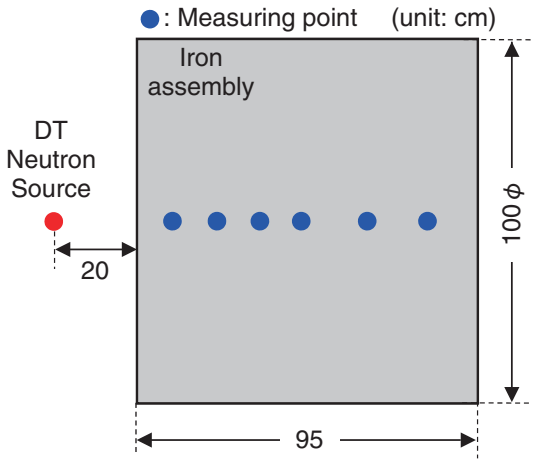

Fig.4-8 Layout sketch of iron experiment (vertical cross section)
Data for neutrons and gammas were measured inside an iron assembly 100 cm in diameter and 95 cm in thickness.

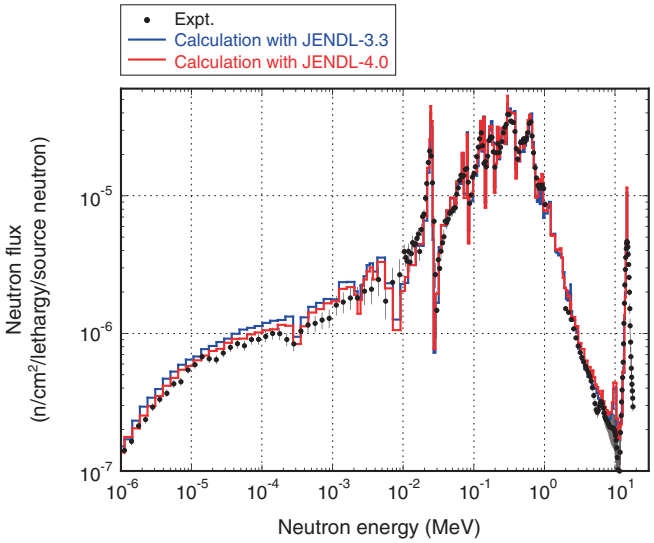

Fig.4-9 Neutron energy spectra at depth of 31 cm in iron assembly
The measured data are plotted as black circles, and the values calculated using the JENDL are shown by colored lines.

Various studies toward the practical use of fusion reactors as a future energy source have been proceeding step by step. Fusion power plants produce 14 MeV neutrons through the reactions of deuterium and tritium in high-temperature plasma. Nuclear reactions of these neutrons with surrounding materials generate thermal energy (nuclear heating) and tritium (tritium production), which is used as fuel in the plants. For safety, the neutrons have to be shielded so that they do not leak outside the fusion power plants (shielding).

The 14 MeV neutrons initiate various nuclear reactions with all the materials surrounding the plasma. Fusion reactor designs estimate the nuclear heating, tritium production, shielding, and so on by considering all the nuclear reactions using a radiation transport code and database (nuclear data library) of nuclear reaction cross sections (nuclear data) to characterize the probability that a nuclear reaction will occur. The typical radiation transport code is the Monte Carlo code MCNP, which is used worldwide because of its few calculation approximations. On the other hand, there are several nuclear data libraries; the Japanese Evaluated Nuclear Data Library (JENDL) in Japan, ENDF/B in the US, and JEFF in Europe. Nuclear data libraries are one of the most important databases that determine the calculation accuracy of fusion reactor design results. It is necessary to examine and improve the accuracy of nuclear data libraries experimentally.

The Fusion Neutronics Source facility in the Japan Atomic Energy Agency (JAEA) can produce the same 14 MeV neutrons as those generated in fusion reactors with an accelerator. We inject these neutrons into various assemblies, as shown in Fig.4-8, and measure the data for neutrons and gammas inside the assemblies. We simulate these experiments with MCNP and the nuclear data libraries and validate the accuracy of the libraries. Fig.4-9 shows a typical example (iron experiment). The calculated neutron spectrum below 0.01 MeV with the previous version, JENDL-3.3, is about 30% larger than the measured one, but the discrepancy between the calculated and measured results decreases to about 15% in the calculation result with the latest version, JENDL-4.0 (some of the cross section data for ^{57}Fe were dramatically modified on the basis of our study).

Reference

Konno, C. et al., Detailed Benchmark Test of JENDL-4.0 Iron Data for Fusion Applications, Fusion Engineering and Design, vol.86, issues 9–11, 2011, p.2682–2685.

4–5 Toward Construction of Intense Neutron Source for Fusion Reactor Conditions
— Measurement of Thickness and Stability of High-Speed Lithium Flow —

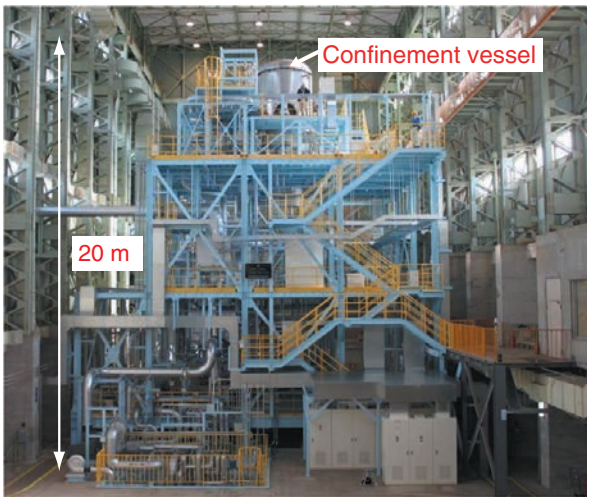

Fig.4-10 View of entire EVEDA Lithium Test Loop
The liquid Li target is produced in the confinement vessel at the top of the EVEDA Li Test Loop, which is the largest Li loop in the world.

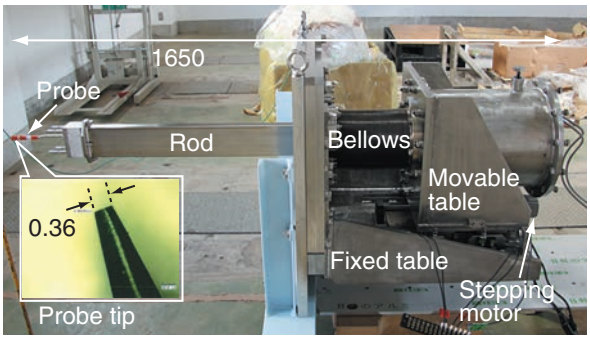

Fig.4-11 Contact-type liquid level sensor (unit: mm)
The probe is connected to the movable table by the rod and can be positioned with high precision by the stepping motor.

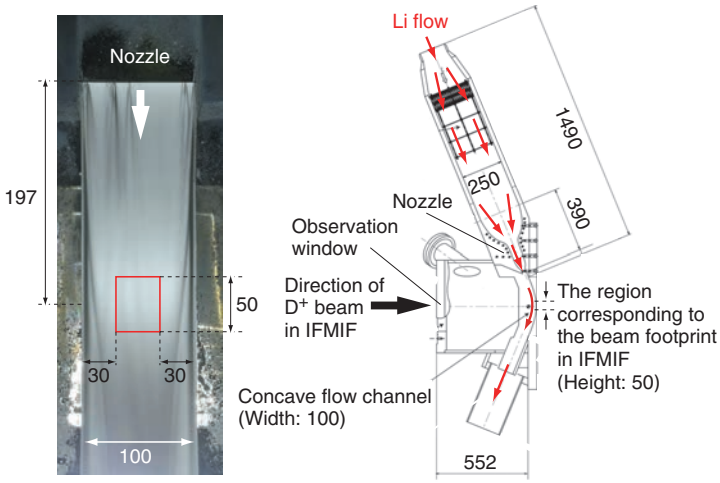

Fig.4-12 Picture of Li target flow and cross-sectional view of Li flow path (unit: mm)
The Li flow was photographed through the observation window at a speed of 20 m/s, which exceeds the IFMIF condition. The red rectangle indicates the deuteron beam footprint in the IFMIF.

To realize a fusion reactor, the development of materials capable of withstanding fusion neutron irradiation is indispensable. The International Fusion Materials Irradiation Facility (IFMIF) is an intense neutron irradiation facility simulating fusion reactor conditions for the development of fusion reactor materials. In the IFMIF, neutrons are generated by the injection of deuterons into lithium (Li). The Engineering Validation and Engineering Design Activities (EVEDA) for the IFMIF are now being conducted as one of the Broader Approach activities. We are performing experiments at the EVEDA Li Test Loop (ELTL, Fig.4-10), which is a prototype of the IFMIF Li loop, with the goal of acquiring validation data toward the construction of the IFMIF.

The most important validation item is the stability of the liquid Li target, which flows at a speed of 15 m/s along a concave flow channel (25 mm in thickness) at a temperature of 250 °C with a free surface (freely deformable liquid surface). The free surface of a high-speed flow is generally unstable. Thus, it is necessary to address the very difficult problem of generating a high-speed stable flow (required flow thickness fluctuation: less than 1 mm). Although we anticipated that the centrifugal force that acts on a concave flow would suppress the fluctuation, we need to measure the actual fluctuation, and we have to develop a precise measurement device.

We developed a contact-type liquid level sensor in a smaller Li loop than the ELTL. This sensor is equipped with a sharp probe and detects contacts between the probe and the liquid as electrical signals. Analysis of the contact signals yields the properties of the free-surface waves. Some issues had to be resolved before this sensor is employed as a diagnostic tool in the ELTL. For instance, although the internal pressure of the smaller loop is equivalent to atmospheric pressure, that of the ELTL is a vacuum, and it is necessary to counter the difference of 0.1 MPa between the inner and outer pressures accordingly. Thus, we employed a strong structure and a powerful motor. On the basis of the above design, we fabricated a sensor for use in the ELTL (Fig.4-11). The performance test results show that the probe can be positioned with high precision (resolution: 0.1 mm, positioning precision: 0.01 mm) as required.

Now, we are measuring the Li target thickness. The Li target was successfully produced at a high speed of 20 m/s (Fig.4-12). The stability of the Li target is almost within the requirement.

Reference

Kanemura, T., et al., Fabrication and Performance Test of Contact–Type Liquid Level Sensor for Measuring Thickness Variation of Liquid Lithium Jet in the IFMIF/EVEDA Lithium Test Loop, Fusion Engineering and Design, vol.88, issues 9–10, 2013, p.2457–2551.

4–6 Realization of Fusion Intense Neutron Source
— Loop Antenna Development for RF Coupling in the RFQ Linac —

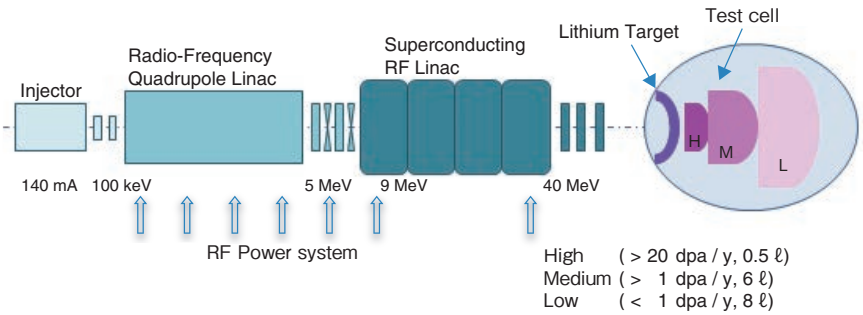

Fig.4-13 Configuration of IFMIF
A 40 MeV deuteron beam with at 250 mA is injected into a liquid lithium flow, and a 14 MeV neutron field similar to that of a D-T fusion reactor is produced by the D-Li stripping reaction. Materials are irradiated with these neutrons to evaluate their robustness for use in fusion reactors.

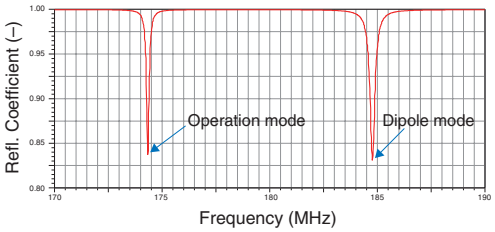

Fig.4-16 Reflection coefficient from RFQ
A frequency shift of less than 0.1% for operation mode is attained, and it is sufficient far from dipole mode.

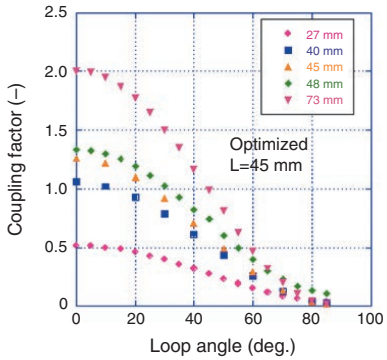

Fig.4-14 Measured results of RF coupling; RF coupling vs. loop angle for the inserted depth

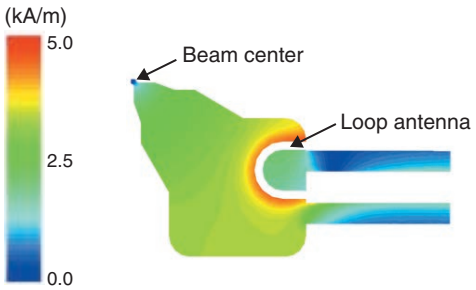

Fig.4-15 Magnetic field profile by 3-D simulation code
RFQ magnetic field profile is satisfied under the design conditions.

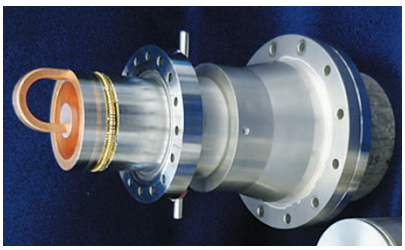

Fig.4-17 Photograph of loop antenna tip module employing an advanced Japanese technology

To realize a demonstration fusion reactor, it is indispensable to evaluate the feasibility for use in fusion reactor materials using 14 MeV neutron irradiation. For this purpose, the International Fusion Materials Irradiation Facility (IFMIF) is being jointly planned by Japan and the European Union under the agreement of Broader Approach Activities agreement.

In the IFMIF, a neutron field is produced by the deuteron (D)-lithium (Li) stripping reaction. The realization of a deuteron beam that can be accelerated and injected into liquid lithium is a key issue (Fig.4-13). In this accelerator facility, two 125mA beam lines are used. Continuous wave (CW) operation is also required, and this is the world's first attempt at developing such a high-current beam and a CW operation linac. One beam line consists of an ion injector, a radio frequency quadrupole (RFQ) linac and a superconducting RF (SRF) linac; their designed output energies are 0.1, 5.0 and 40 MeV, respectively. We developed a new RFQ, because the RFQ had many technical issues to be overcome for the realization of high-current and CW operation.

In this RFQ linac, a driving RF power of 1.4 MW at 175 MHz has to be injected to the RFQ cavity to accelerate a large current of 125 mA in CW mode. For stable and continuous RF power driving, it is indispensable to reduce the deformation of the loop antenna and to avoid frequency shifts in the operation mode. For this purpose, it is crucial to obtain an RF design by employing a small loop antenna and a short insertion depth.

In this study, the precise RF properties (Fig.4-14) were evaluated by measuring a real size RFQ mock-up module and analyzing a 3-D simulation code (Figs.4-15, 4-16). The insertion depth was successfully optimized. For the world's first attempt, an engineering design with cooling water channels in the loop antenna was also developed. To make uniform cooling channels following the loop's curve, an advanced Japanese technology using uniform minute grains of sand was applied. As a result, the loop antenna tip module with cooling channels was successfully manufactured (Fig.4-17). With these results, the development of a loop antenna for CW operation is now in sight.

Reference

Maebara, S. et al., Engineering Design of the RF Input Coupler for the IFMIF Prototype RFQ Linac, Fusion Engineering and Design, vol.88, issues 9–10, 2013, p.2740–2743.

4–7 Progress in Satellite Tokamak Program Project
— Start of Assembly of JT-60SA —

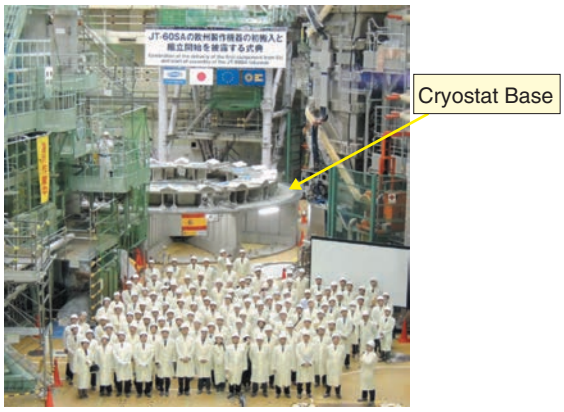

Fig.4-18 Start of assembly of cryostat base
A ceremony marking the start of assembly of the JT-60SA tokamak was held by participants from the Japanese and European governments, local authorities, universities, institutes, and industry in March 2013.

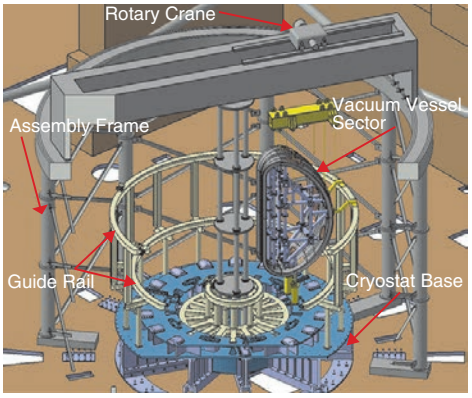

Fig.4-19 Assembly frame for assembly of JT-60SA tokamak
An assembly frame (20 m in diameter) with a dedicated crane is used for effective assembly of JT-60SA tokamak.

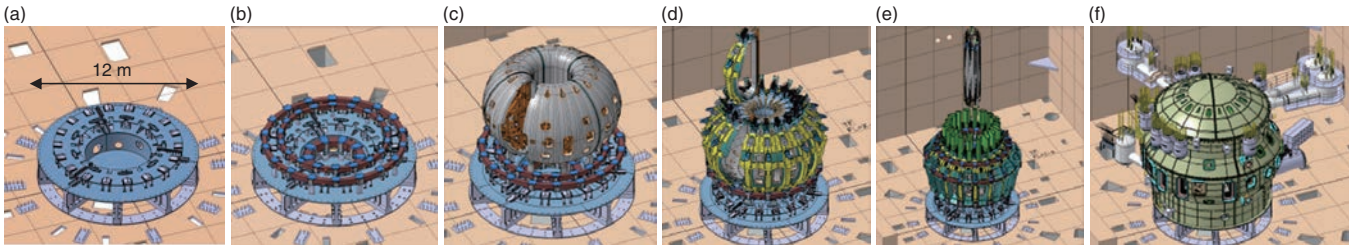

Fig.4-20 Major assembly sequence of JT-60SA tokamak
Assembly of the JT-60SA tokamak being undertaken jointly by Japan and Europe started with the assembly of the cryostat base fabricated by Europe in January 2013. JT-60SA aims at first plasma in March 2019 after an assembly period of six years.

The design and fabrication of components for the Satellite Tokamak Program (JT-60SA), jointly implemented by Europe and Japan, is progressing well toward the goal of first plasma in March 2019. Disassembly of the JT-60U tokamak at the Naka Fusion Institute was completed in October 2012 on schedule. The assembly of the cryostat base (12 m in diameter and 280 t in weight), which is the first component from Europe, started in January 2013, so the assembly of the JT-60SA tokamak began as planned. The cryostat is a vacuum thermal insulation chamber for superconducting coils cooled at 4 K. The cryostat base is a base structure for installation of tokamak components such as the vacuum vessel (VV) as well as the cryostat body. The assembly of the cryostat base was completed with a high accuracy of ±0.5 mm in March 2013 (Fig.4-18). The VV and superconducting toroidal field coils (TFCs) are installed on the cryostat base one by one in the toroidal direction. For effective movement and accurate positioning of these components, an assembly frame (20 m in diameter and 18 m in height), which provides a dedicated rotary crane and guide rails (Fig.4-19), is used. The VV, which is composed of 10 sectors, is assembled using the welding conditions validated by research and development up to the 340° covered by nine sectors, omitting the last sector, which covers 20° (Fig.4-20(c)). Then, each TFC is moved toroidally along the VV through the opening of 20° in the VV. The position of the current center of the TFC defined during fabrication is adjusted within an error of a few millimeters using a precise metrology device with a laser (Fig.4-20(d)).

Two-thirds of the entire VV procured by Japan has already been fabricated. The fabrication of the TFC procured by Europe started in France and Italy, so preparation for the assembly of the TFC is also progressing on schedule.

Reference

Shibanuma, K. et al., Assembly Study for JT-60SA Tokamak, Fusion Engineering and Design, vol.88, issues 6–8, 2013, p.705–710.

4–8 Progress in Predicting the Voltage Holding Capability for Large Negative Ion Source — Key Factor for High-Energy Accelerator toward JT-60SA and ITER —

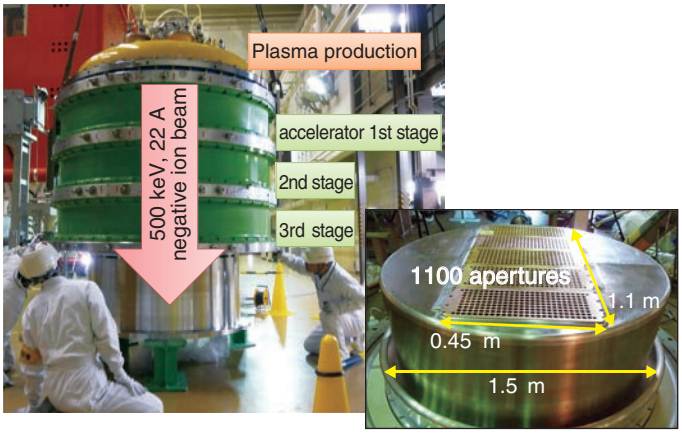

Fig.4-21 JT-60 negative ion source and acceleration grid
The JT-60 negative ion source is the largest negative ion source worldwide with a height of 1.8 m, a diameter of 2 m, and a weight of 6.5 t. It accelerates 500 keV, 22 A deuterium negative ion beams.

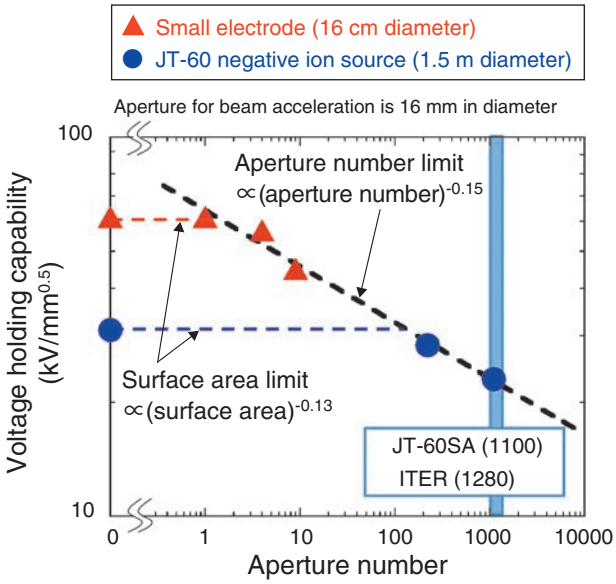

Fig.4-22 Relationship between aperture number and voltage holding capability
The voltage holding capability indicates the increase rate of the sustainable voltage with increasing gap length. Red and blue lines show the limits imposed by the surface area. Black line shows the limit imposed by the aperture number.

In fusion devices, high-energy deuterium beams (over several hundreds of keV) are required to drive the plasma current. To meet this requirement, a neutral beam injector based on a negative ion source (Fig.4-21) was developed for JT-60U and applied to plasma experiments for the first time worldwide. Recently, a beam energy of 500 keV was achieved by improving the voltage holding capability of an accelerator whose energy had been limited to below 400 keV.

The voltage holding capability of the accelerator is determined by the acceleration grids, which are characterized by a large number of apertures and a large grid size. A locally strong electric field is generated around the 1100 apertures on a wide surface 1.5 m in diameter in the JT-60 negative ion source, as shown in Fig.4-21. However, the voltage holding capability was designed on the basis of results obtained with a small electrode (0.2 m in diameter) without a locally strong electric field. The voltage holding capability with a locally strong electric field on a large grid has not been studied yet.

First, to investigate the weak points for voltage holding, we developed a visualization system for the breakdown positions. As a result, light emission accompanied by breakdowns was observed around the apertures; these breakdowns occurred at the 1100 apertures in random order. This led us to consider that the large aperture number might restrict the voltage holding capability. Next, the dependence of the voltage holding capability on the aperture number was investigated, as shown in Fig.4-22. In this figure, because the sustainable voltage depends on the square root of the gap length, the voltage holding capability is defined as the sustainable voltage normalized by the square root of the gap length. We found that the voltage holding capability depends on not only the size but also the number of apertures. This result also indicates that the voltage holding capability of the JT-60 negative ion source is limited by the aperture number.

The key point of the progress is the clarification of the breakdown positions that restrict the voltage holding capability. This result represents progress in the prediction of the voltage holding capability of the Satellite Tokamak Program (JT-60SA) and ITER ion sources. Moreover, it contributes to a better understanding in terms of the vacuum discharge between electrodes with a locally strong electric filed.

Reference

Kojima, A. et al., Vacuum Insulation of the High Energy Negative Ion Source for Fusion Application, Review of Scientific Instruments, vol.83, issue 2, 2012, p.02B117–1–02B117–5.

4–9 Realization of Compact Joint for Superconducting Coil

— Development of Butt Joint Technique for Central Solenoid of Fusion Device —

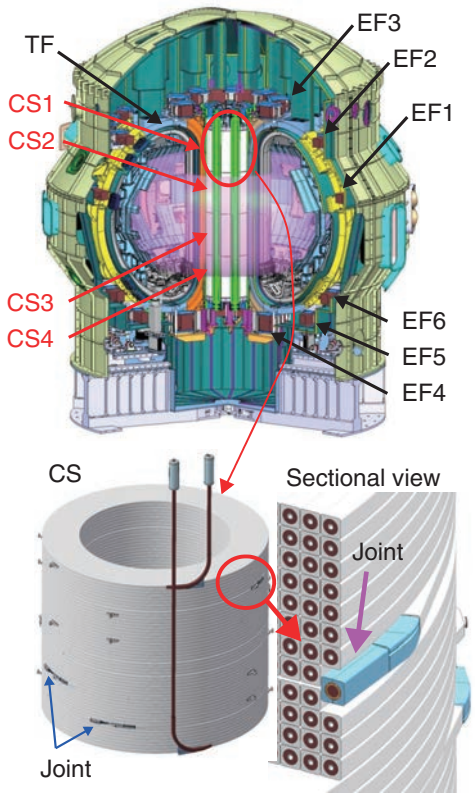

Fig.4-23 Superconducting coil system for JT-60SA and joint part for CS
The diameter of the CS could be maximized within the limited space by embedding the joint in the coil winding.

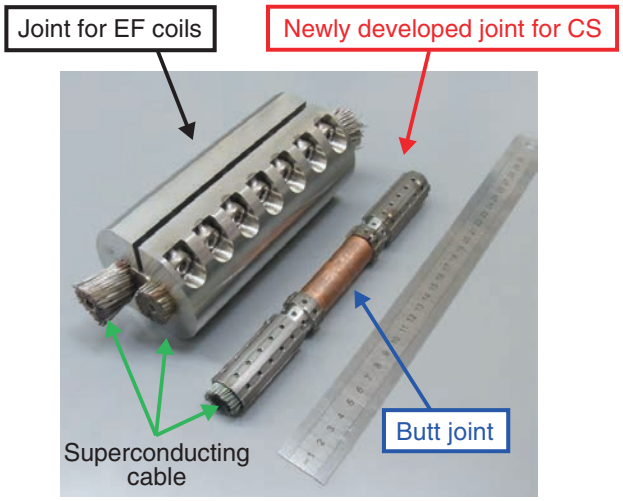

Fig.4-24 Comparison of joints
A compact joint could be attained by making a butt joint using diffusion bonding.

To obtain a high-performance plasma of long duration, a superconducting coil system is constructed for the Satellite Tokamak Program (JT-60SA). The system, which is one of the largest after ITER, consists of 18 D-shaped toroidal field (TF) coils, four stacks of central solenoids (CSs), and six plasma equilibrium field (EF) coils, as shown in Fig.4-23. The manufacturing of these coils is shared between Japan and Europe. Japan is manufacturing the superconductors for the CS and EF coils, and the CS and EF coils themselves. Italy is manufacturing the superconductors for the TF coils, and France and Italy are manufacturing the TF coils.

Because even the smallest coil needs >3 km of superconductor, the connection of superconductors through normal conducting copper after coil winding is essential. If the heat caused by electrical resistance at the joint is large, a superconducting state around the joint cannot be sustained, so the capacity of the cryoplant has to be increased. The required electrical resistance of the joint is <5 nΩ. The conventional joint adopted for the EF coils (Fig.4-24, left) is manufactured by overlapping the cables and soldering. However, the diameter of the CS, which induces the plasma current, had to be maximized as far as possible within the limited space, as shown in Fig.4-23. Therefore, the butt joint technique (Fig.4-24, right) was developed by improving the joint technique used for the ITER CS Model Coil. The newly developed device can connect superconductors after coil winding and can locate joints in the coil winding. The butt joint is obtained by diffusion bonding with 30 MPa of bonding pressure and heat treatment at 650 °C. A joint sample made by this technique was fabricated and tested. The joint sample reached 2 nΩ (<5 nΩ) of electrical resistance under the most severe operational condition of 2 T, 7 K, and 20 kA. Because all the manufacturing processes were confirmed, mass production of CSs was started.

Reference

Kizu, K. et al., Development of Central Solenoid for JT–60SA, IEEE Transactions on Applied Superconductivity, vol.23, no.3, 2013, p.4200104–1–4200104–4.

4–10 Clarification of Hydrogen Isotope Dependence of Plasma Heat Diffusion
— Contribution to the Prediction of Fusion Power in ITER —

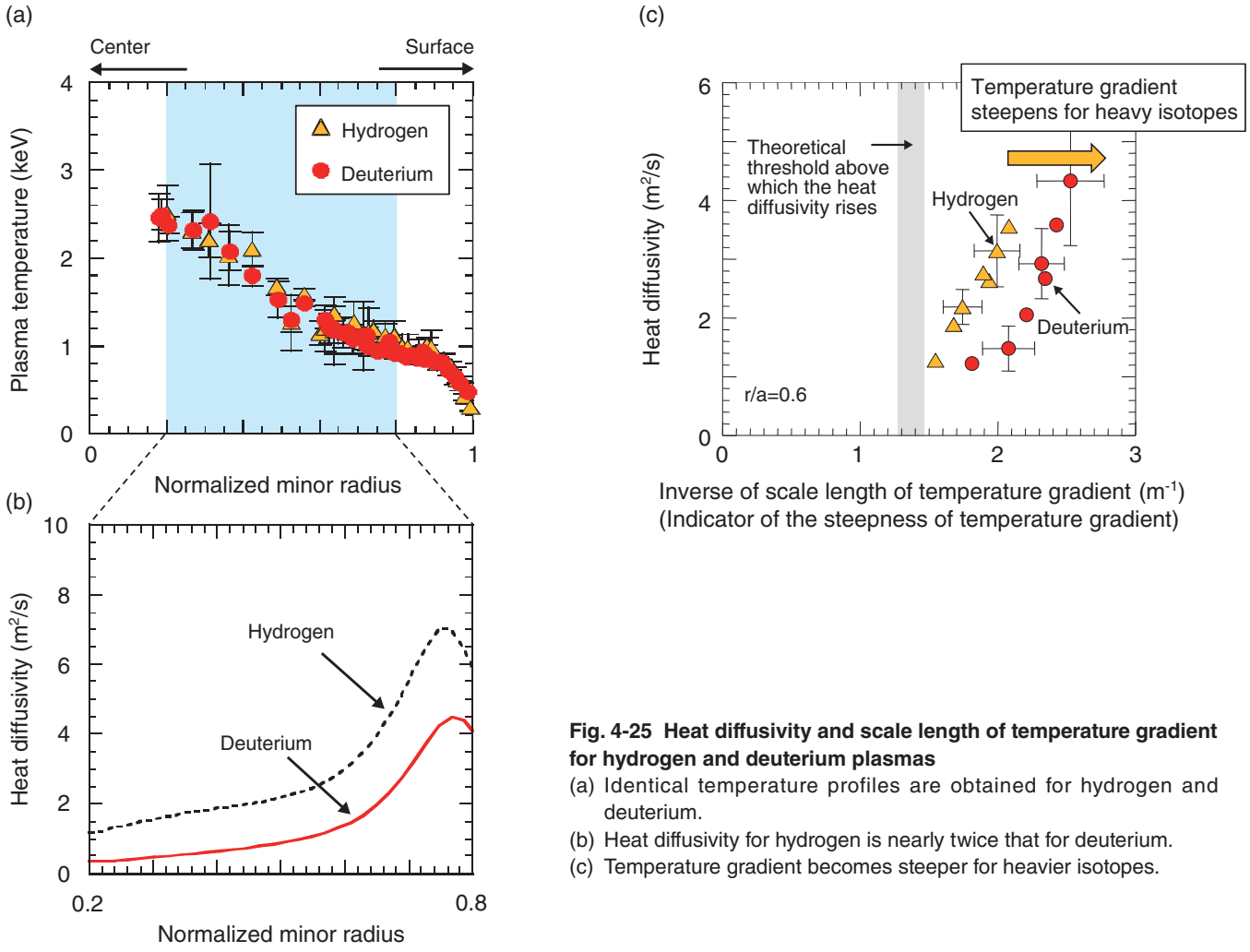

Fig. 4-25 Heat diffusivity and scale length of temperature gradient for hydrogen and deuterium plasmas
(a) Identical temperature profiles are obtained for hydrogen and deuterium.
(b) Heat diffusivity for hydrogen is nearly twice that for deuterium.
(c) Temperature gradient becomes steeper for heavier isotopes.

For a fusion reactor, the physical processes of heat and particle diffusion have been intensively studied. Specifically, next-step devices such as ITER will operate in burning plasma using tritium. However, current fusion research generally treats hydrogen or deuterium. Therefore, it is a critical issue to clarify the effects of hydrogen isotopes on the process of plasma heat diffusion.

In JT-60, the effects of the isotopes of hydrogen and deuterium on the heat diffusion process have been examined. As a result, identical temperature profiles were obtained for hydrogen and deuterium, as shown in Fig.4-25(a). However, the hydrogen case requires nearly twice the heating power of the deuterium case to sustain this temperature profile. In other words, the heat diffusivity for hydrogen is nearly twice that for deuterium, as shown in Fig.4-25(b). It is known that, when the plasma heating power is increased, the temperature gradient in the plasma core becomes larger and eventually drives an instability that rapidly enhances the heat diffusion at its threshold. In this case, owing to its large heat diffusivity, the temperature gradient is not changed greatly. However, it is not known how this characteristic of the heat diffusion depends on the hydrogen isotopes. This experiment revealed for the first time worldwide that the indicator of the steepness of the temperature gradient becomes larger for heavier isotopes, whereas the heat diffusivity becomes smaller for heavier isotopes if the temperature profiles are the same, as shown in Fig.4-25(c). This result indicates that the growth rate of the temperature-gradient-driven instability depends on the hydrogen isotopes.

This study has remarkably advanced the understanding of the physical process of heat diffusion. The result not only contributes to the prediction of the fusion power in ITER but also provides information for the design of the DEMO reactor.

Reference

Urano, H. et al., Small Ion–Temperature–Gradient Scale Length and Reduced Heat Diffusivity at Large Hydrogen Isotope Mass in Conventional *H*–Mode Plasmas, Physical Review Letters, vol.109, issue 12, 2012, p.125001–1–125001-5.

4–11 Fast Ion Transport Study Using HELIOS

— Fast Ion's Dance with Alfvén Waves in ITER Plasma —

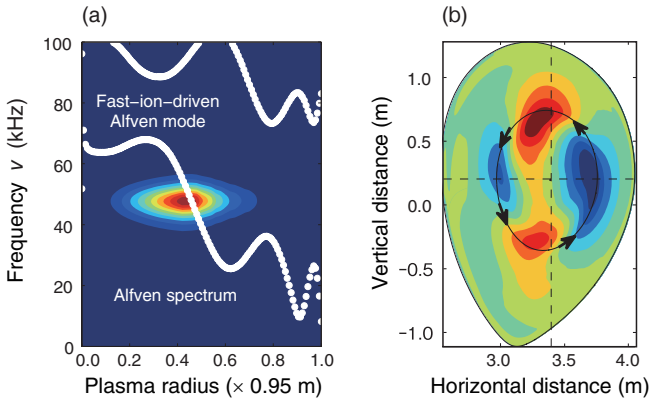

Fig.4-26 Properties of the fast-ion-driven Alfvén mode

(a) Radial profile and frequency. The radius is normalized by the volume-averaged plasma radius of 0.95 m. The mode frequency of 45 kHz is consistent with experimental data, in which mode activity in the 30–70 kHz range is observed, and lies precisely on the continuous Alfvén spectrum (white dots).

(b) Mode structure in the poloidal cross section of the torus. The mode has toroidal mode number 1, consistent with experimental results.

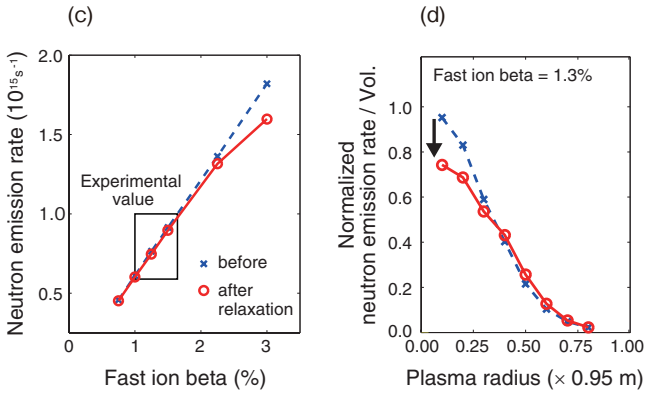

Fig.4-27 Effect on the neutron emission rate

(c) Dependence of the neutron emission rate on the fast ion beta. The box indicates experimental values, which are reproduced with beta values around 1%–1.5%.

(d) Radial profile of the neutron emission rate per unit volume, normalized by the central value of the initial profile Blue: initial, red: after relaxation. As in the experiment, the central value decreases by 25% when the initial fast ion beta used in the simulation is 1.3%. This is half the beta predicted by classical calculations without Alfvén waves.

ITER is an experimental reactor intended to create the conditions required to sustain nuclear fusion reactions that can serve as a source of energy. It will confine deuterium-tritium plasmas at 100 million degrees Celsius and produce neutrons and helium ions via fusion reactions. The helium ions are born with a kinetic energy 100 times larger than that of the bulk plasma and are used to heat it via collisions. However, the fast helium ions move with a rhythm that is similar to that of plasma waves called Alfvén waves, so they dance together and exchange energy. If the waves reach large amplitudes, the fast ions are pumped out of the confinement region. Thus, it is important to evaluate the fast ion transport.

Together with the National Institute for Fusion Science, we conducted simulations of fast ion transport using HELIOS, a supercomputer operated by the International Fusion Energy Research Center. The simulation model was validated by simulating scenarios from the JT-60U fusion experimental device and by comparing the results with experimental data. To mimic the ITER conditions in JT-60U, energetic deuterium ions were introduced by powerful beams. The fast ions were observed to drive intensive cyclic bursts of Alfvén wave activity. Because the bursting phenomena depend on the form of the fast ion distribution in phase space, a novel method was developed that allows us to initialize simulations with fast ion distributions computed by an orbit-following Monte Carlo code for realistic beam geometry and collisions.

The simulation results show that the frequency and mode number of the instability, which triggers profile relaxation accompanied by the burst, are consistent with experimental observation (Fig.4-26). By varying the fast ion beta value, we obtained a value that reproduced the fast ion redistribution and the resulting changes in the neutron emission rate seen in experiments (Fig.4-27). In classical calculations, the total neutron emission rate is overestimated because Alfvén wave activity is not taken into account. Our simulations indicate that the true value of the confined fast ion beta is about a factor of two lower.

This work was partially supported by a Japan Society for the Promotion of Science (JSPS) KAKENHI Grants-in-Aid for Scientific Research (No.22860081, No.23360416, No.25820443).

Reference

Bierwage, A. et al., Role of Convective Amplification of n =1 Energetic Particle Modes for N–NB Ion Dynamics in JT–60U, Nuclear Fusion, vol.53, no.7, 2013, p.073007–1–073007–12.

5 Quantum Beam Science Research

Research & Development on Quantum Beam Technology

"Quantum beam" is a generic name for neutron beams, ion beams, electron beams, high-intensity lasers, and synchrotron X-rays, which are generated by accelerators, high-intensity laser facilities, and research reactors. Recently, quantum beam technology has been developed considerably, with the most advanced manufacturing and observations being performed using highly controlled quantum beams.

Quantum beams function as probes in observations of atomic- or molecular-level information by control of the beam parameters. They also allow us to process materials at the nanometer level (i.e., the atomic or molecular level) by interacting with the constituent atoms of a material to change their configuration, composition, and electronic state. In medical applications, they are used for radiotherapy, in which a beam is focused on a cancer cell (Fig.5-1).

We own various quantum beam facilities, such as JRR-3 and J-PARC (Tokai area), TIARA, electron beam and γ-ray irradiation facilities (Takasaki area), J-KAREN and other lasers (Kizu area), and the SPring-8 beamlines (Harima area). We have been conducting research and development (R&D) on advanced beam technology and promoting a variety of fundamental and applied research studies in various fields (materials science, environment and energy, medicine and biotechnology) by using the creating and probing functions of quantum beams. In this chapter, we introduce our recent research topics related to advanced beam technology and the application of quantum beams to those fields (Fig.5-2).

In addition, we are contributing to the recovery from the accident at the Tokyo Electric Power Company, Incorporated Fukushima Daiichi Nuclear Power Station, for example, by developing improved decontamination materials (Chapter 1, Topic 1-9).

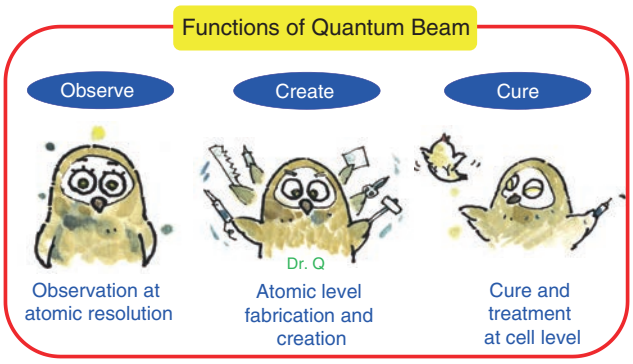

Fig.5-1 Characteristics of quantum beams

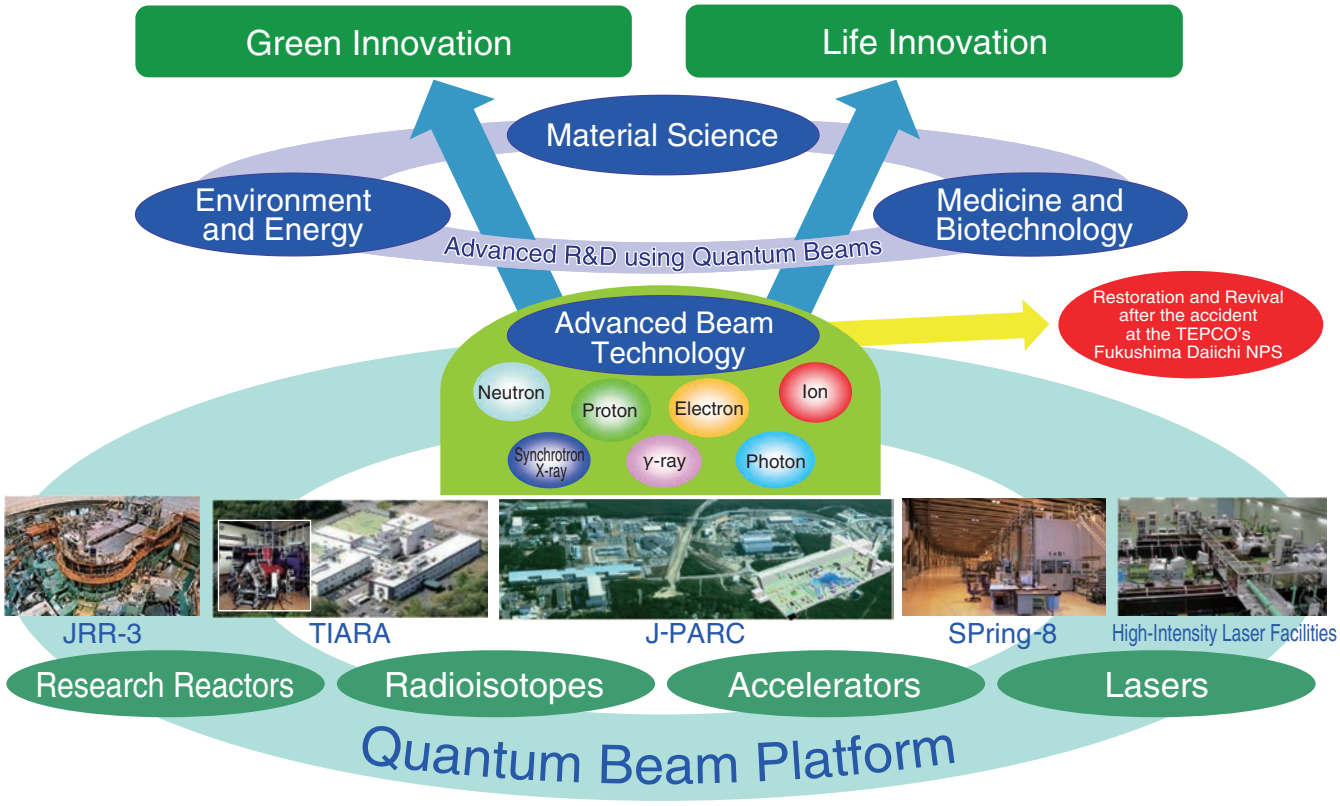

Fig.5-2 Quantum beam facilities in Japan Atomic Energy Agency

5–1 Enhancement of Thermal Stability of Nanocomposites

— The Role of Nano-Additives on Order-Disorder Transition of Nanocomposites —

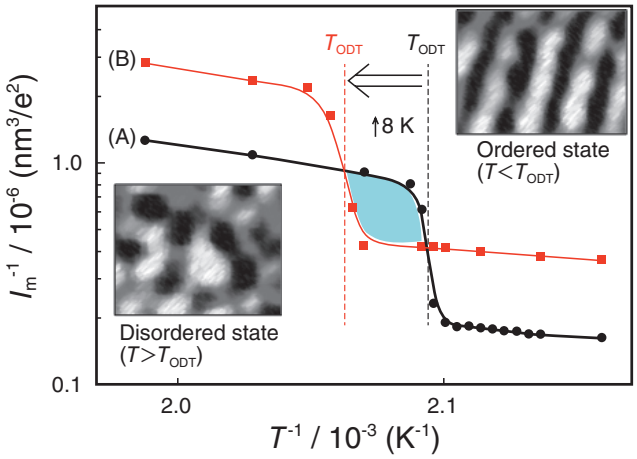

Fig.5-3 Effect of $(Pd)_n$s on ODT
I_m^{-1} plotted as a function of T^{-1} for *A* (neat PS-*b*-PMMA) and *B* (nanocomposite). T_{ODT} is defined as the temperature at the discontinuous change in I_m^{-1}. Black and bright patterns are transmission electron microscopy images of the bcp template in the disordered and ordered states, respectively.

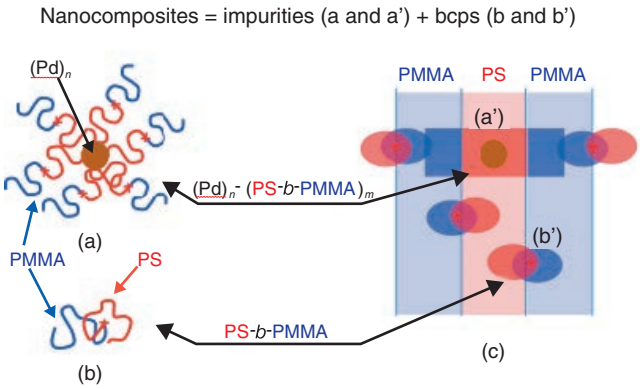

Fig.5-4 Interpretation of how $(Pd)_n$s increase T_{ODT}
(a) Single $(Pd)_n$ tethered by *m* PS blocks, $(Pd)_n$-(PS-*b*-PMMA)$_m$, and (b) single PS-*b*-PMMA chain, and their respective coarse-grained models (a') and (b') for their chain conformations and spatial segment distributions in the field of the lamellar template (c). The impurities (a') serve as anchors to thermally stabilize the template made by the major component (b').

Nanocomposites made of block copolymer (bcp) templates and nano-additives have attracted much attention because bcps are well known to organize into diverse multiphase structures with nanoscale periodicity, and the incorporation of nano-additives is of great importance for manufacturing optoelectronic and mechanical devices. The nano-additives incorporated into bcps perturb the nature of the order-disorder transition (ODT) and the ODT temperature (T_{ODT}), which influences the thermal stability of the nanocomposites. Thus, the nanocomposite is thermally tunable, which might offer technological opportunities in the future. In this research, we describe how the incorporation of palladium nanoparticles, $(Pd)_n$s, into a lamella-forming poly(styrene)-*block*-poly(methyl methacrylate) (PS-*b*-PMMA) alters its ODT.

$(Pd)_n$s were incorporated into a PS-*b*-PMMA template by thermal reduction of $Pd(acac)_2$ at 403 K. The ODT behavior of the neat bcp and the nanocomposites was investigated by small-angle X-ray scattering as a function of temperature (*T*). The plot of the inverse scattering intensity maximum (I_m^{-1}) vs. T^{-1} in Fig.5-3 indicates that the incorporation of ~1 wt% of $(Pd)_n$s is sufficient to increase T_{ODT} by 8 K. This finding should be attributed to the fact that $(Pd)_n$s increase the effective segregation power between the PS and PMMA block chains; a proposed explanation for this is selectively better incorporation of $(Pd)_n$s into PS lamellae (~70 wt%) than into PMMA lamellae (~30 wt%). As illustrated in Fig.5-4, the attractive interactions bind some of the PS block chains to the surface of $(Pd)_n$s and form impurities of $(Pd)_n$-(PS-*b*-PMMA)$_m$ (a, a') against neat bcps (b, b') inside the lamellar template (c). The impurities serve as anchors that suppress Brownian motion of the bcp chains in the template both parallel and normal to the interfaces; hence, they thermally stabilize the lamellae and increase T_{ODT}.

Most importantly, the addition of $(Pd)_n$s to the bcp template, as a strongly correlated system normal to the interface, is evidently able to change the ODT significantly, which offers new opportunities for the development of these nanocomposites.

Reference

Zhao, Y. et al., Order–Disorder Transition of Nanocomposites: Polystyrene–*block*–Poly(Methyl Methacrylate) with Palladium Nanoparticles, Macromolecules, vol.46, 2013, p.957-970.

5–2 Quantitative Analysis of Conformational Changes in Proteins upon DNA Binding

— Toward an Understanding of the Molecular Mechanisms of Protein-DNA Recognition —

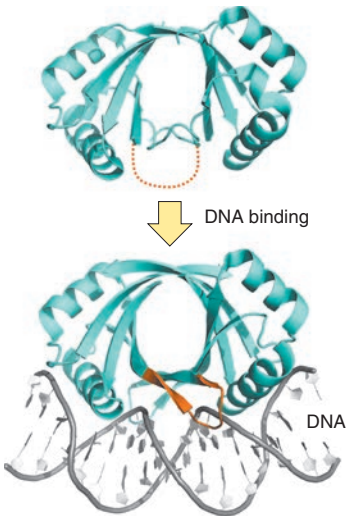

Fig.5-5 Conformational changes in bovine papillomavirus E2 protein upon DNA binding
Cervical cancer is caused by infection with papillomaviruses. This E2 protein is directly involved in viral DNA replication. When this protein binds to DNA, an unstructured region (in orange) in DNA-free form adopts a stable conformation so that it can bind to DNA.

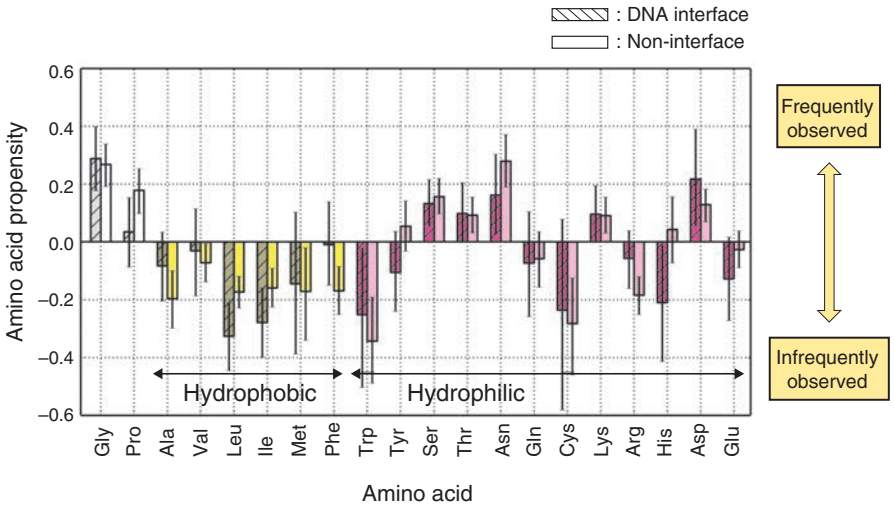

Fig.5-6 Propensities of amino acid residues in conformationally changed fragments
A positive propensity value indicates that an amino acid is observed more frequently in conformationally changed fragments than in conformationally unchanged fragments. Conformationally changed fragments in DNA interfaces and non-interfaces have high amounts of glycine (Gly), proline (Pro), and hydrophilic residues. Error bar indicates statistical uncertainty.

Protein synthesis is controlled by DNA-binding proteins that bind to specific sites in genomic DNA. Therefore, to understand the fundamentals of gene regulation, it is important to elucidate the molecular mechanisms by which DNA-binding proteins recognize specific DNA targets.

Structural studies of DNA-bound as well as DNA-free forms have been conducted to clarify the molecular mechanisms of individual DNA-binding proteins. However, the generic mechanisms of protein-DNA recognition are not yet fully understood.

It is often reported that the DNA interfaces of proteins undergo conformational changes in order to recognize specific DNA targets (e.g., Fig.5-5), but the changes are likely to depend on individual proteins. To assess the structural rearrangement quantitatively, we developed a new method. In this method, protein structures are described as a one-dimensional string of letters. Each letter expresses the conformation of a contiguous four-residue fragment. This enables us to rapidly compare structures and detect the conformational changes in proteins. Using this method, we analyzed a set of proteins whose structures were solved in both DNA-free and DNA-bound forms.

We found that DNA interfaces have higher conformational flexibility than non-interfaces, and that conformationally changed fragments in DNA interfaces have a large amount of glycine, proline, and hydrophilic residues (Fig.5-6). Those residues have previously been observed in intrinsically disordered regions. These characteristics of the amino acids indicate that DNA interfaces evolve to have amino acids that can exhibit high flexibility for accommodating DNA conformations.

DNA recognition by proteins is one of the fundamental processes in gene regulation. Our findings may contribute to the development of a method that accurately predicts DNA binding sites in proteins. Such information can be used to develop drugs that prevent proteins from binding to their target DNA.

Reference

Sunami, T. et al., Local Conformational Changes in the DNA Interfaces of Proteins, PLOS ONE, vol.8, issue 2, 2013, p.e56080–1–e56080–12.

5–3 Clear Imaging of Tumor with D-Amino Acid

— Development of a Novel Amino Acid Tracer, D-[^{18}F]FAMT, for PET Diagnosis of Cancer —

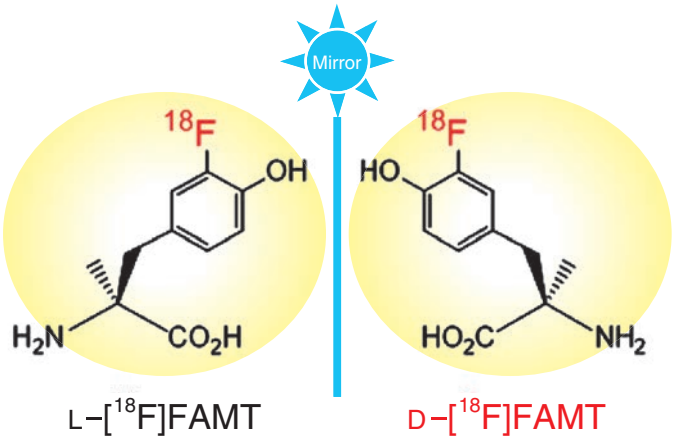

Fig.5-7 Structure of L-[^{18}F]FAMT and D-[^{18}F]FAMT
L-[^{18}F]FAMT (left) and D-[^{18}F]FAMT (right) are enantiomers of each other. Their structures are mirror images of each other, as in the relationship between the left and right hands.

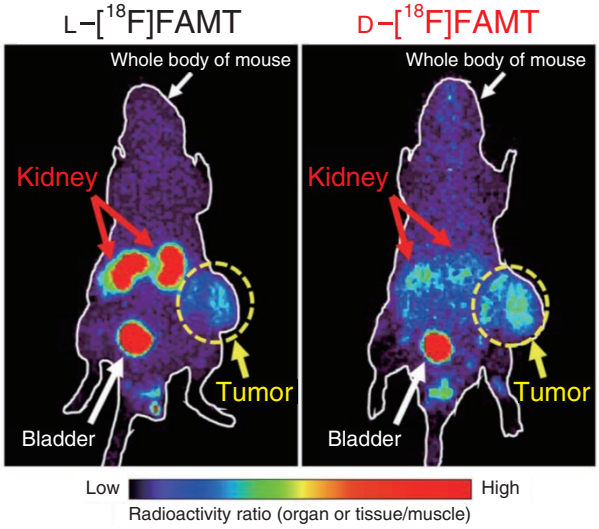

Fig.5-8 Comparison of images with L-[^{18}F]FAMT and D-[^{18}F]FAMT
In the image with L-[^{18}F]FAMT (left), renal accumulation was high and the tumor contrast was low, whereas, in the image with D-[^{18}F]FAMT (right), the renal accumulation was low and the entire tumor was clearly imaged. (The same mouse was used for all PET imaging.)

Diagnosis with positron emission tomography (PET) is a useful tool for understanding the physiological status of cancer, as well as for early detection. In PET diagnosis, γ-rays emitted from the patient are quantitatively detected outside of the body after the injection of PET tracers, and reconstructed images are used for diagnosis. 3-[^{18}F]fluoro-α-methyl-L-tyrosine (L-[^{18}F]FAMT), an amino acid derivative, is clinically used for definitive diagnosis because it is selectively taken up by malignant tumors. However, because L-[^{18}F]FAMT is also accumulated and retained in the kidney and pancreas, it exhibits slow clearance from the blood. Therefore, the border between a malignant tumor and benign tissue in the images is unclear, making it hard to distinguish the region of the tumor accurately. For accurate diagnosis, we aimed to develop a new tracer that enables clear visualization of tumors by improving the non-specific accumulation and retention of L-[^{18}F]FAMT.

The new tracer should have a low affinity to both renal and pancreatic cells. The chemical structure is generally modified to avoid uptake into the cells. However, we thought that accumulation and retention in the kidney and pancreas could be suppressed while retaining the advantage of L-[^{18}F]FAMT, not by modification of the chemical structure, but by using the fact that D-amino acids, the enantiomers of L-amino acids, rarely accumulate in normal tissue and are rapidly excreted from the kidney to urine. Consequently, we developed 3-[^{18}F]fluoro-α-methyl-D-tyrosine (D-[^{18}F]FAMT) (Fig.5-7).

Biodistribution studies in tumor-bearing mice showed that D-[^{18}F]FAMT rapidly cleared from the blood, and less of it accumulated in the kidney and pancreas, compared to L-[^{18}F]FAMT. Although the amount of D-[^{18}F]FAMT in the tumor was reduced, the tumor-to-blood ratio of D-[^{18}F]FAMT was higher than that of L-[^{18}F]FAMT. PET imaging with D-[^{18}F]FAMT showed high tumor-to-background contrast and low accumulation in the kidney, indicating that D-[^{18}F]FAMT could exhibit lower renal accumulation and enable clear visualization of the tumor (Fig.5-8).

If PET using D-[^{18}F]FAMT is widely applied, cancer therapy based on more accurate diagnosis would be expected. Furthermore, D-[^{18}F]FAMT would be an effective tracer for renal and pancreatic cancer, which cannot be detected using L-[^{18}F]FAMT. In the future, we will perform a toxicological analysis of D-[^{18}F]FAMT to support practical application.

Reference

Ohshima, Y. et al., Biological Evaluation of 3–[^{18}F]Fluoro–α–Methyl-D–Tyrosine (D–[^{18}F]FAMT) as a Novel Amino Acid Tracer for Positron Emission Tomography, Annals of Nuclear Medicine, vol.27, no.4, 2013, p.314–324.

5–4 Use of Diamonds for Single Ion Detection

— Real-Time Detection of Ion Impact Position by Fluorescence of Nitrogen Vacancy Centers —

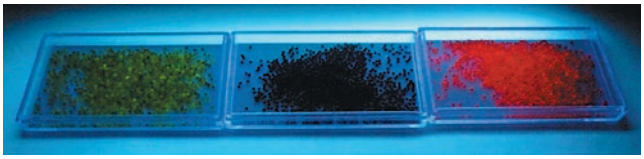

Fig.5-9 Photograph of diamonds irradiated by ultraviolet light
Photographs of diamonds containing dense nitrogen (left), electron-irradiated diamonds (middle), and diamonds containing NV centers after thermal treatment (right). The colors are peculiar to the impurities and defects.

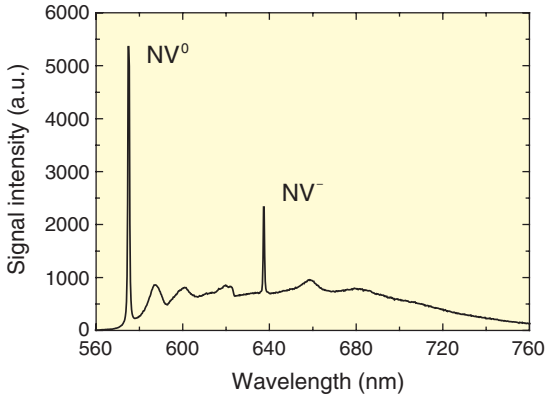

Fig.5-10 Photoluminescence spectrum of created NV center
After electron irradiation and thermal treatment, the diamonds contain electrically neutral NV^0 centers and negatively charged NV^- centers.

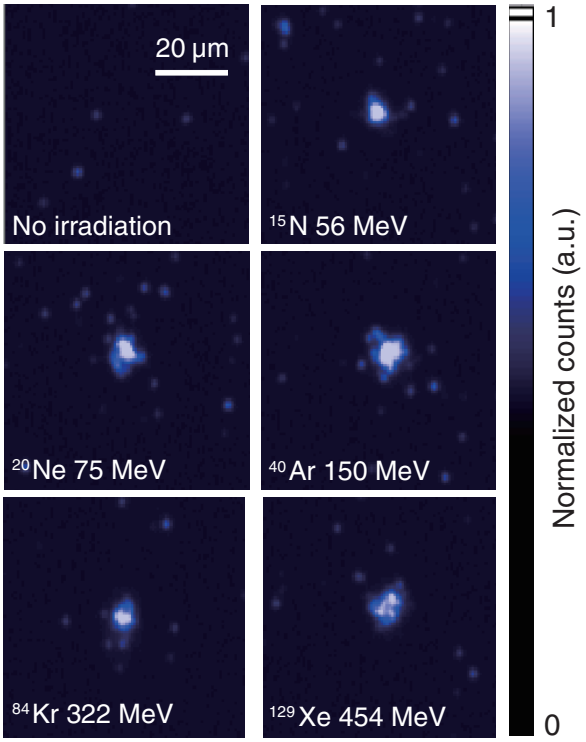

Fig.5-11 CCD images when an ion strikes a diamond
When an ion strikes a diamond containing NV centers, the very weak luminescence light from the ion impact position is successfully detected.

A single ion causes temporary malfunctions and permanent failures in semiconductors, which are called single event effects (SEEs). To use semiconductors in harsh radiation environments such as space, it is necessary to clarify the mechanism of SEEs. This requires a technique for detecting a single ion in real time. The technique of detecting the position of fluorescence induced by a single ion on a luminescent sheet is currently used. Therefore, we are exploring a luminescent sheet having strong fluorescence intensity capable of detecting a single ion. In this study, we focus on the features of nitrogen-vacancy defects (NV centers), which efficiently absorb ultraviolet light and emit high-intensity fluorescence.

First, diamonds containing dense NV centers were created from synthetic diamonds containing dense nitrogen impurities. By irradiating the sample with a 2 MeV electron beam, vacancies were introduced into the diamond by the displacement damage mechanism. After electron irradiation, thermal treatment at 800 °C was performed for 2 h. By combining nitrogen impurities with vacancies, we successfully created a diamond containing dense NV centers (Fig.5-9). Photoluminescence spectrum analysis clearly revealed that electrically neutral NV^0 centers and negatively charged NV^- centers were created (Fig.5-10). As shown in the figure, additional defects other than NV centers were not found. Next, the sample was irradiated with several ions at various energies. A measurement system consisting of a highly sensitive CCD camera and an image intensifier was developed. Using the system, fluorescence was successfully detected in real time (Fig.5-11). The spots are detected in the diamonds containing NV centers, but not in those without NV centers. This result is regarded as demonstrating a fundamental technology for elucidating the mechanism of SEEs that reduce the reliability of semiconductors.

This work was partially supported by the Strategic Japanese–German Joint Research Program of the Japan Science and Technology Agency (JST).

Reference

Onoda, S. et al., Diamonds Utilized in the Development of Single Ion Detector with High Spatial Resolution, Transactions of the Materials Research Society of Japan, vol.37, no.2, 2012, p.241–244.

5–5 Toward Nondestructive Assay of Fissile Materials
— Generation of 500 keV Electron Beam from DC Photoemission Gun —

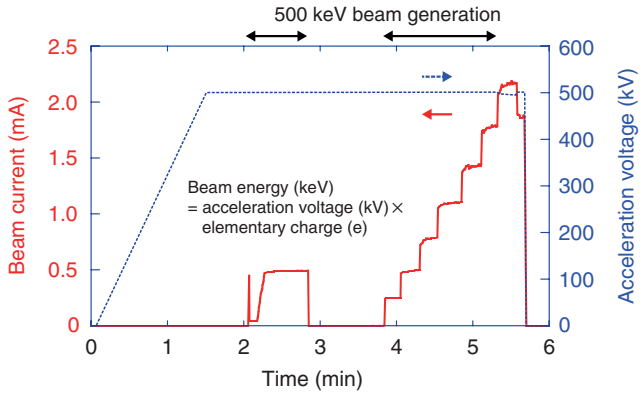

Fig.5-12 Generation of a 500 keV electron beam
A DC photoemission gun generates an electron beam upon laser irradiation. The black arrows represent the periods where a 500 keV electron beam was generated. The blue dashed line represents acceleration voltage; and the red solid line, the beam current.

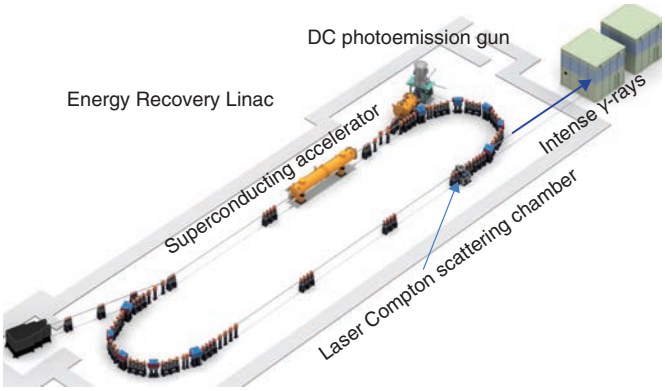

Fig.5-13 γ-ray source based on energy recovery linac
An energy recovery linac is under development at KEK. The accelerated electron beam is delivered to the Compton scattering chamber for γ-ray generation. A proof–of-principle experiment for the proposed nondestructive isotope identification will be conducted next year.

The quantification of fissile materials such as uranium-235 (^{235}U), plutonium-239 (^{239}Pu), and minor actinides in spent fuel assemblies requires isotope-specific identification. We propose the use of nuclear resonance fluorescence (NRF) to identify the isotopic composition of sample materials nondestructively. A mono-energetic γ-ray beam tuned to the resonance state of the target nuclear isotope is injected into the spent fuels, and NRF γ-rays generated spherically from the fuels are detected with a γ-ray detector.

The proposed nondestructive isotope identification system requires a high-intensity mono-energetic γ-ray beam. Although a mono-energetic γ-ray beam can be generated using a conventional laser Compton scattering technique, the generation of a high-intensity γ-ray beam requires an electron beam of unprecedentedly high brightness, which can be generated with an advanced accelerator system known as the energy recovery linac (ERL). A technological challenge of the ERL system, which we have addressed, is the development of a high-brightness, high-current electron gun.

The generation of high-brightness beam requires a gun exit energy of $\geqq$ 500 keV to avoid the beam degradation that occurs due to nonlinear space charge effect. The gun operational voltage has, however, been limited to 350 keV because of a discharge problem. We have successfully solved this problem by employing a segmented insulator and optimizing the gun configuration.

Fig.5-12 shows the result of a beam generation test. The electron beam is generated upon laser irradiation. The beam current is proportional to the laser power. As shown in the figure, we successfully generated a 500 keV electron beam with a current of up to 2 mA.

The gun was recently moved to the compact ERL (cERL) facility at KEK, where it is connected to an adjoining superconducting accelerator, as shown in Fig.5-13. Mono-energetic γ-ray generation using Compton scattering will be commenced next year.

This work was supported by the Ministry of Education, Culture, Sports, Science and Technology of Japan (MEXT), Quantum Beam Technology Program, “Development of a next-generation compact, high-brilliance light source using superconducting accelerator technology” and partially supported by the Japan Society for the Promotion of Science (JSPS) KAKENHI Grant-in-Aid for Scientific Research (C) No.23540353, “Study of micro-bunching instability using sub-picosecond bunch measurement.”

Reference

Nishimori, N. et al., Generation of a 500–keV Electron Beam from a High Voltage Photoemission Gun, Applied Physics Letters, vol.102, issue 23, 2013, p.234103–1–234103-4.

5–6 Relativistic Harmonics from Tenuous Plasma

— Discovery of a New Compact Coherent X-ray Source —

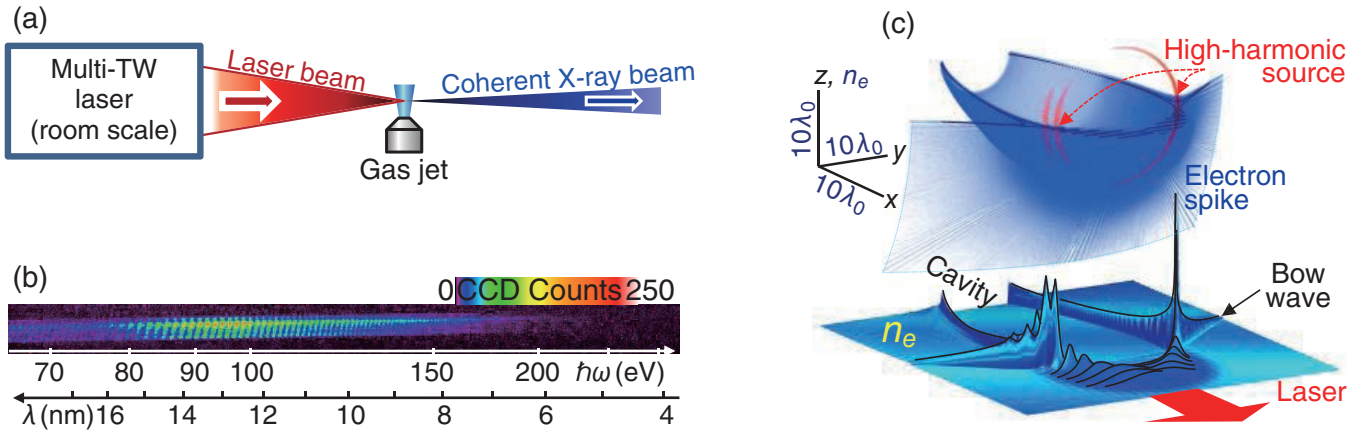

Fig.5-14 New regime of high-order harmonic generation by relativistic laser focused onto gas jet target
(a) Experimental setup. (b) Typical single-shot raw data. (c) 3D PIC simulations demonstrating electron density spike at the joint of the boundaries of the wake and bow waves and location of high-harmonic source.

Bright X-ray sources are necessary for fundamental research and applications in the life sciences, material sciences, nanotechnology, and other fields. The ultimate performance requires temporally and spatially coherent X-ray pulses that are compressible to the shortest durations, focusable to the tiniest spots, and capable of producing fine interference and diffraction patterns. Two broad classes of bright X-ray sources are available, those based on large-scale accelerators (synchrotrons, X-ray free-electron lasers) and those based on compact lasers (e.g., laser plasma X-ray emission, plasma-based X-ray lasers, atomic high-order harmonics, and betatron sources). The great advantages of the laser-based sources are their accessibility for university-scale laboratories and their ultrashort pulses with durations from picoseconds down to <100 as (10^{-16} s). However, because of fundamental limitations, it has been overwhelmingly difficult to achieve laser-based bright coherent X-ray sources with keV and especially multi-keV photon energies. Our aim is to develop a new generation of such sources to create new fields of fundamental research and applications.

We discovered a new regime of high-order harmonic generation by high-power (10–200 TW) relativistic irradiance (>10^{18} W/cm^2) femtosecond lasers (~30–50 fs) focused on gas jet targets, as shown in Fig.5-14(a). Comb-like spectra with hundreds of even and odd harmonic orders (Fig.5-14(b)), reaching a photon energy of 360 eV, including the "water window" spectral range, were generated by either linearly or circularly polarized pulses from the J-KAREN (KPSI, JAEA) and Astra Gemini (CLF, RAL, UK) lasers. A 120 eV harmonic contained up to 4 × 10^9 photons. Using particle-in-cell (PIC) simulations and mathematical catastrophe theory, we introduced a new mechanism of harmonic generation by sharp, structurally stable, oscillating electron spikes at the joint of the wake wave and bow wave boundaries, as shown in Fig.5-14(c).

Our compact bright coherent X-ray source can be built on a university-lab-scale repetitive laser and accessible, replenishable, and debris-free gas jet target. Importantly, the photon energy and number of photons are scalable with the laser power. This will affect many areas of fundamental research and applications requiring a bright X-ray/extreme ultraviolet source for pumping, probing, imaging, or attosecond science.

We acknowledge the financial support from the Japan Atomic Energy Agency (JAEA) (Research and Development Adjustment Funding for Exploratory Research, "Relativistic extreme ultraviolet harmonics from underdense plasma," 2009) and the Japan Society for the Promotion of Science (JSPS) [KAKENHI Grant-in-Aid for Young Scientists (B) No.23740413, "New high harmonic generation mechanism," 2011].

Reference

Pirozhkov, A.S. et al., Soft–X–Ray Harmonic Comb from Relativistic Electron Spikes, Physical Review Letters, vol.108, issue 13, 2012, p.135004–1–135004–5.

5–7 Heatproof Seismic Sensors Guard Aging Nuclear Power Plants
— Application of Femtosecond Laser Processing to Maintenance Study —

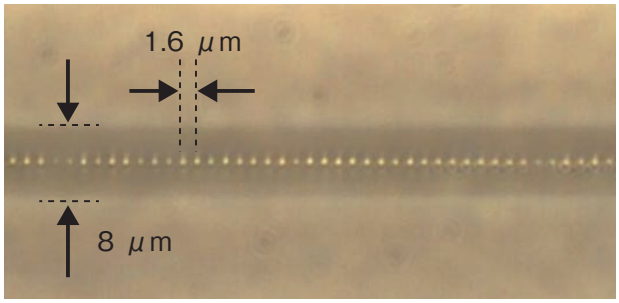

Fig.5-15 Fiber Bragg grating
Dots with 1.6 μm pitch along an optical fiber core 8 μm in diameter processed by femtosecond laser pulses.

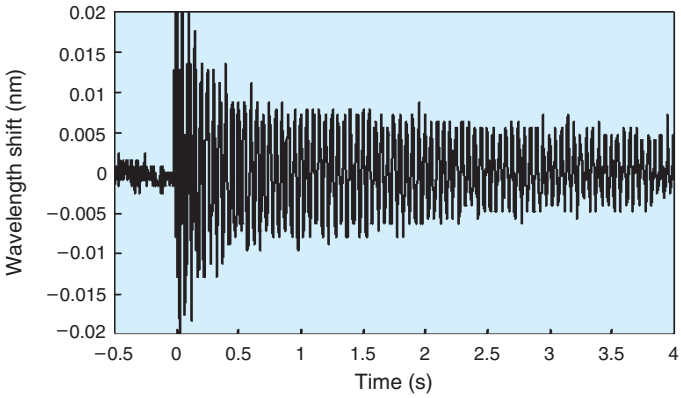

Fig.5-16 Vibration monitoring by FBG sensor
Damping oscillation of Cr in steel below 400 °C.

It is necessary to monitor the structural health of the coolant piping systems in operational nuclear power plants to reduce the risk of cracking accidents due to thermal expansion stress or intense seismic force. However, commercially available sensors cannot be used at the operational temperature of fast breeder reactors.

We successfully developed fiber Bragg grating (FBG) sensors by femtosecond laser processing that can realize index modulation along an optical fiber core. The reflectivity was enhanced at the wavelength that corresponded to the periodic spacing of the modulation. If the sensors are installed along pipe lines, the wavelength shift can tell us the deformation or oscillation caused by an intense external force. The high sensitivity ensures structural monitoring for not only extraordinary events but also daily operation.

When femtosecond laser pulses are focused inside silicate glass, the locally heated zone expands far beyond the melting point. After quenching, the central heated zone exhibits low density, whereas the outer zone exhibits high density. Thus, femtosecond laser processing, called the optical knife technique, can generate index modulation in glass material that can be maintained permanently below the melting temperature. The wavelength of ultraviolet lasers cannot be used because of the absorption in the clad glass around the surface. The pulse duration of nanosecond lasers is too long to produce thermal cracks in the fiber core. Only an infrared femtosecond laser can process the periodic dot that can act as the grating (Fig.5-15).

In addition, the most important technology for the installation of FBG sensors on the piping systems in nuclear power plants is reinforcement with heatproof fabric. Here we selected SiC fiber, which is strong enough to protect the optical fiber from degradation caused by heat and radiation. The combined optical fiber and SiC fabric successfully strengthen the sensor for handling. We found the appropriate temperature conditions for each heatproof epoxy and ceramic adhesive. The strengthened FBG sensor exhibited superior linearity from room temperature to 600 °C. Further, it demonstrated monitoring of the seismic vibration of a piping system below 400 °C (Fig.5-16).

Japan has many nuclear power plants and petrochemical complexes that were constructed during periods of strong economic growth. These facilities are now facing aging problems. We experienced a massive earthquake and huge tsunami on March 11, 2011. Now we should reconsider the possibility that more catastrophic massive earthquakes might hit Japan again in the near future. To maintain the piping systems in these aging facilities by sensing technology is one of the minimum obligations of the facilities managers.

Reference

Shimada, Y., Nishimura, A., Development of Optical Fiber Bragg Grating Sensors for Structural Health Monitoring, Journal of Laser Micro/Nanoengineering, vol.8, no.1, 2013, p.110–114.

5–8 How Does a Cocatalyst Enhance the Activity of the Oxygen Reduction Reaction?
— Improvement of Fuel Cell Performance —

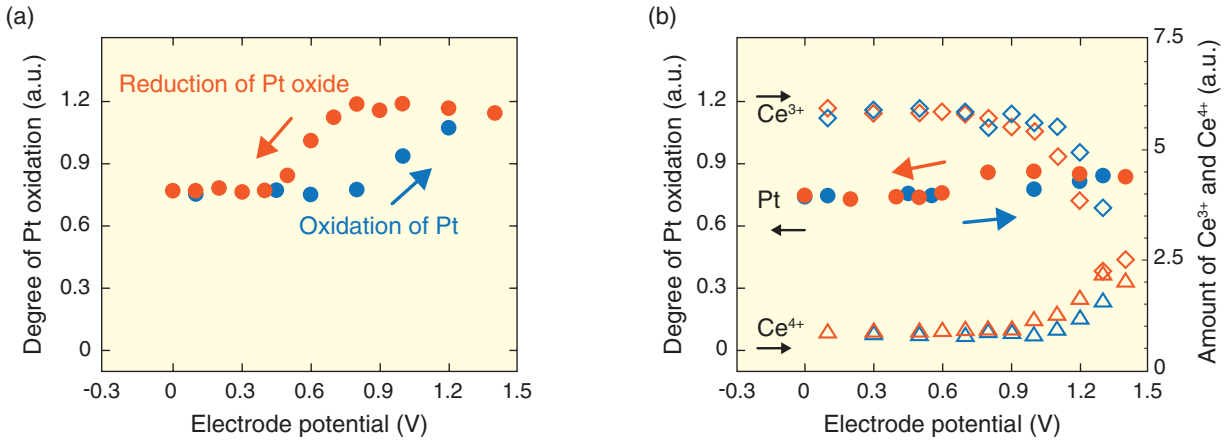

Fig.5-17 Oxidation status of Pt and Ce
Oxidation status of (a) Pt in the conventional Pt catalyst and (b) Pt and Ce in Pt–CeO_x nanocomposite catalyst. In the Pt–CeO_x nanocomposite catalyst, oxidation of the Pt surface is greatly suppressed. Blue and red data points correspond to positive- and negative-going scans, respectively.

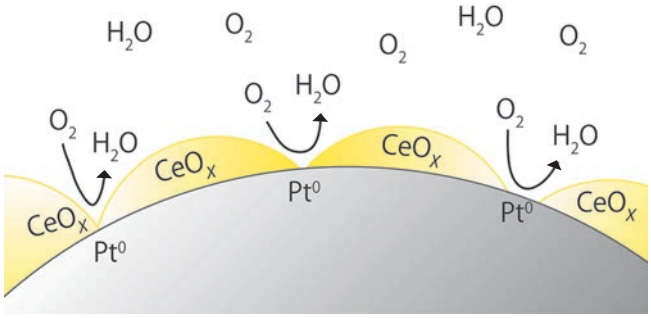

Fig.5-18 Schematic illustration of oxygen reduction reaction at the surface of the Pt–CeO_x nanocomposite
It was confirmed that oxidation of the Pt surface is suppressed by the CeO_x/Pt interface, and the intrinsic high catalytic activity remains enhanced.

The polymer electrolyte fuel cell (PEFC) is a clean and compact power generation system that can perform below 100 °C, can be miniaturized easily, and emits only water as exhaust. These features enable integration of the PEFC into automobiles and mobile electronic devices. On the other hand, the PEFC demands a large amount of an expensive precious metal (platinum, Pt), which limits its wide adoption. In the last decades, many studies for reducing the amount of Pt in PEFCs have been carried out. For example, high-performance electrode materials with efficiencies close to the theoretical value have been explored.

The Global Research Center for Environment and Energy based on Nanomaterials Science (GREEN) at the National Institute for Materials Science (NIMS) investigated the nanocomposite catalyst Pt–CeO_x, which exhibits higher oxygen reduction reaction (ORR) activity than the conventional Pt catalyst, and established its synthetic method. A joint research group comprising researchers from GREEN and JAEA investigated the role of cerium oxide in the Pt–CeO_x catalyst and elucidated the mechanism by which the ORR activity on the catalyst is enhanced.

To elucidate the valence of platinum and/or cerium atoms in the Pt–CeO_x catalyst and the conventional Pt catalyst under ORR, in situ X-ray absorption fine structure measurements were carried out at SPring-8. The results revealed that on the conventional Pt catalyst, a surface oxide began to form at the potential at which ORR starts to occur. However, on the Pt–CeO_x catalyst, Pt oxide formation was suppressed, but Ce^{3+} was oxidized to Ce^{4+} at the potential at which Pt is oxidized (Fig.5-17). These results suggest that on the Pt–CeO_x catalyst, charge transfer at the Pt/Ce interface occurs, and Ce^{3+} in the Ce oxide is oxidized instead of Pt (Fig.5-18). Previous studies reported that the Pt surface oxide reduces the ORR activity. Finally, it is concluded that the Pt–CeO_x catalyst exhibits intrinsic high ORR activity due to the suppression of Pt oxide formation.

Reference

Masuda, T., Tamura, K. et al., Role of Cerium Oxide in the Enhancement of Activity for the Oxygen Reduction Reaction at Pt–CeO_x Nanocomposite Electrocatalyst – An In Situ Electrochemical X–ray Absorption Fine Structure Study, The Journal of Physical Chemistry C, vol.116, issue 18, 2012, p.10098–10102.

5–9 Self-Assembled Structure of Coordination Species Clarified by Quantum Beam Techniques
— Development of Reprocessing Techniques by Elucidation of Solution States —

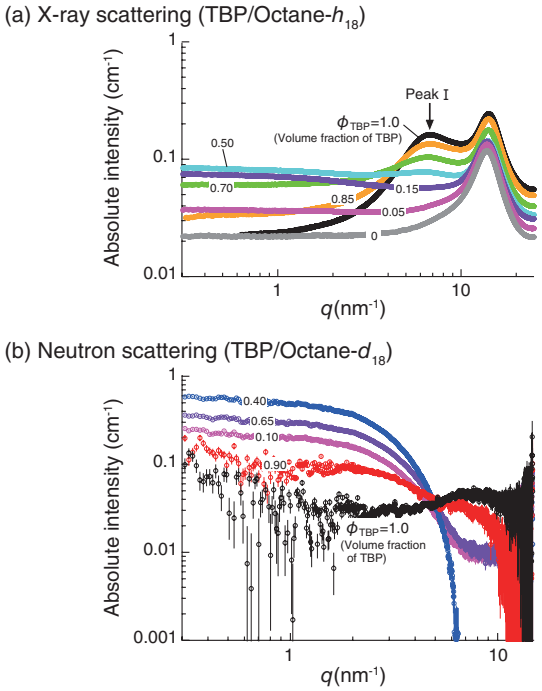

Fig.5-19 X-ray and neutron scattering profiles obtained for TBP/octane mixtures
Scattering maxima (peak I) arising from the intermolecular interactions of two TBPs were observed in (a), whereas in (b) the scattering contribution from the ellipsoidal ordered structure was observed at lower q.

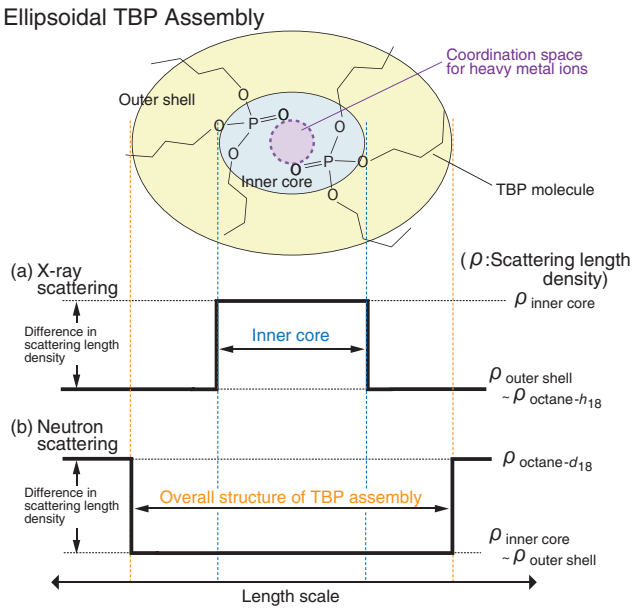

Fig.5-20 Diagram for scattering contrast and partial structure of ellipsoidal TBP assembly in X-ray and neutron scattering experiments
Schematic of TBP assembly, consisting of a hydrophilic inner core (light blue) and a hydrophobic outer shell (yellow), in octane, and schematic of the spatial distribution of scattering contrast (a) for X-rays across a TBP assembly in octane-h_{18} and (b) for neutrons across a TBP assembly in octane-d_{18}.

Tri-*n*-butyl phosphate (TBP) is an important extractant for separating hexavalent uranium, U(VI), and tetravalent plutonium, Pu(IV), from used nuclear fuel by solvent extraction. However, little was known on the structure and characteristic features of the TBP assembly and its coordination species with the heavy metal ions; thus, further study is needed to identify them. We aim to address these problems using scattering techniques; therefore, we collected X-ray and neutron scattering data for the TBP/octane mixtures as the first step of this study. As a result, we clarified the ordered structure formed by TBPs in octane.

In Fig.5-19(a), scattering maxima (peak I) due to the intermolecular interactions of two TBPs were clearly observed. It is evident that TBP forms a self-assembly in octane. In Fig.5-19(b), on the other hand, scattering from the overall structure of the assembly was observed at $q < 6.0$ nm^{-1}. This indicates that TBPs form an ellipsoidal ordered structure, as illustrated in Fig.5-20, where the inside core is capable of incorporating a heavy metal ion.

The diagrams in Fig.5-20 indicate that (a) with X-rays the scattering length densities of the hydrophobic butyl groups in TBP (ρ_{butyl}) and octane-h_{18} ($\rho_{octane\text{-}h18}$) are roughly equal to each other, but that of the hydrophilic phosphate ester of TBP ($\rho_{hydrophilic}$) is larger than those of both hydrocarbon chains; and (b) with neutrons, the difference in the scattering length density between the hydrophobic and hydrophilic parts of TBP (ρ_{butyl} and $\rho_{hydrophilic}$) is negligible as compared with the scattering length density of octane-d_{18} ($\rho_{octane\text{-}d18}$). Note that X-rays and neutrons, respectively, enable the scattering to be effectively observed from the inner core of the TBP assembly and from its overall structure, respectively. In fact, the q dependence of the obtained scattering profiles differs greatly between X-rays and neutrons, elucidating the structural and characteristic features of TBP assemblies.

The quantum beam technique is a powerful tool for investigating the microscopic structures of the various organic molecules and their coordination species with heavy metal ions. Anticipated applications include the development of not only fuel reprocessing but also diverse research topics such as the recycling of valuable metals from the waste products or the polluted solutions.

Reference

Motokawa, R. et al., Microscopic Structures of Tri–*n*–Butyl Phosphate/*n*–Octane Mixtures by X–ray and Neutron Scattering in a Wide q Range, The Journal of Physical Chemistry B, vol.116, issue 4, 2012, p.1319–1327.

5–10 Elucidation of Electronic Excitation in Novel High-T_c Superconductor

— Resonant Inelastic X-ray Scattering Study of Iron-Pnictide Superconductor —

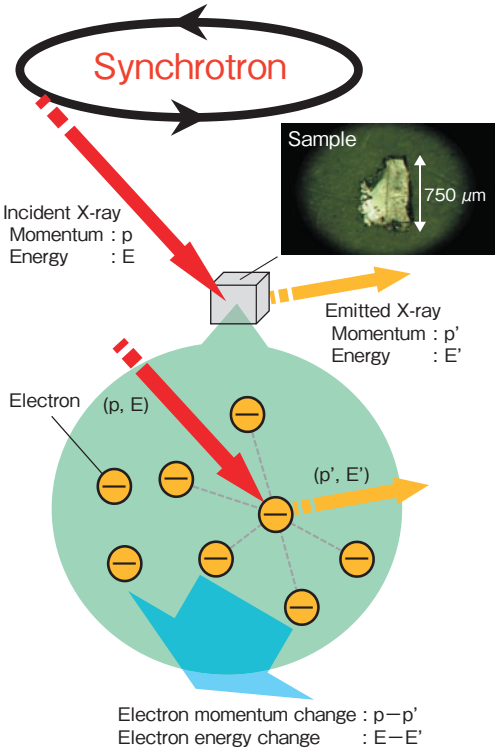

Fig.5-21 Schematic representation of RIXS
Systematic inspection of the momentum change and energy loss of X-rays in scattering enables us to study the momentum-dependent electronic excitation spectra.

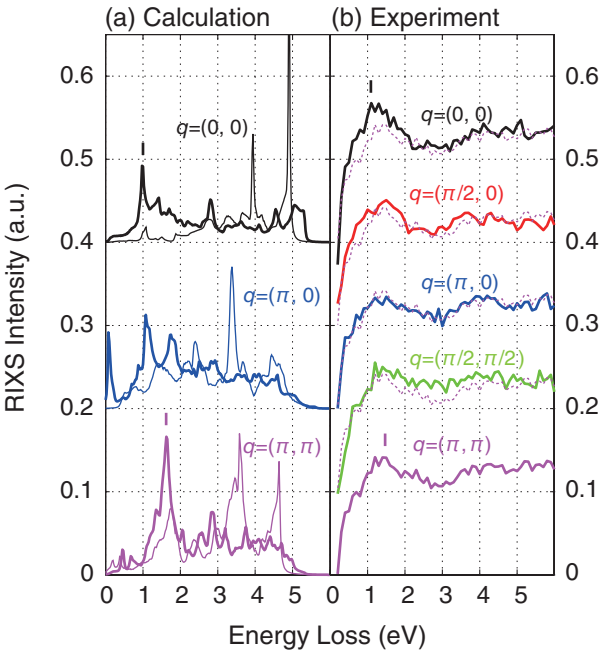

Fig.5-22 Calculated and experimental spectra
Theoretical calculation (left) was performed for non-magnetic and magnetic ground states (thin and thick lines, respectively). The experimental spectrum (right) at q = (π, π) (dashed line) is overlaid with the spectra at other momenta.

Quantum beams such as neutron beams and X-rays have been extensively used to clarify elementary excitations in various strongly correlated electron systems. A lot of studies using quantum beams have been intensively carried out for the recently discovered iron-pnictide high-T_c superconductors, to elucidate their superconducting mechanism.

Recently, resonant inelastic X-ray scattering (RIXS) utilizing the hard X-rays at transition-metal K-edges has become a unique technique to observe momentum-dependent charge excitation spectra of strongly correlated electrons. In K-edge RIXS, the incident X-ray with the 1s-4p absorption energy resonantly excites the 1s electron to the 4p state. In the final state, the excited 4p electron returns to the 1s state, emitting an X-ray, where the emitted X-ray loses momentum and energy in amounts equal to those transferred to the correlated electrons (Fig.5-21).

We recently succeeded in the first observation of RIXS for a typical iron-pnictide high-T_c superconductor $PrFeAsO_{1-y}$. The experimentally observed and theoretically calculated RIXS spectra for various X-ray momentum changes q's are displayed in Fig.5-22. We found a characteristic momentum-dependent low-energy feature around 1-2 eV, as indicated by the ticks in the right panel of Fig.5-22. To analyze the spectral properties, we also performed a theoretical calculation (left panel of Fig.5-22). From comparison between the calculated and experimental spectra, spectral shape and momentum dependence obtained experimentally agree well with the calculation by assuming the magnetically ordered state rather than the non-magnetic state. This suggests that at least short-range local magnetic correlations exist, consistently with other experiments. By further analysis, we also succeeded in verifying that the local Coulomb repulsion among the Fe 3d electrons should be intermediately strong (2-3 eV) in the present iron-pnictide superconductor. This evaluation of electron correlation could play a key role in discussions of the microscopic mechanisms of the iron-pnictide high-T_c superconductivity.

Reference

Jarrige, I., Nomura, T. et al., Resonant Inelastic X-ray Scattering Study of Charge Excitations in Superconducting and Nonsuperconducting $PrFeAsO_{1-y}$, Physical Review B, vol.86, issue 11, 2012, p.115104-1-115104-4.

Evaluation of the Safety of Various Nuclear Facilities

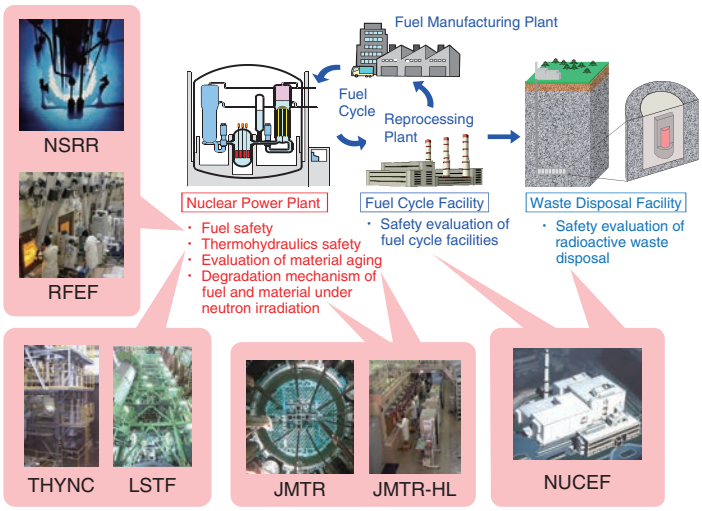

Fig.6-1 Nuclear safety research areas and related JAEA facilities
The NSRC experimentally obtains data using various Japan Atomic Energy Agency (JAEA) facilities. These data for risk assessment and safety evaluation of nuclear facilities contribute internationally to the development of evaluation methods and criteria.

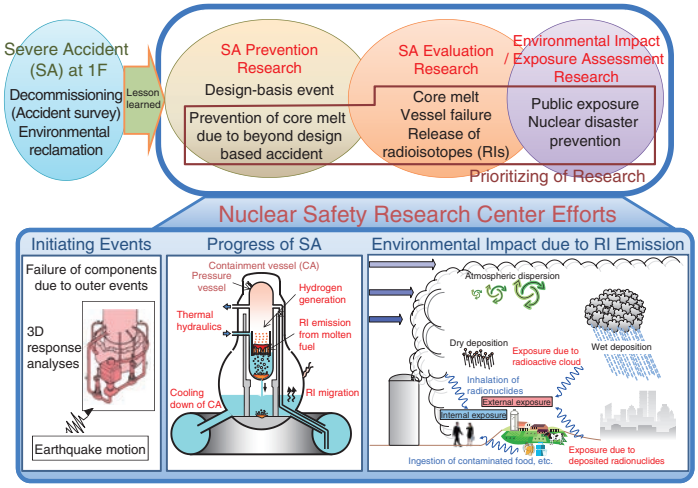

Fig.6-2 Future directions of nuclear safety research
In accordance with lessons learned from the accident at 1F, in addition to safety assessments within design basis events, we will conduct research with a priority on severe accident prevention efforts and nuclear emergency preparedness activities such as environmental impact assessments.

The possibility of serious accidents in nuclear installations and their consequences have been studied at the Nuclear Safety Research Center (NSRC) to ensure the safe use of current nuclear facilities. A massive and severe accident occurred at the Tokyo Electric Power Company, Incorporated Fukushima Daiichi Nuclear Power Station (1F) as a result of the Great East Japan Earthquake and tsunami. The NSRC has been collaborating with the Japanese government to institute appropriate emergency response procedures based on research findings and developments. Most specialists at the NSRC regret that they were unable to prevent the accident.

Continuous efforts should be made to avoid serious damage while we use nuclear energy. A proper understanding of the situation and continuous improvement of developed technologies are important for making the best and safest use of the technologies. The International Atomic Energy Agency, which investigated the accident at 1F, pointed out the importance of “continuous improvement.” To contribute to “continuous improvement aimed at the highest level of safety,” we are committed to safety research using the various facilities shown in Fig.6-1. Radionuclides are handled and accident conditions are safely simulated at these special facilities.

In this chapter, the results of recent safety research on the following topics are presented: prediction of the amount of fission product (FP) gas stored in high-burnup fuel (Topic 6-1), a structural integrity evaluation method for piping (Topic 6-2), a method of evaluating isotope elements in the spent fuel (Topic 6-3), and thermal aging embrittlement of cast stainless steel (Topic 6-4).

To reduce the risk to nuclear facilities and enhance the preparedness for emergency conditions that are postulated to lead to a severe accident, as shown in Fig.6-2, we are planning to conduct nuclear safety research with a priority on the prevention and evaluation of severe accidents as well as on disaster prevention measures such as environmental impact assessment.

The following topics related to the accident at 1F by the NSRC are described in Chapter 1:

(1) Assessment of Doses to the Inhabitants Living in Fukushima Prefecture (Chapter 1, Topic 1-10)
(2) Dose Estimate for Workers and Public with Incineration and Disposal of Dehydrated Sludge (Chapter 1, Topic 1-11)
(3) Review of Five Investigation Reports on Fukushima Accident (Chapter 1, Topic 1-18)

6–1 Evaluating the Amount of Fission Gas in Fuel with Higher Accuracy
— Development of a Rate-Law Model of Fission Gas Bubble Growth —

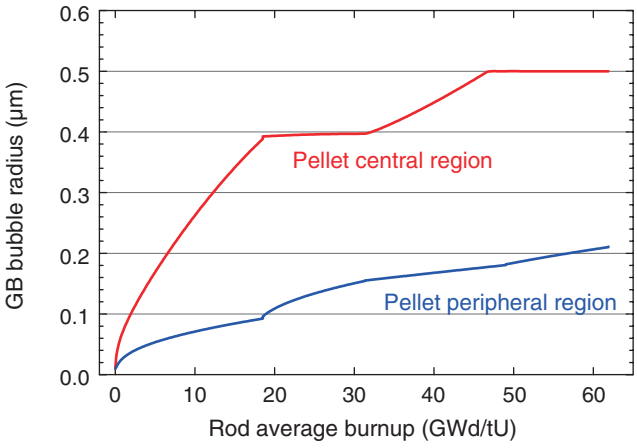

Fig.6-3 Fission gas bubble growth in central and peripheral regions of fuel pellet
The growth of fission gas bubbles in a fuel pellet during irradiation is shown. Growth is faster in higher-temperature central region of pellet.

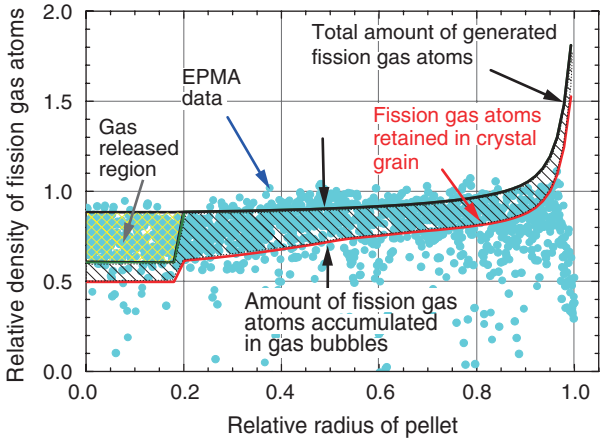

Fig.6-4 Distributions of densities of fission gas in the radial direction of fuel pellet
The red and black curves indicate calculated values. The hatched area enclosed by the red and black curves corresponds to the amount of gas accumulated in gas bubbles, while some fraction is released to the outside of the pellet. The red curve and blue dots (relative values from EPMA measurement) indicate gas atom densities retained in crystal structure of pellet.

In high burnup light water reactor fuel pellets, a large number of fission gas atoms is retained through an extended period of irradiation. The gas is accumulated in gas bubbles in the fuel crystal structure and could swell the pellet, or gas released from the bubbles could increase the internal pressure of the fuel rod and expand the cladding outward, which has undesirable effects on the integrity of the fuel rod. Accordingly, to accurately evaluate the growth of gas bubbles in pellets, a new model was developed that allows better prediction of gas bubble growth. The model was installed in the fuel performance code FEMAXI-7.

The gas bubble grows as the excess bubble internal pressure exceeds the external resistance from the surrounding structure. However, because an earlier model assumes that the bubble gas pressure is always in balance with the external resistance, reliable evaluation has been difficult. In this study, the bubble growth was modeled by a process in which the gas bubble pressure is enhanced and extends the bubble outward into the surrounding crystallite structure.

Next, a calculation was performed to predict the bubble growth and accumulated amount of fission gas. When the radius reaches 0.5 μm, gas release occurs, and growth ceases. Fig.6-3 shows the bubble growth (bubble radius) with burnup. Regarding the final accumulation of gas atoms after this irradiation process, Fig.6-4 compares the calculated and measured profiles of the fission gas atoms density. The latter were obtained by an electron probe microanalyzer (EPMA). The red curve and blue dots indicate the density of gas atoms retained in the crystallites of the fuel pellet. The red curve represents the distribution trend of the blue dots fairly well. The hatched area between the red and black curves corresponds to the accumulated amount of gas, which is calculated to be about 18% of the total generated.

In an experiment on a simulated reactivity-initiated accident conducted in the Nuclear Safety Research Reactor using this fuel, the fission gas release rate was estimated to be about 22% of the total generated, which proves the satisfactory predictability of the model. The result of another experiment indicated that the gas is released mainly from grain boundary gas bubbles. The proximity of the calculated and measured values supports this result.

Thus, this new model has enabled us to more accurately predict fission gas bubble growth behavior as one of the factors related to the integrity of fuel rod.

Reference

Suzuki, M. et al., Model Development and Verifications for Fission Gas Inventory and Release from High Burnup PWR Fuel during Simulated Reactivity-Initiated Accident Experiment at NSRR, Proceedings of Topical Conference on Water Reactor Fuel Performance (TopFuel 2012), Manchester, U.K., 2012, 6p., in USB Flash Drive.

6–2 Predicting Crack Growth in Reactor Piping under Large Seismic Loading
— Proposed Method of Evaluating Crack Growth under Random Cyclic Loading —

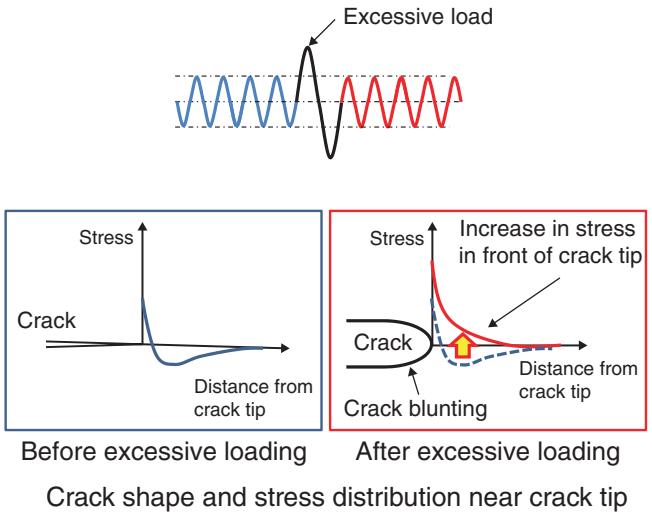

Fig.6-5 Stress distribution shift and crack blunting at crack tip under large seismic loading
Retardation and acceleration of the crack growth rate under large seismic loading are caused by crack blunting due to excessive tensile loading and a stress distribution shift in front of the crack tip due to excessive loading.

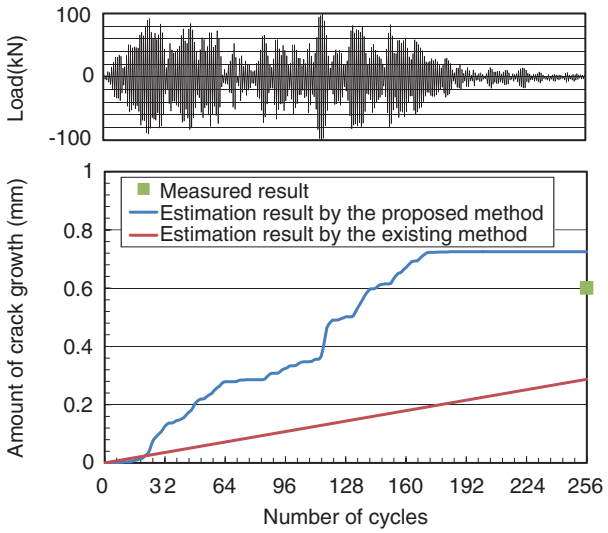

Fig.6-6 Amount of crack growth under simulated seismic load
The method of estimating the crack growth in reactor piping subjected to seismic loading beyond the SSY condition was validated by a crack growth test of pipes 114.3 mm in outer diameter and 11.1 mm in thickness. The measured amount of crack growth is compared with that estimated by the proposed and existing methods.

Accurately predicting crack growth is important for evaluating plant safety. The existing method of evaluating crack growth under constant-amplitude cyclic loading was based on the small-scale yielding (SSY) condition. The objective of this study is to propose a crack growth evaluation method in pipes beyond the SSY condition under seismic loading.

We demonstrated that the crack growth rate beyond the SSY condition and during cyclic loading can be evaluated using the elastic-plastic fracture mechanics parameter (J-integral). Crack growth experiments using cyclic loads with excessive tensile and compressive loads showed the acceleration and retardation effects of the excessive load on crack growth. This indicates that deformation at the crack tip and the change in the stress distribution in front of the crack tip play a key part in crack growth under large seismic loading. Finite element method analyses revealed that the effect of acceleration and retardation on crack growth is attributed to an increase in the stress in front of the crack tip from the excessive compressive load and crack blunting from the excessive tensile load, respectively, as schematically shown in Fig.6-5. A crack growth evaluation method based on these features has been proposed in which ΔJ is calculated in each cycle to estimate the amount of crack growth.

The method of evaluating the crack growth in reactor piping subjected to seismic loading beyond the SSY condition has been validated by piping crack growth tests using a simulated seismic load. Fig.6-6 shows the obtained amount of crack growth (■) together with that evaluated by the present and existing methods. The proposed method can accurately estimate the amount of crack growth given by the test result because the method considers the condition beyond SSY and the crack growth under individual loading of irregular amplitude, unlike the existing method. The validity of the proposed method was confirmed for different materials and loading patterns.

The present study was sponsored by the Japan Nuclear Energy Safety Organization (JNES).

Reference

Yamaguchi, Y. et al., The Proposal of Crack Growth Evaluation Method for Piping under Seismic Loading, Nippon Kikai Gakkai Ronbunshu, A Hen, vol.79, no.802, 2013, p.730-734 (in Japanese).

6–3 Measuring Amount of Nuclides in Spent Nuclear Fuel

— Development of Method of Assaying Barely Measurable Elements in Spent Nuclear Fuel —

Fig.6-7 Induced coupled plasma mass spectrometry (ICP-MS)
High-sensitivity, high-resolution measurement of isotopic ratio measurement for REEs.

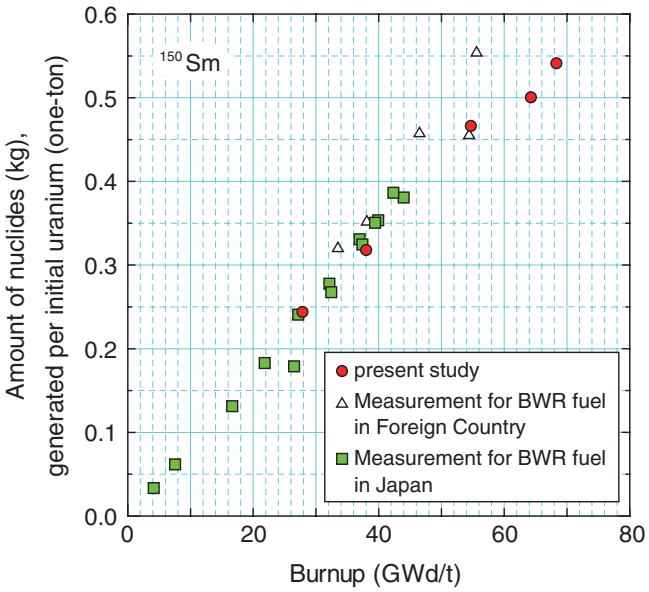

Fig.6-8 Comparison of measurement between past and present studies for ^{150}Sm as an example
Good agreement is shown in the low-burnup region and the linearity of the amount against burnup.

The amount of nuclides in spent nuclear fuel (SNF) is a type of basic data used to evaluate the characteristics of SNF and radioactive waste. To establish a method of measuring it, we have been conducting experiments to assay the amount of fission products (FPs) in a boiling water reactor 9 × 9 fuel assembly during four years beginning in FY 2008. For handling the radioactive materials and because of the requirement for knowledge of the chemical separation of several elements, this experiment was conducted under the collaboration of several departments in the Japan Atomic Energy Agency.

Similar experiments have usually adopted a γ-ray measurement technique, but it is not applicable to stable isotopes. In some cases, after the ion exchange separation of elements, thermal ionization mass spectrometry (TIMS) was used. It has high accuracy, but we should be careful of the radiation dose control because it requires a relatively large quantity of the dissolution sample. Furthermore, for rare earth elements (REEs), the chemical separation and measurement procedure become too complicated because there are several isotopes that have the same mass number. Thus, it has been difficult to measure many samples or to measure repeatedly to reduce the measurement error.

To establish a method of assaying FP elements in SNF simply and quickly using a smaller amount of the dissolution sample of SNF, we have been studying an efficient FP measurement technique combining REE separation by ion chromatography and high sensitivity inductively coupled plasma mass spectrometry (ICP-MS) (Fig.6-7). In this study, we established a procedure for measuring FP nuclides by isotope dilution mass spectrometry with ICP-MS, measuring the isotopic ratio after chemical separation of REE.

This method enables us to separate neodymium, samarium, and gadolinium; the present results agree well with past experimental data obtained with TIMS (Fig.6-8). Using this method, we can obtain the required data by using a very small amount (less than 10 μg) of the resolved sample, so the problem of radiation dose control is reduced. In addition, it is a very efficient method that requires less than five days from the chemical separation to the measurement. This opens the possibility of obtaining reliable data by using repeated measurements and a larger number of samples. We plan to measure FPs other than REEs in a future program.

This work was conducted under a research contract with the Japan Nuclear Energy Safety Organization (JNES), "Measurement experiment of nuclide composition of fission products in spent fuel burnt in light water reactors, F.Y. 2008 to F.Y. 2011."

Reference

Fukaya, H., Suyama, K. et al., Examination of Measurement Method of Isotopic Composition of Fission Products in Spent Fuel, JAEA-Research 2013-020, 2013, 81p. (in Japanese).

6–4 Research on Thermal Aging Embrittlement of Cast Stainless Steels
— Study of Thermal Aging Embrittlement in "FUGEN" Nuclear Reactor —

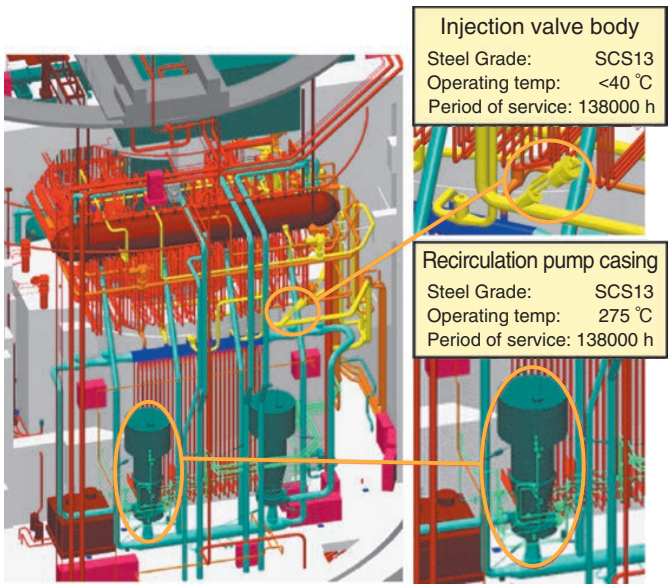

Fig.6-9 Sampling point schematics and service condition of test specimens collected from "FUGEN" reactor
Specimens of cast stainless steels were collected from recirculation pump casing and injection valve body with different service temperatures in "FUGEN" reactor.

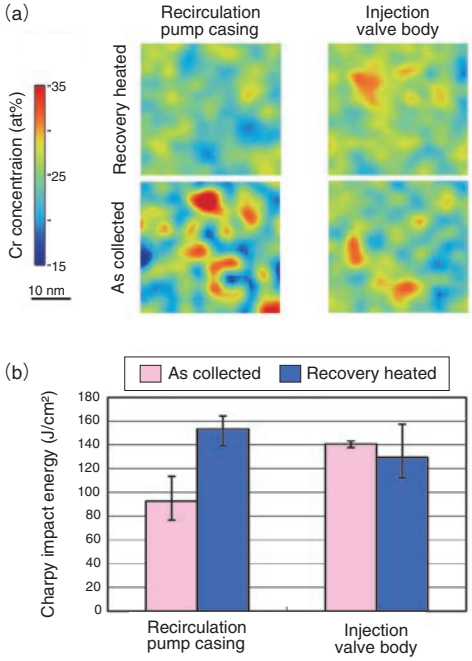

Fig.6-10 Results of analyses of samples collected from "FUGEN" reactor
(a) Cr concentration distribution map obtained using 3DAP. (b) Result of Charpy impact test. Phase separation and thermal aging embrittlement have progressed in recirculation pump casing.

Cast stainless steels are extensively used in light water reactors to fabricate valve bodies, pump casings, and primary coolant piping. Previous studies have shown that thermal aging around 300 °C causes embrittlement. Predictions of the degree of loss in toughness suffered during extended reactor service life would be valuable for assessing the reliability of cast stainless steel reactor components. Therefore, some models for predicting changes in the mechanical properties because of thermal aging have been developed. However, to maintain the toughness of the components in service within a reasonable time period, the aging process in the test material must be accelerated at high aging temperatures. Thus, it is very important to examine the thermal embrittlement mechanism using data obtained from materials that have aged on site for a long period.

A program is currently underway for a decommissioning plan that considers the progress and dismantling of the "FUGEN" reactor. The reactor contains valuable structural materials that have been used for 25 years. In this study, the degree of toughness and the microstructural characterization of cast stainless steel components dismantled from the "FUGEN" reactor were investigated to determine the long-term thermal aging effect at low temperatures (Fig.6-9). We studied the microstructural changes due to thermal aging using the three-dimensional atom probe (3DAP) technique, which is suitable for nanometer-scale analysis of the materials. The analysis of the sample material, which was collected from the "FUGEN" reactor, under thermal aging at 275 °C shows that the initial homogeneous distribution of the Cr concentration becomes modulated as the structure progresses into spinodal decomposition (Fig.6-10(a)). This microstructural change is probably related to hardening, and it causes the thermal aging embrittlement. The results of Charpy impact tests ensure the reliability of the injection valve body. On the other hand, the results from the recirculation pump casing show early signs of an ongoing thermal aging effect (Fig.6-10(b)). We are planning to investigate the underlying mechanism of the embrittlement process to validate and improve the accuracy of the prediction model by using the valuable material data obtained from the "FUGEN" reactor.

The present study was sponsored by the Japan Nuclear Energy Safety Organization (JNES).

Reference

Nogiwa, K. et al., Influence of Thermal Aging on Cast Stainless Steels Used in JAEA's Nuclear Reactor Fugen, Journal of Nuclear Science and Technology, vol.50, no.9, 2013, p.883–890.

For the Evolution of Nuclear Science

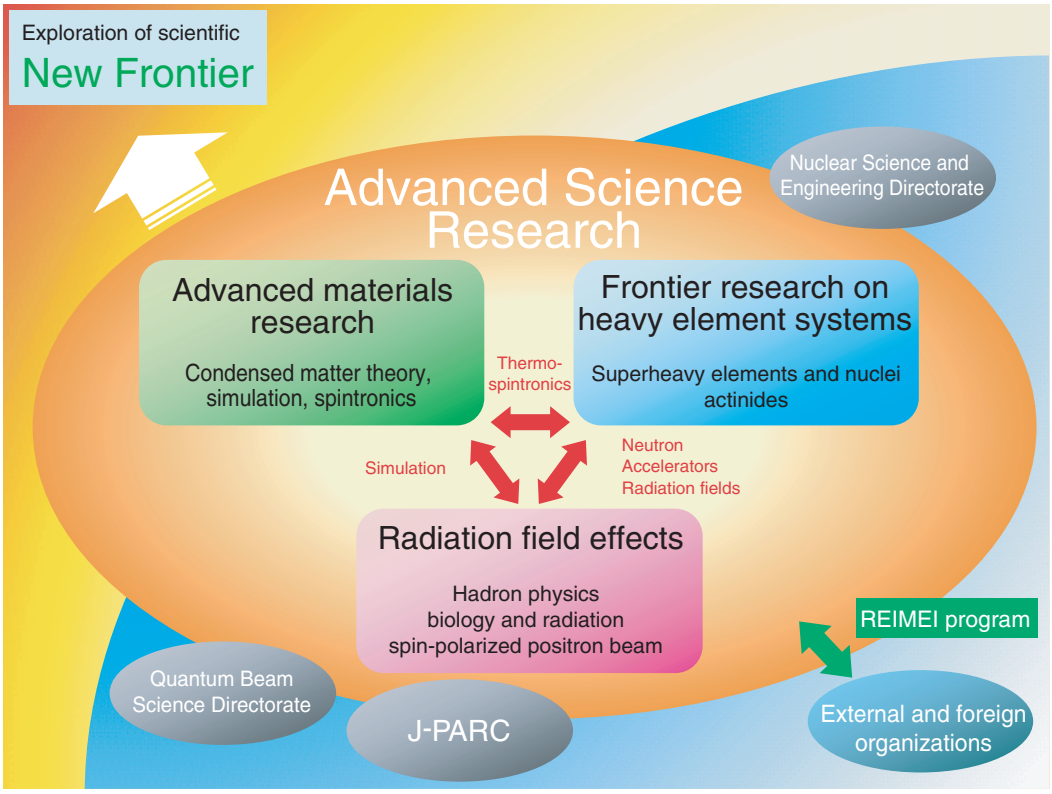

Fig.7-1 Exploration of scientific new frontier in various collaborations

Because we are the sole institute for atomic energy research in Japan, both basic and goal-oriented research are within the scope of our mission. Nuclear engineering is supported by many fields of basic science and technology, and innovations in each research field would contribute to the evolution of nuclear engineering.

The purpose of the Advanced Science Research Center (ASRC) is to promote cutting-edge research on selected topics in basic sciences, which would enable the exploration of new frontiers in nuclear science.

The ASRC Visions for the midterm starting April 2010 are to promote the most advanced basic research, to establish an international center of excellence, and to create new research and technologies. The research projects being pursued can be categorized into three fields: basic research on advanced materials, frontier research on heavy element systems, and basic research on radiation fields.

The research topics in the first research field include the development of molecular spin transport materials and condensed matter theory. Frontier research on nuclear physics, the characterization of superheavy elements, and actinide compounds constitutes the second research field. The third field spans from hadron physics to biology. Collaboration among different research groups in the ASRC and with other directorates is essential to explore the frontiers depicted in Fig.7-1. The research highlights for 2012 are power generation by applied spintronics (Topic 7-1); measurement of the ionization energy of Lr, the 103rd element (Topic 7-2), and the phase transition of URu_2Si_2 (Topic 7-3); a new mechanism of DNA damage (Topic 7-4); and the development of a spin-polarized positron beam (Topic 7-5). Our research activities also include a Fukushima-related activity (Chapter 1, Topic 1-6).

ASRC members are also involved in outreach activities regarding nuclear science. Fig.7-2 shows a 3D chart of nuclides (the horizontal axes are the numbers of neutrons and protons, and the heights represent the half-lives). It facilitates understanding of the synthesis processes of elements, including the r-process, which produces nuclear fuel elements in supernovae.

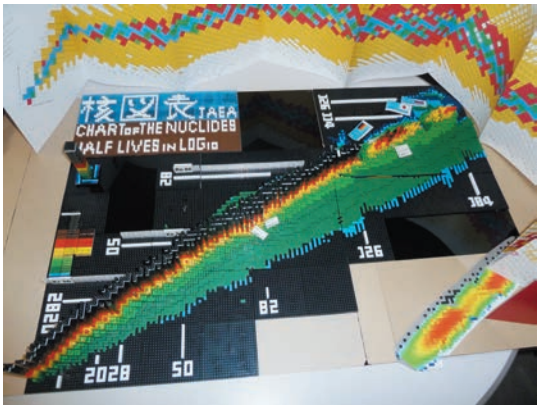

Fig.7-2 3D chart of nuclides

7–1 Electricity Generation by Nanomagnet Dynamics
— Magnetic Power Inverter Based on Spinmotive Force —

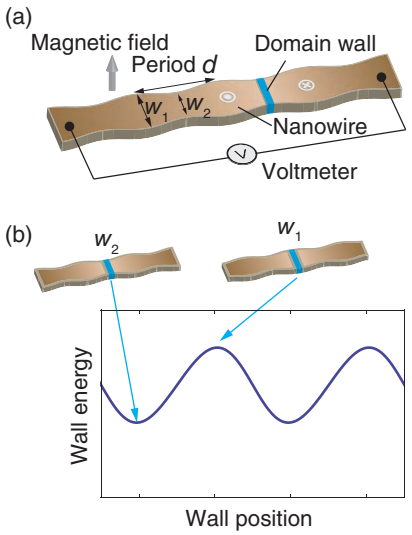

Fig.7-3 Schematics of magnetic power inverter
(a) A magnetic field is applied to induce domain wall motion in a nanowire that is periodically patterned with wider (W_1) and narrower (W_2) widths. (b) The wall energy is proportional to the wire width and becomes larger (smaller) at W_1 (W_2).

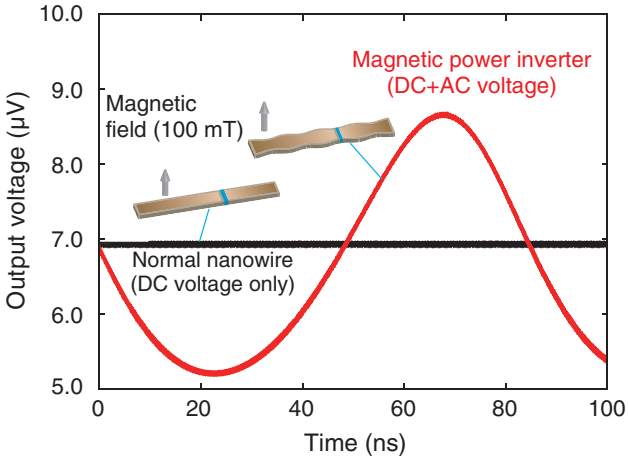

Fig.7-4 Output voltage of magnetic power inverter
In a normal nanowire, a DC magnetic field induces a DC output voltage (— line), whereas, in a periodically patterned nanowire, we have theoretically shown that an AC output voltage is superposed in addition to the DC component (— line).

In 1831, M. Faraday, a British scientist, found that a time-varying magnetic field induces an electromotive force (EMF) in an external circuit. Faraday's law of induction is a fundamental law in electromagnetism and plays a pivotal role as an operating principle for various electrical devices ranging from power generators to electrical appliances.

Recent advances in nanotechnology have made it possible to fabricate and handle magnets ultimately as tiny as one likes. During this progress, we discovered a new mechanism that directly converts magnetic energy to electrical energy in a completely different manner from the conventional inductive EMF. The mechanism is called the spinmotive force (SMF), so called because it relies on the electron's spin, a source of the electron's magnetic properties. Contrary to conventional wisdom, the SMF can induce electricity from a static (direct current, DC) magnetic field and is now regarded as a key building block in spintronics, a research field in next-generation green technology.

An SMF can be induced using a magnetic domain wall (DW), i.e., an interface between different magnetic domains, in a magnetic nanowire (a tiny magnetic strap). When an external magnetic field is applied to the nanowire, a DW is displaced along the nanowire through an energy relaxation process. The released magnetic energy is transferred to the conduction electrons via the magnetic exchange interaction, producing an SMF.

In this work, by further controlling the DW motion, we propose the magnetic power inverter, a new conversion scheme from a DC magnetic field to an alternating current (AC) voltage. Temporal oscillation of the magnetic energy is realized by patterning a magnetic nanowire with periodically varying widths, as shown in Fig.7-3(a). In such a patterned wire, a DW behaves like an elastic membrane, and the DW energy changes with the DW position, as shown in Fig.7-3(b). In this case, the output voltage has an AC component reflecting the alternating DW energy in addition to a normal DC component due to the input DC magnetic field (Fig.7-4). The characteristics of the AC component, such as the amplitude (several μV) and frequency (MHz to GHz), can be tuned by the design of the wire shape, choice of materials, and magnitude of the applied magnetic fields.

This work introduces a novel concept that directly bridges different types of energies with frequency modulation and opens a new route for highly efficient energy conversion technology in nanodevices.

Reference
Ieda, J. et al., Magnetic Power Inverter: AC Voltage Generation from DC Magnetic Fields, Applied Physics Letters, vol.101, issue 25, 2012, p.252413–1–252413–4.

7–2 Toward Experimental Determination of the First Ionization Potential of the Heaviest Actinide
— New Ionization Potential Measurement Using Surface Ionization Process —

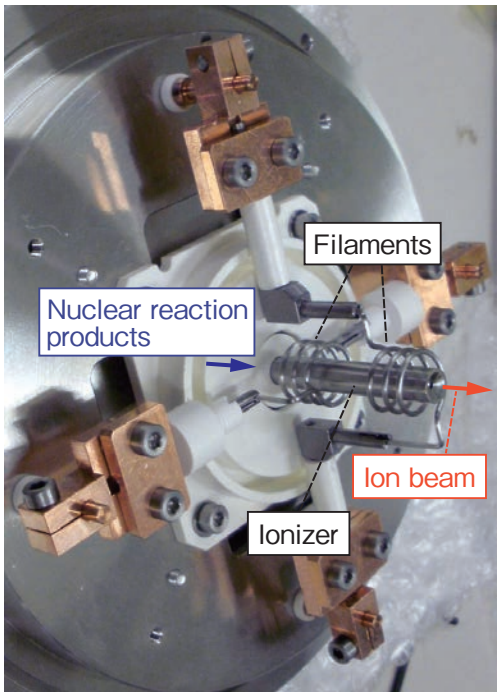

Fig.7-5 Newly developed ion-source coupled to a He/CdI_2 gas-jet transport system for JAEA-ISOL
Nuclear reaction products produced in the nuclear reaction are quickly transported to an ionizer and ionized.

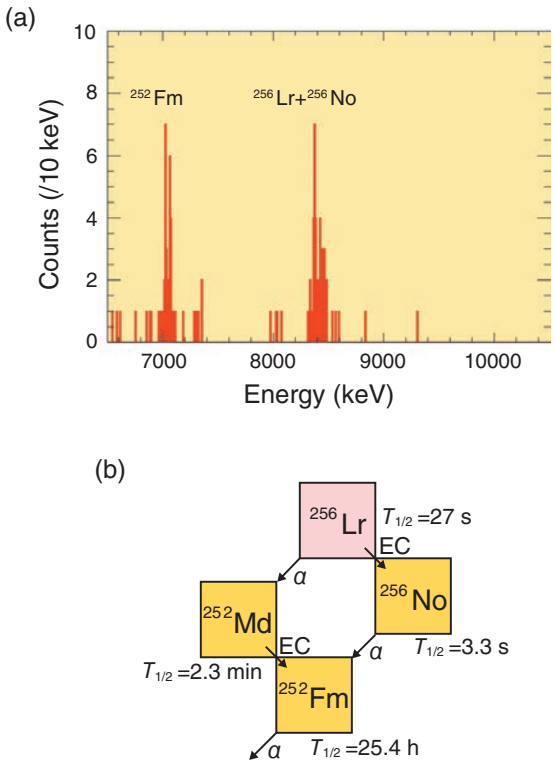

Fig.7-6 (a) Measured α-particle spectrum of mass-separated ions with mass number A = 256. (b) Decay scheme of ^{256}Lr ($T_{1/2}$: half-life, α: α-decay, EC: electron capture)

The first ionization potential (IP) is a fundamental quantity in physical and chemical research on an element. Information on the IP of the heaviest elements can provide a better understanding of relativistic effects in the electronic configuration, which are significantly noticeable for heavy elements. The heaviest elements, which have atomic numbers greater than 100, can be produced at accelerators using reactions of heavy ions with heavy target materials. Owing to the short half-lives and low production rates of the isotopes, they are usually available in quantities of a few atoms at a time. It has, therefore, been impossible to measure the IP values of the heaviest elements so far.

For this purpose, we have been developing a new method to measure the IP value of the heaviest elements based on a surface ionization process. In surface ionization, an atom is ionized via an interaction with a solid surface at a high temperature. The ionization efficiency depends on the temperature and work function of the surface, and the IP of the atom.

To ionize the heaviest actinide element, lawrencium (Lr, Z = 103), via surface ionization, we developed a surface-ionization type ion-source coupled to a gas-jet transport system installed in the Isotope Separator On-Line (ISOL) system of the Japan Atomic Energy Agency (JAEA) (Fig.7-5).

We successfully ionized and mass-separated a short-lived Lr isotope, ^{256}Lr, produced in the ^{249}Cf(^{11}B, 4n) reaction for the first time by applying the present system. As shown in Fig.7-6, α-particles originating from ^{256}Lr and the daughter and the granddaughter nuclides, ^{256}No and ^{252}Fm, respectively, were clearly observed. It is theoretically predicted that Lr would have a lower IP than other actinide elements and lutetium (Lu), the lanthanide homolog of Lr. The ionization efficiency of Lr was obviously higher than that of Lu. This result indicates that the IP of Lr would be lower than that of Lu. We conclude that the surface ion-source is a promising apparatus for measuring the IP of Lr. The IP of Lr is being determined using the present system.

Reference

Sato, T. K. et al., First Successful Ionization of Lr (Z=103) by a Surface–Ionization Technique, Review of Scientific Instruments, vol.84, issue 2, 2013, p.023304–1–023304–5.

7–3 Manipulation of Electrons by Pressure

— Coupling between Lattice and Electrons in Superconductor URu_2Si_2 —

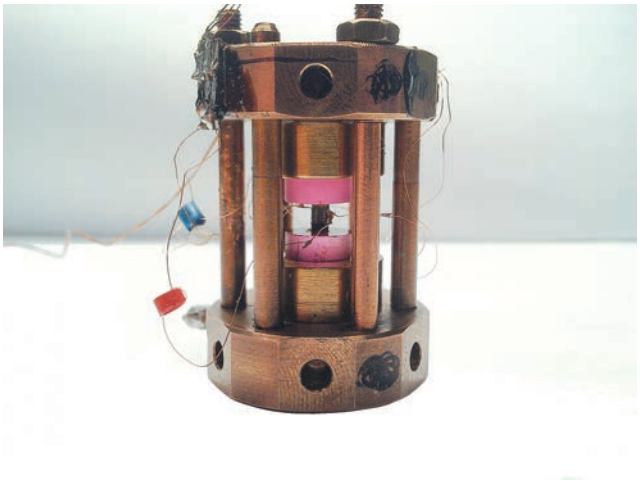

Fig.7-7 Uniaxial pressure cell
Uniaxial pressure is applied vertically to the sample (back one), which breaks the four-fold symmetry.

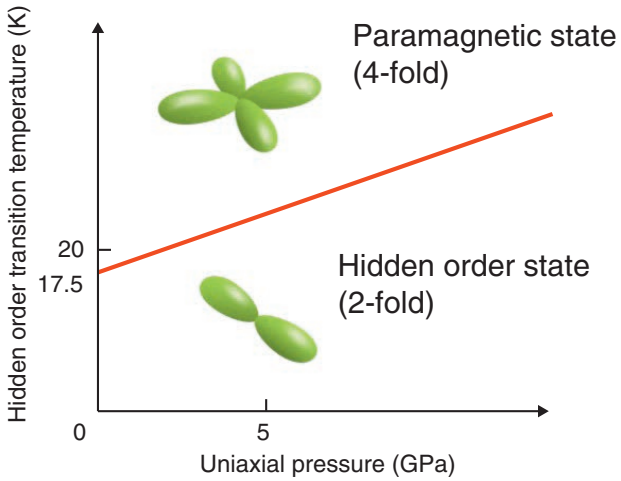

Fig.7-8 Uniaxial pressure dependence of hidden order transition temperature (— line)
The transition temperature increases with increasing uniaxial pressure.

In the superconducting state, two electrons form a superconducting pair. An attractive interaction between the electrons is necessary for the formation of paired electrons. In conventional superconductors, the attractive interaction originates in lattice vibration. In contrast, magnetic fluctuation is considered to be the origin in actinide superconducting compounds. Because a high superconducting transition temperature *T*c can be expected for a magnetic-fluctuation-induced superconductor, it is important to clarify the mechanism for the fluctuation.

In URu_2Si_2, the so-called hidden order state appears below 17.5 K (-256 °C). Because the superconducting state appears at a lower temperature of 2 K (-271 °C), magnetic fluctuation in the hidden order state is considered to induce superconductivity. However, the hidden order was not identified for 25 years, which is an important issue in condensed matter physics.

This compound has four-fold symmetry in the paramagnetic state above 17.5 K. Recently, however, it was revealed that the electronic state exhibits symmetry breaking from the four-fold to the two-fold state with hidden order. In this study, the hidden order is investigated in a two-fold lattice state artificially induced by uniaxial pressure. To apply uniaxial pressure at low temperatures, we developed a uniaxial pressure cell (Fig.7-7). As shown in Fig.7-8, the hidden order transition temperature increases under uniaxial pressure, indicating that electrons and the lattice are coupled, and we can manipulate the magnetic fluctuation that induces superconductivity. This technique is expected to yield an understanding of magnetic fluctuation and to facilitate the development of high-temperature superconducting materials.

A future new superconductor with a higher *T*c is expected to be realized in a magnetic-fluctuation-mediated superconducting system, because the *T*c value of phonon-mediated superconductors has already reached its peak. If a new superconductor with a room temperature *T*c is found, it will be quite useful for improving the energy efficiency.

We are going to investigate actinide compounds to clarify the mechanism of superconductivity in detail.

Reference

Kambe, S. et al., Thermal Expansion under Uniaxial Pressure in URu_2Si_2, Physical Review B, vol.87, issue 11, 2013, p.115123–1–115123–6.

7–4 Novel Mechanism of Radiation Damage to DNA

— An Advance in Elucidating the Radiation Process in DNA Damage —

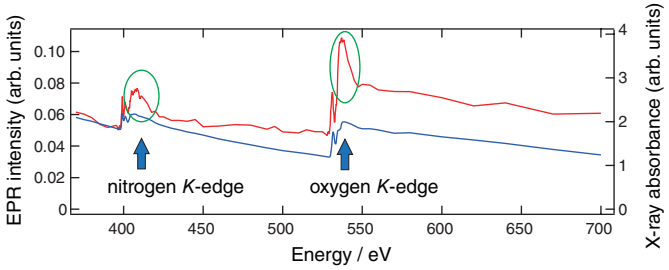

Fig.7-9 Anomalous enhancement of EPR signal at nitrogen and oxygen *K*-edges
EPR signal intensity (— line, left axis) is anomalously enhanced (○) at energies slightly above the nitrogen and oxygen *K*-edges when compared with the dependence of the X-ray absorption probability of DNA (— line, right axis) on the X-ray energy (abscissa).

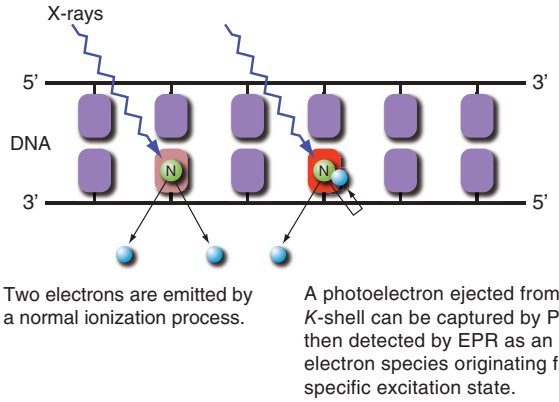

Fig.7-10 *K*-shell photoabsorption processes at specific atoms in DNA (nitrogen *K*-shell photoabsorption is shown as an example)
We revealed that when DNA is exposed to X-rays with an energy slightly above the *K*-shell ionization threshold, an ejected electron is re-captured by the DNA as an unpaired electron.

Risk assessment for low-dose irradiation has been one of the most urgent issues. In particular, the research field of radiation damage to DNA coding genetic information and its biological repair has not yet been fully understood. In this study we revealed a novel mechanism of the radiation process in DNA damage.

When a living cell is exposed to ionizing radiation, particularly high-energy charged particles, energy over a wide range is deposited from the particle to the DNA. Depending on the deposited energy level, various DNA damage processes might proceed simultaneously. To fully understand the damage processes, each one should be individually analyzed. Previous studies, however, lacked suitable techniques to realize this goal.

We addressed this difficulty using highly monochromatized soft X-rays. In an irradiated DNA molecule, an unpaired electron remaining in the outermost shell after ionization is one of the short-lived intermediates that cause damage. We exposed DNA to soft X-rays obtained from a synchrotron facility (SPring-8) while sweeping the energy. The precise dependence of the yields of the unpaired electron species on the soft X-ray energy was investigated, particularly around the *K*-shell ionization thresholds of the DNA constituent atoms nitrogen and oxygen. Previously it was difficult to directly observe the highly reactive and short-lived species. To realize "*in situ*" observation of the short-lived species, we connected an electron paramagnetic resonance (EPR) apparatus to the soft X-ray beamline.

The result shows that the EPR intensity (— line in Fig.7-9) corresponding to the yield of the unpaired electron species changes roughly in proportion to the X-ray absorption probability by *K*-shell electrons (— line in Fig.7-9). Further, exposure to X-rays with an energy slightly above the ionization thresholds causes, very interestingly, an anomalous enhancement of the EPR signal intensity (shown by circles in Fig.7-9). A theoretical analysis revealed that the enhancement is caused by recapturing of an ejected slow electron at the ionized atom through a Post Collision Interaction (PCI) process, which is a novel mechanism of radiation damage to DNA (Fig.7-10).

These results are expected to advance understanding of DNA damage, particularly that originating from *K*-shell ionization.

This work was supported by a Japan Society for the Promotion of Science (JSPS) KAKENHI Grant-in-Aid for Scientific Research (B) (No.21310041).

Reference

Oka, T., Yokoya, A. et al., Unpaired Electron Species in Thin Films of Calf-Thymus DNA Molecules Induced by Nitrogen and Oxygen *K*-Shell Photoabsorption, Physical Review Letters, vol.109, issue 21, 2012, p.213001-1–213001-5.

7–5 Evaluation of Electron Spin Using Its Antiparticle

— Development of a Positron Beam with the World's Highest Spin Polarization —

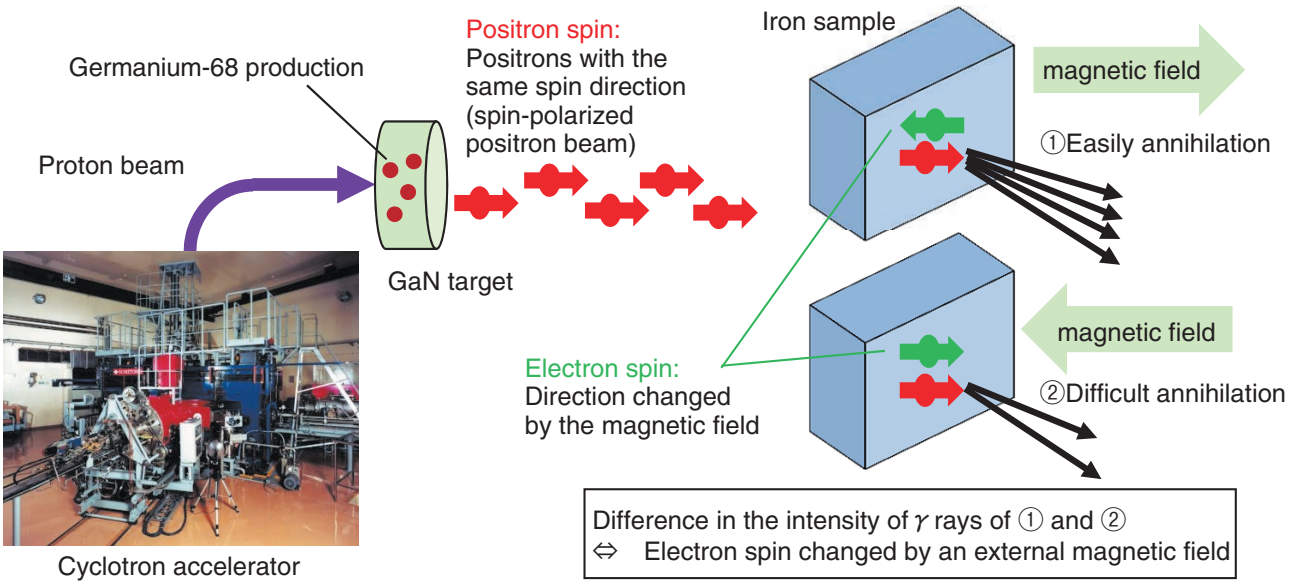

Fig.7-11 Evaluation of electron spins of iron sample using spin-polarized positron beam
A positron beam with a high spin polarization of 47% is irradiated on the iron sample. The spin direction of electrons in the iron sample is changed by an external magnetic field. As positrons and electrons are easily annihilate when their spin directions are antiparallel, the state of the electron spin that relates to the magnetism can be evaluated by measuring the difference in the intensity of γ rays in (1) and (2).

Spintronics is a new technology that uses the up and down electron spins like the "0" and "1" values in a digital circuit. This technology is expected to lead to the development of new devices with features such as very low power consumption, which cannot be achieved through conventional semiconductor technology. In advanced research on magnetic substances for spintronics, the evaluation of the electron spin is important. By using positron annihilation spectroscopy (PAS), we can obtain information on the electron spin existing in the material surface or interface more easily than by the conventional technique.

A positron, which is the antiparticle of an electron, annihilates with the electron in the material, and γ rays are emitted. In the conventional PAS method, only the electron momentum is measured from the energy spectrum of the γ rays. We tried to detect the direction of the spin in addition by developing a spin-polarized positron beam, because positrons, like electrons, also have spin.

The positron beam can be formed by collecting the positrons that are emitted from a radioisotope. When the spin polarization is improved by selecting the spin direction of the positrons, the beam intensity decreases. To achieve both high spin polarization and sufficient beam intensity, we used a germanium-68 radioisotope that emits highly spin-polarized positrons. By using this radioisotope produced by proton beam irradiation of a gallium nitride target in a cyclotron accelerator, a positron beam with a high spin polarization of 47% was successfully produced (Fig.7-11). This value is almost twice that of a positron beam produced by the commonly used sodium-22 radioisotope. When a pure iron sample was irradiated with this spin-polarized positron beam, the intensity of the γ rays was increased when the spin direction was controlled, so positrons annihilated easily with electrons. This result shows that detailed information about the electron spin, which causes the magnetism of magnetic substances, can be extracted.

The PAS method using the spin-polarized positron beam is expected to be a new evaluation technique that is necessary for the future development of spintronics.

This work was supported by a Japan Society for the Promotion of Science (JSPS) KAKENHI Grant-in-Aid for Scientific Research (B) (No.24310072).

Reference

Maekawa, M. et al., Development of Spin–Polarized Slow Positron Beam using a ^{68}Ge–^{68}Ga Positron Source, Nuclear Instruments and Methods in Physics Research B, vol.308, 2013, p.9–14.

8 Nuclear Science and Engineering Research

Promoting Basic R&D on Nuclear Energy and Creation of Innovative Technology to Meet Social Needs

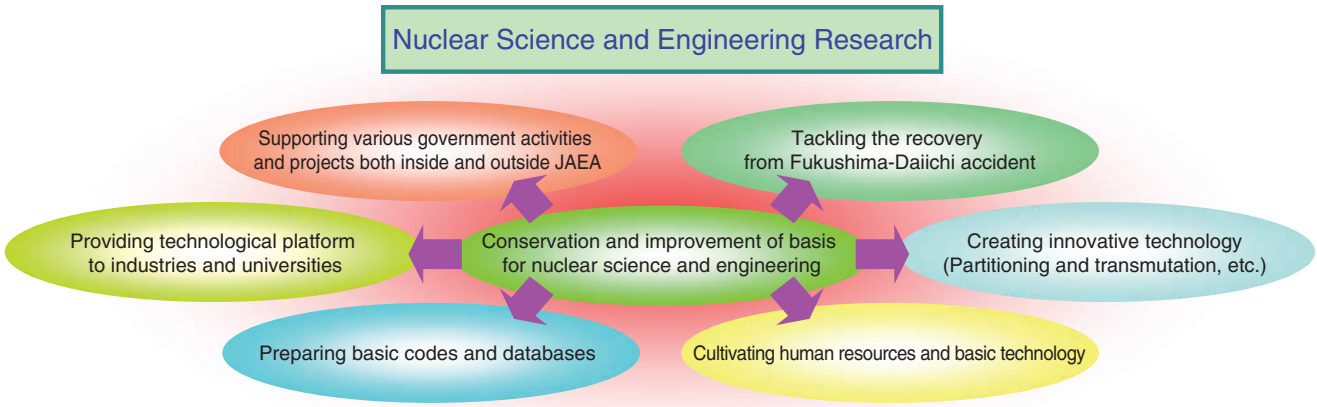

Fig.8-1 Roles of nuclear science and engineering research
We play various roles in the conservation and improvement of the basis for nuclear science and engineering.

Nuclear science and engineering research aims to promote various activities, as shown in Fig.8-1, including recovery from the accident at the Tokyo Electric Power Company, Incorporated Fukushima Daiichi Nuclear Power Station (1F). To this end, research is being conducted in the areas of nuclear data and reactor engineering, fuels and materials engineering, nuclear chemistry, and environment and radiation science. Joint research with industry and academia is also being promoted via the Nuclear Engineering Research Collaboration Center.

In the area of nuclear data and reactor engineering, the Japanese Evaluated Nuclear Data Library (JENDL) is being edited, and nuclear data are being measured to improve it. Calculation methods for nuclear reactor design (Topic 8-1), transmutation technologies to reduce the amount of long-lived radioactive waste (Fig.8-2), and so on are also being studied. Regarding the accident at 1F, the decay heat in the reactor cores was evaluated (Chapter 1, Topic 1-17).

In the area of fuels and materials engineering, research on the nuclear fuels and materials used in nuclear reactors and fuel cycle facilities is being promoted (Fig.8-3, Topic 8-3). Regarding the accident at 1F, the properties of the fuel debris and materials immersed in sea water are being investigated.

In the area of nuclear chemistry, research is being promoted on basic data for reprocessing, separation of long-lived nuclides from nuclear wastes, and detection of extremely small amounts of nuclear materials (Topics 8-4, 8-5, 8-6, 8-7). These technologies are also being applied to the recovery from the accident at 1F.

In the area of environmental and radiation science, studies of the behavior of radionuclides in the environment and the development of a database for radiation protection are being promoted (Topics 8-2, 8-8, 8-9). The behaviors of ^{137}Cs released by the accident at 1F in the marine sediment and forest topsoil are being studied in order to predict the long-term environmental consequences (Chapter 1, Topics 1-1, 1-8).

In collaboration with industry, a production technique for medical radio-isotopes using an accelerator-driven neutron source has been being developed. A new corrosion-resistant material is also being developed.

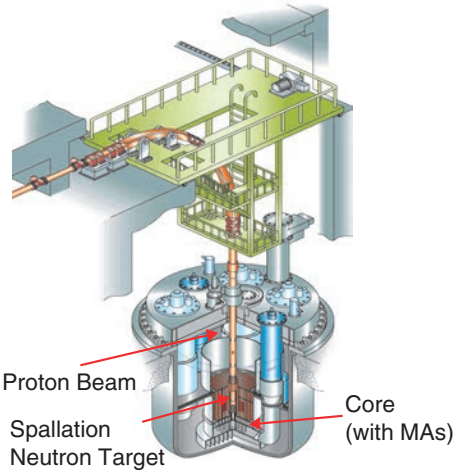

Fig.8-2 Accelerator-driven system (ADS) to transmute minor actinides (MAs)
An 800 MWt ADS can be operated with a 1.5 GeV, 30 MW proton beam at maximum power. Through operation of one ADS, the amount of long-lived MA nuclides discharged from 10 units of a 1 GWe light water reactor can be transmuted into short-lived or stable ones.

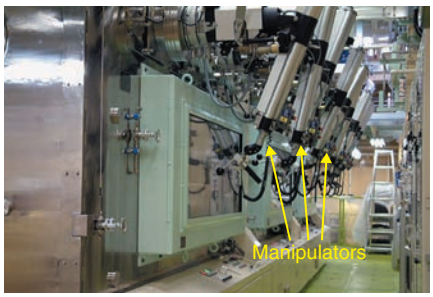

Fig.8-3 TRU High-Temperature Chemistry (TRU-HITEC) module installed at NUCEF
Various thermochemical data are being measured for highly radioactive trans-uranic (TRU) elements in an inert gas atmosphere.

8–1 Method of Accurately Designing New Types of Reactors
— Advanced Method Using Experiments (Extended Cross Section Adjustment) —

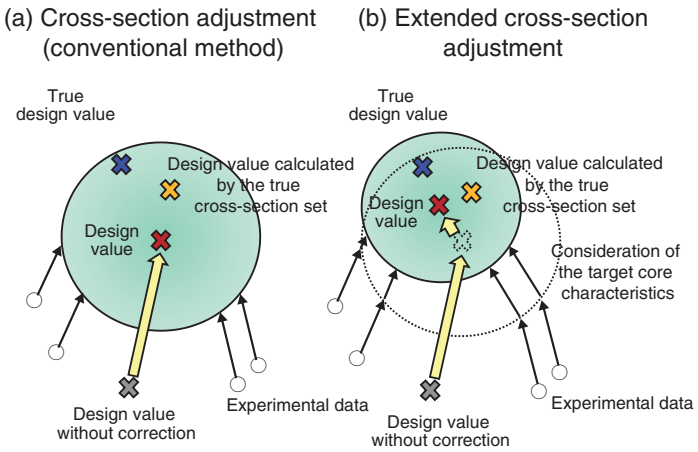

Fig.8-4 Features of the new adjustment method
The conventional method (a) aims to produce a design value close to the calculation value by using the directly unknowable true cross section set. In contrast, the present method (b) makes the design value closer to the true design value by considering the target core characteristics.

Table 8-1 Comparison of prediction accuracy
The "prediction" is the ratio of the design value to that without correction. The "uncertainty" represents the sum of the design value uncertainty components induced by the experiment, analysis method, and nuclear data. The extended cross section adjustment improves the prediction accuracy more efficiently than the conventional method.

Design target core parameters	(a) Cross-section adjustment (conventional method)		(b) Extended cross-section adjustment	
	Prediction	Uncertainty (%)	Prediction	Uncertainty (%)
Criticality	0.9977	0.30	0.9982	0.21
Power distribution	1.000	1.4	0.996	0.9
Control rod worth	0.969	1.4	0.968	1.1

Improved prediction accuracy

To design a new-type of reactor, it is necessary to accurately predict the nuclear characteristics of the reactor core parameters, which are determined by the reactions between neutrons and nuclei. These core parameters can be predicted by nuclear data and computer codes. The former describe the features of the nuclear reactions, whereas the latter analyze the behavior of neutrons. The accuracy of the predicted value can be validated with a full-scale, well-simulated experiment, a so-called mock-up experiment. However, such an experiment would be very difficult because it incurs huge costs and requires full-scale nuclear fuels.

To solve these problems, a design method called cross section (set) adjustment has been used in fast reactor core design study. The cross section set consists of nuclear data converted to be applicable to the computer codes. The cross section adjustment method based on the Bayes theorem enables us to improve the prediction accuracy of the core parameters by adjusting the cross section set to existing experimental data. In this method, the target core parameters calculated by the adjusted cross section set are used directly as the design values. This method, therefore, has the advantage that all the design values are physically consistent with each other.

On the other hand, another design method called the extended bias factor method was developed in a previous study by the Japan Atomic Energy Agency. This method has the advantage that it can give the most accurate design values. However, the extended bias factor method does not attempt to maintain consistency among the design values.

In the present study, a new design method called extended cross section adjustment is developed. The new method theoretically integrates the two existing design methods mentioned above. The conventional adjustment method alters the cross section set in order to maximize its correctness by optimizing it to the existing experimental data. In contrast, the present method adjusts the cross section set to minimize the uncertainty of the design value by taking into account the target core characteristics. Therefore, it is possible to improve the prediction accuracy further (Fig.8-4). By applying the new method to a typical large fast reactor design analysis, it is demonstrated that the prediction accuracy is improved more efficiently than in the conventional method (Table 8-1).

The new method not only clarifies the theoretical relation between the conventional cross section adjustment method and the extended bias factor method, but also successfully improves the prediction accuracy. In the future, the new method will be used for a reactor design study as a design method that efficiently improves the prediction accuracy.

Reference

Yokoyama, K. et al., Extended Cross-Section Adjustment Method to Improve the Prediction Accuracy of Core Parameters, Journal of Nuclear Science and Technology, vol.49, no.12, 2012, p.1165–1174.

8–2 Accurate Prediction of Nuclear Fragmentation by Energetic Radiation

— Fragmentation Cross Section Measurement by New Method and Theoretical Model Development —

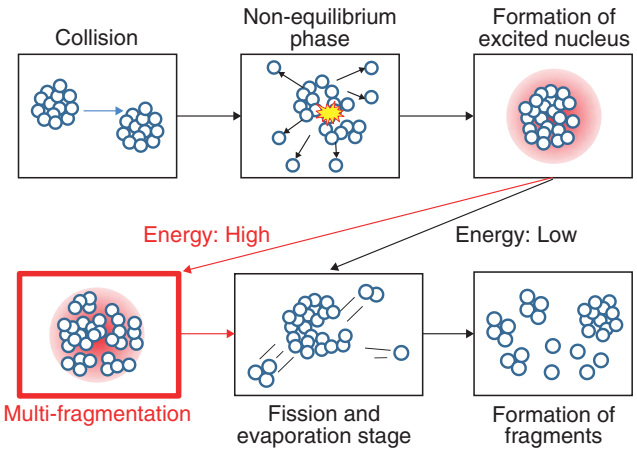

Fig.8-5 Simulation flow of high-energy nuclear fragmentation reactions
A model for simulating the multi-fragmentation process, indicated in red, was added in this research. In the revised simulation flow, energetic nuclei form fragments through a reaction that forms multiple fragments.

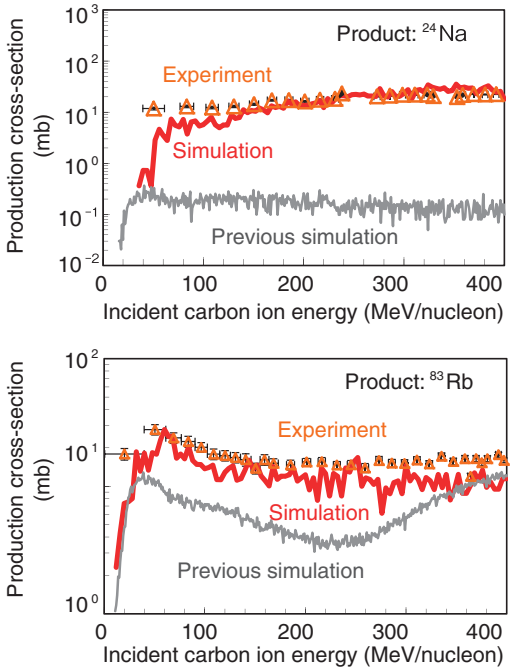

Fig.8-6 Comparison of fragment production reaction cross sections (upper: ^{Nat}Pb(C,x)^{24}Na reaction, lower: ^{Nat}Pb(C,x)^{83}Rb)
The previous simulation underestimates the cross sections by a factor of 10 to 100 compared to the measurement data, whereas the new calculation using PHITS as revised in this research agrees with the measurement data very well.

In accelerator facilities, various radioactive fragments are produced by spallation of nuclei by high-energy radiation. Because radioactive fragments become radiation sources in accelerators after the operation period, the fragments must be considered, e.g., for safety management in maintenance. However, the radiation transport simulation codes used for shielding calculations cannot accurately predict fragment production from heavy elements.

To solve this problem, we measured the fragment production cross sections of lead bombarded by carbon ions at the National Institute of Radiological Sciences heavy ion therapy facility, HIMAC, and revised the reaction models of the Particle and Heavy Ion Transport code System (PHITS) on the basis of the experimental data. In the experiment, cross sections in a wide energy range (from 50 to 400 MeV/nucleon) were measured by a new method, in which stacked lead plates were irradiated and the fragments in each plate were measured. Calculation by the previous version of PHITS underestimated the cross sections by a factor of 100 at the maximum. We assumed that the underestimation was attributed to the absence of a multi-fragmentation process. In this process, nuclei are disintegrated into multiple small fragments, whereas the old PHITS assumes that all the excited nuclei undergo a fission/evaporation process to form fragments. Therefore, a new model, the statistical multi-fragmentation model, was added to the calculation model of PHITS; it determines the partition of nuclei on the basis of the probabilities of various partitioning patterns calculated using statistical mechanics (Fig.8-5). The fragment production cross sections calculated by the revised PHITS reproduced the measured ones accurately (Fig.8-6).

In this research, accurate prediction of the radioactive fragment production cross sections by PHITS was realized; this contributes remarkably to the precise evaluation of radiation safety in high-energy accelerator facilities.

This work was partially supported by a Japan Society for the Promotion of Science (JSPS) KAKENHI Grant-in-Aid for Research Activity Start-up (No.24860072). This article includes the results of the Research Project with Heavy Ions at NIRS-HIMAC.

Reference

Ogawa, T. et al., Analysis of Multi–Fragmentation Reactions Induced by Relativistic Heavy Ions using the Statistical Multi–Fragmentation Model, Nuclear Instruments and Methods in Physics Research A, vol.723, 2013, p.36–46.

8–3 Life Prediction of Material in Nuclear Reprocessing Plants

— Corrosion Characteristics of Stainless Steel in Boiling Nitric Acid Solution Including Np —

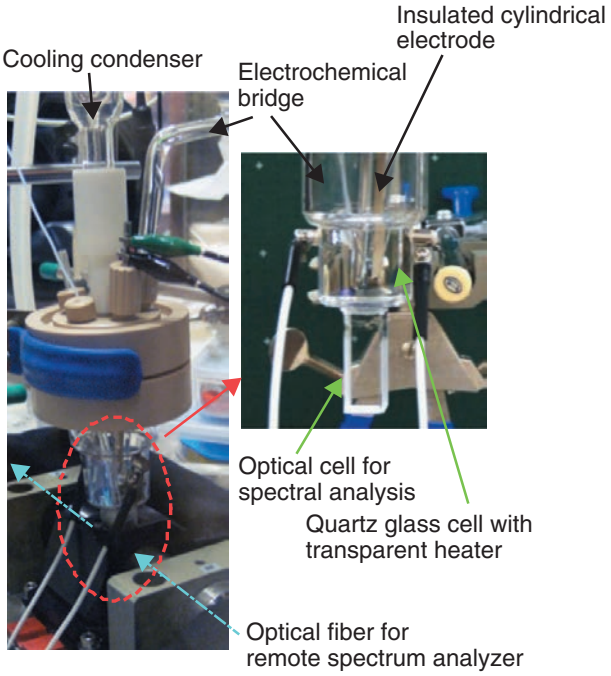

Fig.8-7 Appearance of developed electrochemical cell including optical cell for spectral analysis
The test cell is combined with a transparent heater, a potential probe, and an optical cell. It is operated remotely. The amount of solution is approximately 15 cm³.

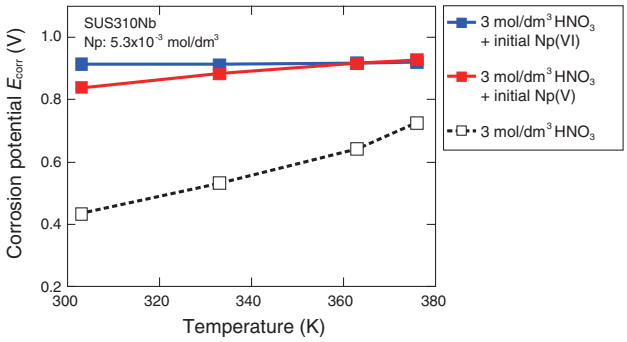

Fig.8-8 Effect of temperature on corrosion potential of stainless steel (SUS310Nb)
The increasing corrosion potential caused by a slight amount of Np accelerates corrosion; the behavior depends on the valence of the Np and the temperature.

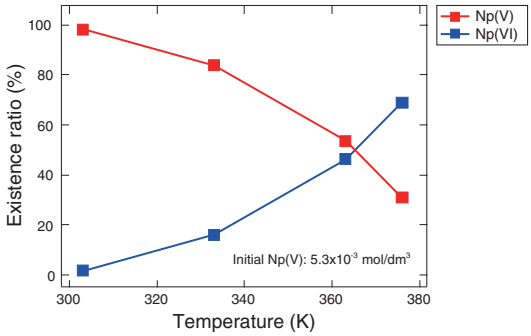

Fig.8-9 Effect of temperature on valence change in Np
Pentavalent Np(V) is oxidized to hexavalent Np(VI) by increasing the temperature of the solution. This suggests that the oxidized Np(VI) ions accelerate corrosion.

Nuclear reprocessing has been promoted for the reuse of uranium (U) and plutonium (Pu) in spent reactor fuels worldwide. A corrosive nitric acid solution is used in nuclear reprocessing, which involves materials containing metallic ions that accelerate corrosion. Therefore, accelerated corrosion of stainless steel, one of the component materials, is an issue in nuclear reprocessing plants.

It is well known that among metallic ions, Pu and neptunium (Np), which are oxidized in boiling nitric acid solution to metallic ions in higher oxidation states, accelerate corrosion the most. Furthermore, the amount of Pu and Np that can be handled in an experiment is restricted because they are radioactive elements.

We developed a specially designed small electrochemical test cell integrated with an optical cell for spectroscopic analysis in order to concomitantly evaluate the oxidation states of Np ions and the polarization curves of stainless steel in boiling nitric acid solution. The goal of this study is to understand the corrosion acceleration mechanism of stainless steel.

The test cell shown in Fig.8-7 enables (1) the handling of a small amount (ca.15 cm³) of test solution, (2) simultaneous spectroscopic characterization and electrochemical monitoring of the solution, and (3) stable electrochemical measurements in a boiling nitric acid solution.

Fig.8-8 shows that the corrosion potential E_{corr} of the stainless steel increases with increasing temperature when the solution contains Np ions. The presence of Np ions accelerates the corrosion of stainless steel by increasing the corrosion potential. Further, the corrosion potential in the solution containing Np(VI), in a higher valence state, does not change with increasing temperature, whereas that of a solution containing Np(V), in a lower valence state, increases.

Fig.8-9 shows the existence ratios of Np(VI) and Np(V) in 3 mol/dm³ HNO_3 with initial Np(V) ions at various temperatures. The existence ratio of Np(VI) increases with increasing temperature.

In conclusion, Np(VI) oxidized by nitric acid was found to raise the corrosion potential and accelerate the corrosion of stainless steel.

This work was part of work commissioned by the Japan Nuclear Energy Safety Organization (JNES).

Reference

Kato, C. et al., Electrochemical Measurements in Boiling Nitric Acid Solutions Containing Radioactive Elements by using Small Cell with a Portion for Spectral Analysis Function, Zairyo to Kankyo, vol.60, no.2, 2011, p.69-71 (in Japanese).

8–4 Discovery of Thermochromic Uranium Complexes

— Coordination Chemistry in Ionic Liquids Using Time-Resolved Laser-Induced Fluorescence Spectroscopy —

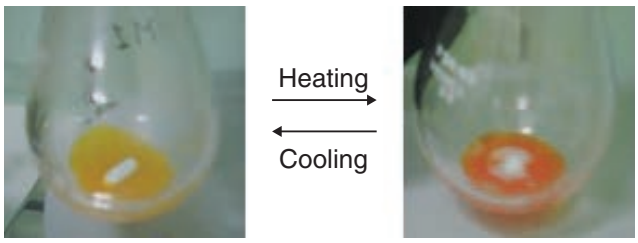

Fig.8-10 Thermochromic behavior of $[C_4mim]_3[UO_2(NCS)_5]$
Reversible change in color: solid (left, -196 °C) to sol (right, 90 °C). An orange uranium complex is uncommon.

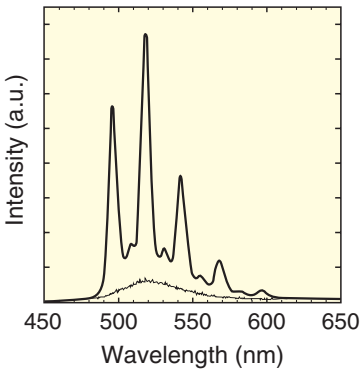

Fig.8-12 Time-resolved luminescence spectra of $[C_4mim]_3[UO_2(NCS)_5]$ recorded under UV irradiation
The weak luminescence at 90 °C (thin line) becomes enhanced at -196 °C (bold line).

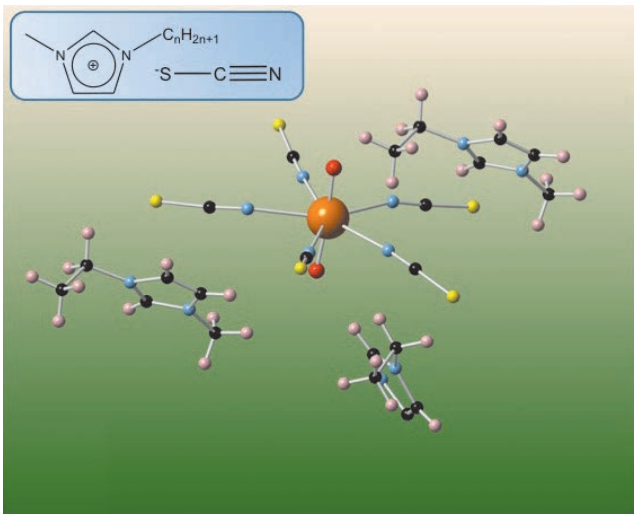

Fig.8-11 Crystal structure around $[UO_2(NCS)_5]^{3-}$ (-196 °C)
There are five NCS^- ions on the equatorial plane coordinated to a uranyl ion (UO_2^{2+}), surrounded by three 1-ethyl-3-methylimidazolium cations. This salt forms a bright yellow solid at -196 °C. The symbols are as follows: oxygen: red, nitrogen: blue, carbon: black, sulfur: yellow, and hydrogen: pink. The chemical structure of the ionic liquid is shown above.

Inductively coupled plasma mass spectrometry or other mass spectrometric methods are used in chemical analysis of actinides in water or organic solvents instead of radiation measurements. These techniques, however, are inapplicable to in-situ observations of the dissolved chemical species. In contrast, time-resolved laser-induced fluorescence spectroscopy (TRLFS) enables qualitative analysis of solutions. Investigating the energy dissipation processes after irradiation by laser pulses is of necessity our approach to studying the chemistry of actinide complexes.

Observation of dissolved metal ions at high concentrations using TRLFS has revealed the coordination structure of the uranium complex, which has remained unknown in water or organic solvents. Ionic liquids are a series of salts that are composed entirely of ions and melt at room temperature. Because they are stable at 100 °C, novel physical properties of these solvents at higher temperatures can be designed. We performed a dissolution test of uranyl ions (UO_2^{2+}) in 1-butyl-3-methyl imidazolium thiocyanate ([C_4mim][NCS]; the structure is shown in Fig.8-11), which formed a liquid at very high concentrations. Further addition of uranium affords a metal salt with a $[UO_2^{2+}]$:$[NCS^-]$ composition ratio of 1:5, which remains a sol at room temperature. Surprisingly, this substance reveals thermochromism, that is, temperature-dependent color changes due to external stimuli (Fig.8-10). There have been no studies describing this property of uranium complexes; this salt becomes yellow on solidification when cooled at the liquid nitrogen temperature, whereas it melts on heating, becoming red.

To understand this phenomenon, the thermochromic ionic liquid was crystallized at low temperature, resulting in the crystal structure shown in Fig.8-11, where the coordination number around uranium on the equatorial plane at low temperature is five. In addition, the luminescence spectrum under irradiation by ultraviolet light is shown in Fig.8-12; it exhibits quenching of luminescence at room temperature. The symmetrical structure around the U moiety, therefore, affects the spectrum by reducing the coordination number on heating. The orange or red $U^{VI}O_2^{2+}$ compounds are uncommon, so a coordination number of four is attributed to the local environment between the uranyl and the ligand as well as to cation–anion interactions.

This work was financially supported by a Japan Society for the Promotion of Science (JSPS) KAKENHI Grant-in-Aid for Young Scientists (B) (No.22760679). The Excellent Young Researcher Overseas Visit Program (No.21-5317) of JSPS is also acknowledged.

Reference

Aoyagi, N. et al., Thermochromic Properties of Low-Melting Ionic Uranyl Isothiocyanate Complexes, Chemical Communications, vol.47, issue 15, 2011, p.4490–4492.

8–5 Attempt to Establish a Reprocessing System That Uses Monoamides

— Continuous Extraction of Uranium and Plutonium Using Mixer-Settler Extractors —

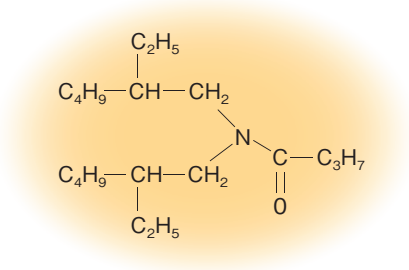

Fig.8-13 Structure of *N,N*-di(2-ethylhexyl) butanamide (DEHBA)

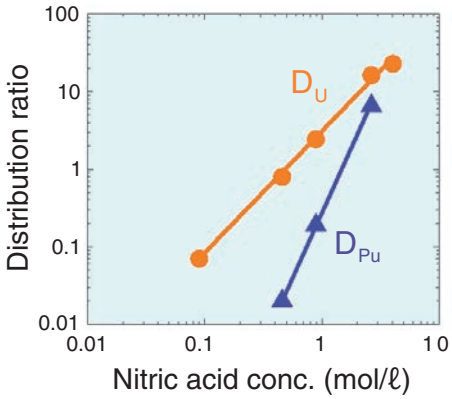

Fig.8-14 Effects of nitric acid concentration on the distribution ratios of U (D_U) and Pu (D_{Pu}) by DEHBA
Distribution ratios of U and Pu were obtained using DEHBA in dodecane as the organic phase and nitric acid containing U or Pu as the aqueous phase.

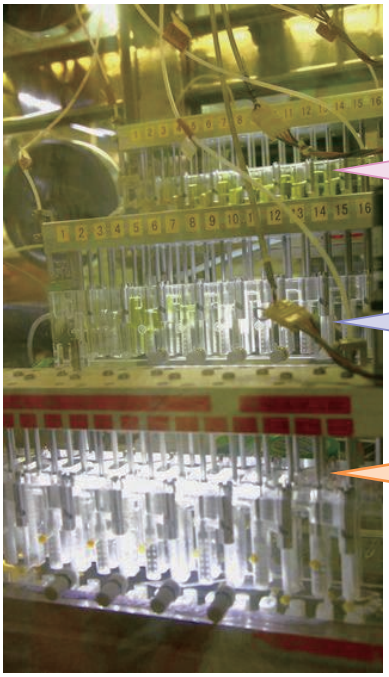

Fig.8-15 Photograph of continuous extraction experiment using mixer-settler extractors for U and Pu extraction
Extraction properties of DEHBA toward uranium and plutonium were revealed using mixer-settler extractors in a glove box.

We have been advancing research on solvent extraction using monoamide extractants for spent nuclear fuel reprocessing. Because monoamides do not contain phosphorus, they can be decomposed into gases by incineration, reducing the secondary waste generation. In addition, monoamides can be diluted in dodecane, which is used in the commercially operating process (PUREX process); thus, current technologies developed for reprocessing equipment can be applied. The PUREX process uses tributyl phosphate (TBP) as an extractant, and monoamides are as stable as TBP against radiolysis. Furthermore, the degraded products of monoamides do not have detrimental effects on solvent extraction.

The extraction properties of monoamides toward uranium (U) and plutonium (Pu) depend on their structures. As an example, the effects of the nitric acid concentration on the distribution ratios of U (D_U) and Pu (D_{Pu}) by *N,N*-di(2-ethylhexyl) butanamide (DEHBA, Fig.8-13) are shown in Fig.8-14. Here, the values of D_U and D_{Pu} indicate the extraction power of monoamides toward U and Pu, respectively, and the ratios of U and/or Pu extracted by monoamides increase with increasing distribution ratio.

As shown in Fig.8-14, DEHBA extracts U and Pu when the nitric acid concentration is ca. 3 mol/ℓ. DEHBA still extracts U when the nitric acid concentration decreases to 0.7–1 mol/ℓ, whereas it extracts very little Pu. We focused on the specific features of DEHBA and proposed a reprocessing system in which U and Pu are separated by adjusting the nitric acid concentration. The PUREX process requires reducing agents for Pu. On the other hand, our system using DEHBA does not require reducing agents, which simplifies reprocessing.

We conducted a continuous U and Pu extraction experiment using mixer-settlers, with the goal of establishing a reprocessing system that uses DEHBA (Fig.8-15). The results showed that the ratios of U and Pu extracted from a simulated dissolution solution of spent nuclear fuel are more than 99.9%, and the ratio of Pu recovered in the U+Pu fraction is more than 97%. These results have supported the realization of a reprocessing system that uses DEHBA.

Part of this study was the result of research entrusted to the Japan Atomic Energy Agency (JAEA) by the Ministry of Economy, Trade and Industry (METI).

Reference

Ban, Y. et al., Distribution of U(VI) and Pu(IV) by *N,N*-di(2-Ethylhexyl)Butanamide in Continuous Counter-Current Extraction with Mixer-Settler Extractor, Solvent Extraction and Ion Exchange, vol.30, issue 2, 2012, p.142–155.

8–6 One-Pot Biofabrication of Protein-Decorated Gold Nanoparticles

— Facile, Rapid, and Efficient Biofabrication and Immunoassay —

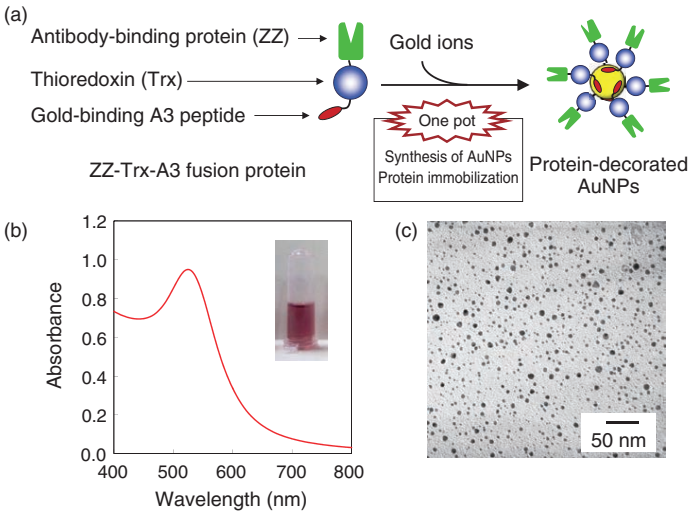

Fig.8-16 Synthesis of AuNPs and immobilization of protein using ZZ-Trx-A3 fusion protein

(a) The ZZ-Trx-A3 construct can simultaneously direct both the synthesis of AuNPs and the immobilization of the protein on the AuNPs in a single step.
(b) The synthesized AuNPs display the SPR band at 525 nm and yield a reddish solution.
(c) TEM shows that the synthesized AuNPs exhibit spherical morphologies with a narrow size distribution (4.4±1.6 nm).

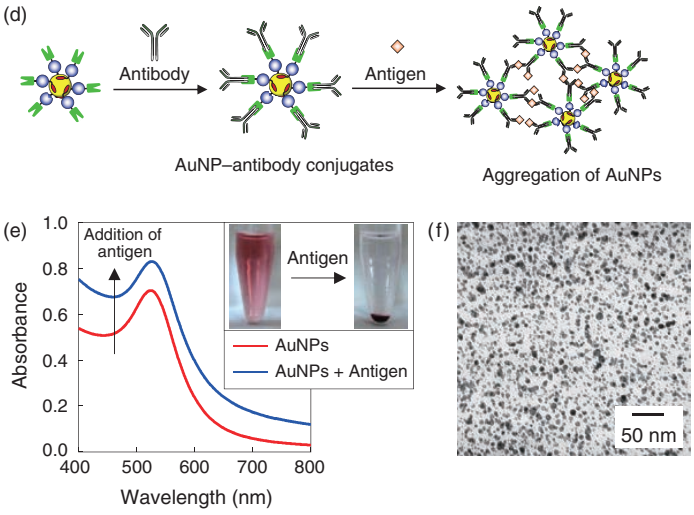

Fig.8-17 Immobilization of antibody on AuNPs and immunoassay

(d) AuNP–antibody conjugates are readily prepared through specific binding of the antibody to the ZZ domain on the AuNPs; they can detect the target antigens based on AuNP aggregation.
(e) Addition of target antigens to the AuNP solution yields a turbid solution and generates AuNP precipitation, which is clearly visible to the naked eye.
(f) TEM demonstrates the formation of AuNP aggregates through the antigen–antibody reaction.

Gold nanoparticles (AuNPs) have received increasing attention in the field of nanotechnology because of their attractive optical properties. AuNP–antibody conjugates are particularly valuable in biomedical applications such as immunoassays for the detection of target antigens and are actually used in a pregnancy test kit. However, the typical fabrication of AuNP–antibody conjugates is time-consuming and requires multiple steps: AuNP synthesis followed by antibody immobilization. In addition, the physical adsorption method, which is commonly employed to immobilize antibodies on the surface of AuNPs, usually yields randomly oriented proteins.

To address this issue, we demonstrate a simple and new strategy for biofabrication of AuNP–antibody conjugates using peptide-functionalized proteins. The strategy is based on a one-pot direct approach that couples peptide-mediated biomineralization and protein immobilization in one simultaneous process. We prepared a tripartite fusion protein (ZZ-Trx-A3) consisting of an antibody-binding protein (ZZ domain), a AuNP-stabilizing protein (thioredoxin) and a gold-binding A3 peptide. By mixing ZZ-Trx-A3 with gold ions, intensely reddish solutions were obtained, and the surface plasmon resonance (SPR) band was observed at 525 nm (Fig.8-16). This indicates the formation of AuNPs from gold ions. Using transmission electron microscopy (TEM), we confirmed that the AuNPs showed spherical morphologies with a narrow size distribution (average diameter 4.4±1.6 nm). The novel method enables facile and rapid fabrication of protein-decorated AuNPs within 20 min and is preferable to conventional methods requiring a few days. In addition, the AuNPs remained suspended in the solution for at least 6 months and in salt solutions adjusted to high concentrations, indicating the high stability of the AuNPs in aqueous media.

As shown in Fig.8-17, protein-decorated AuNPs can be readily derivatized with intact antibodies owing to the specific binding to the ZZ domain on the AuNPs. The addition of target antigens to the AuNP solution yielded a turbid solution owing to AuNP aggregation through the antigen–antibody reaction, which increased the background absorbance. Furthermore, AuNP precipitation was observed after the solution stood for a few hours, and this precipitation was clearly visible to the naked eye.

We expect that our approach can be expanded to produce a variety of biomolecule-decorated AuNPs and can be used in versatile applications in addition to biomedical applications.

Reference

Shimojo, K. et al., Facile, Rapid and Efficient Biofabrication of Gold Nanoparticles Decorated with Functional Proteins, Analyst, vol.137, issue 10, 2012, p.2300–2303.

8–7 Analysis of Age Determination of Individual Plutonium Particles

— Contribution of Development of Ultra-Trace Analytical Technique to IAEA Safeguard Activity —

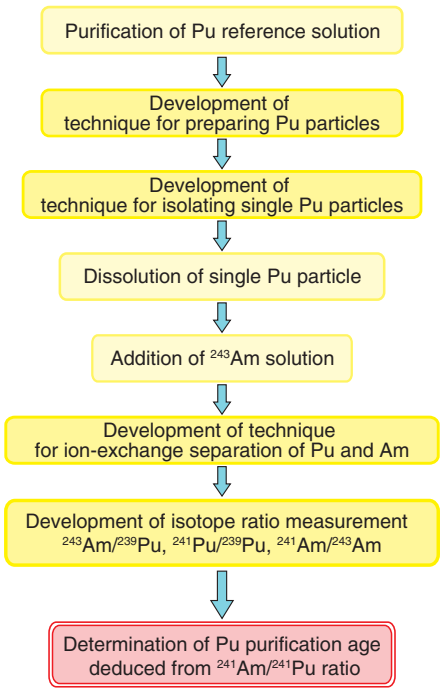

Fig.8-18 Development of analytical procedure for Pu purification age determination
An analytical technique for determining the purification age of an ultrafine Pu particle was realized by combining techniques for preparing a single Pu particle and for chemical separation.

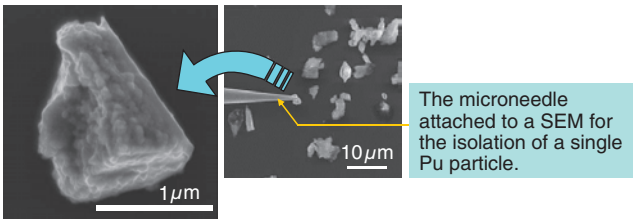

Fig.8-19 Pu particles prepared from a Pu reference solution
Micron-size age-known Pu oxide particles (right) were prepared. A technique for isolating a single particle was developed. The age of an isolated Pu particle (left) was determined.

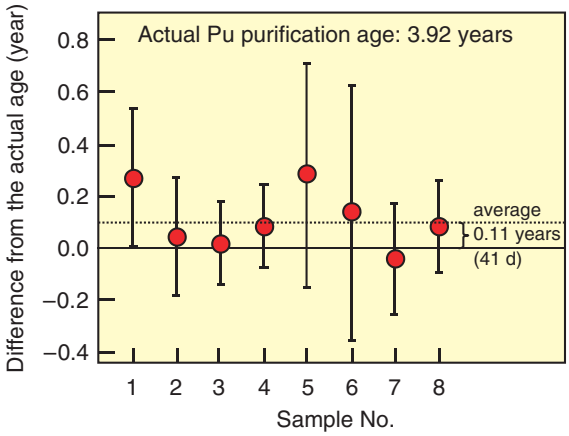

Fig.8-20 Pu purification age of single Pu particles determined by ^{243}Am spike method
The average age of eight Pu particles was in good agreement with the actual age (3.92 years) with a difference of 0.11 years (41 d).

Inspectors from the International Atomic Energy Agency (IAEA) take an environmental sample such as dust by wiping the floors in a nuclear facility, and the amount and isotopic composition of ultra-trace (10^{-15}–10^{-12} g) uranium (U) and plutonium (Pu) are analyzed to detect undeclared nuclear activities.

We developed a technique for isolating a single Pu particle and an analytical technique for the precise determination of the Pu purification age to upgrade the methods used to manage nuclear materials in Japan (Fig.8-18). The Pu purification age is evaluated by measuring the americium-241 (^{241}Am)/^{241}Pu atomic ratio precisely. A single Pu particle of ultra-trace amount (<10^{-12} g) should be analyzed because Pu of different origins may be mixed in a sample. ^{241}Am and ^{241}Pu must be chemically separated before they are subjected to mass spectrometry because they have the same atomic mass and cannot be separated with a mass spectrometer. The known techniques cannot provide the precise age of young Pu samples or ultra-trace samples because of the low ^{241}Am/^{241}Pu atomic ratio. It is also necessary to prepare a reference sample of young single Pu particles for evaluating the accuracy and precision of our analytical results. We developed the following techniques: the preparation of micron-diameter Pu oxide particles (Fig.8-19) from Pu purified by ourselves; a technique for isolating a single Pu particle by a microneedle attached to a scanning electron microscope (SEM); and chemical separation and isotope measurement of ultra-trace Pu and Am.

Precise measurement of the ^{241}Am/^{241}Pu ratio in a single Pu particle of 10^{-12} g was achieved. Each Pu particle was dissolved and spiked with pure ^{243}Am. The ^{241}Am/^{241}Pu ratio was obtained from the ^{243}Am/^{239}Pu ratio of a sample solution and the isotope ratios of Pu and Am in the chemically separated fractions. These ratios were measured with an inductively coupled plasma mass spectrometer. The determined age was in good agreement with the actual age (3.92 years), with a difference of 0.11 years (41 d) on average (Fig.8-20). By using this analytical technique, traces of nuclear activity can be detected. We can contribute to the IAEA safeguard activity by analyzing samples with our excellent techniques.

The present study was sponsored by the Ministry of Education, Culture, Sports, Science and Technology of Japan (MEXT).

Reference

Miyamoto, Y. et al., Precise Age Determination of a Single Plutonium Particle using Inductively Coupled Plasma Mass Spectrometer, Radiochimica Acta, vol.101, issue 11, 2013, p.745-748.

8–8 Detailed Simulation of Transfer of Radioactivity in Land Surface Ecosystems

— Development of Nuclide Transport Model for Atmosphere-Vegetation-Soil System —

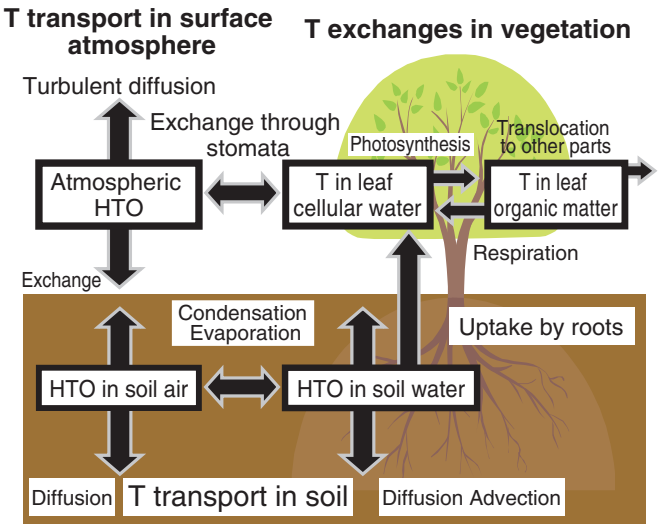

Fig.8-21 T transports and exchanges considered in the developed model
The model simulates the transport of HTO in a multilayered atmosphere and soil, and exchanges of T in vegetation, by considering the water and CO_2 cycles.

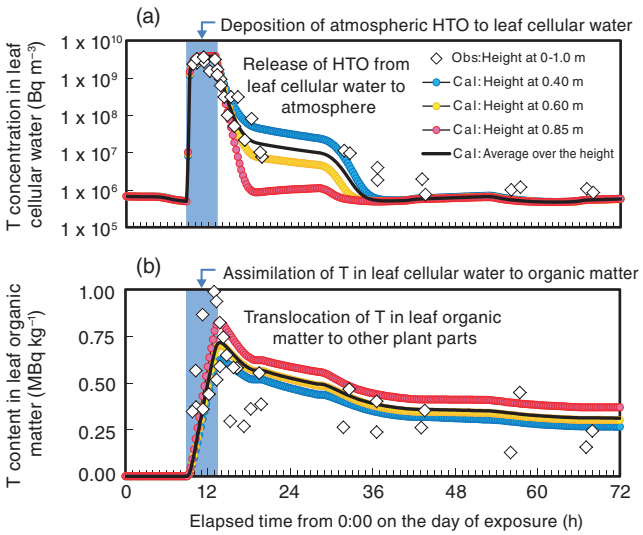

Fig.8-22 Reconstruction simulation of experiment in which grape plants were exposed to atmospheric HTO vapor
(a) The model simulates well the changes in T concentration in leaf cellular water due to deposition of atmospheric HTO during exposure (indicated by hatch marks) and release of HTO from the leaf cellular water after exposure. (b) The model also successfully predicts changes in T content of leaf organic matter that are caused by assimilation of leaf cellular water T by photosynthesis and translocation of T in the leaf organic matter.

Tritium (^{3}H, T) and radiocarbon (^{14}C) are important radionuclides in the assessment of the radiological impact to the public of nuclear industries because of the long half-lives of T (12 years) and ^{14}C (5730 years) and the biological importance of hydrogen and carbon in all life forms. T and ^{14}C are discharged through the operation of nuclear power plants and fuel reprocessing plants; in the natural environment, T and ^{14}C exist mainly in the form of tritiated water (HTO) and $^{14}CO_2$, respectively. Thus, the discharged T and ^{14}C are soon incorporated into the water and C cycles in the surrounding environment and are assimilated to vegetation as organic matter. The assimilated T and ^{14}C eventually deliver a dose to the public through ingestion pathways; therefore, the transfer of T and ^{14}C in land surface ecosystems should be precisely predicted to assess the dose due to nuclear facilities. However, models that dynamically consider the water and CO_2 cycles and the resultant T and ^{14}C transfer within a land surface ecosystem have not been developed; thus, assessments of the T and ^{14}C-derived dose have contained a range of uncertainties.

We developed a model that predicts the transfer of T and ^{14}C in a land surface ecosystem in detail. The dynamics of T (Fig.8-21) and ^{14}C in the surface ecosystem are modeled, and the modeled T and ^{14}C dynamics are incorporated into a land–surface water and CO_2 transport model (SOLVEG-II, developed by the Japan Atomic Energy Agency). The developed model successfully predicted the accumulation of T (Fig.8-22) and ^{14}C in leaves on plants exposed to HTO or $^{14}CO_2$.

For a comprehensive understanding of the land surface T and ^{14}C cycle, we then performed a range of numerical experiments using the model. The results demonstrated that during atmospheric T deposition to the soil, the loadings of HTO to the leaf cellular water due to root uptake of soil HTO significantly control the T concentration in the leaf cellular water, and hence the T content in leaf organic matter. Our results also quantified the increase in the ^{14}C content of vegetation due to below-ground $^{14}CO_2$ production caused by decomposition of ^{14}C-containing soil organic matter originating from ^{14}C-containing plant litter. Clearly, the model can be used to clarify the role or importance of each elemental process in the entire land surface T and ^{14}C cycle; this useful information cannot be obtained from field observations or laboratory experiments.

As a more practical application of the model, we are now investigating the transfer of T and $^{14}CO_2$ discharged at a nuclear facility over the surrounding land surface ecosystems through a simulation coupling the developed model and an atmospheric dispersion model.

Reference

Ota, M. et al., Importance of Root HTO Uptake in Controlling Land–Surface Tritium Dynamics after An–Acute HT Deposition: A Numerical Experiment, Journal of Environmental Radioactivity, vol.109, 2012, p.94–102.

8–9 Subsurface Soils Participate in Global Carbon Cycle

— Carbon Dynamics Revealed by Tracing "Bomb" Radiocarbon over Past Half-Century —

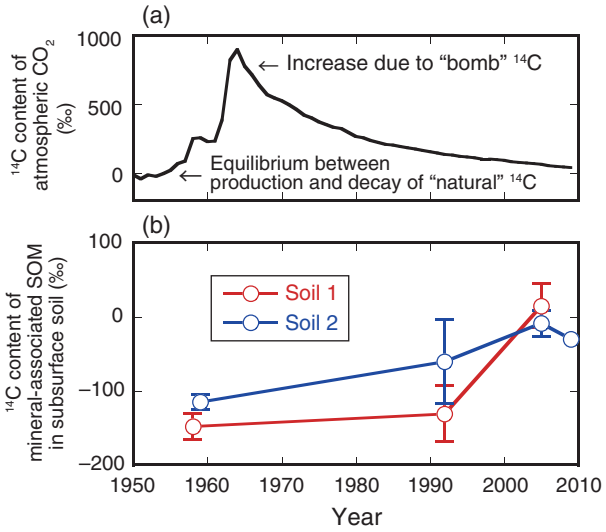

Fig.8-23 Carbon-14 content of atmosphere and subsurface soils
Carbon-14 content is expressed as per mil deviation of $^{14}C/^{12}C$ ratio of sample from that of atmospheric CO_2 in 1950. (a) Carbon-14 content of atmospheric CO_2 rapidly increased due to nuclear weapons testing in the early 1960s. (b) Carbon-14 content of mineral-associated SOM in subsurface soils remained low; however, it increased markedly from 1992 to 2005 owing to incorporation of "bomb" ^{14}C.

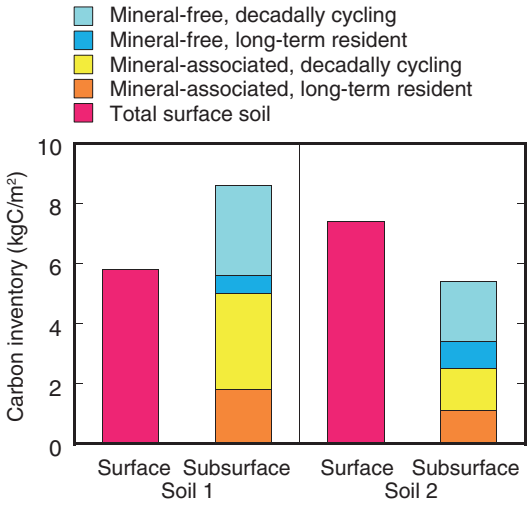

Fig.8-24 Stock and turnover of C in subsurface soils
Subsurface soils store as much C as surface soils (the upper 20 cm). About half of the subsurface soil C was not associated with soil minerals, >70% of which was estimated to be decadally cycling C. Decadally cycling C was also found in mineral-associated SOM. Overall, the amount of C that turns over on decadal timescales in subsurface soils reached 3–6 kg/m².

Soil plays an important role in the global carbon (C) cycle through soil–atmosphere C exchange. Recent studies have shown that soils store more C in the subsurface horizons (20–60 cm depth) than in the surface horizons (the upper 20 cm). However, subsurface soil C has received little attention in terms of its contribution to C exchange because it has been thought to be very stable on the basis of its average age of centuries to millennia.

We used radiocarbon (^{14}C) to identify the dynamic nature of C in subsurface soils. There are two main sources of ^{14}C: "natural" ^{14}C that is produced in the upper atmosphere by cosmic rays, and "bomb" ^{14}C that was produced by atmospheric nuclear weapons testing during the early 1960s (Fig.8-23(a)). Similar to stable ^{12}C, ^{14}C in the atmosphere is fixed as organic matter by plants via photosynthesis and then enters soils. Carbon-14 decays with a half-life of 5730 years in soils; thus, a lower ^{14}C content in soil organic matter (SOM) reflects a longer residence time of C in the soils. On the other hand, the incorporation of bomb ^{14}C into the soils increases the ^{14}C content in SOM. Therefore, we hypothesized that C exchange that occurs on timescales of decades through subsurface soils can be identified by tracing bomb ^{14}C incorporation over the past half-century, if it really exists.

The ^{14}C content was determined for subsurface soil samples taken several times from 1958 to 2009 at two forest sites in California. We found an increase in the ^{14}C content in mineral-associated SOM with a time lag of >20 years after the increase in the atmosphere (Fig.8-23(b)). A model analysis showed that ~40%–70% of the SOM turns over on decadal timescales. We also found bomb ^{14}C incorporation in mineral-free SOM and CO_2 released from subsurface soils collected in 2009.

The results demonstrate that subsurface soils store a large amount of C that is exchanged with the atmosphere (Fig.8-24) and that a lagging response of the C to climate change is possible. The findings will improve our understanding of the global C cycle.

Reference
Koarashi, J. et al., Dynamics of Decadally Cycling Carbon in Subsurface Soils, Journal of Geophysical Research, vol.117, issue G3, 2012, p.G03033–1–G03033–13.

Research and Development on Naturally Safe HTGR and Nuclear Heat Application Technologies

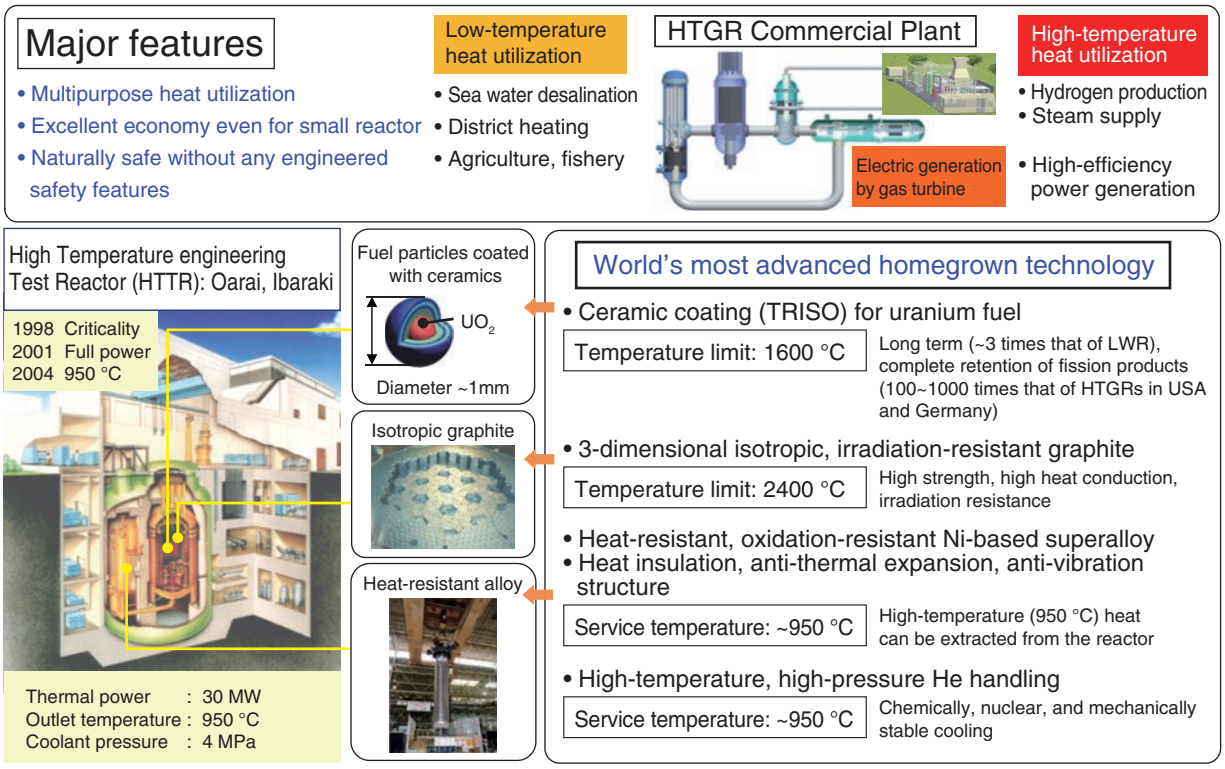

Fig.9-1 Outline of HTGR with features, heat utilization, major specifications, and technologies of HTTR
The HTGR is a thermal neutron reactor, helium gas cooled and graphite moderated, and can meet various heat production requirements. In particular, the HTGR can be a naturally safe nuclear reactor, and it is strongly expected to regain the public trust in nuclear power.

We have been conducting research on the naturally safe High Temperature Gas-cooled Reactor (HTGR) and its applications in our contribution to building a low-carbon society.

The HTGR can supply high-temperature heat at 950 °C, well exceeding the 300 °C of current light water reactors (LWRs), by using inert helium gas instead of water as a coolant. The same amount of fission energy from uranium can produce a greater quantity of electricity and hydrogen when higher temperature heat is obtained from the reactor.

Three other cutting-edge Japanese technologies that make it feasible to obtain such high-temperature heat in the HTGR have been developed by the Japan Atomic Energy Agency. The first is fabrication technology for ceramic-coated fuel particles about 1 mm in diameter. Ceramics remain stable even at 2500 °C and provide superior heat-resistant coating layers to contain radioactive fission products within the fuel particles. The second is fabrication technology for isotropic and irradiation-resistant graphite blocks. Graphite is generally non-isotropic in that its material properties such as strength and thermal conductivity are dimension-dependent, which is to be avoided in reactor construction. The third is a manufacturing technology for heat-resistant and oxidation-resistant superalloys with careful composition of the alloy content. With these major technologies and further development of expertise in high-temperature structural design and helium gas handling, we successfully produced high-temperature heat at 950 °C from the reactor in 2004 for the first time worldwide (Fig.9-1).

The heat from the HTGR is useful not only for power generation but also for the production of hydrogen for fuel cell cars and direct reduction iron-making, and of a steam supply for industry. The waste heat can be used for district heating and desalination. The thermal discharge to the environment can be dramatically reduced to less than 30%, compared to 67% for an LWR.

It is feasible to prevent accidental overheating and oxidation of the fuel coating layers and explosive gas generation using physical phenomena without any engineered safety features. The self-regulating features assure no harmful release of radionuclides to the general population and the environment in any accident. It is this unique safety advantage of the HTGR that is expected to regain the public's trust in nuclear power, which is strongly needed after the accident at the Tokyo Electric Power Company, Incorporated Fukushima Daiichi Nuclear Power Station.

The conceptual design of a small HTGR that has excellent safety and economic potential has been completed, and the first draft of the safety design philosophy for the HTGR hydrogen production system has been presented. Furthermore, research on improving the efficiency of the thermochemical iodine–sulfur process is ongoing (Topics 9-1, 9-2, 9-3).

9–1 Small Nuclear Reactor for Multiple Heat Applications with Attractive Safety Features

— Conceptual Design of Small High-Temperature Gas Cooled Reactor for Developing Countries —

Design targets and results

Design items	Design target	Criteria	Results	Feasibility
①Core	Reduce the number of uranium enrichments	< 6 (HTTR: 12)	3	○
	Increase core power density	3.5 MW/m^3 (HTTR: 2.5 MW/m^3)	3.5 MW/ m^3	○
	Increase refueling interval	730 d (HTTR: 660 d)	730 d	○
②Component	Increase thermal duty of IHX	20 MW (HTTR: 10 MW)	20 MW	○
③System	Satisfy the user requirements for multiple heat applications	Heat supply for district heating network: 0 MW～25 MW (50% partial load operation of steam turbine)	0 MW～25 MW	○
		Demonstration test of gas turbine electricity generation and hydrogen production can be performed	Demonstration test can be performed using IHX	○
④Safety	Design of the engineered safety features of the residual heat removal system (i.e., VCS) as passive methods	Biological shielding concrete temp. at normal operation: <65 ℃	64.8 ℃	○
		Satisfy the acceptance criteria for accidents in safety analysis	All criteria are satisfied	○

Other design results

Design items	Results
Thermal power	50 MW
Reactor inlet temperature	325 ℃
Reactor outlet temperature	750 ℃, 900 ℃※
Primary pressure	4 MPa
Reactor pressure vessel material	Mn-Mo steel

※ demonstration of the gas turbine and hydrogen production

Example of system configuration

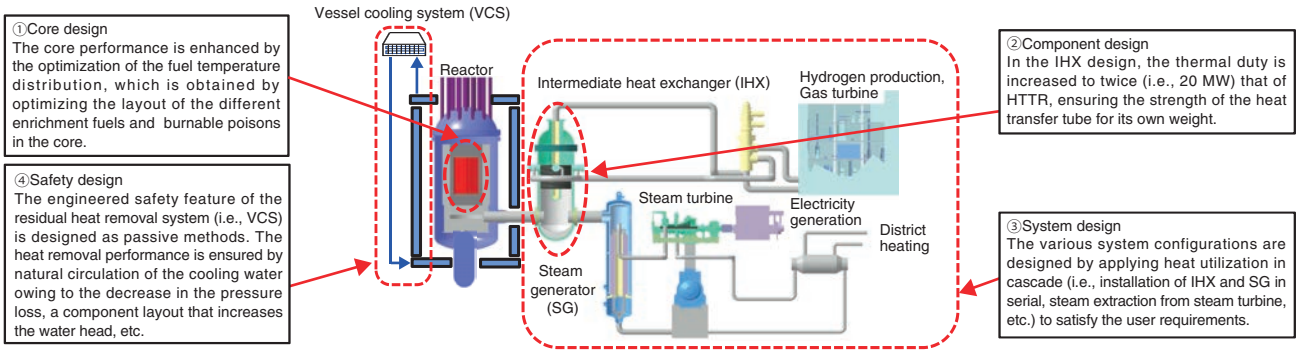

Fig.9-2 Design targets and results of small HTGR system design
The conceptual design of a 50 MWt small HTGR system was completed. It can satisfy the user requirements for multiple heat applications, and its performance is superior to that of the HTTR. The technical feasibility was confirmed by the results of the core, component, and system design, and a safety analysis in the event of representative accidents.

We tested the High-Temperature engineering Test Reactor (HTTR) to establish the high-temperature gas cooled reactor (HTGR) fundamental technologies and to obtain the data required for commercial HTGR design. Since 2010, we also developed the conceptual design for a 50 MWt small HTGR system that can satisfy the user requirements, aiming at construction of a demonstration plant in a developing country in the 2020s. Its performance was improved over that of the HTTR without significant research and development, using the knowledge obtained from HTTR design and operation (Fig.9-2).

In the core design, the number of uranium enrichments was reduced to three (i.e., one-quarter that of the HTTR), and the average core power density was increased to 3.5 MW/m^3 (i.e., 1.4 times that of the HTTR), satisfying the maximum fuel temperature criterion throughout the burnup period of 730 d. In the component design, the thermal duty of the intermediate heat exchanger (IHX) was increased to twice (i.e., 20 MW) that of the HTTR; the strength of the heat transfer tube for its own weight was ensured by increasing the tube diameter to decrease the stress and by increasing the flow rate to increase the heat transfer performance. The system configurations were determined so as to use the nuclear heat for district heating and process heat based on a steam turbine system, and to demonstrate a helium gas turbine and hydrogen production to satisfy the user requirements. In the safety design, the residual heat removal system (the vessel cooling system) was designed as a passive system. The safety was confirmed by a safety analysis of representative accidents.

The Republic of Kazakhstan initiated a development program for the nuclear industry in that country in June 2011, which includes a construction plan for the Kazakhstan high-temperature gas-cooled reactor (KHTR) based on this small HTGR system.

Reference

Ohashi, H. et al., Conceptual Design of Small-Sized HTGR System (IV) –Plant Design and Technical Feasibility–, JAEA-Technology 2013-016, 2013, 176p. (in Japanese).

9–2 Proposal for HTGR Safety Design Criteria upon User Request

— Allow H_2 Plant Construction Coupled to HTGR under Non-Nuclear Regulations —

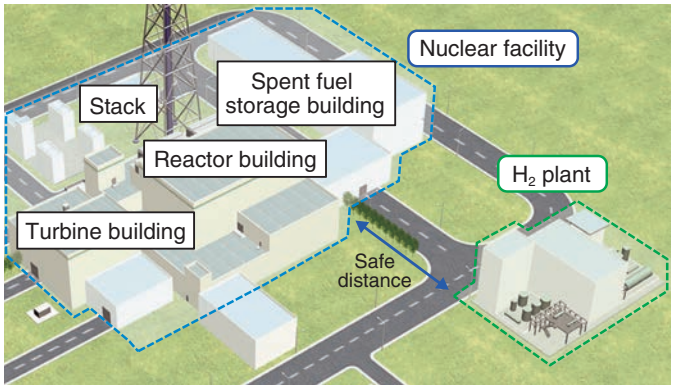

Fig.9-3 Conceptual layout of nuclear facility and H_2 plant
To ensure the integrity of safety functions in the nuclear facility against fire and explosion and the intrusion of hazardous chemicals into the control room owing to leakage in the H_2 plant, an appropriate safe distance is set between the nuclear facility and the H_2 plant.

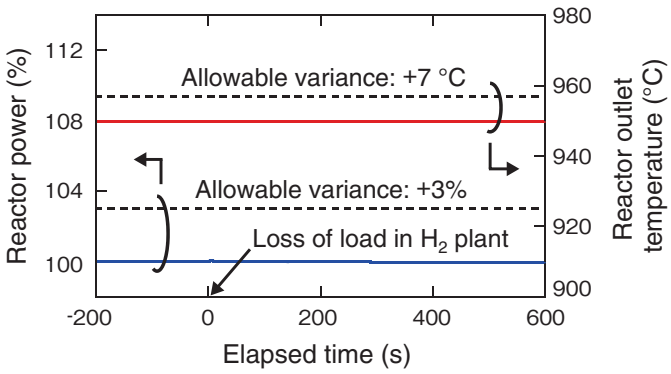

Fig.9-4 Reactor transient response during loss of load in H_2 plant
Variations in the power and coolant temperature in the reactor can be mitigated within the value allowed in normal operation during loss of load in the H_2 plant because of a cooling system installed downstream of the H_2 plant.

Toward the realization of hydrogen production using heat from a high-temperature gas-cooled reactor (HTGR), it is necessary to ensure the safety of the nuclear facility against postulated events initiating in the hydrogen production plant (H_2 plant) and to construct the H_2 plant under non-nuclear regulations upon user request. The present study focuses on a H_2 plant using the thermochemical water splitting iodine–sulfur (IS) process and investigates the safety design criteria, which consist of the requirements for constructing hydrogen production plants under conventional chemical plant regulations as well as the requirements for collocation of a nuclear facility and a hydrogen production plant. In addition, design considerations to meet the criteria are suggested.

The design considerations of the nuclear facility are identified as the assurance of a safe distance between the nuclear facility and H_2 plant, the installation of isolation valves against leakage of combustible gas; and early detection, the assurance of a safe distance between the nuclear facility and H_2 plant against hazardous chemical leakage (Fig.9-3).

The mitigation of fission product migration from the reactor to the H_2 plant and the assurance of continuous reactor operation against abnormal conditions in the H_2 plant are identified as the requirements for constructing the H_2 plant under conventional chemical plant regulations. In addition, the assurance of sufficient capacity for helium purification systems and the installation of a cooling system downstream of the H_2 plant are suggested as design considerations to meet the requirements.

The technical feasibility of the suggested design considerations is evaluated for the HTTR-IS system, an HTGR hydrogen production system coupling the HTTR and a H_2 plant using the IS process. The results showed that a safe distance of 40 m, determined by the chemical plant regulations against fire and explosion of combustible gas, can be ensured. In addition, the toxicity limit issued by the United States National Institute for Occupational Safety and Health against leakage of hazardous chemicals can be satisfied. Furthermore, the results demonstrated the feasibility of H_2 plant construction under non-nuclear regulations by showing that the tritium concentration in the H_2 plant can be maintained below the regulation limit, and normal reactor operation can be achieved during abnormal conditions in the H_2 plant (Fig.9-4).

The proposed criteria can be used for coupling not only a H_2 plant but also other chemical plants such as a steam reforming plant. The adequacy of the criteria will be assessed under an outside committee. We also aim to standardize the criteria internationally under the International Atomic Energy Agency.

Reference

Sato, H. et al., A Proposal for Safety Design Philosophy of HTGR for Coupling Hydrogen Production Plant, JAEA-Technology 2013-015, 2013, 68p. (in Japanese).

9–3 Increased Energy Efficiency for Hydrogen Production
— Study of Ion Permeation Mechanism in Membrane of HI Concentrator —

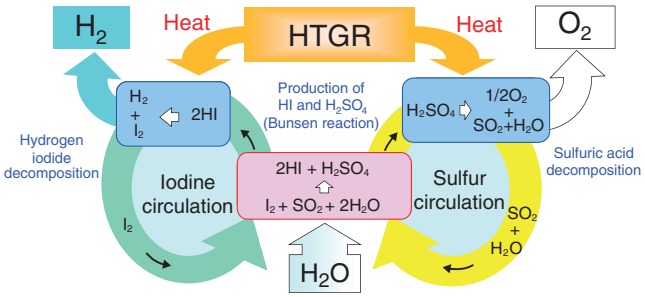

Fig.9-5 Thermochemical water-splitting IS process
Hydrogen and oxygen are produced from water by a combination of three chemical reactions. The process can harness the heat generated by HTGRs.

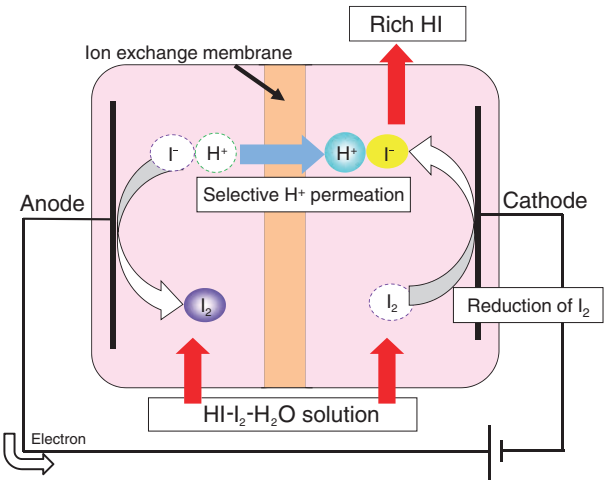

Fig.9-6 Hydriodic acid concentration using HI concentrator
Enriched HI solution can be obtained by reducing iodine (I_2) and permeating protons (H^+) through the ion-exchange membrane.

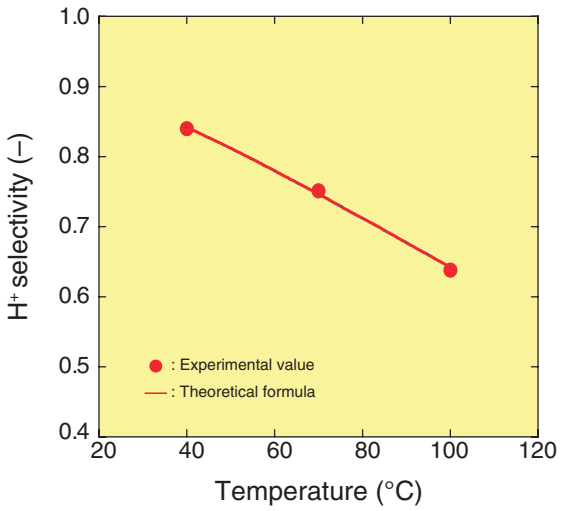

$$t_+ = \frac{D_{H^+} n_{H^+}}{D_{H^+} n_{H^+} + D_{I^-} n_{I^-}}$$

D: diffusion coefficient of ions
n: ions content of membrane

Fig.9-7 Temperature dependence of H^+ selectivity: comparison of experimental results and theoretical formula
Good agreement is observed between the experimental results and the theoretical formula based on the mathematical model of permeation phenomena in the radiation-grafted membrane. This suggests that a high-performance membrane can be prepared by adjusting the membrane properties.

We have been investigating a hydrogen production method known as the iodine-sulfur (IS) process for heat application of high-temperature gas-cooled reactors (HTGRs). The IS process is a water-splitting thermochemical cycle without carbon dioxide emission that proceeds by chemical reactions of iodine and sulfur compounds (Fig.9-5). One of the important R&D goals for industrialization of the process is to improve the hydrogen production efficiency.

A task to improve efficiency is to concentrate the circulating material, hydriodic acid (HI solution, an iodine compound), with low energy consumption; therefore, we have been studying an electro-electrodialysis method. This method can enrich HI in the HI solution with a HI concentrator employing ion-exchange membranes that selectively permeate protons (H^+) (Fig.9-6). Thus far, we successfully prepared novel ion-exchange membranes using a radiation-induced graft polymerization technique (radiation-grafted membranes), which are a key device for low energy consumption in the HI concentrator.

We are currently pursuing studies to improve the performance of the radiation-grafted membrane. For this purpose, we have tried to reveal the ion permeation mechanism using a mathematical model to characterize the performance.

In the model, the driving force of ion movement is assumed to be the electric potential gradient. A theoretical formula for H^+ selectivity, which is an essential performance, was derived as a function of the H^+ content, iodide ion content, and diffusion coefficient. The good agreement between the experimental results and the theoretical formula (Fig.9-7) shows that the model we employed is appropriate.

Next, we plan to modify the model regarding the effects of HI concentration. In addition, we will work on the development of higher-performance membranes by adjusting the membrane properties. One way to do this is by varying the membrane's affinity to HI using grafted polymers to introduce new functional groups.

Reference

Tanaka, N. et al., Effect of Temperature on Electro–Electrodialysis of HI–I_2–H_2O Mixture using Ion Exchange Membranes, Journal of Membrane Science, vols.411–412, 2012, p.99–108.

Executing Decommissioning of Nuclear Facilities and Treatment and Disposal of Radioactive Waste

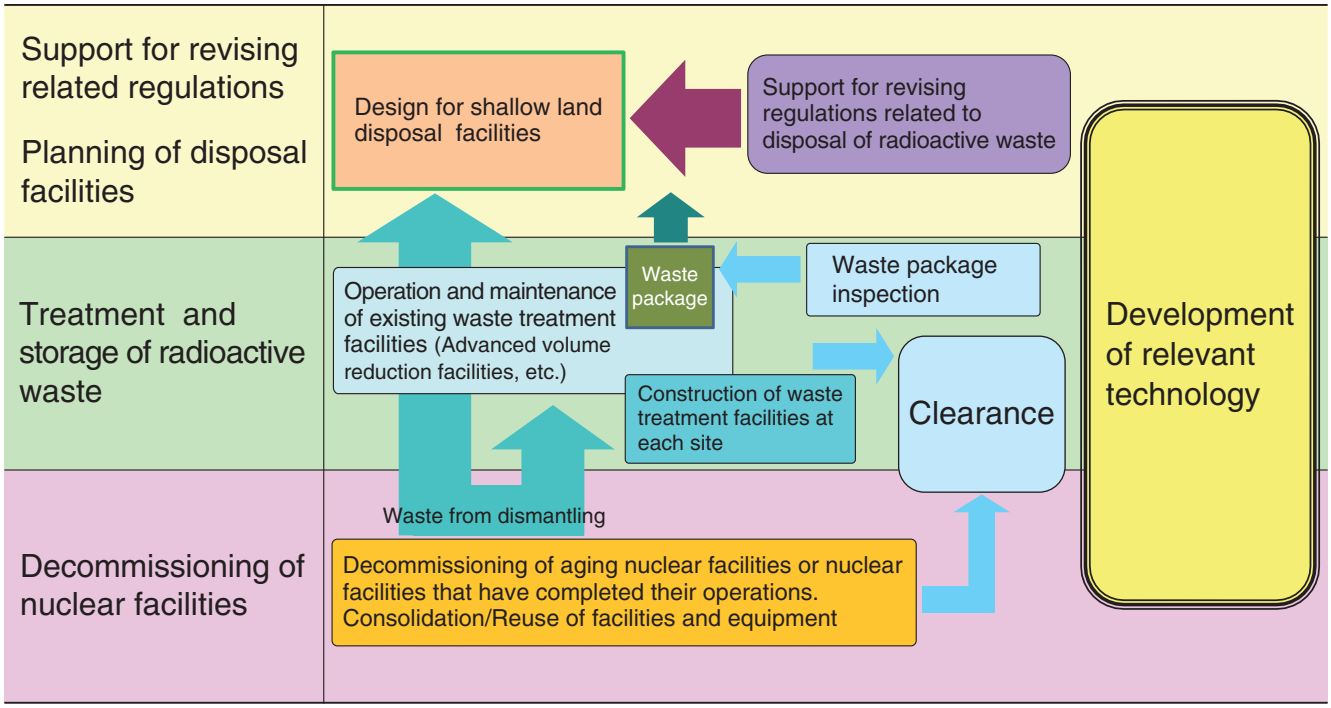

Fig.10-1 Outline of measures for decommissioning and radioactive waste treatment/disposal
We are setting up systems for the purpose of decommissioning nuclear facilities and managing radioactive waste. In addition, we are developing related technology (e.g., decommissioning, treatment, disposal), planning and constructing radioactive waste treatment/disposal facilities, and providing support for the revision of related regulations.

Safe and efficient decommissioning of nuclear facilities and radioactive waste treatment/disposal are two of our major missions in advancing our research and development (R&D) activities. In these missions, we will be disposing of radioactive waste generated not only by our research activities but also by universities, institutes, industrial facilities, and other sites.

We are setting up systems for the decommissioning of nuclear facilities and for managing radioactive waste, and also developing the related technology (Fig.10-1).

Moreover, we are studying the application of our R&D products to deal with the accident at the Tokyo Electric Power Company, Incorporated Fukushima Daiichi Nuclear Power Station.

R&D for Waste Treatment

In radioactive waste processing and disposal, it is important to reduce the expense and to improve the safety of disposal. Liquid waste, including low-level radioactive materials resulting from reprocessing of spent nuclear fuel, is stored by the Japan Atomic Energy Agency and includes large amounts of nitrate salts. Some liquid wastes are solidified with cement, and the solidified cement form is disposed of in an underground facility. Because nitrate salts are harmful to human health, the total concentration of nitrate and nitrite in environmental water and drinking water is required to be less than a standard value. A superior catalyst showing such properties as a high nitrate decomposition rate, decomposition of all nitrate ions, little by-product generation, and high durability should be developed.

The catalyst we are developing was mixed in a sodium nitrate solution, and the mixture was stirred and maintained at a set temperature. We could decompose almost all the nitrate ions by slowly delivering hydradine monohydrate as a reductant dropwise into the mixture (Topic 10-1).

R&D for Waste Disposal

The radioactivity in low-level radioactive wastes generated during decommissioning of nuclear facilities should be identified in order to dispose of the wastes.

The applicability of a capillary electrophoresis–laser-induced fluorescent detection method (CE-LIF) in the development of a rapid analytical method for actinides in radioactive wastes was studied. In this study, several types of emissive probes with different chelating moieties were synthesized and applied to CE-LIF. As a result, an acyclic hexadentate probe achieved successful detection and separation of americium and neptunium (Topic 10-2).

10–1 Successful Development of Nitrate Decomposition Technology
— For Safe Disposal of Low-Level Radioactive Waste —

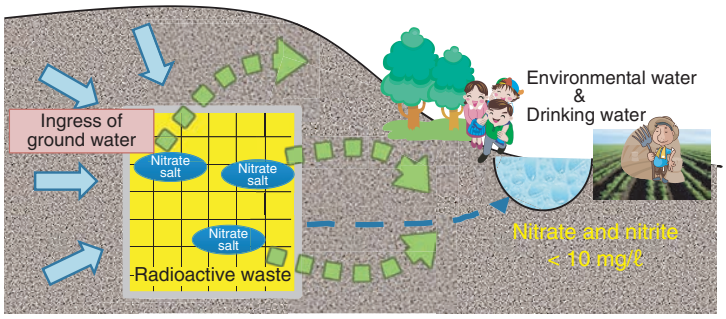

Fig.10-2 Effect of buried radioactive waste including nitrate salts
The nitrate and nitrite concentration in environmental water and drinking water is required by law to be less than 10 mg/ℓ. When radioactive waste including large amounts of nitrate salts is buried, the influence of nitrates leached by contact with groundwater is a concern. Therefore, a technique for removing nitrates from radioactive waste is important.

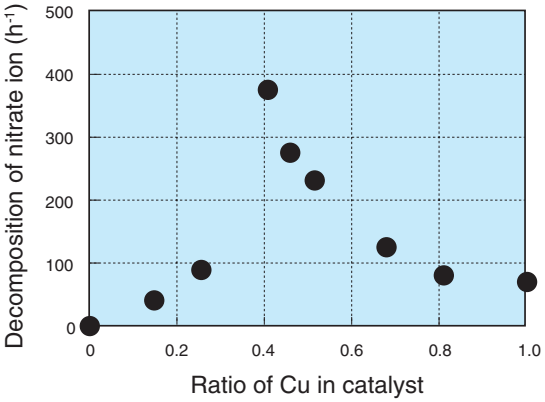

Fig.10-3 Relationship between copper ratio in catalyst and nitrate decomposition rate
The effect of the copper ratio in the catalyst on nitrate decomposition was investigated. A catalyst with a copper ratio of 0.4 was found to decompose nitrate much more rapidly.

When spent nuclear fuel is reprocessed, liquid waste including low-level radioactive materials is generated. The liquid waste includes large amounts of nitrate salts. Because nitrate salts are harmful to human health, the total concentration of nitrate and nitrite in environmental water and drinking water is required to be less than 10 mg/ℓ. When solidified liquid wastes including large amounts of nitrate salts are buried underground, the nitrates in the waste are expected to be eluted into the environment by contact with groundwater (Fig.10-2). Therefore, it is important to remove the nitrate salts before solidification. In industry in general, especially in the field of agriculture, several techniques have been developed for removing nitrate salts at the level of several hundreds of milligrams per liter in agricultural drainage contaminated by fertilization. The nitrate in such waste water is decomposed mainly by using the power of microorganisms in nature. On the other hand, the concentration of nitrate salts in radioactive liquid waste is high, about several hundred thousand milligrams per liter, and a new denitration method is required because microorganisms cannot survive in such harsh conditions. Therefore, we developed a technique for decomposing nitrate by a chemical reaction using a catalyst.

Nitrate ions are reduced to nitrogen using a reductant and a catalyst made of a palladium (Pd) and copper (Cu) alloy. Pd is a precious metal and is expensive, so the performance of the catalyst affects the running cost in practical use. Therefore, a superior catalyst showing such properties as a high nitrate decomposition rate, decomposition of all nitrate ions, little generation of by-products such as nitrogen monoxide and ammonia, and high durability should be developed.

Here we developed a catalyst consisting of micropowders of Pd–Cu alloy supported on the surface of carbon powder and demonstrated its performance. The catalyst was mixed in a sodium nitrate solution including about 300000 mg/ℓ of nitrate ions, and the mixture was stirred and kept at a temperature of 80 °C. We could decompose almost all the nitrate ions by slowly delivering hydradine monohydrate as a reductant dropwise into the mixture. The relationship between the decomposition rate and the Cu ratio in the catalyst was investigated (Fig.10-3), and the maximum decomposition rate was observed when the Cu ratio was around 0.4.

We succeeded in the development of a catalyst that was able to decompose nitrate ions at a high concentration. We will keep developing this technology by enhancing the catalyst's durability.

Reference

Kadowaki, H., Meguro, Y., Applicability of a Catalytic Reduction Method using a Palladium–Copper Catalyst and Hydrazine for the Denitration of a Highly Concentrated Nitrate Salt Solution, Journal of Nuclear Science and Technology, vol.49, no.9, 2012, p.881–887.

10–2 Simplification of Analysis of Actinides in Radioactive Wastes
— Development of an Analytical Method using Capillary Electrophoresis —

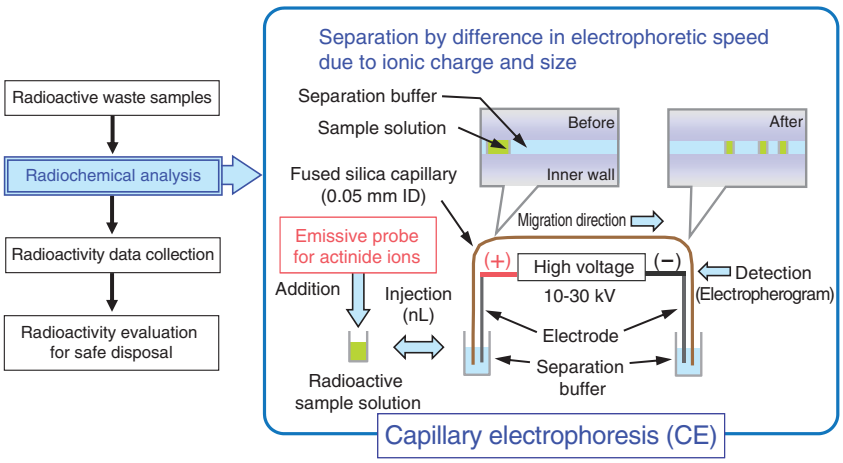

Fig.10-4 Development of a simple and rapid analytical method using capillary electrophoresis
For the disposal of radioactive wastes, it is necessary to collect radioactivity data from radioactive waste samples. To reduce the radiation exposure of operators during the analytical procedure, a simple and rapid analytical method for actinides using capillary electrophoresis and new emissive probes was developed.

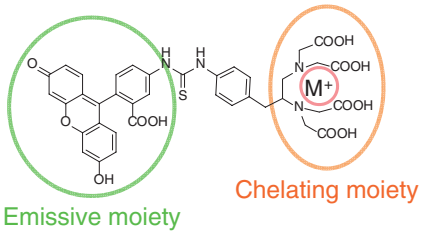

Fig.10-5 Emissive probe L for actinide ions
Probe L is composed of an emissive moiety for improved sensitivity and a chelating moiety for connecting with actinide ions. Here, a probe with an acyclic hexadentate chelating moiety is shown.

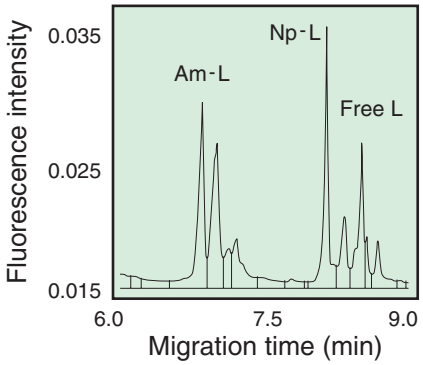

Fig.10-6 Typical electropherogram of actinide complexes of Am and Np
Am and Np were successfully detected and separated using probe L. "Am-L" represents an Am complex of probe L.

For the disposal of radioactive wastes, it is necessary to collect radioactivity data from radioactive waste samples. To reduce the radiation exposure of operators during the analytical procedure, a simple and rapid analytical method of detecting actinides using capillary electrophoresis (CE) has been developed (Fig.10-4). Although CE has been employed for the analysis of ionic species, including actinide ions, and has the advantages of high separation efficiency and simplicity, there is no report of a high-sensitivity CE method amenable to practical use for radioactive waste samples, to our knowledge.

This study focuses on the capillary electrophoresis–laser-induced fluorescent detection method (CE-LIF) for the purpose of dramatically improving the sensitivity. New emissive probes for the actinide ions, americium (Am) and neptunium (Np), suitable for CE-LIF were developed for the first time. The emissive probes designed for detecting actinides by CE-LIF are composed of an emissive moiety for improved sensitivity, a chelating moiety for connecting with actinide ions, and a spacer between them. A chelating moiety, the more important moiety, is required for stability and prevents dissociation during migration. In this study, seven types of newly synthesized emissive probes with different chelating moieties were applied to CE-LIF. As a result, an acyclic hexadentate probe (Fig.10-5) successfully detected and separated Am and Np (Fig.10-6). Detection limits of 11 ppt and 4.7 ppt were obtained for Am and Np, respectively. The sensitivity of this fluorescent detection method was about 90000–200000 times greater than that of a conventional UV detection method. This method, with its short analytical time (within 10 min), has great potential for application to analysis of radioactive waste samples for the reduction of the radiation exposure of operators.

Our research was performed as a part of a collaborative study with Saitama University, "Separation and Detection System for Actinide Ions by Capillary Electrophoresis Using Novel Fluorescent Probes."

Reference

Haraga, T. et al., Capillary Electrophoresis with Laser-Induced Fluorescent Detection Method using Highly Emissive Probes for Analysis of Actinides in Radioactive Wastes, Proceedings of the ASME 14th International Conference on Environmental Remediation and Radioactive Waste Management (ICEM2011), Reims, France, 2011, ICEM2011-59092, 5p., in CD-ROM.

11 Computational Science and E-Systems Research

Computational Science Activity in Nuclear Energy Research and Development

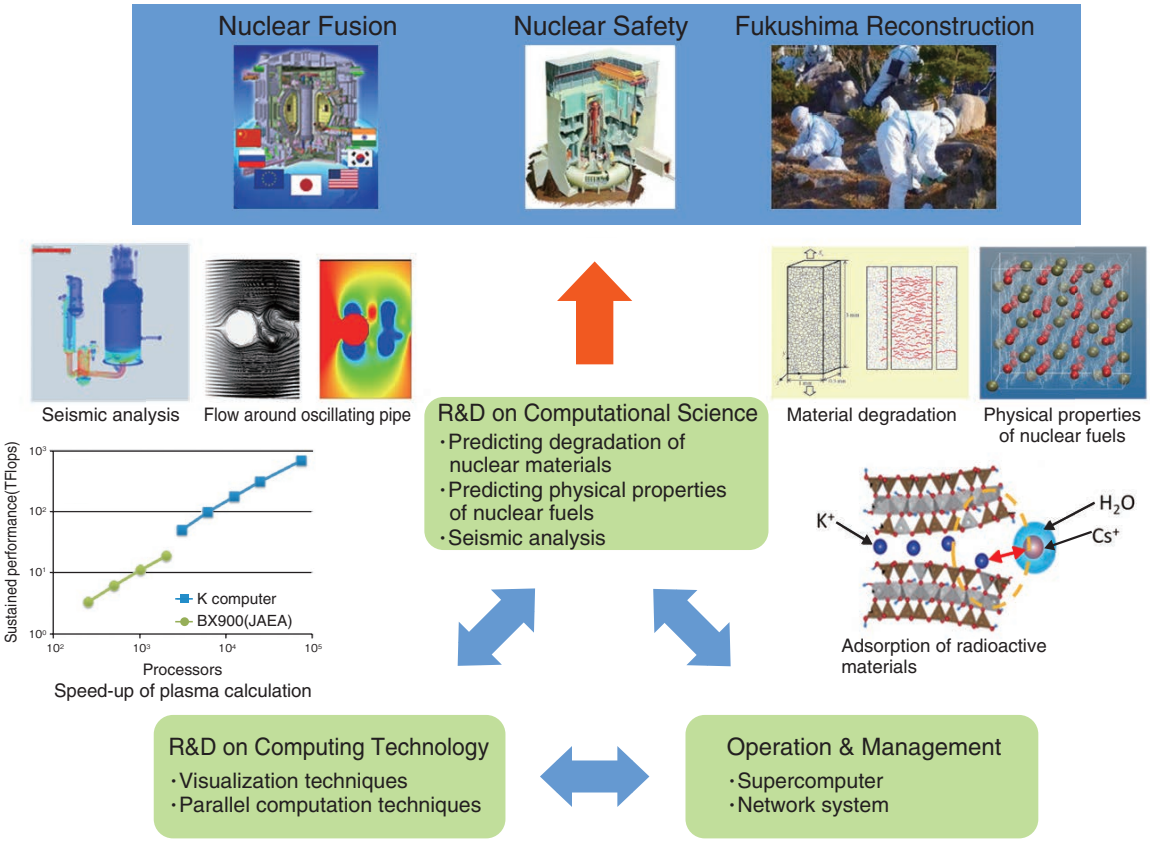

Fig.11-1 Computational science activity in nuclear energy R&D
The CCSE unites computational science research, computing technology research, and computer operation and management, and is creating cutting-edge knowledge and data in order to contribute to nuclear energy R&D and Fukushima reconstruction.

Computational science, which is known as the third type of research methodology after the theoretical and experimental approaches, is indispensable for understanding and predicting phenomena that cannot be resolved theoretically because of their complexity and/or that are difficult to observe experimentally because of cost and/or safety. Recently, the Ministry of Education, Culture, Sports, Science and Technology, which recognized the importance of computational science, officially announced a plan for developing a new supercomputer with a computing speed 100 times faster than that of the K computer. In addition, the news that China had successfully developed the fastest supercomputer in the world astonished the world. Such unremitting progress in computers is based on a background of increasing importance for computational science.

The Center for Computational Science and E-Systems (CCSE) manages and operates rapidly progressing supercomputers and promotes advanced research and development (R&D) on computational science using them. It grapples with important problems in nuclear energy R&D that require complicated large-scale computation, such as material degradation by aging, the high-temperature behavior of nuclear fuel, and evaluation of the earthquake resistance of structures. Furthermore, to create new knowledge about the mechanism of cesium soil pollution, the CCSE recently began a remarkable acceleration of advanced R&D by computer simulation (Fig.11-1).

In Topic 11-1, which aims at understanding the degradation mechanism of nuclear structural materials, the new concept that mobile hydrogen promotes crack growth is reported as a finding from a first principles calculation and thermodynamic analysis. In Topic 11-2, the strange thermal conductivity behavior exhibited by a new functional material, the topological superconductor, is introduced as a result obtained by a state-of-the-art computational science method. Topic 11-3 describes R&D for the international thermal nuclear fusion reactor in which the computation speed of the code for predicting plasma turbulence was materially improved using an innovative calculation method. In Topic 11-4, the effect of pipe oscillation on coolant flow is estimated as an example of seismic analysis. In Topics 1-5 and 1-19, the first principles calculation results for understanding the cesium adsorption mechanism of clay minerals and zeolites are reported as R&D for Fukushima reconstruction.

To contribute to Fukushima reconstruction and nuclear energy R&D, the CCSE will develop a state-of-the-art computer simulation technology as a key to resolving problems and strive continuously to be the leading force in computational science.

11–1 Moving Hydrogen Enhances Cracking in Iron

— Embrittling Effect of Mobile Hydrogen Clarified by First Principles Calculations —

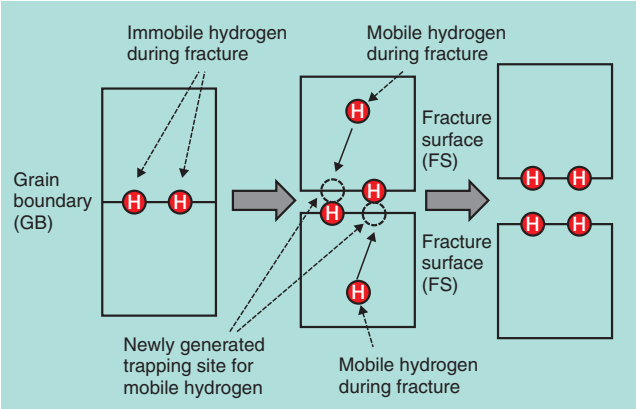

Fig.11-2 Concept of mobile hydrogen
Immobile hydrogen is segregated along grain boundary before fracture. In contrast, mobile hydrogen is segregated at newly generated segregation sites on fracture surfaces as they form during fracturing.

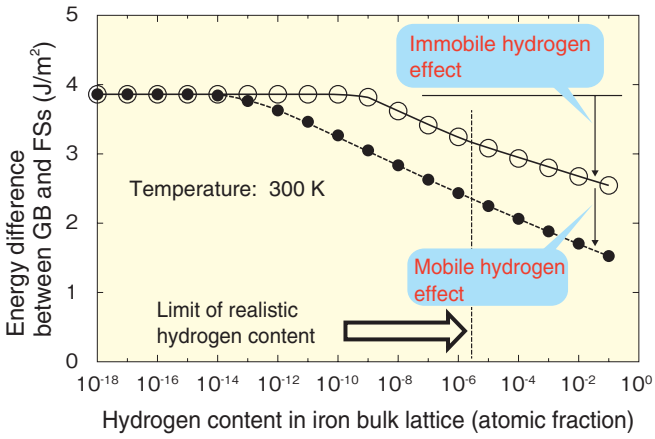

Fig.11-3 Energy difference before and after fracture
The energy difference is calculated between the grain boundary and its fracture surfaces affected by mobile and immobile hydrogen. In a realistic range of hydrogen content in the iron bulk lattice (<10^{-6} atomic fraction), mobile hydrogen plays a dominant role in embrittlement.

Hydrogen-induced embrittlement of steel has been studied for many years, but the mechanism is still not well understood. The wide variety of hydrogen-induced embrittlement implies that there is more than one mechanism. This study focuses on the hydrogen-induced grain boundary embrittlement of high-strength steels. Metallic materials such as steel generally consist of many crystal grains, which are roughly several tens of micrometers in size. The boundary between two grains is called a grain boundary and has disordered atomic structure. It is well known that diffusing hydrogen atoms in the iron lattice can be trapped along the grain boundaries, and then the aggregation (segregation) of hydrogen atoms causes cracking. However, the microscopic (atomistic) mechanism of hydrogen-induced grain boundary embrittlement is still unclear.

We investigated the mechanism by using first principles electronic structure calculations based on quantum mechanics. The results showed that hydrogen atoms can be trapped along grain boundary and fracture surfaces, and then promote cracking along the grain boundaries. Furthermore, we suggested that moving hydrogen in the iron lattice during fracturing assisted the formation of fracture surfaces by being trapped at newly generated atomic sites. This is called the mobile hydrogen effect.

A schematic illustration of the embrittling effect of mobile hydrogen is shown in Fig.11-2. Grain boundary embrittlement is believed to be caused by weakening of atomic bonding across the grain boundary plane. The strength of the bonding is characterized well by the energy difference between the grain boundary and its two fracture surfaces before and after fracturing. This energy difference can be calculated from first principles. We showed that hydrogen segregation along the grain boundary decreases its energy difference, indicating that hydrogen causes embrittlement. Furthermore, hydrogen in iron can diffuse very rapidly and thus can be trapped at newly generated atomic sites on freshly forming fracture surfaces. This can assist the breaking of atomic bonds at the iron grain boundary. Our first principles calculations with a statistical mechanics analysis estimated the embrittling effect of mobile hydrogen for the first time and showed that mobile hydrogen greatly enhances the embrittling effect along grain boundaries in a realistic range of hydrogen content, as shown in Fig.11-3.

Reference

Yamaguchi, M. et al., Mobile Effect of Hydrogen on Intergranular Decohesion of Iron: First–Principles Calculations, Philosophical Magazine, vol.92, no.11, 2012, p.1349–1368. (with Corrigendum, vol.92, no.24, 2012, p.3121–3124).

11–2 Properties of New Materials with Topology

— Classification of the Properties in Superconductors by Topology —

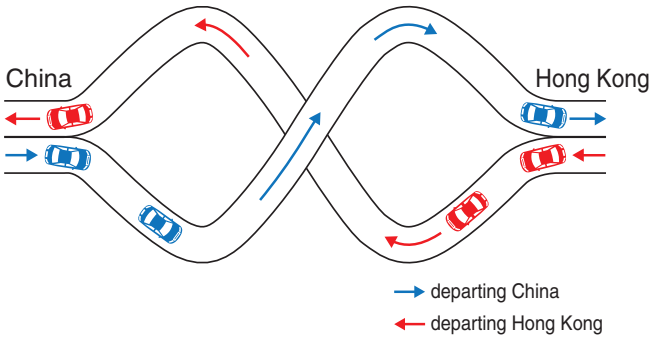

Fig.11-4 Non-trivial topological bridge
Mainland China and Hong Kong drive on opposite sides of the road. The above bridge can naturally connect the two. This bridge has a non-trivial topology.

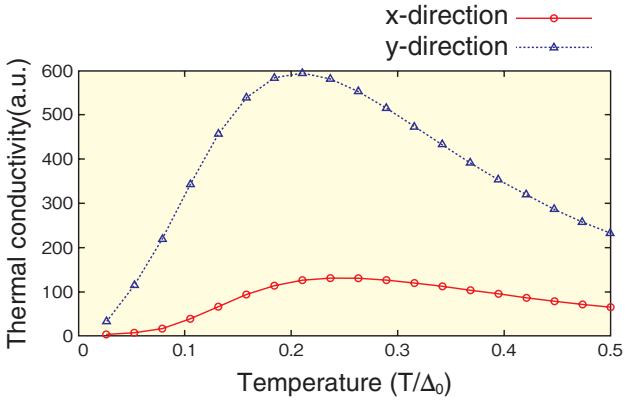

Fig.11-5 Angular dependence of the thermal conductivity
A certain type of topological superconductor has strongly anisotropic thermal conductivity due to the non-trivial topology.

Solids are characterized by the Metal, Semi-metal, Insulator in the conductive-order. Recently, the 4th solids where the bulk is insulating but the surface is metal called Topological insulator have been found. These novel materials can be classified by the mathematics called the Topology so that many scientists are attracted. In addition, this group of the materials has the high thermoelectric power.

Topology is the mathematical study of properties that are preserved under continuous deformations. For example, the bride shown in Fig.11-4 has the non-trivial topology. The topology distinguishes the topological insulators from the conventional solids.

Recently, the researchers have been found the fact that the topological insulator Bi_2Se_3 becomes the superconductor whose transition temperature is 3 K. This kind of the superconductors might be novel functional materials, since superconductivity can transfer the electricity without the energy lost so that it is promising material as the stand-alone device workable in the extreme environment where a human can not enter. However, the physical properties of this superconductor called the topological superconductor have been unknown. Therefore, we investigate the difference between Bi_2Se_3 and the conventional superconductors. Then, by focusing on the fact that the electrons are running ultra fact in Bi_2Se_3, in terms of the theory of the relativity, we can successfully classify the superconductors by the topology. The theory of the relativity hunted the non-trivial topology in the topological superconductors.

In terms of the description about ultra-fast particles in the theory of the relativity, we construct the theory of the thermal conductivity in this material. Then, we find that a certain type of the topological superconductor has the strong anisotropy of the thermal conductivity due to the non-trivial topology as shown in Fig.11-5. This phenomenon is originated from the fact that the twist in the space-time due to the non-trivial topology makes a certain crystal axis special.

We show that the mathematical study of the topology is important even in the superconductors. Novel functional materials and devices can be constructed in terms of the new topological materials in the future.

Reference

Nagai, Y. et al., Rotational Isotropy Breaking as Proof for Spin–Polarized Cooper Pairs in the Topological Superconductor $Cu_xBi_2Se_3$, Physical Review B, vol.86, issue 9, 2012, p.094507–1–094507-5.

11–3 Massively Parallel Fusion Plasma Simulation using 10^5 Processors
— Development of Latency-Hiding Communication Technique —

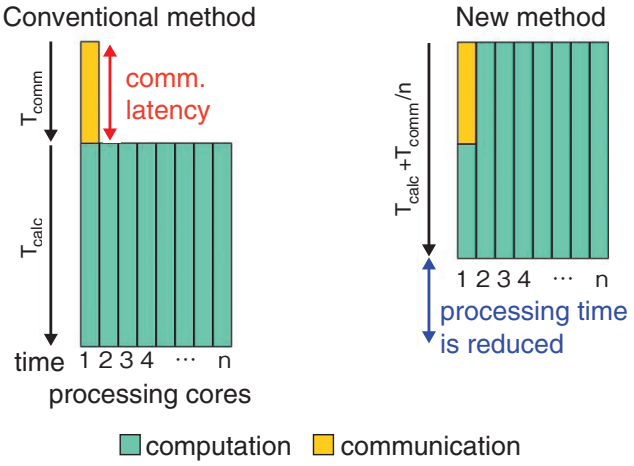

Fig.11-6 Scheduling computation and communication tasks on a processor with *n* processing cores
In the conventional method, computations are processed after communications, and most of the processing cores are idle during the communication latency. In the new method, these tasks are simultaneously processed on different processing cores, and the computing performance is improved by hiding the communication latency.

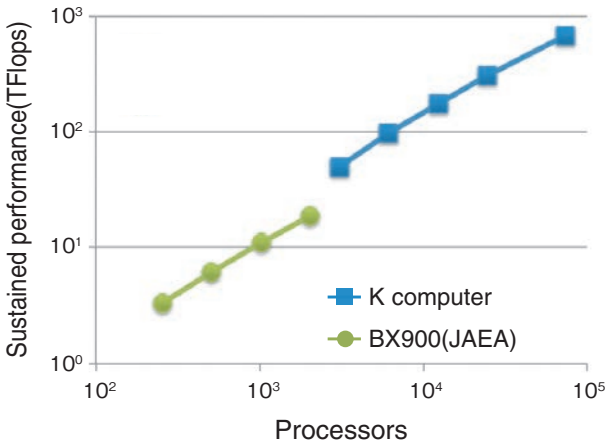

Fig.11-7 Computational performance (TFlops = 10^{12} operations per second) of fusion plasma simulations on the BX900 (JAEA) and the K computer
The maximum sustained performance of the BX900 was ~19 TFlops using 4098 processors with four processing cores. When the new latency-hiding communication technique was applied, the K computer achieved ~682 TFlops using 73728 processors with eight processing cores.

Predicting plasma turbulence is a key issue in estimating the performance of fusion core plasmas in ITER, which is determined by turbulent transport phenomena. A calculation model of fusion plasmas is described in five-dimensional (5D) phase space (three-dimensional position × two-dimensional velocity), which is estimated as requiring $300^3 \times 128 \times 32 \sim 10^{11}$ grids for existing devices such as the JT-60U. The development of modern parallel computers enabled large-scale turbulence simulations of the 5D problem, and computational plasma turbulence research has been significantly advanced. However, ITER is a few times larger than existing devices, and simulating its turbulent transport requires an order of magnitude larger computational resources. Although a next-generation massively parallel computer such as the K computer is a promising solution, the latency due to data communications among ~10^5 processors has been a bottleneck in improving the computational performance of massively parallel simulations.

To resolve this issue, a novel communication technique that dramatically reduces the communication latency is developed. Turbulence simulations based on grids process calculation models in parallel by assigning decomposed small domains to each processor. This computational process, which requires boundary data in the neighboring domain, is normally performed after the boundary data is communicated. In the new technique, the computational performance is dramatically improved by assigning different tasks, computation and communication, to multiple processing cores on a single processor and processing them simultaneously (Fig.11-6). By applying this technique to 73728 processors on the K computer, massively parallel fusion plasma turbulence simulations were accelerated by ~35 times (Fig.11-7). This speedup enables ITER-size simulations, which were estimated to take more than a year on previous machines, to be completed in a week.

This work was supported by a Ministry of Education, Culture, Sports, Science and Technology of Japan (MEXT) grant for the HPCI Strategic Program Field No.4, “Next-Generation Industrial Innovations.”

Reference

Idomura, Y. et al., Communication–Overlap Techniques for Improved Strong Scaling of Gyrokinetic Eulerian Code beyond 100 k Cores on the K-Computer, International Journal of High Performance Computing Applications, 2013, doi: 10.1177/1094342013490973.

11–4 Technology to Speed up Fluid Structure Interaction Simulation
— Simulation Technologies for Flow-Induced Vibration in a Nuclear Power Plant —

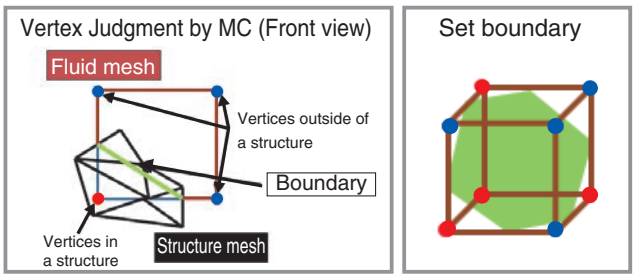

Fig.11-8 Setting of boundaries using MC
Using the results of a judgment regarding whether vertices are included in the structure mesh, the boundaries in a calculation domain are set. The processing cost is significantly reduced because the shape is calculated approximately.

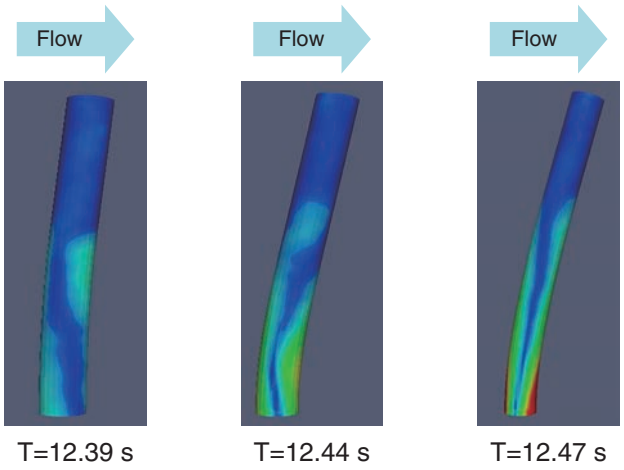

Fig.11-10 Time variations in cylinder deformation
Red shows high-stress region; blue shows low-stress region. The figure indicates that the cylinder deforms because of the pressure difference around it. The deformation amount is enlarged 100 times.

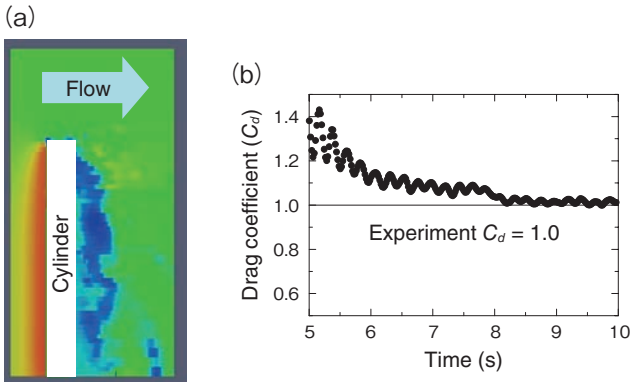

Fig.11-9 Pressure and time variations in drag coefficient
(a) Pressure distributions. High pressure (red) occurs at the upstream side, and low pressure (blue) occurs at the downstream side. (b) Drag coefficient versus time. The simulation result exhibits good agreement with the experimental data.

Flow-induced vibration is a very important phenomenon in a nuclear power plant because it causes breaks in the instruments or pipes. To analyze this phenomenon, fluid structure interaction simulation technologies have received considerable attention in recent years. In a fluid structure interaction simulation, a mesh consisting of small polyhedra is generally used to describe the fluid and structure regions. To date, a method that describes accurately the shape of the boundary between the fluid mesh and the structure mesh has been used. In this method, when the structure shape is highly deformed, the mesh shape also becomes awkward. Consequently, the simulation accuracy and speed are reduced. One of the methods of overcoming this problem is the immersed boundary method. However, setting the boundary conditions in the calculation domain requires considerable time.

In this study, a new algorithm that uses Marching Cube (MC) to set the boundaries approximately was invented (Fig.11-8). The processing speed is more than 20 times faster than that of traditional methods. This makes it possible to finish a simulation that requires half a year by traditional methods within 10 days. Consequently, the method enables us to perform more practical simulations.

For verification, the method was applied to a simulation of the flow-induced vibration around a circular cylinder. Figs.11-9(a) and 11-10 show that the simulation can compute the deformation of a cylinder due to a pressure difference around it. The drag coefficient (Fig.11-9(b)) and amount of deformation of the cylinder are in good agreement with the experimental data. This study confirmed that the proposed method maintains adequate accuracy for application to practical problems.

This method enables us to perform large-scale complex simulations of flow-induced vibration with adequate accuracy within a practical timeframe. It is hoped that the method will contribute to the development of technologies to increase the safety of nuclear power plants.

Reference

Kino, C. et al., Flow Analysis around an In-Line Forced Oscillating Circular Cylinder using IB-Method, Nippon Kikai Gakkai Ronbunshu, B Hen, vol.78, no.796, 2012, p.2113-2126 (in Japanese).

Technology and Human Resource Development in the Area of Nuclear Nonproliferation and Nuclear Security to Support Peaceful Use of Nuclear Energy

The Japan Atomic Energy Agency (JAEA) is conducting the following technology and human resource development activities related to nuclear nonproliferation and nuclear security, in cooperation with relevant domestic and overseas organizations (Fig.12-1).

Nuclear Nonproliferation Technology Development for Japanese and International Applications

We have been developing proliferation resistant nuclear technologies, methodologies for evaluating proliferation resistance, and advanced safeguard technologies through cooperation with international partners such as the U.S. Department of Energy (DOE). In February 2013, we commemorated the twenty-five year anniversary of cooperation with the DOE in the field of nuclear nonproliferation. On the occasion of an annual bilateral meeting, the JAEA was presented with a medallion with a message from Daniel B. Poneman, Deputy Secretary of Energy, which expresses his appreciation and gratitude for the JAEA's cooperation in this field (Fig.12-2).

Development of Measures to Account for and Control Nuclear Material in Response to the Accident at 1F

We are examining the technologies applicable to the nondestructive measurement of nuclear material that remains within the molten core of the reactors at Tokyo Electric Power Company, Incorporated Fukushima Daiichi Nuclear Power Station (1F). As one such candidate technology, we are developing a technology for measuring nuclear material using γ-rays emitted by fission products accompanying nuclear material (Chapter 1, Topic 1-16).

Contributions to the International Community Based on Our Expertise and Experience

With respect to activities relating to the Comprehensive Nuclear-Test-Ban Treaty (CTBT), we operate radionuclide monitoring stations and other related facilities, and thus contribute to the establishment of an international monitoring system for the detection of nuclear tests. The JAEA's activities in this area attracted international attention when radionuclides that are suspected to originate from the nuclear test announced by North Korea in February 2013 were detected in April at Takasaki Radionuclide Monitoring Station.

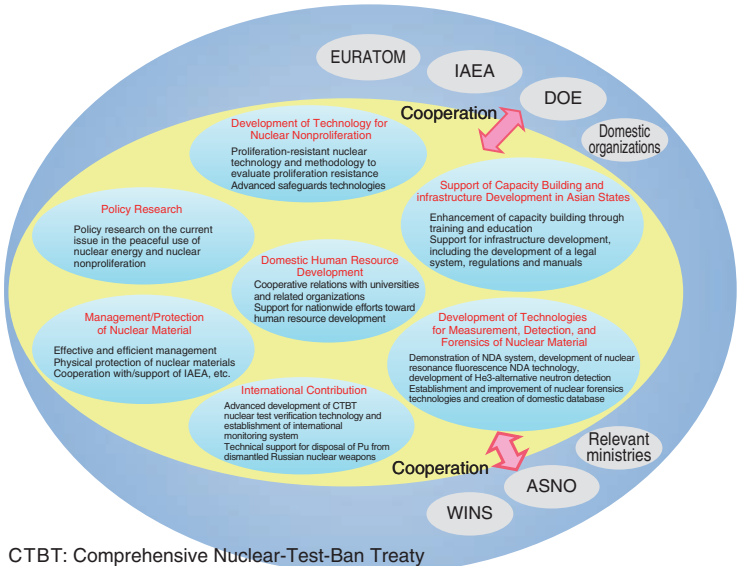

CTBT: Comprehensive Nuclear-Test-Ban Treaty
WINS: World Institute for Nuclear Security
ASNO: Australian Safeguards and Non-Proliferation Office
D O E: Department of Energy

Support for Government Policy Formulation Based on Our Expertise

As a think tank in this area, we conduct research on measures to ensure nuclear nonproliferation and nuclear security on the backend of the nuclear fuel cycle.

Strict Management of Nuclear Material at Our Own Facilities and Utilization of the Experience Gained from Management of Nuclear Material

We strictly manage the nuclear material that the JAEA possesses. Moreover, we assist in increasing the efficiency of inspections by providing technical support to the Japanese government and the International Atomic Energy Agency (IAEA). We also provide support to the IAEA in the field of physical protection and respond appropriately in the event of revisions to the domestic legislation in this area.

New Efforts toward Nuclear Security

On the basis of commitments made by the Japanese government at the Nuclear Security Summit in April 2010, we established the Integrated Support Center for Nuclear Nonproliferation and Nuclear Security (ISCN) in December 2010 and began conducting its mission of capacity building and infrastructure development, focusing on the Asian region.

Approximately 630 participants (approximately 430 from Asian states) participated in the training courses on nuclear security and safeguards and other activities organized by the ISCN in FY 2012. We are proud of the contributions that we are making in the area of capacity building in primarily the Asian region.

Furthermore, we are conducting research on and development of the technology on the measurement of nuclear material, which will contribute to the advancement of accounting for and control of nuclear material, as well as the technology on nuclear detection and forensics technology in cooperation with the United States. We will continue to provide support to the Japanese government in the area of international contributions by establishing accurate technologies and sharing these technologies with the international community.

Fig.12-2 Medallion to commemorate twenty-five year anniversary of cooperation between JAEA-DOE in the area of nuclear nonproliferation presented by DOE

Fig.12-1 JAEA activities in development of science and technology for nuclear nonproliferation
We have two primary missions: to support the government in developing nuclear nonproliferation policies through research and study, and to support government and international organizations by developing nuclear nonproliferation technology. In addition, we appropriately implement the management of nuclear material and the development of related technology and conduct capacity-building activities.

13 Development of Experimental Techniques/Facilities at JAEA R&D Centers

Tsuruga Head Office

We are engaged in checking the unchecked equipment and improving the safety culture and so on to remedy the overdue status of the components inspection schedule for "MONJU" and to return to a normal state as soon as possible from the present status of deviation from the Nuclear Reactor Regulation Law.

We are also working steadily toward the decommissioning of "FUGEN" and related technical development as well as selection tests to determine suitable cutting methods for the dismantling required for the decommissioning of the Tokyo Electric Power Company, Incorporated Fukushima Daiichi Nuclear Power Station (1F) as a result of the accident.

In addition, technical cooperation, such as promotion of research and development (R&D), including that on laser technology, by industry–government–academia collaboration is being advanced substantially. In particular, the industrial application of lasers to fast reactor heat exchanger tube repair technology is in progress (Topic 13-1).

The FBR Safety Technology Center was established in April 2013. The center conducts R&D toward commercial deployment of the fast breeder reactor, mainly in the area of safety studies, such as severe accident analysis and evaluation for "MONJU".

Ceremony launching the FBR Safety Technology Center (April 2, 2013)

Tokai Research and Development Center, Nuclear Science Research Institute (NSRI)

The NSRI facilities, such as research reactors (JRR-3, JRR-4, and NSRR), accelerators (e.g., Tandem), critical assemblies (e.g., STACY, FCA), and hot laboratories (e.g., WASTEF, BECKY) were also damaged during the Great East Japan Earthquake. Because the damaged lifelines were recovered quickly, hot laboratories were able to begin supporting the nuclear fuel R&D activities, and accelerators started operation for common use by researchers from JAEA, universities, and other organizations. In addition, the Fukushima Project Team, which was launched on October 1, performed R&D activity using these facilities (Chapter 1, Topics 1-12, 1-14, 1-15). In the recovery of NSRI security, a new building with an earthquake-resistant structure was completed and established as the urgent activity base in the event of atomic accidents.

Regarding the use of NSRI technology, NSRI cooperated with companies in the development of their technologies. For example, a dosimeter system that can simultaneously measure various weather conditions was produced by a manufacturer using radiation detection and electronics technologies developed at NSRI.

Japan Research Reactor-3 (JRR-3)

Nuclear Fuel Cycle Safety Engineering Research Facility (NUCEF)

Nuclear Safety Research Reactor (NSRR)

Reactor Fuel Examination Facility

Main research facilities at Nuclear Science Research Institute

Tokai Research and Development Center, Nuclear Fuel Cycle Engineering Laboratories

At the Plutonium Fuel Development Center, basic data on mixed oxide (MOX) fuels was acquired, and treatment tests of MOX fuel powder were conducted as part of a technical collaboration with Japan Nuclear Fuel Limited.

At the Tokai Reprocessing Technology Development Center, cold tests on the vitrification of high-level radioactive liquid waste and cementation of low-level radioactive liquid waste were conducted.

The Waste Management Department developed decommissioning technologies for old nuclear facilities, planned and built the Tokai Waste Treatment Facility for treating uranium and trans-uranic wastes, conducted fundamental and applied studies to increase the reliability of waste disposal technologies, and developed safety assessment methods.

At the Radiation Protection Department, the concentrations of radioactive materials and the ambient dose rate were measured on and off site, and analytical methods for environmental samples were developed (Topic 13-2).

The Department of Fukushima Technology Development has supported the activity of the Fukushima Project Team and has conducted R&D for decommissioning of the damaged Fukushima reactors (Chapter 1, Topics 1-13, 1-20).

Sampling of seabed soil with a monitoring boat

J-PARC Center

In fiscal year 2012 (FY2012), J-PARC provided neutron beams to users for 8 run cycles (176 d). We successfully achieved steady and reliable operation at the target beam power of 200 kW, which was one of our goals for FY2012, by September, and also increased the power to 300 kW in October at the Materials and Life Science Facility (MLF). As a result of this power increase at the MLF the world's strongest neutron intensity of 6.5×10^{13} neutrons per pulse, was generated. This intense neutrons enabled many experimental outcomes, such as the development of high-performance structural materials (Topic 13-3) and the development of high-performance elliptical super-mirror (Topic 13-4). In addition, the MLF muon source produced 250×10^{6} muons per pulse, which exceeds 3×10^{4} muons at a similar facility in the UK and became world's record. A total of 526 proposals were submitted to the MLF user programs which was much more than in any year before the Great East Japan Earthquake. Other major progresses on the dominantly JAEA projects at J-PARC is as follows: (1) the new neutron instrument, the Energy Resolved Neutron Imaging System, which aims to measure elements, magnetic fields and crystalline structure in matter, is under construction at the MLF; and (2) Acceleration cavities with an annular-ring coupled structure were fabricated (Topic 13-5).

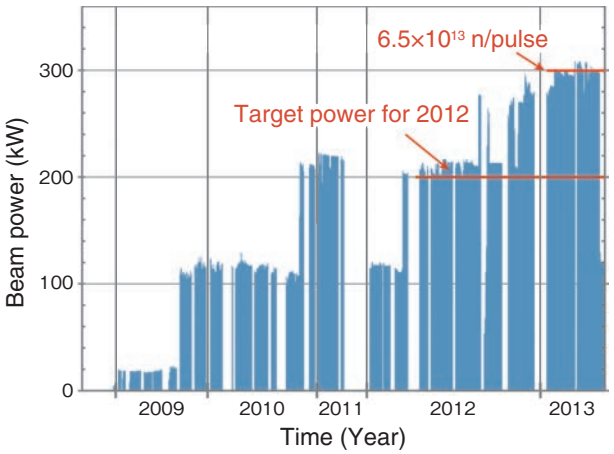

Operational history of J-PARC

Oarai Research and Development Center

Restoration work was performed and safety measures were taken for the facilities and equipment damaged by the Great East Japan Earthquake.

In the Japan Materials Testing Reactor (JMTR), the confirmation of the integrity of the facilities after the Great East Japan Earthquake was completed, and the results were reported to the regulatory agency with the goal of re-operation. A light water reactor water environment demonstration test facility was fabricated and installed with funding from the Leading-edge Research Promotion Fund, which was provided by the Ministry of Education, Culture, Sports, Science and Technology (MEXT) in Japan. A real-time system for monitoring radiation workers' locations, health conditions, and exposed doses using portable radio devices was developed and put into operation. To enable domestic ^{99}Mo production, a technique for fabricating a high-density pellet was developed (Topic 13-6).

In the Experimental Fast Reactor "JOYO," equipment for use in repair work was designed and fabricated. A mock-up test using those pieces of equipment was started. The compatibility of a zirconium alloy with high-temperature sodium was examined (Topic 13-7).

In the High Temperature engineering Test Reactor (HTTR), an inspection of the facilities and a comprehensive evaluation of the integrity of the equipment were conducted with the goal of resuming operation. A damage detection method for the neutron detector was established (Topic 13-8).

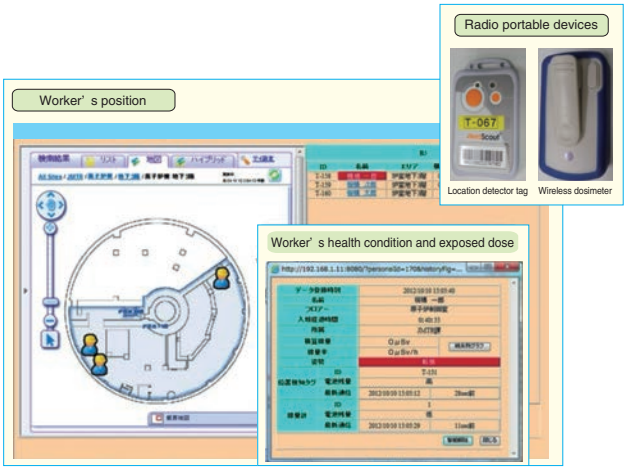

Development of real-time personal exposure and health condition monitoring system in the JMTR
The system can monitor workers' locations, health conditions, and exposed radiation doses in real time using wireless portable devices.

Naka Fusion Institute

The Naka Fusion Institute conducts R&D toward the practical use of fusion energy.

Currently, it is involved mainly in the procurement and development of the JA-shared apparatuses as a domestic agency of the ITER project and in the upgrade of the large tokamak device JT-60 to the satellite tokamak device JT-60SA, which will be used for research supporting and complementing ITER as Broader Approach activities in cooperation with the European Union.

In 2012, the production of the superconducting conductor for ITER was advanced, and the production of the superconducting coil was begun. Moreover, the disassembly of the main body of JT-60 was completed; the cryostat base, which was procured from Europe, was accepted, and the assembly of JT-60SA began.

The production of JT-60SA components was proceeded, and the smallest superconducting poloidal magnetic field coil (EF4) was completed. In addition, three 40° sectors of the vacuum vessel for the actual machine were welded, and a total of six were completed.

Celebration of the delivery of the first component from the EU and the beginning JT-60SA tokamak assembly (March 25, 2013)

Takasaki Advanced Radiation Research Institute

Takasaki Ion Accelerators for Advanced Radiation Application (TIARA) consisting of four ion accelerators, an electron accelerator, and gamma irradiation facilities are made available to researchers in JAEA and other organizations for R&D activities on new functional and environmentally friendly materials, biotechnology, the radiation effects of materials, and quantum beam analysis. Practical technology development activities that are currently in progress involve microbeams, single ion hits, techniques for uniform wide-area irradiation at the cyclotron, three-dimensional in-air PIXE analysis, and a three-dimensional microfabrication technique (Topic 13-9) at the electrostatic accelerators. In 2012, a beam shape control technique was developed that transforms a complicated transverse intensity distribution into a Gaussian-like one through multiple scattering using a thin metallic foil. A 70 mm × 40 mm beam with ±10% uniformity was obtained by focusing the transformed beam with multipole magnets.

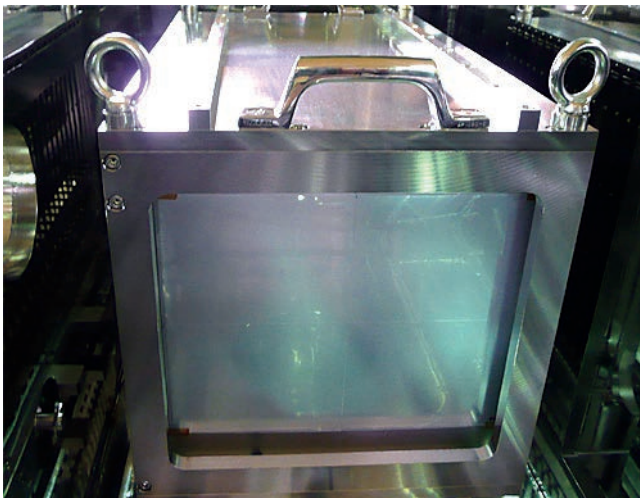

A container of 22 radiochromic dosimetry films for measuring the size and uniformity of a beam, installed in the chamber for formation and irradiation of a large-area uniform beam

Kansai Photon Science Institute

In the Kizu District, we are in the process of improving the laser facilities, e.g., improving the quality of the high-intensity lasers. Regarding high-intensity short-pulse lasers, we worked on improving the position stability of the beam and, by exchanging the mirror mount and reducing the wobbling in the position, improved the reproducibility of experimental results. In addition, in the Consortium for Photon Science and Technology, we are in the process of developing ultrawideband light sources ranging from terahertz to X-rays to quantum beams.

In the Harima District, we have been developing and improving a state-of-the-art analysis technique for the functional expression mechanism and reaction mechanism of materials using the JAEA synchrotron radiation beamlines at SPring-8. They are also applied to studies related to nanotechnology, energy, and the environment, for instance, a decontamination technique for revitalization in Fukushima. Further, under the Nanotechnology Platform Project entrusted to us by MEXT, external researchers are being supported.

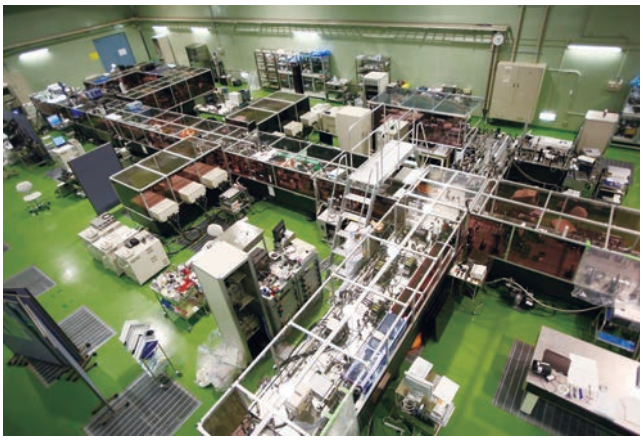

JAEA Kansai Advanced Relativistic ENgineering (J-KAREN) laser system

Horonobe Underground Research Center

We are currently constructing the Horonobe Underground Research Laboratory for conducting geoscientific research and R&D on geological disposal technologies targeted at sedimentary rocks.

In FY2012, the west shaft was excavated to depths ranging from 50 m to 350 m (the east and ventilation shafts already reached 350 m in depth in the last fiscal year). In addition, the 350 m research gallery passed through the ventilation shaft to join the east shaft. About 400 m of the 700-m-long gallery have been completed.

In geoscientific research, we have continuously developed techniques for investigating the geological environment and for deep underground engineering, and studied the long-term stability of the geological environment. On the other hand, in our R&D on geological disposal, we investigated the impact of low-alkaline cement materials, including high fly-ash and silica fume content cement, to the surrounding groundwater and rock mass. In addition, the use of materials in spraying techniques was tested in situ during the construction of the 350 m research gallery.

Penetration of 350 m research gallery between the ventilation and east shafts

Tono Geoscience Center (TGC)

The TGC's task is to provide the scientific and technical foundations for developing a safe technique for the geological disposal of high-level radioactive waste. This involves research into the long-term stability of the geological environment, the development and improvement of techniques for the characterization of the deep geological environment, and a wide range of engineering techniques for deep underground applications at an underground research laboratory in crystalline rock, referred to as the Mizunami Underground Research Laboratory. Approximately 150 m of horizontal excavations (Sub Stage, Access/Research Galleries-North and South) were completed for the GL −500 m stage (meters below ground level). While planning the construction, it was necessary to obtain reliable preliminary information on the bedrock conditions in terms of the rock mass stability and hydrogeology. Therefore, site characterization borehole investigations were conducted before excavation began (Topic 13-10). Research and development activities, such as geological mapping during excavation and borehole investigations, were also conducted.

Breaking through at part of the GL –500 m Sub Stage (July 30, 2012)

Ningyo-toge Environmental Engineering Center

The Ningyo-toge Environmental Engineering Center has advanced the environmental remediation of the Ningyo-toge and Togo Uranium Mines after decades of mine-related activities, including uranium exploration and mining, were terminated. The main purposes of the remediation are to take measures to ensure the safety and protection from radiation via exposure pathways to humans in the future, and to prevent the occurrence of mining pollution.

As part of the remediation, the upstream part of the Yotsugi Mill Tailings Pond, the highestprioritized facility among all of the mine-related facilities, was remediated to FY2012. In the remediation, a multi-layered capping was constructed on the ground surface after the specifications and the entire remediation procedure were determined. Monitoring data will be accumulated to confirm the effectiveness of the remediation, and the results will be used for remediation of the downstream part of the Pond.

The Center also performed the required maintenance of related facilities and promoted technology development. In addition, a sense of security among local residents and active use of local features (Topic 13-11, "Investigation of Properties of Radon Hot Springs") have been sought as another indispensable aspect of the Center's activities.

Upstream part of the Yotsugi Mill Tailings Pond

Aomori Research and Development Center

In the Rokkasho District, R&D toward developing the fusion DEMO reactor is in progress, for example, a fusion simulation using a supercomputer that has the second-best performance in Japan, and the development of the fusion reactor structural material using various material analysis and testing devices. In addition, the injector for the prototype accelerator of the International Fusion Materials Irradiation Facility (IFMIF) was delivered, and commissioning is planned to begin this autumn.

In the Mutsu District, a research survey of reasonable and economical large assembly dismantling methodologies for the operation of a waste disposal plant for research facilities, and decommissioning of the nuclear-powered ship Mutsu (e.g., surveying the contaminant content and developing technology to analyze ultra-trace elements using accelerator mass spectrometry) are conducted continuously.

Delivery of the injector for the prototype accelerator to the IFMIF/EVEDA (Engineering Validation and Engineering Design Activities) accelerator building

13–1 Challenge of Industrial Application of Repair Technologies for FBR Heat Exchanger Tubes — Success in High-Accuracy Wire Feeding to Laser-Irradiated Spot —

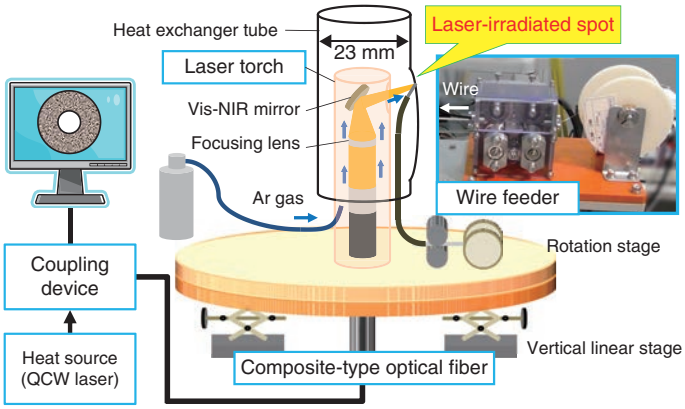

Fig.13-1 Schematic view of laser cladding system in heat exchanger tube
This system was designed to work around the edge of a 23 mm tube. A laser beam was focused on the tube wall by optical lenses and a vis-near-infrared (NIR) heatproof mirror. A wire and Ar gas were supplied to the laser spot. QCW: quasi continuous wave.

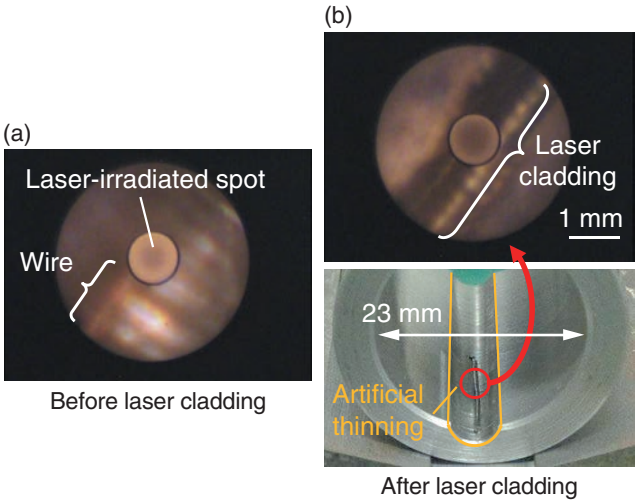

Fig.13-2 Laser cladding on wall of 1 in. tube
(a) Wire moves toward the center of the laser spot. (b) Line cladding deposited on wall was about 1 mm in width and 0.2 mm in height. It is possible to suppress wall thinning by using erosion–corrosion-resistant wire.

We developed an inspection and repair system for use in a heat exchanger tube in a fast breeder reactor (FBR). The key technology in this system was a composite-type optical fiber consisting of a central fiber to deliver the laser beam and surrounding fibers to transmit the visible image. We could observe a crack in the tube wall in the visible image and repair it by laser welding.

Inspection and repair technology for use in a limited tubular space is expected to have wide industrial applications outside of the field of nuclear energy. We are promoting the technical development of a method of repairing wall thinning in heat exchanger tubes in a petrochemical plant. Wall thinning appears as a dimple on the tube wall and is repaired by melting and bonding wires to the base metal. Arc welding is typically used for repairing metal parts. However, in the limited tubular space, the excess heat of the arc often breaks the welding devices and causes inferior welding. A laser beam can be delivered by an optical fiber and concentrate the energy in a local spot, so it is suitable for use in a narrow space.

Precise wire feeding to a small laser-irradiated spot is very important for successful laser cladding. A composite-type optical fiberscope is useful for this purpose. It is necessary to use a welding wire thinner than the typical one because an allowable bending radius is about 10 mm in a 23 mm tube We developed a new wire feeder in cooperation with an excellent machining company in Fukui (Fig.13-1). This device can continuously feed 0.4 mm wire by adjusting the roller gripping force and varying the feeding speed. Its size is about 10 cm^3.

The developed wire feeder, laser torch, and composite-type optical fiber were assembled (Fig.13-1), and the laser cladding in a 23 mm carbon steel tube was examined using this system. As a result, we succeeded in continuously feeding the wire to the laser-irradiated spot and producing a line cladding layer that was about 1 mm in width and 0.2 mm in height (Fig.13-2).

In the future, we will control this laser cladding system automatically so that it will fit inside a tube for practical use in petrochemical plants. In this experiment, the wire was comparable in hardness to the base metal. We will try to use a wire that has high erosion–corrosion resistance to suppress wall thinning.

Reference

Nishimura, A., Terada, T. et al., Instrumentation Device and Surface Control Technology for Coolant Piping System of Nuclear Power Plants, Proceedings of the 2012 20th International Conference on Nuclear Engineering Collocated with the ASME 2012 Power Conference (ICONE20), California, USA, 2012, ICONE20–POWER2012–54406, 5p., in DVD–ROM.

13–2 Radiocesium in the Environment

— Radiation Situation in Tokai Two Years after the 1F Accident —

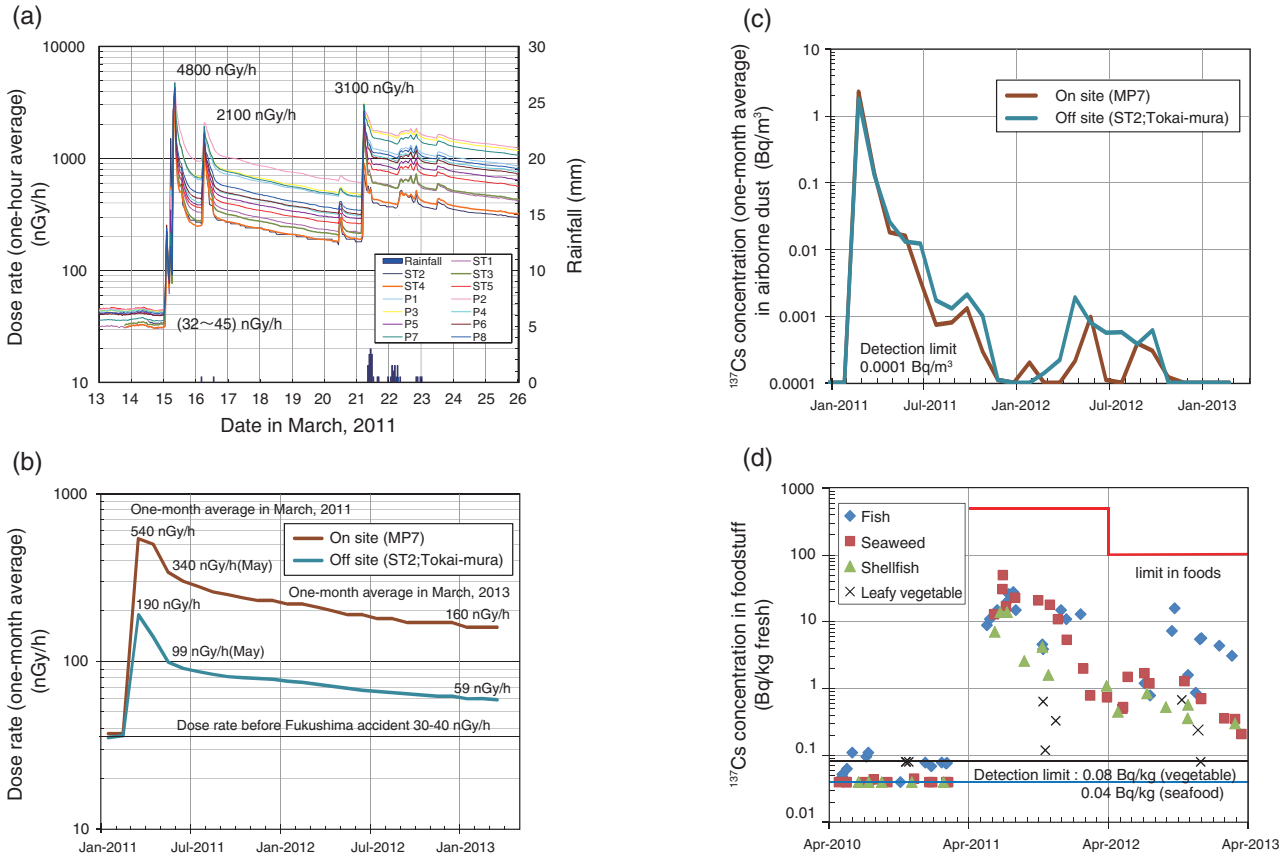

Fig.13-3 Chronological change in dose rate and ^{137}Cs concentration observed in Tokai for two years around 1F accident

Because of the release of radioactive materials during the accident at the TEPCO's Fukushima Daiichi NPS (1F), an increase in the dose rate and radiocesium concentration were observed in the Nuclear Fuel Cycle Engineering Laboratories (Tokai, Ibaraki Prefecture), which is located about 115 km from 1F, after March 15, 2011. This was reported by the Japan Atomic Energy Agency (JAEA-Review 2011-035). The dose rates (1-h averages) just after the 1F accident are presented in Fig.13-3(a). We report the chronological change in the radiation in Tokai for two years after the 1F accident.

The dose rates (one-month averages) are presented in Fig.13-3(b) for monitoring post-7 (MP7; on site) and monitoring station-2 (ST2; off site) as representative locations. Because of the differences in the environments (e.g., the presence or absence of trees), the observed dose rates varied by a factor of two or three. Because the half-lives of cesium-134 (^{134}Cs) and cesium-137 (^{137}Cs) are about 2 and 30 years, respectively, they contributed most of the dose rate. From May 2011, when the contribution from short-life nuclides almost disappeared, to March 2013, the dose rate decreased by around 60%. Thus, 25% of the ^{134}Cs and ^{137}Cs were transported elsewhere or shielded by immersion, in addition to the decrease by radiological decay (at a rate of 35% in 22 months).

The ^{137}Cs concentrations in airborne dust (one-month averages) also tended to decline (Fig.13-3(c)). The concentration off site is likely to be slightly higher than that on site. The origin of recent ^{137}Cs in airborne dust is believed to be not 1F itself but soil on which ^{137}Cs was deposited two years ago. Outside of the Laboratories, strong winds could resuspend and transport soil particles from cultivated fields.

The ^{137}Cs concentrations in foodstuffs are presented in Fig.13-3(d). Taking into account ^{134}Cs, the concentration of ^{134}Cs plus ^{137}Cs was less than half of the limit in foods (100 Bq/kg fresh for ^{134}Cs plus ^{137}Cs, 500 Bq/kg fresh before April 2012). The ^{137}Cs concentration generally decreased, but the concentration in demersal fish, which could be influenced by ^{137}Cs in seabed sediment, did not decrease as much. Because the transfer of Cs from the soil to vegetables is smaller than that from sea water to seafood, the ^{137}Cs concentration in vegetables was less than 1 Bq/kg fresh.

Reference

Fujita, H. et al., Special Environmental Monitoring around Tokai-Mura after the Accident of the Fukushima Dai-Ichi Nuclear Power Station, Proceedings of the 13th International Congress of the International Radiation Protection Association (IRPA-13), Glasgow, Scotland, U.K., 2012, P12.31, 7p.

13–3 Neutrons in Development of High-Performance Materials

— Role of Deformation-Induced Transformation in TRIP Steels Revealed by Neutrons at J-PARC —

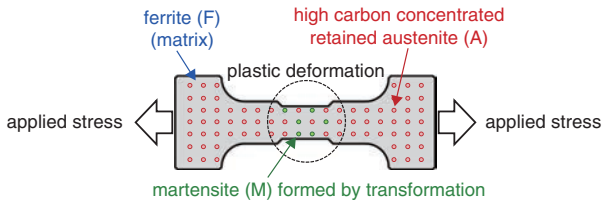

Fig.13-4 Illustration of TRIP effect
The M phase is formed during plastic deformation, and the material's strength and elongation are increased.

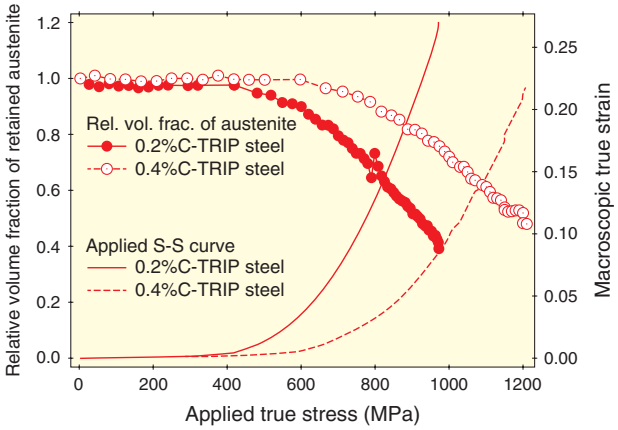

Fig.13-5 Changes in relative volume fraction of retained austenite and stress–strain curve of TRIP steels
Phase ratio does not change during deformation in common steels, whereas it varies in TRIP steels.

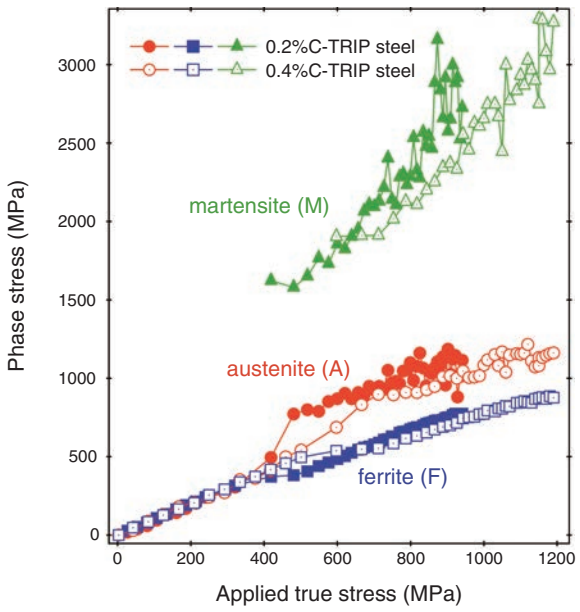

Fig.13-6 Stress partitioning among constituent phases of TRIP steel during deformation
The stresses were calculated from the phase lattice strains obtained from an *in-situ* neutron diffraction study during tensile deformation. We successfully separated the diffraction peaks to elucidate the stress partitioning between the M and F phases, which was not possible using the conventional instruments of ISIS and JRR-3 with low d-spacing resolution.

Transformation-induced plasticity (TRIP) is an important effect in steel that improves the strength and ductility and realizes excellent high-speed deformation behavior. Steels with 0.2%C-TRIP and 0.4%C-TRIP are known to have excellent shock absorption in collisions and are expected to be used in car bodies. The TRIP effect, as shown in Fig.13-4, occurs in steel having a metastable phase (the A phase) that can transform into a stronger phase (the M phase) during plastic deformation. However, there is almost no quantitative research on the behavior causing the TRIP effect that directly shows the contribution of the M phase to the strength. We attempt to understand this behavior using neutron diffraction.

We performed *in-situ* neutron diffraction experiments during tensile loading at room temperature using the Engineering Materials Diffractometer TAKUMI at the Materials and Life Science Experimental Facility of J-PARC. TAKUMI can perform an *in-situ* neutron diffraction experiment during deformation without interruption of the load or displacement because of its high intensity and instantaneous data collection system. The relative volume fractions of the A phase obtained from neutron diffraction, as shown in Fig.13-5, are gradually decreased with increasing applied stress after the onset of plastic deformation, showing that a deformation-induced martensitic transformation occurs. Fig.13-6 shows the phase stresses that are shared by the constituent phases in the TRIP steels during tensile deformation. The M phase stresses are found to be the highest and the ferrite phase stresses are the lowest among the constituent phases. Moreover, the bulk stresses that are estimated using these phase stresses and the volume fractions show good agreement with the applied stresses.

Reference

Harjo, S. et al., TRIP Steel Deformation Behavior by Neutron Diffraction, Materials Research Society Symposium Proceedings, vol.1528, 2013, 7p.

13–4 Development of Ultraprecise Focusing Supermirrors with Elliptical Surface
— Focusing Gain of 52 Achieved for Advanced Instrumentation at J-PARC —

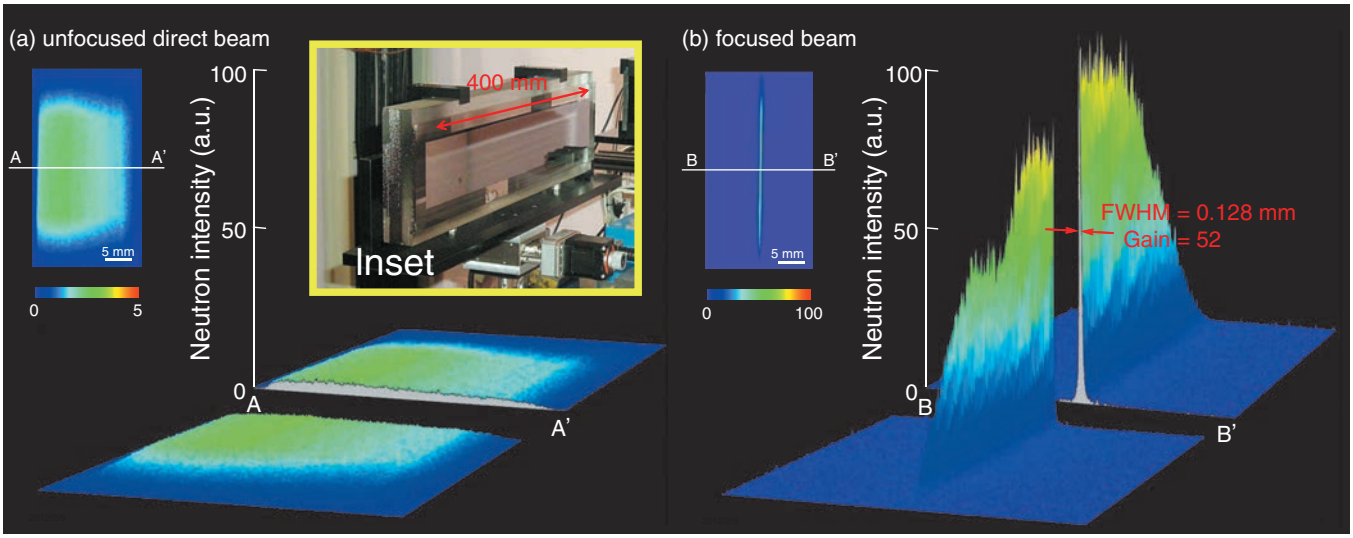

Fig.13-7 Neutron focusing images obtained by large-scale elliptical supermirror ((a): unfocused direct beam; (b): focused beam)
The FWHM of the focused beam was 0.128 mm, and a focusing gain of 52 was observed using an imaging plate. Inset photograph shows elliptical NiC/Ti supermirror with m = 4 coated on 400-mm-long substrate.

Slow neutrons, which exhibit quantum mechanical wave properties, are used to investigate crystal and molecular structures and dynamics in solid-state physics, polymer and biological sciences, and so on.

Neutron focusing devices play the important roles of focusing neutrons on samples and increasing the available neutron intensities or improving the experimental resolutions in various experiments such as small-sample diffraction and small-angle scattering. Therefore, high-performance focusing mirrors have been aggressively developed to accelerate the exploration of new scientific phenomena at neutron experimental facilities worldwide, such as J-PARC.

We successfully developed focusing supermirrors with a large critical angle, high reflectivity, and low diffuse scattering by using ion beam sputtering (IBS). A precise surface figure was obtained on the focusing mirror by using the numerically controlled local wet etching (NC-LWE) on the mirror substrate. The NC-LWE technique enables an aspherical shape to be figured deterministically with sub-micrometer form accuracy because it uses a noncontact chemical removal process that is insensitive to external disturbances such as vibration and/or thermal deformation.

We designed and fabricated one-dimensional neutron focusing with a large beam divergence by a 400-mm-long elliptical supermirror. A NiC/Ti supermirror with 1200 layers was deposited on the substrate using the IBS instrument. We successfully obtained a figure error of 0.43 μm peak-to-valley with a surface roughness of less than 0.2 nm root mean square. The neutron reflectivity was measured using the BL17 SHARAKU instrument at J-PARC/MLF. The reflectivity of the m = 4 supermirror was ≃0.6.

The focusing performance of the fabricated elliptical supermirror was evaluated at BL10 NOBORU. The wavelength of the neutron beam was varied from 3.5 to 10 Å. The upstream width of the slit in this experiment was 0.10 mm.

Fig.13-7 shows neutron profiles of the unfocused direct beam and the focused beam. The full width at half-maximum (FWHM) of the focused beam was 0.128 mm, and a focusing gain of 52 in terms of the peak intensity was achieved compared with the unfocused direct beam. Note that the tail of the focused beam is no larger than that of the unfocused beam profile, which suggests that the focusing mirror produces little diffuse scattering.

Reference

Nagano, M., Yamazaki, D. et al., One–Dimensional Neutron Focusing with Large Beam Divergence by 400mm–Long Elliptical Supermirror, Journal of Physics: Conference Series, vol.340, 2012, p.012034–1–012034–6.

13–5 Beam Acceleration by Axially Symmetric Field
— Development of J-PARC Annular-Ring Coupled Structure —

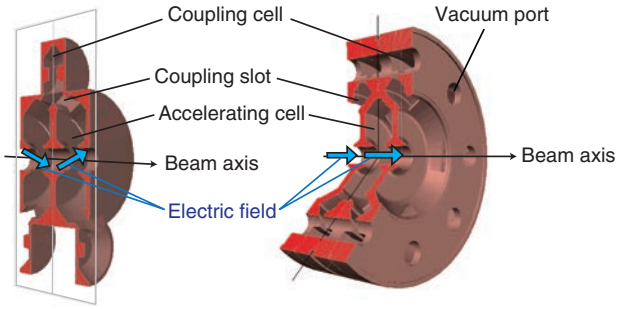

Fig.13-8 Side-coupled structure (SCS, left) vs. annular-ring coupled structure (ACS, right)
The coupling cell of the ACS surrounds the accelerating cell circularly. Compared to the SCS, the ACS has the advantage of axial symmetry around the beam axis.

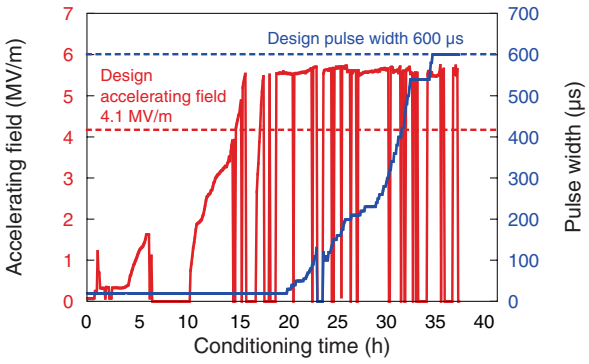

Fig.13-10 Power test result of ACS
The present ACS module was successfully conditioned up to an accelerating field of 5.3 MV/m (30% higher than the designed field of 4.1 MV/m), a pulse width of 600 μs, and a repetition rate of 50 Hz. This corresponds to an input power of 600 kW.

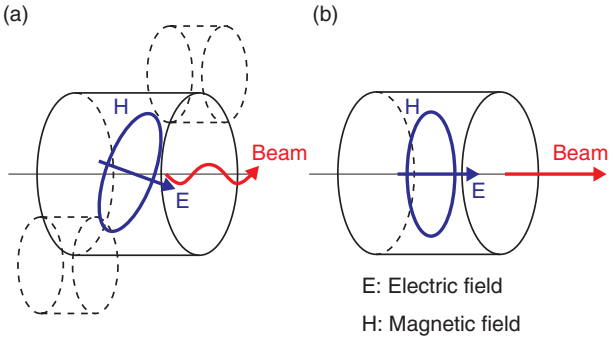

Fig.13-9 Schematic comparison of accelerating field of SCS (left) and ACS (right)
The accelerating field of the SCS contains a transverse field component of 1% due to the configuration of the coupling cell. In contrast, this component of the ACS is negligibly small because the coupling cell is axially symmetric.

The J-PARC linac is a 181 MeV linear accelerator that injects protons generated by an ion source to the Rapid Cycling Synchrotron (RCS) with a repetition rate of 25 Hz. The goal of J-PARC is to achieve a 1 MW output beam power, which would be the largest worldwide, for the Materials and Life Science Experimental Facility.

Minimizing the beam loss to maintain machine activation within the permissible level is one of the most important issues for high-intensity proton linacs, including J-PARC. The space-charge effect arising from Coulomb repulsive forces among beam particles is one of the causes of beam loss in the RCS. This effect can be reduced by increasing the injection energy of the proton beam. Thus, an injection energy upgrade of the J-PARC linac from 181 to 400 MeV is planned. An annular-ring coupled structure (ACS) has been developed for this energy upgrade (Fig.13-8).

Because of the axially asymmetric structure of the ACS, it has a negligibly small transverse accelerating field component, which kicks the proton beam perpendicularly to the beam axis and is smaller in the ACS than in the side-coupled structure (SCS) (Fig.13-9). Proton linacs use several types of accelerating structure depending on the beam energy. The ACS realizes energy efficiency and stability comparable to those of the SCS, which has been used for the same energy region as the ACS. Consequently, the injection energy can be increased while reducing the beam loss of the linac.

A prototype module for the ACS for the J-PARC linac was designed and fabricated, and it was successfully conditioned up to the designed accelerating field (Fig.13-10). This is considered to be a big step toward the energy upgrade of the linac and realization of 1 MW beam operation. A total of 25 ACS modules have been completed to date and are being prepared for installation. In FY2013, we will finish the installation and start the world's first beam acceleration by an ACS.

Reference

Ao, H. et al., First High–Power Model of the Annular–Ring Coupled Structure for Use in the Japan Proton Accelerator Research Complex Linac, Physical Review Special Topics – Accelerators and Beams, vol.15, issue 1, 2012, p.011001–1–011001–13.

13–6 Development of Domestic ^{99}Mo Production by (n, γ) Method
— Fabrication Technology for High-Density MoO_3 Pellet —

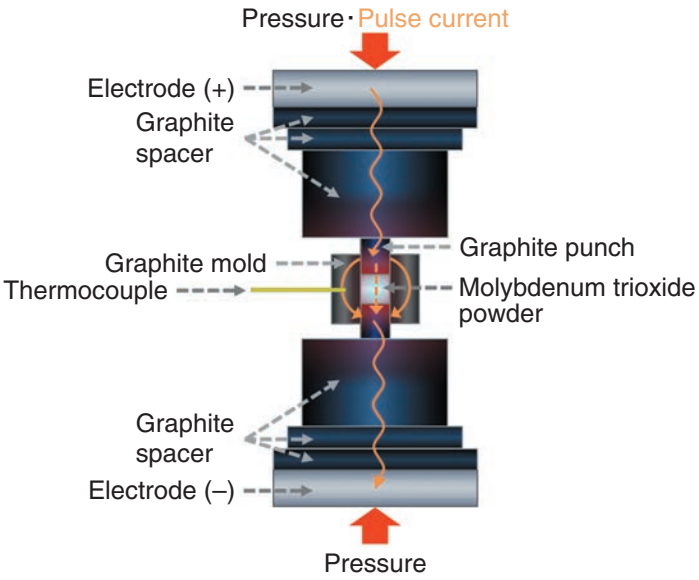

Fig.13-11 Schematic diagram of spark plasma sintering method
Starting powder is installed in graphite mold. Sintering and molding are simultaneously performed by pulse electricity under pressure. During this operation, powder surfaces are cleaned and activated, and local temperature increase produces high-density pellet under lower temperature.

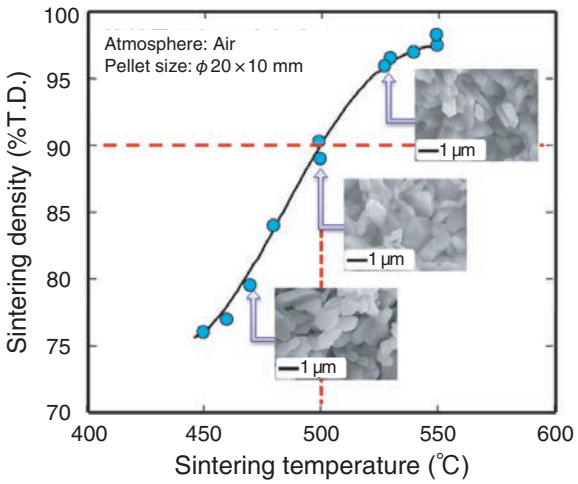

Fig.13-12 Relationship between sintering temperature and sintering density of MoO_3 pellet
The sintering density increases with increasing sintering temperature. The target density (90%T.D., T.D.: theoretical density) was attained by sintering at about 500 °C. On the other hand, changes in grain growth were not observed below a sintering temperature of 550 °C.

In Japan, about 1400000 cases are diagnosed using nuclear medicine every year. About 900000 of these nuclear medicine diagnoses use technetium-99m (^{99m}Tc), whose half-life is 6 h. ^{99m}Tc is produced as a daughter nuclide from molybdenum-99 (^{99}Mo), whose half-life is 66 h. The quantity of ^{99m}Tc demanded in Japan is ranked as second in the world, after only the U.S.A., but all of the ^{99m}Tc is imported from abroad. A stable supply of ^{99}Mo in Japan might be difficult to obtain because of troubles with transportation and other problems. Therefore, the establishment of domestic production of ^{99}Mo is an important issue for Japan. Two methods are used to produce ^{99}Mo by nuclear reactors, the nuclear fission method and the neutron activation method [(n, γ) method]. The Japan Materials Testing Reactor (JMTR) is developing the (n, γ) method for ^{99}Mo production from the viewpoints of physical protection of nuclear materials and the reduction of highly radioactive waste.

^{99}Mo is produced in molybdenum trioxide (MoO_3, sublimation temperature: 795 °C) by the (n, γ) method in nuclear reactors. Next, irradiated MoO_3 is resolved into 6M sodium hydroxide (NaOH), and then ^{99m}Tc is extracted from the solution. The technical issues in this method are the establishment of a high production rate of ^{99}Mo and the extraction of ^{99m}Tc with a high purity and radioactivity concentration. For that purpose, a fabrication method for high-density MoO_3 pellets was also developed in this study to increase the amount of ^{98}Mo per unit volume and to optimize the characteristics such as solubility.

As the first step, fabrication tests of high-density MoO_3 pellets were conducted using the spark plasma sintering method, as shown in Fig.13-11.

This method results in a high-purity pellet because no binder is added, and the sintering temperature is low. The pellet properties were measured for various sintering temperatures and sintering densities. In this result, the target density was attained by sintering at a temperature above 500 °C, as shown in Fig.13-12. Scanning electron microscopy observation of the MoO_3 pellet revealed that grain growth did not occur below a sintering temperature of 550 °C, and the grain size of the MoO_3 pellet was almost the same as that of the starting powder. Next, MoO_3 pellets were oxidized in atmosphere as an oxidization treatment, and the solubility into 6M NaOH was measured. The result confirmed that the MoO_3 pellet dissolved within the target time, and the obtained solution was clear and exhibited high purity.

The above results demonstrate that a technique for fabricating high-density MoO_3 pellets from an irradiated target was established, and the prospects are bright for domestic ^{99}Mo production by the (n, γ) method.

The present study was performed as part of the program "Technology development of domestic ^{99}Mo/^{99m}Tc production by (n, γ) method in JMTR" commissioned by the Ministry of Education, Culture, Sports, Science and Technology of Japan (MEXT).

Reference

Nishikata, K. et al., Fabrication and Characterization of High-Density MoO_3 Pellets, Proceedings of the 2012 Powder Metallurgy World Congress & Exhibition (PM 2012), Yokohama, Japan, 2012, 8p., in CD-ROM.

13–7 Corrosion Behavior of Metals in Sodium
— Compatibility of Zirconium Alloy with High-Temperature Sodium —

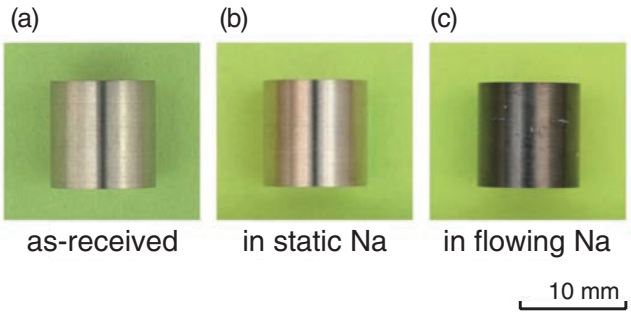

Fig.13-13 Zr alloys exposed to sodium at 500 °C for 1000 h
The surface of the specimen exposed to static sodium (b) was the same as that of the as-received specimen (a). On the other hand, the specimen immersed in flowing sodium (c) became black because dissolved oxygen in sodium penetrated.

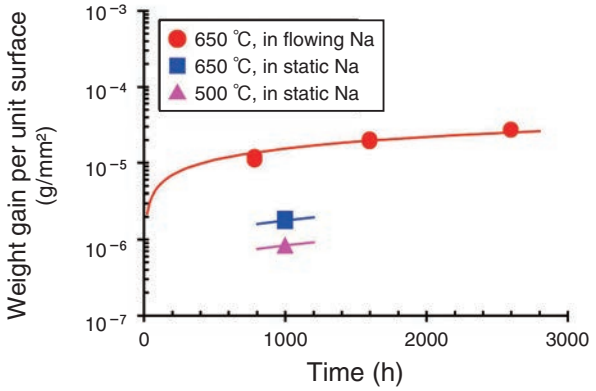

Fig.13-14 Weight change of Zr alloys in high-temperature sodium
The weight of the specimens increased in proportion to the 1/2 power of the elapsed time by oxygen diffusion into the metals. The amount of weight gain increased with increasing temperature.

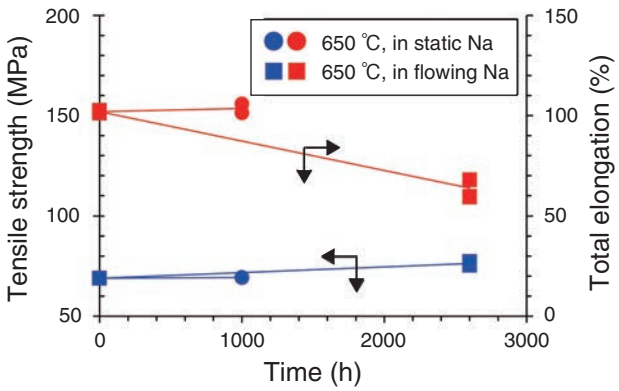

Fig.13-15 Tensile properties of Zr alloys after sodium exposure
The data for "time = 0" show the tensile properties of the as-received material. It was understood that the tensile strength increased and the total elongation decreased as the elapsed time increased.

The materials used in sodium-cooled fast breeder reactors undergo long-term exposure to high-temperature sodium. Therefore, it is necessary to estimate the compatibility of these materials with sodium, that is, the corrosion behavior and its effect on the mechanical strength, as well as the inherent mechanical properties of the materials.

For the experimental fast reactor "JOYO", the application of zirconium (Zr) alloy as a neutron reflector is being examined. The alloy does not contact sodium in the normal operating condition because it is inserted into a protective tube made from stainless steel. However, for reactor safety, it is necessary to ensure that a significant effect does not occur even if the protective tube is ruptured.

In this study, the compatibility of the Zr alloy with high-temperature sodium was examined. It was found that the surface became blackened only after exposure to flowing sodium, as shown in Fig.13-13. Moreover, a weight gain was observed with increasing temperature and elapsed time, as shown in Fig.13-14. It was due to oxygen diffusion into the Zr alloy from dissolved oxygen in the sodium. In the static sodium condition where the fill ratio of sodium was limited by the container size, the progress of oxygen diffusion was suppressed as the elapsed time increased because the amount of dissolved oxygen was also limited. On the other hand, oxygen diffusion into the Zr alloy continued in the flowing condition because dissolved oxygen was continually supplied by the flowing sodium. The behavior occurred because the affinity of Zr with oxygen was much higher than that of other steels such as stainless steel, so Zr tends to form a stable oxide thermochemically.

The mechanical properties were also changed by the environmental effect. Fig.13-15 shows the relationship between the tensile properties and the elapsed time. In flowing sodium, it was observed that the tensile strength increased and the total elongation decreased as the elapsed time increased. These were the typical embrittlement behaviors; however, the properties changed sluggishly.

We are advancing the investigation towards the application of the Zr alloy as the neutron reflector in "JOYO".

Reference

Furukawa, T. et al., Compatibility of Zirconium Alloys in High-Temperature Sodium, JAEA-Research 2011-039, 2012, 20p. (in Japanese).

13–8 Reliable Management of Instrumentation to Ensure Reactor Safety

— Establishment of Damage Detection Method for Neutron Detector in High-Temperature Gas-Cooled Reactor —

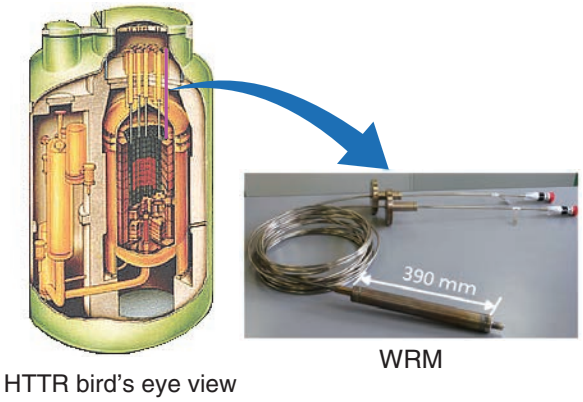

Fig.13-16 Wide-Range Monitor (WRM)
The WRM is a reactor safety instrument that is installed in the core to measure the neutron flux.

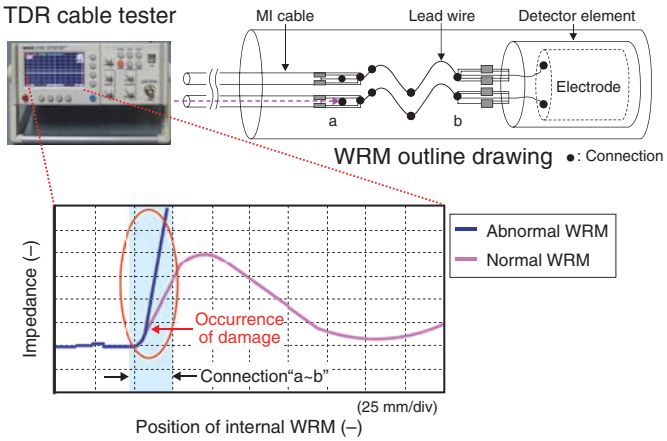

Fig.13-17 Application of electrical inspection method to WRM
Wave patterns of characteristic impedance observed by TDR in normal and abnormal WRMs are compared. For the abnormal WRM, damage was identified by recognizing a significant change in the wave pattern of the characteristic impedance around connection "a" in the figure.

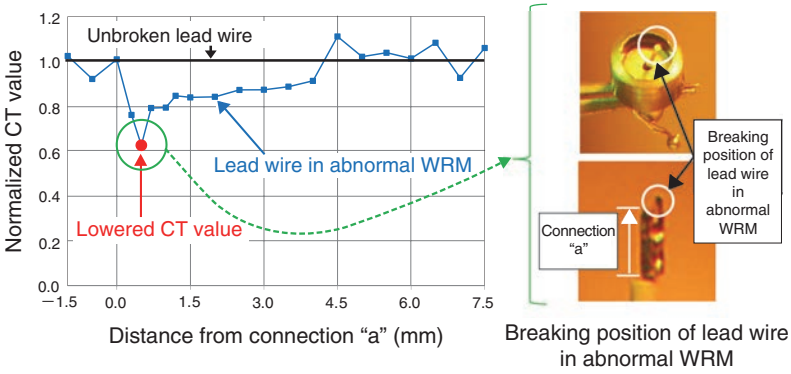

Fig.13-18 Non-destructive and destructive inspections of abnormal WRM
Non-destructive inspection showed a local decrease in the CT value at the damaged part (a broken lead wire around connection "a" as shown in outline of WRM, Fig.13-17), which was identified by the newly proposed electrical inspection method. On the other hand, the breaking of a lead wire was directly observed in the specified part by destructive inspection.

Wide-Range Monitors (WRMs) are installed inside the reactor pressure vessel of the High-Temperature engineering Test Reactor (HTTR). The WRMs are very important safety instruments that measure the neutron flux to transmit the reactor scram signal and prevent such abnormal power excursion events in the HTTR (Fig.13-16). Because the WRM is activated by neutrons, it is difficult to examine its intactness from outside of the core. For this reason, it has been expected that a reliable inspection method would be developed to guarantee its intactness in operation by detecting signs of damage to the WRM. Therefore, a new damage detection technique was examined using an electrical inspection method. An abnormal WRM, which became malfunctioning in the HTTR, was inspected in detail to verify the proposed method and also to investigate the cause of the malfunction.

Here, the selected electrical inspection method was Time-Domain Reflectometry (TDR), which is generally used to detect the breaking of cable wires. First, the observed wave patterns of the characteristic impedance of normal and abnormal WRMs were compared. As a result, the existence of damage in the lead wire of the WRM was successfully identified by recognizing a significant change in the wave pattern of the characteristic impedance (Fig.13-17). Second, non-destructive and destructive inspections were applied to the abnormal WRM to verify the result of the electrical inspection method. A high-energy X-ray Computed Tomography (CT) inspection confirmed that the CT value was lower at the same part where the damage was detected by the proposed electrical inspection method. The destructive inspection directly verified that the lead wire was broken at the specified damaged part (Fig.13-18).

Thus, a new damage detection method was established that uses electrical inspection while keeping the WRM installed in the core. The results contribute to upgrading of the High-Temperature Gas-cooled Reactor (HTGR) technology and could be a promising technology for future commercial HTGRs.

Reference
Shinohara, M. et al., Investigation on Cause of Malfunction of Wide Range Monitor (WRM) in High Temperature Engineering Test Reactor (HTTR) –Sample Tests and Destructive Tests–, JAEA-Technology 2012-032, 2012, 29p. (in Japanese).

13–9 Microfabrication of Teflon with Ion Microbeams

— Development of New Microfabrication Techniques for Polymer Surfaces —

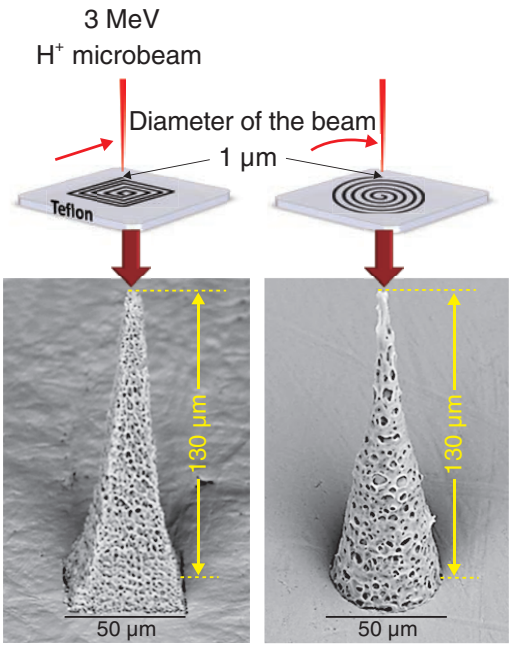

Fig.13-19 Microstructures on Teflon surfaces fabricated with scanned MeV H^+ microbeams
When a 3 MeV H^+ microbeam is scanned spirally from the center of a square or a circle, a pyramid or a cone is formed, respectively.

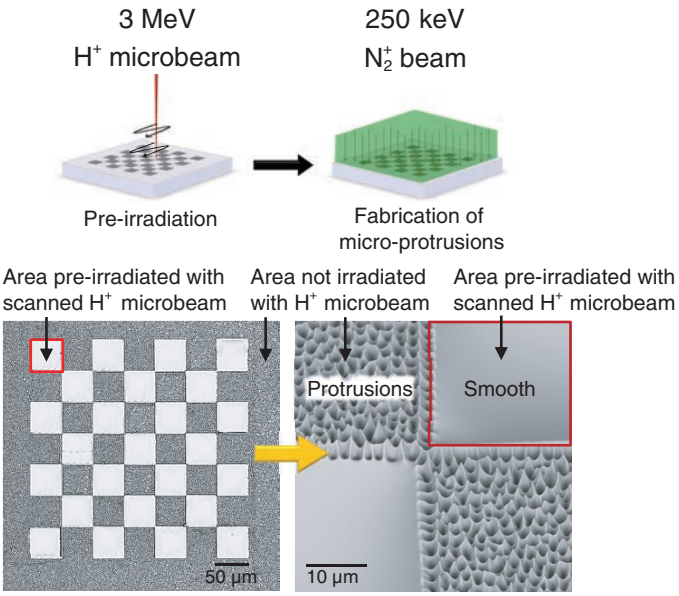

Fig.13-20 Checkerboard pattern consisting of smooth and micro-protrusion areas fabricated with a scanned H^+ microbeam before uniform N_2^+ beam irradiation
A 3 MeV H^+ microbeam is scanned horizontally to make a checkerboard pattern; subsequently, the entire surface is irradiated with a 250 keV N_2^+ beam. Only the H^+-irradiated areas become smooth.

At the TIARA ion accelerator facility at the Japan Atomic Energy Agency/Takasaki, a microfabrication technique called proton (H^+) beam writing (PBW) has been established on the basis of the techniques of focusing down an ion beam to a 1 μm spot size and scanning it arbitrarily over a target surface. Concerning the resist materials, we have demonstrated PBW's specific ability to fabricate high-aspect-ratio microstructures with chemical etching after irradiation. We have attempted to apply the technique to Teflon® (fluoropolymer), on which is difficult to fabricate microstructures because of its chemical inertness, and started research on microfabrication to be realized only with ion microbeams.

First, a revolutionary technique using a MeV H^+ microbeam was developed: fabrication of microstructures on a Teflon surface through a process of local rising (Fig.13-19). A 3 MeV H^+ beam travels in a straight line to a depth of approximately 100 μm in Teflon. Along the trajectories, main-chain scission is induced, and consequently degradation gases are formed. The amount of the gases depends on the irradiation conditions such as the beam current, irradiation time, and scanning pattern. When the gases leave the inside of a Teflon target as bubbles, they raise the irradiated area; as a result, the morphology is changed, as shown in Fig.13-19.

When a Teflon surface is irradiated with keV nitrogen molecular ion (N_2^+) beams, an initial flat surface changes into a lawn-like one covered with dense micro-protrusions. In addition, we found the conditions under which H^+ microbeam irradiation does not induce any surface morphological change due to the degradation gases but instead reduces the molecular weight. Subsequent N_2^+ beam irradiation makes the H^+-irradiated surface evaporate uniformly and very smoothly. This morphological change was also applied to make a smooth surface with micro-protrusion areas at the same ground level (Fig.13-20).

It is shown that only ion beam irradiation can enable the microfabrication of chemically inert materials without any chemical processes. We intend to expand this technique to various materials other than Teflon.

Reference

Kitamura (Ogawa), A. et al., Microfabrication on Teflon Surface by MeV–Proton–Microbeam and keV–Nitrogen–Ion–Beam Irradiation, Nuclear Instruments and Methods in Physics Research B, vol.307, 2013, p.610–613.

13–10 Excavation of Galleries at -500 m Depth

— Construction of Shafts and Research Galleries for the Mizunami Underground Research Laboratory —

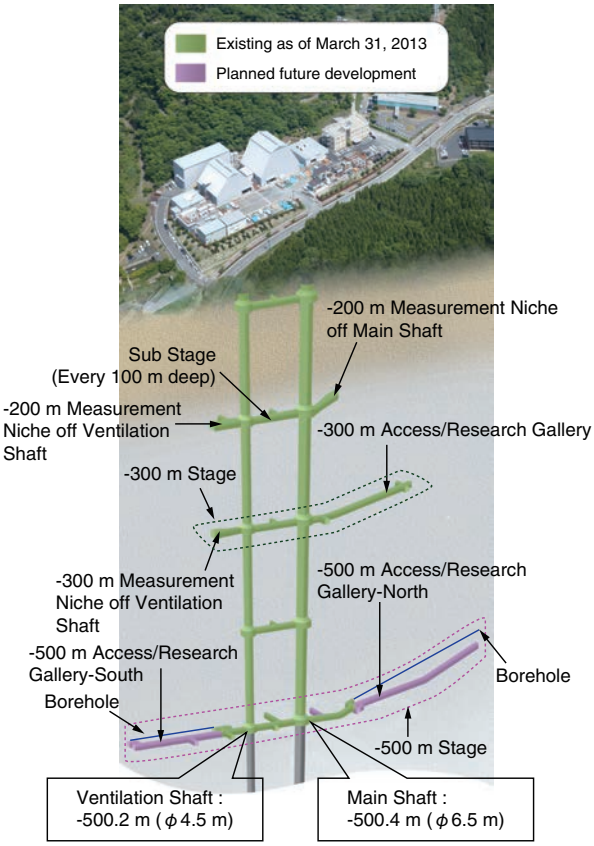

Fig.13-21 Layout of the Mizunami Underground Research Laboratory
Layout shows existing Shafts and Research Galleries on March 31, 2013 and planned future development.

Fig.13-22 -500 m Access/Research Gallery-North
View is from -500 m A/R Gallery-North (5 m wide, 4.5 m high) toward Main Shaft.

Fig.13-23 Borehole investigation site
View shows borehole investigation in Measurement Niche in -500 m A/R Gallery-North.

The Mizunami Underground Research Laboratory is currently under construction in Mizunami City. As of March 2013, approximately 150 m of horizontal excavations were completed for the GL -500 m stage (meters below ground level, Figs.13-21, 13-22).

To mitigate the potential excess groundwater inflow, pre-excavation grouting was conducted before excavating the shafts and galleries. Grouting is the injection of material such as cement into open fractures in a rock mass to stabilize and seal the rock. While planning the construction of the URL, it was necessary to obtain reliable preliminary information on the bedrock conditions in terms of the rock mass stability and hydrogeology. Therefore, site characterization borehole investigations were conducted prior to any excavations. These investigations indicated that potentially large groundwater inflows could occur during excavation of the Ventilation Shaft at around GL -200 m, from GL -400 m to -460 m and near the -300 m Access/Research Gallery.

Borehole investigations were also conducted before excavation of the Research Galleries at GL -500 m to obtain reliable information on the bedrock conditions (Fig.13-23). These investigations indicated that high conductivity of the rock mass, in the range of 10^{-7} -10^{-5} m/sec, could occur during excavation of the -500 m A/R Gallery-South. Therefore pre-excavation grouting was conducted before the excavation of the shafts and galleries at this depth.

In planning the construction, the target for reduction in water inflow was established by theoretical analysis of the groundwater flow in terms of the bedrock conditions. Observations during the excavations indicate that the pre-excavation grouting was successful and that the targeted reduction in inflow was achieved. Thus, the results indicate that this methodology is effective in reducing water inflow.

Reference

Ishii, Y., Ikeda, K. et al., Results and Considerations on the Pre-Excavation Grouting below Four Hundreds Meter Depth of the Ventilation Shaft, JAEA-Technology 2010-044, 2011, 92p. (in Japanese).

13–11 Investigation of Properties of Radon Hot Springs
— Radon-Induced Biological Responses and Its Biokinetics —

Fig.13-24 Animal test chamber for radon inhalation

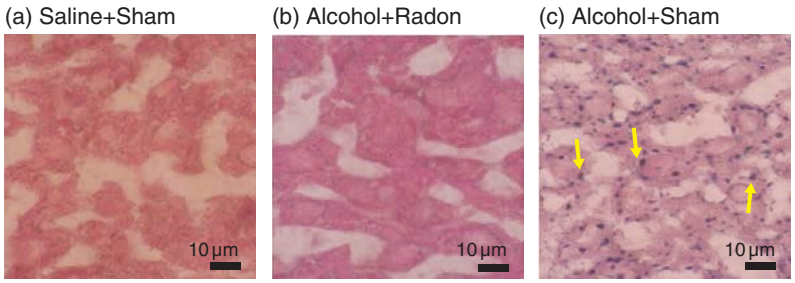

Fig.13-25 Radon inhalation inhibits alcohol-induced oxidative injury in mouse liver

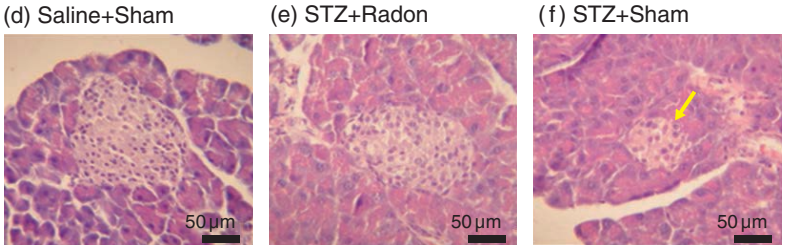

Fig.13-26 Radon inhalation inhibits Streptozocin (STZ)-induced diabetes in mouse pancreas

According to legend, one of the hot springs in Misasa, Tottori was first found in 1164, about 850 years ago. Misasa means “third morning” in Japanese and was named for another legend that people who went there for a hot spring cure were healed completely by the third morning. The hot springs in Misasa are famous worldwide due to the high radon concentration of the water. The Misasa hot springs are believed to stimulate the body’s healing mechanism and enhance immunity, especially against reactive-oxygen- or free-radical-related diseases. There is some possibility that radon, a radioactive noble gas, plays an important role in these properties.

Okayama University and JAEA Ningyo-toge have conducted a collaborative study of the physiological effects of inhaled radon in the low-dose range. The main assignments were as follows. On the basis of clinical knowledge, Misasa Medical Center (Okayama University Hospital) clarified the issues that should be addressed. The Graduate School of Health Sciences (Okayama University) supervised the research and studied the biological responses. The JAEA Ningyo-toge developed and controlled a facility for radon inhalation experiments and the investigation of the biokinetics and exposure doses of radon. From 2007 to 2011, the following results were obtained.

- The first Japanese large-scale facility was developed for radon inhalation experiments with small animals (Fig.13-24).
- The relationships between the radon concentration and inhalation time, which are the most basic parameters, were widely examined to understand the change in antioxidative functions due to radon.
- The inhibitory effects of radon on oxidative damage were observed using model mice with reactive-oxygen- or free-radical-related diseases such as alcohol-induced oxidative damage and type I diabetes (Figs.13-25, 13-26).
- To discuss the biological responses to radon inhalation quantitatively, the biokinetics of inhaled radon was examined, and a model for the calculation of absorbed doses for organs and tissues was obtained.

A comprehensive discussion, including considerations of the radiation risk and safety, is required.

Reference

Ishimori, Y. et al., Animal Study on Biological Responses by Radon Inhalation Making Use of Waste Rock Which Contains Feeble Activity of Uranium (Joint Research), JAEA-Research 2013-005, 2013, 60p. (in Japanese).

About the Design of the Cover

The cover is designed to envisage a hopeful future shining in the sky, which is a clear blue resembling the color of the JAEA logo. This is accompanied by white hexagons similar to the pattern in a tortoise shell, an ancient Japanese symbol of people's wish for longer lives. Coincidentally, this shape is the same as that of core fuel assemblies for both the prototype fast breeder reactor "MONJU" and the high-temperature engineering test reactor "HTTR".

The images on the cover show the dose rate distribution map around the Tokyo Electric Power Company, Incorporated (TEPCO) Fukushima Daiichi Nuclear Power Station (NPS), which was traced out using an unmanned helicopter (top left), and atomic-scale cesium absorption on a type of zeolite called mordenite (bottom right).

The former shows the results of the dose rate at 1 m above the ground, which were converted from monitoring data obtained by a flight at 80 m above the ground around the TEPCO's Fukushima Daiichi NPS (from 3 km to 5 km from 1F) by a radiation monitoring system using an unmanned helicopter. The dose rate was normalized to that on March 21, 2013, which was the last day of measurement (Topic 1-3, p.14).

The latter shows that mordenite, a type of zeolite, is effective for cesium decontamination. We numerically simulated cesium absorption on mordenite at the atomic scale (Topic 1-19, p.30).

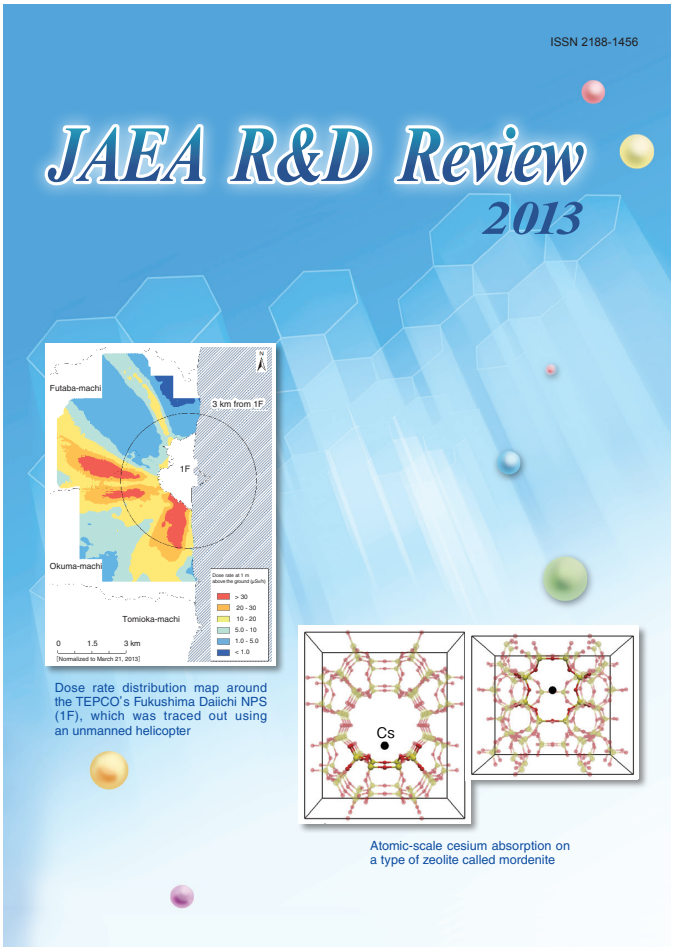

JAEA R&D Review 2013

Published by
Japan Atomic Energy Agency in February 2014

This publication is issued by Japan Atomic Energy Agency (JAEA) on a yearly basis.
Inquiries about availability and/or copyright of the contents in this publication should be addressed to Intellectual Resources Section, Intellectual Resources Department, Japan Atomic Energy Agency.

Address: 2-4 Shirane, Shirakata, Tokai-mura, Naka-gun, Ibaraki-ken 319-1195, Japan
Phone: +81-29-282-6387, **Facsimile:** +81-29-282-5920, **e-mail:** ird-seika_shi@jaea.go.jp

Japan Atomic Energy Agency